THE UNIVERSITY
of EDINBURGH

Single-Photon Avalanche Diode Receivers for Optical Wireless Communications

Elham Sarbazi

A thesis submitted for the degree of Doctor of Philosophy.

School of Engineering
The University of Edinburgh

2019

Abstract

Single-photon avalanche diodes (SPADs) have been widely applied in many applications over the past few decades thanks to their high sensitivity, high photon detection efficiency and high timing resolution. Nowadays, they are drawing particular attention in the field of optical wireless communication (OWC), resulting in wider and deeper studies among the scientific research community. Compared with positive-intrinsic-negative (PIN) diodes and avalanche photodiodes (APDs), SPADs provide much higher internal gains and sensitivities, thereby easily overcoming the thermal noise and enabling the detection of individual photons without the need for transimpedance amplifiers (TIAs). However, upon detecting a photon, the SPAD is unable to respond to subsequent incident photons for a certain period of time, called dead time. This dead time is caused by the quenching circuit, which is of two principal modes: active quenching (AQ) and passive quenching (PQ). Depending on the structure of this circuit, the dead time can be constant or variable, in any case, it degrades the photon counting performance of the SPAD.

In this thesis, a comprehensive analytical approach is presented for modelling the counting statistics of SPAD detectors in the presence of dead time. To the best of author's knowledge, this is the first in-depth study of the impact of dead time in the context of OWC. Using the concepts of arrival processes and renewal theory, the exact photocount distributions and the count rate models are derived for AQ and PQ single SPADs. It is shown that, unlike ideal photon counting detectors, in AQ and PQ single SPADs, the photocounts do not follow a Poisson distribution. The results confirm that AQ single SPADs generally exhibit less counting losses and therefore, higher count rates compared to PQ single SPADs and the count rate gap in high photon rate regimes is substantial. It is also shown that the photocount distribution of a SPAD array can be well approximated by a Gaussian distribution, for which the mean and variance are dead time dependent. The numerical results suggest that as the size of the array increases, the gap between the photon counting performance of AQ and PQ SPAD arrays tends to vanish.

Furthermore, in this thesis, the bit error performance of SPAD-based OWC systems with AQ single SPADs, PQ single SPADs and AQ SPAD arrays are evaluated. The results show that the SPAD dead time significantly degrades the bit error ratio (BER) of the systems. The system with an AQ single SPAD exhibits better BERs compared to the system with a PQ single SPAD. The effect of dead time is mitigated to some extent when an array is employed. The analytical and Monte Carlo simulation results are provided for various dead time values, background count levels and SPAD array sizes.

From a communication theory point of view, the dead time also limits the achievable data rate of SPAD-based systems. In this thesis, the information transfer rate of SPAD detectors is also investigated. To this end, the SPAD is modelled as a communication channel. Using an information theoretic approach, the channel capacity and the capacity-achieving input distributions for AQ single SPADs and AQ SPAD arrays are obtained for various dead time values, background count levels, and array sizes.

Lay summary

Single-photon avalanche diodes (SPADs) are highly sensitive devices capable of detecting very weak light signals. Nowadays, they are drawing particular attention in the field of optical wireless communication (OWC), resulting in wider and deeper studies among the scientific research community. Thermal noise is one of the main sources of noise in any electronic circuit. In most of the light detectors, the thermal noise is considerable and it significantly limits the sensitivity of the device. SPADs can overcome this noise thanks to their unique operating mechanism, thereby offering very high sensitivities. This makes them a promising candidate for OWC applications dealing with very weak light levels or involving data transmissions through long distances.

During the light detection, the SPAD experiences inevitable periods of inactivity, called dead time. Depending on the SPAD physical structure, this dead time can be constant or variable, in any case, it degrades the SPAD light detection performance. In particular, when the SPAD is used as a receiver in an OWC system, the dead time results in data loss.

In this thesis, the impact of dead time is deeply studied. A novel analytical method is proposed for modelling the detection process of a SPAD detector considering the effect of different types of dead time. First, a single SPAD is studied, and then the approach is extended to an array of multiple SPADs. The detailed mathematical analyses lead to a number of novel expressions, which are straightforward to use in other researches. In addition, the accuracy of the proposed models are evaluated and compared with the experimental results available in the literature.

The proposed models are then applied to study the performance of SPAD-based communication systems. The effects of a number of parameters and different signalling schemes are addressed, however, the focus is on investigating the impact of dead time. In SPAD-based OWC systems, the relative length of dead time compared to the system time slots is the determining factor, rather than the absolute length of dead time. The results in this thesis show that in systems employing single SPADs, if this relative length is small, the data loss is negligible. However, for larger values, the system error probability is significantly increased. From this study, it is also found that SPAD arrays are more robust to the dead time, and sufficiently large arrays can tolerate dead time periods equal to the system time slots without any noticeable increase in the error probability.

In OWC systems, the system time slots during which data is transmitted, determine the data transmission speed, i.e. the data rate. However, the presence of dead time does not allow the use of arbitrarily short time slots. In the last part of this thesis, the impact of dead time, and a number of other parameters on the information rate of single SPADs and SPAD arrays are studied. The optimum signalling schemes for achieving the highest information rates are numerically obtained. The results show that the limiting effect of dead time on the maximum achievable information rate is mitigated in SPAD arrays, and they can offer higher information rates.

Declaration of originality

I hereby declare that the research recorded in this thesis and the thesis itself were composed and originated entirely by myself in the Light-Fidelity (Li-Fi) Research and Development (R&D) Centre, Institute for Digital Communications, School of Engineering, University of Edinburgh.

Elham Sarbazi

Acknowledgements

This thesis would not have come into being, if it were not for the help and support of many wonderful people. I would like to foremost express my deepest gratitude to my supervisor, Professor Harald Haas, who gave me the opportunity to pursue my Ph.D. on a novel research area. He is an ever sparkling fountain of ideas and enthusiasm and has taught me to be a confident researcher. I am grateful to his consistent guidance, support and encouragement for hard work.

Also, I am indebted to Dr. Majid Safari for spending hours in his office, having substantial and constructive discussions on how a single photon can put us into trouble. Although, I was not his Ph.D. student, he treated me as one of his own. Many thanks to Professor Robert Henderson, Dr. Edward Fisher, Oscar Almer, and John Kosman for their invaluable help through discussions, suggestions and experiments. I would also like to acknowledge and thank our principal assistant and my wonderful friend, Ms. Hannah Brown, for her continuous support and assistance in proofreading my research papers and this thesis.

My Ph.D. journey would not have been possible without the support of my colleagues and all my friends from home and abroad. I will never forget the enjoyable moments we spent together and all the laughter we shared. I am not attempting to write down a list of all past and present friends and colleagues, as I am sure that I will forget someone. But, a special thanks goes to my lifelong friend, Raziyeh, for lending me an ear during difficult times and for reminding me of my capabilities, strengths and goals.

My warmest gratitude goes to my parents and my lovely sisters who have always supported me throughout my life. I will be forever indebted to my family for their endless love and trust. Without them, I would not have been where I am today.

Last, but not least, I would like to express my wholehearted gratitude to my husband, Hossein, for his unconditional love, support, encouragement, and patience during my studies. He never fails to put a smile on my face and did a great job in keeping me entertained, while writing up this thesis. The least I can do is to dedicate this thesis to my beloved ones, Hossein and my family.

Contents

List of figures

Acronyms and abbreviations

ACO-OFDM	Asymmetrically Clipped Optical OFDM
AGSDN	Additive Gaussian Signal-Dependent Noise
APD	Avalanche Photodiode
AQ	Active Quenching
BER	Bit Error Ratio
BPPM	Binary Pulse Position Modulation
CDF	Cumulative Distribution Function
CG	Conditionally Gaussian
CLT	Central Limit Theorem
CMOS	Complementary Metal-Oxide-Semiconductor
DCO-OFDM	DC-biased Optical OFDM
DD	Direct Detection
DMC	Discrete Memoryless Channel
DMOS	Double-diffused Metal-Oxide-Semiconductor
FET	Field-Effect Transistor
FF	Fill Factor
FSC	Finite-State Channel
FSO	Free Space Optics
FWHM	Full-Width at Half Maximum
Ge	Germanium
GF	Generating Function
HD	Hard Decision
iid	Independent and Identically Distributed
IM	Intensity Modulation

IM/DD	Intensity Modulation and Direct Detection
InGaAs	Indium Gallium Arsenide
IR	Infrared
ISI	Inter-Slot Interference
LED	Light Emitting Diode
LD	Laser Diode
LIDAR	Light Detection and Ranging
LPF	Lowpass Filter
LT	Laplace Transform
MIMO	Multiple-Input Multiple-Output
ML	Maximum Likelihood
MLSD	Maximum-Likelihood Sequence Detection
MPPC	Multi-Pixel Photon Counter
OFDM	Orthogonal Frequency Division Multiplexing
OOK	On-Off Keying
OSC	Optical Scattering Communication
OWC	Optical Wireless Communication
PAM	Pulse Amplitude Modulation
PWM	Pulse Width Modulation
PD	Photodetector
PDE	Photon Detection Efficiency
PDF	Probability Density Function
PET	Positron Emission Tomography
PIN	Positive-Intrinsic-Negative
PMF	Probability Mass Function
PMT	Photomultiplier Tube
PN	Positive-Negative
PPM	Pulse Position Modulation
PQ	Passive Quenching

RF	Radio Frequency
SD	Soft Decision
Si	Silicon
SiPM	Silicon Photomultiplier
SNR	Signal-to-Noise Ratio
SPAD	Single-Photon Avalanche Diode
TCSPC	Time-Correlated Single Photon Counting
TH	Threshold
TIA	Transimpedance Amplifier
ToF	Time of Flight
UWC	Under Water Communication
UWVLC	Under Water Visible Light Communication
UV	Ultraviolet
VL	Visible Light
VLC	Visible Light Communication

Nomenclature

Mathematical and physical constants

π	3.141592654	Ratio of the circumference over the diameter of a circle
e	2.718281828	Base of the natural logarithm (Euler's number)
h	$6.626 \times 10^{-34}\mathrm{J.s}$	Planck constant
k_B	$1.380 \times 10^{-23}\mathrm{J/K}$	Boltzmann constant
q_e	$1.602 \times 10^{-19}\mathrm{C}$	Electron charge

Mathematical operators and functions

$\delta(\cdot)$	Dirac delta function
$\Gamma(\cdot)$	Gamma function
$\Gamma(\cdot,\cdot)$	Incomplete Gamma function
$\mathbb{E}[\cdot]$	Statistical expectation
$\exp(\cdot)$	Natural exponential function
$\log_2(\cdot)$	Logarithm in base 2
$\mathrm{Q}(\cdot)$	Q-function
$U(\cdot)$	Unit step function

Mathematical and physical variables and functions

$\gamma(s,x)$	An auxiliary mathematical function
δ	Dead time ratio
ζ	Carrier ionization ratio in APD
η	Quantum efficiency
η_array	Power gain of SPAD array
$\mathit{\Lambda}$	Rate or intensity of the Poisson arrival process (for SPAD arrays)
$\mathit{\Lambda}_\mathrm{n}$	Background noise intensity (for SPAD arrays)
$\mathit{\Lambda}_\mathrm{s}$	Optical signal intensity (for SPAD arrays)
$\mathit{\Lambda}'$	SPAD array effective count rate
$\mathit{\Lambda}'_\mathrm{AQ}$	AQ SPAD array effective count rate

Λ'_{PQ}	PQ SPAD array effective count rate
λ	Rate or intensity of the Poisson arrival process (for single SPADs)
λ_{n}	Background noise intensity (for single SPADs)
λ_{s}	Optical signal intensity (for single SPADs)
λ'	Single SPAD effective count rate
λ'_{sat}	SPAD saturation count rate
μ_0	Mean of a Poisson counting process
μ_{n}	Mean of the number of photocounts for a bit '0'
μ_I	Mean of the photocurrent $i(t)$
μ_K	Mean of the number of photocounts K
μ_{sn}	Mean of the number of photocounts for a bit '1'
ν	Optical frequency
ξ	Variance to mean ratio of the number of photocounts
σ_0^2	Variance of a Poisson counting process
σ_{n}^2	Variance of the number of photocounts for a bit '0'
σ_I^2	Variance of the photocurrent $i(t)$
σ_K^2	Variance of the number of photocounts K
σ_{sn}^2	Variance of the number of photocounts for a bit '1'
σ_{dark}^2	Shot noise variance due to dark current
σ_{load}^2	Thermal noise variance due to load resistor
σ_{shot}^2	Shot noise variance
$\sigma_{\mathrm{shunt}}^2$	Thermal noise variance due to shunt resistance
σ_{th}^2	Thermal noise variance
τ	SPAD dead time
τ_1	Dead time of detected photons
τ_2	Dead time of lost photons
$\Phi(s)$	LT of $\phi(t)$
$\Phi^{\mathrm{p}}(s)$	LT of $\phi^{\mathrm{p}}(t)$
$\phi(t)$	Probability of no events in $(0, t]$, given one event at $t = 0$
$\phi^{\mathrm{p}}(t)$	Probability of no events in $(0, t]$, given one event at $t = 0$, in paralyzable mode
ψ_x	Input constellation
ψ_p	Input probability measure

$\psi_x^*(\mathcal{A}, \mathcal{E})$	Capacity-achieving input constellation
$\psi_p^*(\mathcal{A}, \mathcal{E})$	Capacity-achieving input probability measure
$\psi(i, \lambda)$	An auxiliary mathematical function
$\mathcal{A}$	Peak power constraint
$\mathcal{A}_{\mathrm{x}}, \mathcal{A}_{\mathrm{y}}$	Alphabet sets of X and Y
$A_i(z)$	Auxiliary mathematical functions
B	LPF single-sided bandwidth
BER	Bit error ratio
b	Number of mass points
C	Channel capacity
C^{HD}	AQ single SPAD capacity with HD binary signalling
C^{SD}	AQ single SPAD capacity with SD binary signalling
C_{FF}	FF coefficient of the SPAD array
$\mathcal{E}$	Average power constraint
$f_1(t)$	Product density of order one
$f_1^{\mathrm{p}}(t)$	Product density of order one in paralyzable mode
$f_2(t_1, t_2)$	Product density of order two
$f_k(t_1, t_2, \ldots, t_k)$	Product density of order k
F	APD excess noise factor
$F_1(s)$	LT of $f_1(t)$
$F_1^{\mathrm{p}}(s)$	LT of $f_1^{\mathrm{p}}(t)$
$f_{W_i}(w_i)$	PDF of W_i
G	Random variable for the APD gain
g	APD average gain
$G(z, t)$	GF of $p(k, t)$
$g(z, s)$	LT of $G(z, t)$
H_0, H_1	Binary hypotheses
$h(t)$	Receiver impulse response
$H(X), H(Y)$	Entropies of X and Y
$h(X), h(Y)$	Differential entropies of X and Y
$H(\mathcal{X})$	Entropy rate of $\mathcal{X}$
$H(Y\|X)$	Entropy of Y conditioned on X
$h(Y\|X)$	Differential entropy of Y conditioned on X

I	Information rate
I_{dark}	Average dark current
I_{ds}	Average surface leakage current
I_{db}	Average bulk leakage current
I_{L}	Lower bound on the SPAD array capacity
I_{U}	Upper bound on the SPAD array capacity
$I_{\mathrm{L}}^{\mathrm{HD}}$	Lower bound on the capacity of AQ single SPAD with HD binary signalling
$I_{\mathrm{L}}^{\mathrm{SD}}$	Lower bound on the capacity of AQ single SPAD with SD binary signalling
$I_{\mathrm{U}}^{\mathrm{HD}}$	Upper bound on the capacity of AQ single SPAD with HD binary signalling
$I_{\mathrm{U}}^{\mathrm{SD}}$	Upper bound on the capacity of AQ single SPAD with SD binary signalling
$I(X;Y)$	Mutual information between X and Y
$I(\mathcal{X};\mathcal{Y})$	Information rate between $\mathcal{X}$ and $\mathcal{Y}$
$i(t)$	Photocurrent
$i_{\mathrm{dark}}(t)$	Dark current
$i_{\mathrm{th}}(t)$	Thermal noise current
K	Random variable for the number of photocounts
$K(t)$	Number of events in the interval $(0,t]$
$\widetilde{K}(t,t')$	Number of events in the interval $(t-t']$
K_{n}	Average number of background noise photons in a bit interval (for single SPADs)
$\overline{K_{\mathrm{n}}}$	Average K_{n} per bit interval (for single SPADs)
$K_{\mathrm{n}}^{\mathrm{a}}$	Average number of background noise photons in a bit interval (for SPAD arrays)
K_{s}	Average number of signal photons in a bit interval (for single SPADs)
$\overline{K_{\mathrm{s}}}$	Average K_{s} per bit interval (for single SPADs)
$K_{\mathrm{s}}^{\mathrm{a}}$	Average number of signal photons in a bit interval (for SPAD arrays)
k	Instant realization of K
$k_{\max}$	Maximum number of photocounts
k_{th}	Optimum threshold of OOK (for single SPADs)
$L(k), L(s)$	Likelihood ratio

M	Random variable for the number of released electrons in APD
m	Instant realization of M
N	Random variable for the number of background noise photons in the SPAD channel
N_{array}	Number of SPAD array elements
N_{dc}	Average number of dark carriers
n	Instant realization of N
P_{e}	Probability of error
P_{n}	Background noise power
P_{s}	Optical signal power
$P(k,s)$	LT of $p(k,t)$
$P_X(x)$	CDF of X
$P_X^*(\mathcal{A},\mathcal{E})$	Capacity-achieving CDF of X with peak and average power constraints
$\mathcal{P}_X$	Set of all admissible $P_X(x)$'s
p_{a}	Avalanche probability
p_{dc}	Dark count probability
$p_0(k)$	PMF of a Poisson counting process
$p_1(k)$	Probability of k photocounts corresponding to $\{\mathcal{R}_1\}$
$p_2(k)$	Probability of k photocounts corresponding to $\{\mathcal{R}_2\}$
$p_{\text{n}}(k)$	Probability of k photocounts for a bit '0'
$p_{\text{sn}}(k)$	Probability of k photocounts for a bit '1'
$p_K(k)$	PMF of K, the SPAD dead time-modified photocount distribution
$\tilde{p}_K(k)$	The single SPAD dead time and ISI-modified photocount distribution
$p_M(m)$	PMF of M
$p_S(s)$	PMF of S
$\tilde{p}_S(s)$	The SPAD array dead time and ISI-modified photocount distribution
$p_X(x)$	PMF of X
$p_Y(x)$	PMF of Y
$p_{XY}(x,y)$	Joint probability of X and Y
$p_{Y\|X}(y\|x)$	Conditional probability of Y given X
$p^{(k)}(t_1,t_2,\ldots,t_k)$	Joint probability density for the first k arrival times t_1, t_2, …, t_k
$p(k,t)$	Probability of k events during the interval $(0,t]$
PDE	Photon detection efficiency

q	*a priori* probability for a bit '1' in binary signalling
R_{b}	Data rate
R_{dc}	Dark count rate
R_{L}	Load resistor
R_{s}	Photodiode shunt resistance
R_{q}	Quenching resistor
$\{\mathcal{R}\}, \{\mathcal{R}_1\}, \{\mathcal{R}_2\}$	Sets of admissible arrival time values
$\mathcal{S}$	Stochastic process corresponding the channel states
S	Random variable for the number of photocounts in SPAD array
s	Instant realization of S
s_{th}	Optimum threshold of OOK (for SPAD arrays)
SNR	Signal-to-noise ratio
$\mathrm{SNR}_{\mathrm{SL}}$	Shot-noise-limited SNR
$\mathrm{SNR}_{\mathrm{QL}}$	Quantum-limited SNR
T	Counting interval
T_{b}	Bit interval
T°	Temperature (in Kelvin)
T°_{eq}	Equivalent temperature (in Kelvin)
$\{t_i\}$	Photon arrival time sequence
$\{w_i\}$	Inter-arrival time sequence
V_{bias}	Bias voltage
V_{br}	Breakdown voltage
V_{ex}	Excess bias voltage
V_{S}	SPAD output voltage
V_{th}	Threshold voltage
W_i	Random variable for the inter-arrival times
w_i	Instant realization of W_i
$\mathcal{X}$	Stochastic process corresponding the channel inputs
X, X_i	Random variables for the SPAD channel input
x, x_i	Instant realizations of X and X_i
$\mathcal{Y}$	Stochastic process corresponding the channel outputs
Y, Y_i	Random variables for the SPAD channel output
y, y_i	Instant realizations of Y and Y_i

Chapter 1
Introduction

1.1 Motivation

Optical wireless communication (OWC) has been proposed as a complementary technology to radio frequency (RF) data communication and as a potential solution to the exponential increase in demand for wireless data transmission. An OWC system relies on optical signals to convey information through the atmosphere whether in terrestrial (indoor or outdoor links) or satellite applications. The optical frequencies range from infrared (IR) to ultraviolet (UV), including the visible light (VL) spectrum. The total bandwidth available in the optical spectrum is several hundreds of THz, which is much wider than the RF spectrum [1]. Apart from this abundant spectral resource, other advantages of OWC over RF communication include, but are not limited to [2]: i) the optical spectrum is unlicensed; ii) the optical signal does not interfere with RF-based wireless systems; and iii) OWC can be used in radio radiation restricted environments.

The high speed OWC has been achieved with significant advances in optoelectronic devices, which are employed as the front-end elements in OWC systems. At the transmitter side, the key front-end device is the light source which converts the electrical signal to an optical signal. Additionally, optics are used to shape the emission pattern of the light source. The conventional light sources in OWC systems include light emitting diodes (LEDs) and laser diodes (LDs) [3]. LEDs are semiconductor devices with p-n junctions. An electric current flow through the p-n junction generates photons by spontaneous radiation, releasing energy in the form of light. Generally, LEDs have a diffused emission pattern. The emission pattern defines the angular dependence of the LED output optical power. With decades of research and development, highly efficient LEDs have been manufactured and utilized in a wide range of applications [3, 4]. LDs are typically composed of an optical cavity inside which the carriers and photons are confined in order to maximize their chances for stimulated radiation and light generation. Compared to LEDs, LDs operate at higher levels of driving current. In addition, LDs have higher electrical-to-optical conversion efficiencies and wider modulation bandwidths.

However, they are more expensive than LEDs, and their highly focused emission pattern is a drawback on account of eye safety regulations. This necessitates the use of appropriate optics to convert the LD output into a diffused emission pattern in indoor communication and lighting applications [3].

At the receiver side, light sensing devices, i.e. photodetectors (PDs), are the key element. Furthermore, optical filters and concentrators may be used to improve the connection quality. In OWC systems, positive-intrinsic-negative (PIN) diodes and avalanche photodiodes (APDs) are widely used as PDs. A PIN diode is a diode with a wide, undoped intrinsic semiconductor region between two heavily doped p-type and n-type semiconductor regions. When a large reverse biased voltage is applied across the diode, an electrical field is established and the flow of free electrons and holes, caused by arriving photons, produces a photocurrent. PIN diodes have no internal gain mechanism, hence, they are unity gain PDs. Since PIN diodes are semiconductor devices, depending on the choice of the semiconductor materials, the responsivity of these PDs varies at different wavelengths. The bandwidth of PIN diodes ranges from several hundreds of MHz to more than 100 GHz [3, 5].

APDs operate with much higher reverse bias voltages than the PIN diodes. In APDs, the impact ionization and avalanche multiplication mechanisms lead to high internal gains in the range of 50–500. Consequently, APDs have higher responsivities compared with PIN diodes. However, the avalanche effect also results in gain-dependent excess noise and extra sensitivity to temperature changes. Typical bandwidths of APDs range from 100 MHz to 4 GHz in visible wavelengths [3, 5].

The PIN diodes and APDs have been successfully used in practical OWC links. However, the performance of these PDs is not satisfactory in photon starving conditions such as long distance links of space optical communications [6], gas well downhole monitoring systems [7], and data transmission over plastic optical fibres [8]. In such cases, the optical signal may be received at levels below the sensitivity of these PDs and get lost in the thermal noise, despite the use of high gain transimpedance amplifiers (TIAs). Therefore, a PD with a much higher sensitivity is required to achieve the desired performance. Recently, a novel single-photon detector, namely single-photon avalanche diode (SPAD), has been proposed for OWC scenarios involving extremely low signal levels [9, 10]. SPAD is also a semiconductor device with a p-n junction. The SPAD is operated in the so-called *Geiger mode*, in that it is biased beyond its breakdown voltage. So, the absorption of a single photon can initiate an avalanche of charge

carriers, leading to a very large internal gain. The extremely high gain allows single photons to be detected effectively [11–13]. After each photon detection, the SPAD needs to be quenched to recover from the excess charge carriers, and this is accomplished by a proper electronic circuit known as the *quenching circuit*. The unavoidable *dead time* caused by the quenching circuits, is a major concern when designing the SPAD photodetectors, as it can considerably degrade the photon counting performance [14–16].

Although the history of single-photon detectors dates back to 1920s [17], the first efforts for developing solid-state single-photon detectors were made in the late 1960s after the invention of APDs. In 1989, Cova [18] introduced the Geiger mode operation of the APDs and this opened the way for the development of SPAD devices. Since this first demonstration, many groups have contributed internationally to remarkable improvements in the device performance. The major advances happened in the early 2000s, when the SPADs were implemented within complementary metal-oxide-semiconductor (CMOS) processes [19–21].

The physical characteristics of the SPAD devices are well defined in literature [22–27]. The device limitations have been examined through extensive experiments [15, 16, 28, 29]. However, SPADs have just recently found applications in the OWC domain, and are not fully characterized from a communication perspective. Many questions regarding their performance reliability for OWC applications are still unanswered. Therefore, it is necessary to deeply understand the characteristics and limitations of these devices from a communication theory point of view and analyse their performance in this context.

1.2 Contribution

This thesis investigates the application of SPAD PDs in OWC where the SPAD is characterized from a communication theory perspective. There are a number of contributory factors playing a role in the SPAD photon counting functionality, among which the dead time is the most impactful one. Therefore, this research primarily focuses on the dead time effects. This thesis aims at addressing the following three research objectives in a systematic approach:

- Establishing a statistical model for the photon counting process of the SPAD.
- Evaluating the error performance of SPAD-based OWC systems.
- Finding the capacity of the SPAD receiver.

By following these objectives, several contributions have been made.

With regard to the first objective, the aim is to derive dead time-modified photon counting distributions for the SPAD. The effect of dead time on the count rate of SPAD PDs has been widely studied in the literature. The existing count rate models are not exact, but provide reasonable estimations of the SPAD actual count rate [29–31]. Some other useful metrics, such as blocking probability and photon detection efficiency, have also been proposed in this context [32–34]. However, non of them provides a complete description of the SPAD photon counting process which is required for the performance evaluation of SPAD-based communication systems. As the first contribution of this thesis, a comprehensive analytical framework is proposed for modelling the statistical behaviour of the SPADs in the presence of dead time. The rigorous analysis is established based on the concepts of arrival processes and renewal processes. Exact analytical expressions are derived for the probability mass function (PMF), mean and variance of the SPAD photocounts. Also, exact count rate models are established and compared with the existing models in the literature. The study is conducted for both single SPADs and SPAD arrays and expounds the effect of various dead time types imposed by different quenching circuits, including active quenching (AQ), passive quenching (PQ), and mixed AQ/PQ circuits. These analytical derivations and mathematical modellings are published in [35–37].

Following the second research objective leads to the second contribution of this thesis: the error performance analysis of SPAD-based OWC systems. A major concern for employing

SPAD PDs in communication systems is whether the existence of dead time causes significant data loss during the data reception. This question is addressed for SPAD-based OWC systems with on-off keying (OOK) and binary pulse position modulation (BPPM). Separate case studies are considered for OWC systems consisting of AQ and PQ single SPADs and SPAD arrays. For OOK modulation, the optimum threshold for minimizing the error probability is derived. In addition, the effects of a number of other factors, such as background counts and array size on the error performance of the system are discussed. The work conducted on the performance evaluation of SPAD-based OWC systems has led to the publication of [37].

Regarding the third objective, the dead time is a major issue in high data rate links. It results in inter-slot interference (ISI) and severely degrades the bit error ratio (BER) of the system in high data rates. Thus, the presence of dead time does not allow the use of arbitrarily narrow time slots and limits the maximum achievable data rate. As the third contribution of this thesis, the SPAD is modelled as a communication channel with memory. Using an information theoretic approach, the information transfer rates and the capacity of the SPAD channel are investigated. In particular, two case studies are considered. In the first study, the capacity of single SPADs with a binary signalling scheme is analysed. In the second study, the capacity of SPAD arrays with a pulse amplitude modulation (PAM) signalling is investigated. In each study, two auxiliary discrete memoryless channels (DMCs) are proposed and an upper bound and a lower bound on the capacity are developed. For the regimes where the bounds are tight and the auxiliary channels well characterize the SPAD channel, the properties of the capacity-achieving input distributions are discussed. Furthermore, using a numerical algorithm, the capacity and the capacity-achieving input distributions, subject to peak and average power constraints, are presented for various array sizes, dead time values and background count levels. Part of the research conducted on the capacity of SPAD PDs has led to [38, 39] and the rest is under preparation for publication.

1.3 Layout

The rest of this thesis is organised as follows. Chapter 2 provides the relevant background for understanding the operating principle of photon counting receivers. First, the concept of photodetection is presented and then the conventional PDs used in OWC systems are reviewed. In particular, the performance specifications of PIN diodes and APDs, in terms of noise, gain, bandwidth and signal-to-noise ratio (SNR) are reported from the literature. Furthermore, a brief overview of the applications of the SPADs is given. Also, the operating mechanism and the main performance metrics of SPAD receivers are discussed.

In Chapter 3, the photon counting behaviour of SPAD receivers in the presence of dead time is precisely modelled. The concepts of arrival processes and renewal theory are applied for deriving the exact dead time-modified photocount distributions of AQ, PQ, and mixed AQ/PQ single SPADs. The approach is also extended to the case of SPAD arrays.

In Chapter 4, the error performance evaluation of SPAD-based OWC systems is presented. First, OWC systems with single SPAD receivers are considered and the impact of AQ and PQ dead times on the BER of OOK and BPPM systems is studied. Several case studies are considered to analyse the effect of various dead time durations, signal and background count levels. The analysis is then extended to OWC systems with SPAD array receivers.

In Chapter 5, the impact of dead time on the input-output information transfer rate of the SPAD receivers is investigated. The SPAD is modelled as discrete channel with memory. Upper and lower bounds on the information rates and the capacity of the SPAD channel are provided. The capacity of AQ single SPADs is analysed for a binary signalling scheme, and for AQ SPAD arrays, a PAM signalling scheme is addressed.

In Chapter 6, the key findings of this thesis are summarised, and some concluding remarks are provided. Finally, the limitations of the presented work are discussed along with possible future directions.

Chapter 2
Background

Optical wireless communication (OWC) technology was first developed over a hundred years ago and recently has attracted a renewed interest. In this chapter, a short overview of the OWC technology is given. The photodetectors (PDs) commonly used in OWC systems are then reviewed. The principal function of a PD is converting the received optical signal into an electrical current through the photodetection process. The underlying physical characteristics of the photodetection process allow each PD to have its own unique features, satisfying specific application requirements. Conventional photodetectors in OWC systems are positive-intrinsic-negative (PIN) diodes and avalanche photodiodes (APDs). In this chapter, both of these PDs are referred to. In particular, the details of the physical mechanism of operation, noise properties and performance specifications in terms of gain, bandwidth and signal-to-noise ratio (SNR) are reported from the literature. In photon starving applications and long distance transmissions, the optical signal may be received at levels below the sensitivity of PIN diodes and APDs. In such applications, single-photon detectors are employed which can enable detection of individual photons without the need for transimpedance amplifiers (TIAs). For decades, photomultiplier tubes (PMTs) have been the primary choice for OWC systems among various single-photon detectors. However, they are being replaced by single-photon avalanche diodes (SPADs) due to their numerous disadvantages. In this chapter, SPADs are introduced and their operating mechanism and main performance metrics are reviewed. The related works are also discussed in this chapter.

The rest of this chapter is organized as follows. The literature review on the OWC systems and the conventional PDs is given in Section 2.1. In Section 2.2, the SPAD PDs are discussed in detail. Section 2.3 covers the related works. A summary of this chapter is provided in Section 2.4.

2.1 Optical Wireless Communication (OWC) Systems

The purpose of designing any communication system is to transfer information from one point to another. This is accomplished by modulating the information onto an electromagnetic carrier wave, which is propagated to the destination. The electromagnetic wave is then received and the information is recovered. Depending on the location of the carrier frequency in the electromagnetic spectrum, various categories of communication systems are realized: radio systems, microwave or millimetre systems, and optical systems [1].

In recent years, OWC has attracted substantial attention. An OWC system relies on optical signals to convey information through the atmosphere whether in terrestrial (indoor or outdoor links) or satellite applications. The optical frequencies range from infrared (IR) to ultraviolet (UV) including the visible light (VL) spectrum. This abundant spectral resource is a potential solution for satisfying the ever increasing demand for wireless capacity. Apart from its high capacity, OWC offers inherent security while remaining cost effective [1].

The block diagram of a generic OWC system with intensity modulation and direct detection (IM/DD) is shown in Fig. 2.1. At the transmitter side, intensity modulation (IM) is employed where the information is modulated onto the intensity of an optical signal. This is achieved by changing the driving current of an optical source directly in accordance with the transmitted data or using an external modulator. Light emitting diodes (LEDs) and laser diodes (LDs) are widely used as the optical sources in OWC systems in order to convert the input electrical signal into the corresponding optical signal. Some transmitter optics might be used for collimating and directing the optical signal towards the receiver at the other end of the optical channel. The receiver is composed from receiver optics, a PD, and a TIA, if necessary, followed by a demodulator. The optics help to collect and focus the received optical beam to the PD. To minimize the effects of background noise collected by optical elements with large apertures, the received signal is usually required to pass through an optical filter before reaching the PD. After being amplified by the TIA, the original signal is recovered by the demodulator. This detection process is known as direct detection (DD), meaning that the receiver detects the instantaneous intensity or power of the optical signal reaching the PD.

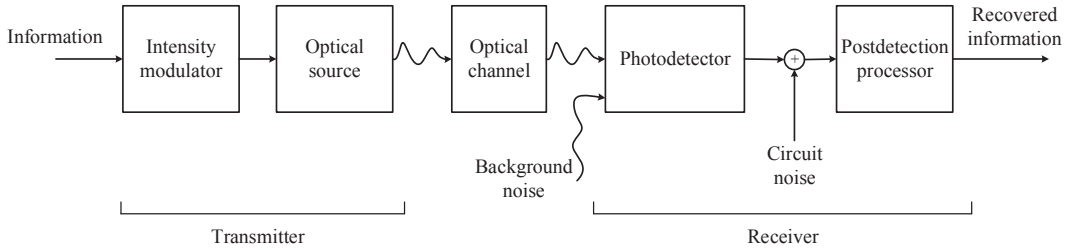

Figure 2.1: *Block diagram of an OWC system [1].*

2.1.1 Photodetection

The key task of a PD is *photodetection*, i.e. converting the collected light field into a current or voltage waveform for subsequent postdetection processing. It is necessary to take into account the characteristics of the photodetection operation when designing a PD for a specific application. Particularly, in OWC applications, the system performance depends explicitly on the statistics of the PD output, thus a proper mathematical model of the PD is required for designing the optimum detection and decoding schemes.

Photodetection is achieved by using a photosensitive material to respond to incident photons by producing free charge carriers. These carriers are forced to drift in a given direction by an externally applied electric field. This carrier flow is seen as a current flow at the PD output. The general photodetection operation can be represented by the simplified diagram in Fig. 2.2 showing the incident light beam and the external bias circuitry producing the output current flow. The output photocurrent can also be converted to a voltage by passing through a load resistor [1, 5].

Typical PDs in OWC applications are primarily of two types: phototube devices and solid-state devices. In phototubes, the free carriers are produced from a photosensitive material and are released into a vacuum cavity, where they are collected by a charged anode plate. The PMT is a phototube device with very high sensitivity [1, 5]. Despite their unique sensitivity, PMTs have various disadvantages which will be discussed later in this chapter. Therefore, they are being replaced by solid-state devices in many applications. In solid-state devices, the incident photons excite electrons at a positive-negative (PN) junction, and the photocurrent corresponds to an electron flow across the junction [1, 5]. The most widely employed solid-state devices in OWC systems are PIN diodes and APDs [1, 5].

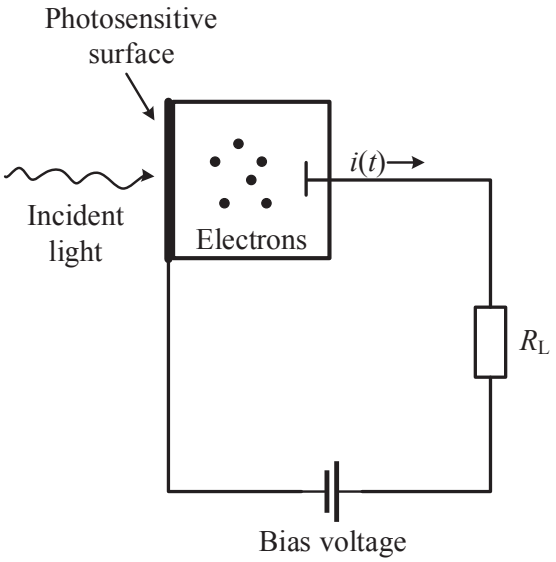

Figure 2.2: *The basic photodetection model [1, 5].*

If during the photodetection, the excited electrons regenerate additional free carriers, the *photomultiplication* happens. As a result of this phenomenon, the accumulated current flow is many times higher than for the primary carriers alone. In phototube devices, photomultiplication can be achieved by using multiple anode plates to produce secondary electron emissions and in solid-state devices by avalanching effects [1, 5].

The optical to electrical conversion and the photomultiplication process are both probabilistic in nature, and the output photocurrent always evolves as a random process in time. As the PD induces its inherent randomness when responding to any optical field (whether stochastic or not), this randomness must be properly accounted for in the system design [1].

2.1.2 Photodetectors

The detection of optical radiation differs from conventional radio frequency (RF) field detection in that the optical signal intensity, not the amplitude of the field, is detected [1]. The basic physical principle of operation in solid-state PDs is the same. However, they differ in the subsequent processing of the photogenerated carriers. In the following, the PIN diodes and APDs are reviewed in detail.

2.1.2.1 Positive-Intrinsic-Negative (PIN) Diodes

A PIN diode is easy to fabricate. It is basically a diode with a wide, undoped intrinsic semiconductor region between two heavily doped p-type and n-type semiconductor regions. As a PD, the PIN diode is reverse biased. Under reverse bias and in the absence of light radiation only a small leakage current will flow through the diode. When an incident photon of sufficient energy strikes the diode, an electron-hole pair may be generated. The ratio of the number of carriers generated by the PD to the number of photons incident on the PD is known as the *quantum efficiency* and is denoted by η. The quantum efficiency depends on the photosensitive material of the diode and also the optical wavelength. The reverse bias electric field rapidly sweeps the charge carriers out of the junction creating a photocurrent pulse [1, 5, 40, 41].

Commercially available PIN diodes are typically made of silicon (Si), germanium (Ge) or indium gallium arsenide (InGaAs). Ge and InGaAs PIN diodes have high quantum efficiencies ($> 80\%$) in the IR region (~ 1500 nm). Si PIN diodes have even higher quantum efficiencies, but can only detect wavelengths below the band gap of Si (~ 1100 nm) [5, 40]. PIN diodes are unity gain devices, i.e. there is no internal gain mechanism. Therefore, the bandwidth of PIN diodes is limited only by the time it takes the carriers to travel through the depletion region. With their fast response times, bandwidths of more than 100 GHz can be easily achieved, making them ideal for high speed OWC applications [5, 40].

Counting Statistics

Let the incident optical signal power and the background noise power be denoted by P_{s} and P_{n}, respectively. Even if the incident optical power is constant, the number of detected photons, k, is random and usually modelled by an ergodic and wide-sense stationary Poisson random process with the following probability mass function (PMF) [1, 41]:

$$p_0(k) = \frac{\mu_0^k}{k!} e^{-\mu_0}, \tag{2.1}$$

where μ_0 denotes the average number of detected photons during a time interval of length T, and is given by [1, 41]:

$$\mu_0 = \frac{\eta(P_{\mathrm{s}} + P_{\mathrm{n}})T}{h\nu}, \tag{2.2}$$

where h is the Planck constant and ν is the optical frequency. If μ_0 is relatively large, the Poisson process can be approximated with a Gaussian process [42]. It is very common to use the terms *intensity* or *rate* as the average number of photons per second. If the intensities of the received optical signal and the collected background noise be denoted by $\lambda_{\rm s}$ and $\lambda_{\rm n}$, respectively, then $\lambda_{\rm s} = \eta P_{\rm s}/h\nu$ and $\lambda_{\rm n} = \eta P_{\rm n}/h\nu$ [1].

Noise Sources

The main types of noise commonly associated with the PIN diodes are: photocurrent shot noise, dark current shot noise and thermal noise. The photocurrent shot noise is the random fluctuations of the PIN diode photocurrent and arises from the input signal and/or background radiation. This shot noise is modelled as a Gaussian process with a variance of [1, 41]:

$$\sigma^2_{\rm shot} = 2q^2_{\rm e}(\lambda_{\rm s} + \lambda_{\rm n})B, \tag{2.3}$$

where $q_{\rm e}$ is the electron charge and B is the single-sided bandwidth of the postdetection lowpass filter (LPF) with a unit transfer function.

Other than the photocurrent shot noise, the PIN diode dark current also contributes to the shot noise effects [1, 41]. The dark current is the relatively small current that flows through the PIN diode in the absence of any external radiation. The PIN diode dark current consists of two components: the diode surface leakage current and the bulk leakage current. The surface leakage current originates from some minority charge carriers generated on the photosensitive surface of the device. The bulk leakage current arises from the generation of some minority carriers in the depletion region. Denoting the average dark current by $I_{\rm dark}$, the average surface leakage current by $I_{\rm ds}$ and the average bulk leakage current by $I_{\rm db}$, we have $I_{\rm dark} = I_{\rm ds} + I_{\rm db}$. Typical values for $I_{\rm dark}$ vary from 1 to 10 nA for Si-based PIN diodes, from 50 to 500 nA for Ge-based PIN diodes, and from 1 to 20 nA for InGaAs-based PIN diodes [41]. The variance of the dark current shot noise is given by [1, 41]:

$$\sigma^2_{\rm dark} = 2q_{\rm e}I_{\rm dark}B. \tag{2.4}$$

The photocurrent shot noise and dark current shot noise are also known as *external* and *internal quantum noises*, respectively [43].

The thermal noise in PIN diodes can arise from the photodiode shunt resistor, $R_{\rm s}$, which is typically on the order of 100 kΩ to 1 GΩ. The corresponding internal thermal noise is modelled as a zero mean Gaussian process of variance [40, 41]:

$$\sigma^2_{\rm shunt} = \frac{4k_{\rm B}T^{\circ}B}{R_{\rm s}}\,, \tag{2.5}$$

where $k_{\rm B}$ is the Boltzmann constant and T° is the temperature (in Kelvin). In addition to the PD self thermal noise, the electronic circuitry also produces major thermal noise. This noise component is mainly caused by the load resistor, $R_{\rm L}$, and is modelled as a zero mean Gaussian process of variance [40, 41]:

$$\sigma^2_{\rm load} = \frac{4k_{\rm B}T^{\circ}B}{R_{\rm L}}\,. \tag{2.6}$$

Other post-amplification components (e.g. the TIA) and the LPF circuitry also add some thermal noise to the signal. To take them into account, usually T° in (2.6) is replaced by an equivalent temperature $T^{\circ}_{\rm eq}$. Therefore, the PIN diode thermal noise is modelled as a zero mean Gaussian process of variance $\sigma^2_{\rm th} = \sigma^2_{\rm shunt} + \sigma^2_{\rm load}$ [40, 41].

Photocurrent

The output photocurrent of the PIN diode is the superposition of the PD response to the absorbed photons, plus the device dark and thermal noise currents [1, 40]:

$$i(t) = \sum_{\{t_j\}} q_{\rm e} h(t - t_j) + i_{\rm dark}(t) + i_{\rm th}(t). \tag{2.7}$$

In (2.7), the summation is extended over the photon arrival times $\{t_j\}$, $h(t)$ is the receiver impulse response, $i_{\rm dark}(t)$ is the PD dark current, and $i_{\rm th}(t)$ is the thermal noise current. It is commonly assumed that the PIN diode photocurrent has a Gaussian distribution, $\mathcal{N}(\mu_I, \sigma_I^2)$, with [40, 41]:

$$\mu_I = q_{\rm e}(\lambda_{\rm s} + \lambda_{\rm n}) + I_{\rm dark}, \tag{2.8a}$$

$$\sigma_I^2 = \sigma^2_{\rm shot} + \sigma^2_{\rm dark} + \sigma^2_{\rm th}, \tag{2.8b}$$

where $\sigma^2_{\rm shot}$ and $\sigma^2_{\rm dark}$ are given in (2.3) and (2.4), respectively. Also, $\sigma^2_{\rm th} = \sigma^2_{\rm shunt} + \sigma^2_{\rm load}$ with $\sigma^2_{\rm shunt}$ and $\sigma^2_{\rm load}$ provided in (2.5) and (2.6), respectively.

Signal-to-Noise Ratio

The direct detection *electrical* SNR with a PIN diode is given by [1]:

$$\mathrm{SNR} = \frac{\left(q_{\mathrm{e}}\lambda_{\mathrm{s}}\right)^2}{2B\left[q_{\mathrm{e}}^2(\lambda_{\mathrm{s}}+\lambda_{\mathrm{n}}) + q_{\mathrm{e}}I_{\mathrm{dark}} + \frac{2k_{\mathrm{B}}T^{\circ}}{R_{\mathrm{s}}} + \frac{2k_{\mathrm{B}}T_{\mathrm{eq}}^{\circ}}{R_{\mathrm{L}}}\right]}. \tag{2.9}$$

The main disadvantage of PIN diodes in OWC systems is their low gain. When operating at extremely low signal levels, the thermal noise generated by the PD itself can be more significant than the signal. This thermal-noise-limited situation can severely degrade the SNR of the system and increase the error probability.

2.1.2.2 Avalanche Photodiodes (APDs)

APDs are similar to PIN diodes, in that they operate under the reverse bias condition [5, 40, 41]. However, unlike PIN diodes, APDs operate with high internal electric fields. Thereby, the released carriers are accelerated to high velocities and are able to ionize other carriers through a mechanism known as *impact ionization*. The secondary carriers in turn generate additional carriers. When carriers undergo many consecutive impact ionizations, an avalanche photomultiplication occurs, such that the APD output current flow is many times larger than that of a PIN diode [1, 5, 40, 41]. In fact, the avalanche breakdown provides an internal gain which enables the PD to operate above its own thermal noise limit. The impact ionization process and the avalanche breakdown are random processes. Thus, each primary carrier is associated with a random gain, G, where the gains associated with different photon detection events are independent [1, 40]. The exact distribution of g is difficult to characterize [44, 45]. However, for most practical applications, it is sufficient to characterize the APD by its excess noise factor F, defined as [1, 5, 46]:

$$F = \frac{\mathbb{E}\left[G^2\right]}{\mathbb{E}^2\left[G\right]}. \tag{2.10}$$

where $\mathbb{E}\left[\cdot\right]$ denotes the expected value. Denote by g the average gain of the APD, that is $g = \mathbb{E}\left[G\right]$. The excess noise factor is usually approximated by $F = g^x$ where x is some exponent obtained through experiments. For example, x is between 0.2 and 0.5 for Si-based APDs [40]. The average APD gain, g, depends on the bias voltage and is typically in the range of 100 to 500 for Si APDs and 10 to 40 for most Ge and InGaAs APDs [1, 5, 40].

The excess noise factor is a function of the carrier ionization ratio, ζ, where ζ is usually defined as the ratio of hole to electron ionization probabilities. According to Mclntyre's model, F is related to ζ by [44]:

$$F = g\zeta + (1-\zeta)(2-\frac{1}{g}). \tag{2.11}$$

The Mclntyre's model given in (2.11) considers the statistical nature of the avalanche multiplication. For a well designed APD, ζ should be much smaller than 1. Typical values for ζ are between 0.002 to 0.06 for Si APDs, 0.7 to 1 for Ge APDs, and 0.4 to 0.7 for InGaAs APDs, respectively [44–46].

Furthermore, the response time, and hence, the bandwidth of the APD depends on ζ. After the initial avalanche, the signal persists until no further avalanche is detected. In the best case where $\zeta = 0$, the detector response time is limited only by the time it takes for a single electron to travel through the avalanche region. Typical bandwidths of the APD range from 100 MHz to 4 GHz for visible wavelengths [1, 5].

Counting Statistics

Similar to the PIN diode, in the APD, the number of absorbed photons k (also known as the primary counts) follows a Poisson distribution given by (2.1) with the mean value given in (2.2). In response to these k photons, the APD generates m electrons with the conditional probability distribution $\Pr\{m|k\}$ derived by McIntyre in [44] and experimentally verified by Conradi in [45]:

$$\Pr\{m|k\} = \frac{k\Gamma(\frac{m}{1-\zeta}+1)}{m(m-k)!\,\Gamma(\frac{\zeta m}{1-\zeta}+k+1)} \times \left[\frac{1+\zeta(g-1)}{g}\right]^{\frac{k+\zeta m}{1-\zeta}} \left[\frac{(1-\zeta)(g-1)}{g}\right]^{m-k}, \tag{2.12}$$

where $\Gamma(\cdot)$ is the gamma function. The PMF of m is obtained by averaging the above expression over the Poisson distributed random variable k:

$$p_M(m) = \sum_{k=0}^{\infty} \Pr\{m|k\} p_0(k). \tag{2.13}$$

In [47], Webb has provided an approximation to (2.13) which is given by:

$$p_M(m) = \frac{1}{\sqrt{2\pi g A}\left(1+\frac{B(F-1)}{A}\right)^{3/2}} \times \exp\left(-\frac{B^2}{2gA\left(1+\frac{B(F-1)}{A}\right)}\right), \tag{2.14}$$

where $A = g\mu_0 F$, $B = m - g\mu_0$ and $m \geq -g\mu_0/(F-1)$. The PMF in (2.14) provides a much simpler expression for analytical calculations. When $\mu_0 F/(F-1)^2$ is large, the distribution in (2.14) can be further approximated by a Gaussian distribution [47].

Noise Sources

The principal noises at the output of an APD are: photocurrent shot noise, dark current, and thermal noise. Modelling these noises is different from the PIN diode case, as the effect of the avalanche breakdown should be taken into account. The variance of the photocurrent shot noise is given by [1, 41]:

$$\sigma^2_{\rm shot} = 2g^2 F q_{\rm e}^2(\lambda_{\rm s} + \lambda_{\rm n})B. \tag{2.15}$$

In APDs, the bulk leakage current is gain-dependent and is amplified by the APD gain. Therefore, the average dark current of the APD is expressed as $I_{\rm dark} = I_{\rm ds} + gI_{\rm db}$. The typical values for $I_{\rm dark}$ vary from 0.1 to 1 nA for Si APDs, 50 to 500 nA for Ge APDs, and 1 to 5 nA for InGaAs APDs [41]. The shot noise arising from the dark current is modelled as a Gaussian process with variance [1, 41]:

$$\sigma^2_{\rm dark} = 2q_{\rm e}\left(g^2 F I_{\rm db} + I_{\rm ds}\right)B. \tag{2.16}$$

In contrast to PIN diodes, the APD self thermal noise is insignificant. This is due to the large internal gain of the APD. However, the thermal noise contribution of the TIA load resistor, $R_{\rm L}$, and the electronic circuitry is considerable. This thermal noise is modelled as a zero mean Gaussian process of variance [1, 41]:

$$\sigma^2_{\rm th} = \frac{4k_{\rm B}T^{\circ}_{\rm eq}B}{R_{\rm L}}\,. \tag{2.17}$$

Another type of noise in APDs is the noise associated with the avalanche gain mechanism. When the avalanche process is generated by carriers of higher mobility, the avalanche noise is

smaller and can be ignored. The reason for this is that the carriers with higher mobility spend less time within the avalanche region and consequently, a smaller number of secondary carriers can induce further ionizations. Thus, the avalanche noise becomes negligible.

Photocurrent

The output photocurrent of an APD is expressed as [40]:

$$i(t) = \sum_{\{t_j\}} g_j q_{\mathrm{e}} h(t - t_j) + i_{\mathrm{dark}}(t) + i_{\mathrm{th}}(t), \tag{2.18}$$

where g_j is the gain associated with the jth photon detection event, and $h(t)$ is the APD impulse response. The mean and variance of the APD output photocurrent are given by Campbell's theorem [40, 41]:

$$\mu_I = g q_{\mathrm{e}}(\lambda_{\mathrm{s}} + \lambda_{\mathrm{n}}) + g I_{\mathrm{db}} + I_{\mathrm{ds}}, \tag{2.19a}$$

$$\sigma_I^2 = \sigma_{\mathrm{shot}}^2 + \sigma_{\mathrm{dark}}^2 + \sigma_{\mathrm{th}}^2. \tag{2.19b}$$

where σ_{shot}^2, σ_{dark}^2 and σ_{th}^2 are given in (2.15), (2.16) and (2.17), respectively.

Signal-to-Noise Ratio

The direct detection *electrical* SNR of the APD is given by [1, 40]:

$$\mathrm{SNR} = \frac{(g q_{\mathrm{e}} \lambda_{\mathrm{s}})^2}{2B\left[g^2 F q_{\mathrm{e}}^2(\lambda_{\mathrm{s}} + \lambda_{\mathrm{n}}) + g^2 F q_{\mathrm{e}} I_{\mathrm{db}} + q_{\mathrm{e}} I_{\mathrm{ds}} + \dfrac{2k_{\mathrm{B}} T_{\mathrm{eq}}^{\circ}}{R_{\mathrm{L}}}\right]}, \tag{2.20}$$

which can also be written as:

$$\mathrm{SNR} = \frac{\lambda_{\mathrm{s}}}{2B\left[F(1 + \dfrac{\lambda_{\mathrm{n}}}{\lambda_{\mathrm{s}}}) + \dfrac{F I_{\mathrm{db}}}{q_{\mathrm{e}} \lambda_{\mathrm{s}}} + \dfrac{I_{\mathrm{ds}}}{g^2 q_{\mathrm{e}} \lambda_{\mathrm{s}}} + \dfrac{2k_{\mathrm{B}} T_{\mathrm{eq}}^{\circ}}{g^2 q_{\mathrm{e}}^2 \lambda_{\mathrm{s}} R_{\mathrm{L}}}\right]}. \tag{2.21}$$

According to (2.21), a high gain reduces the effects of both the dark current and the thermal noise. As a result, APDs with high gains tend to have less noise and are more sensitive. When the dark current and the thermal noise are negligible in (2.21), the APD is called

shot-noise-limited [1]. In this case:

$$\mathrm{SNR_{SL}} \triangleq \frac{{\lambda_\mathrm{s}}^2}{2BF(\lambda_\mathrm{s}+\lambda_\mathrm{n})}\,. \tag{2.22}$$

The shot-noise-limited SNR depends only on λ_s and λ_n. Increasing g beyond the point at which the shot-noise-limited operation is achieved does not further improve SNR. If the background noise intensity λ_n is strong relative to the optical signal intensity λ_s, (2.22) can be approximated as [1]:

$$\mathrm{SNR} \approx \frac{{\lambda_\mathrm{s}}^2}{2BF\lambda_\mathrm{n}}\,. \tag{2.23}$$

The detected SNR improves as the square of λ_s. Denoting by $\lambda_\mathrm{s}/\lambda_\mathrm{n}$ the *optical* SNR, (2.23) particularly shows that a low value of optical SNR does not necessarily mean a low electrical SNR. If $\lambda_\mathrm{s} \gg \lambda_\mathrm{n}$, (2.22) becomes [1]:

$$\mathrm{SNR_{QL}} \triangleq \frac{\lambda_\mathrm{s}}{2B}\,. \tag{2.24}$$

The above SNR is called the *quantum-limited* SNR of the APD, and denotes the maximum SNR obtainable during the photodetection. Even if the background and circuit noises are attenuated, the maximum SNR does not increase without bound, but rather approaches the quantum-limited value given in (2.24) [1]. This is because of the inherent shot noise effects in OWC systems. In fact, OWC systems appear to have an additive quantum noise added during the photodetection, even in the absence of all circuit and background noise sources. This quantum noise places an ultimate limit on the APD performance. Also, according to (2.24), the APDs with low quantum efficiencies produce reduced quantum-limited SNRs, and this is why the APD efficiency can significantly affect the overall system performance [1].

2.1.2.3 Towards Higher Sensitivities: Single-Photon Detectors

When the detection of extremely weak optical signals is required, the direct detection SNR of the PIN diodes and the APDs degrades appreciably because of the strong thermal and/or background noise. That's where single-photon detectors can be of great help. Numerous types of single-photon detectors exist, each with their own set of unique features. Among them are PMTs, members of the class of phototubes. The PMT is a vacuum tube containing a photosensitive surface called *photocathode*, an *electron multiplier*, and an output terminal known as *anode*. The electron multiplier is a series of secondary electrodes known as *dynodes*

which create an avalanche effect [1, 5].

The photodetection process in the PMT can be described as follows: When an incident photon is absorbed, a primary electron is generated at the photocathode. For larger light intensities several primary electrons are generated almost simultaneously. The electric field, established by the bias network, accelerates the electron towards the first dynode in the tube. Upon reaching the first dynode, the electron creates secondary electrons that are also accelerated by the electric field towards the second dynode. This trend continues until the electrons hit the anode. By this time, the primary electron has been amplified considerably. Therefore, with every single photon, a large average number of electrons, and thus, a very high current gain, is produced at the anode. PMTs typically have gains in the range of 10^5 to 10^6. Consequently, the PMT thermal noise is usually insignificant and the PMTs are essentially quantum-limited devices with very high sensitivities [1, 5].

However, providing such high gains requires high bias voltages (1 to 3 kV). In addition, since the output photocurrent is so high, the device is required to be electrically reset following each photon detection. This leads to a *dead time* during which no further photon can be detected. Also, because of the time it takes the electrons to traverse the dynode chain, PMTs have an inherent bandwidth limitation. Typical bandwidths for PMTs are around $20 - 200$ MHz. Such bandwidths are considerably lower than the desired information bandwidth in high speed OWC systems. Some PMTs employ a magnetic field in addition to the electric field in order to reduce the temporal dispersion of the electrons and to obtain a faster response [1, 5].

While various materials may be used for the photocathode depending on the wavelength range of interest, traditional vacuum PMTs generally exhibit the best sensitivity in the short visible and UV ranges. Thereby, the lack of suitable materials at the long visible and near IR wavelengths is a significant disadvantage. The PMT quantum efficiency is typically on the order of $10 - 20\%$ at visible wavelengths, and drops off rapidly in the near IR region. In addition to being slow and inefficient, PMTs are bulky, and require extensive thermal cooling. Furthermore, PMTs often have high dark current levels and are prone to afterpulsing, an effect whereby a false output pulse is generated although no photon has been detected. In summary, the extremely high sensitivity comes at the price of all these disadvantages [1, 5].

Most of the above challenges can be overcome with solid-state counterparts. The solid-state single-photon detectors have an inherently higher bandwidth because of their smaller size. They

exhibit higher quantum efficiencies. Typical quantum efficiencies for solid-state detectors range from 20 to 90% throughout the visible and near IR ranges [26]. In recent years, SPADs are gaining a growing interest among the research and industry communities. SPADs are basically specially constructed APDs operated in the so-called *Geiger mode*. In the Geiger mode, the APD is biased above its breakdown voltage, as opposed to the linear mode in which the APD is biased below the breakdown voltage. This generates a very large internal gain that enables single photon detection. The SPAD dark current is orders of magnitude lower than that of the conventional APDs and PMTs. In addition, SPADs generally have higher quantum efficiencies. So, in ultra-low-light applications, SPADs are superior to the conventional APDs.

SPADs are also subject to an unavoidable dead time which limits their count rate. More recently, SPAD arrays have been developed to keep pace with the ongoing demand for higher counting rates. SPAD arrays are also known as silicon photomultipliers (SiPMs) and multi-pixel photon counters (MPPCs). They appear to be a promising technology, with advantages such as relatively low production costs thanks to the complementary metal-oxide-semiconductor (CMOS) fabrication technology, compact sizes, immunity to magnetic fields, and low bias voltage requirements. These devices also offer high photon detection efficiency and excellent timing resolution [26]. In the next section, the potential applications, the operating mechanism, and the performance metrics of the SPADs are discussed in detail.

2.2 Single-Photon Avalanche Diode (SPAD)

Since the 2000s, the applications of SPAD PDs have expanded significantly. Nowadays, SPADs are the key enabling technology for many applications requiring single-photon sensitivity. Examples include, but are not limited to, light detection and ranging (LIDAR) [48], time of flight (ToF) three-dimensional imaging [49], positron emission tomography (PET) scanning [50], fluorescence lifetime microscopy [51], and single-photon experimentation within physics.

Owing to their high power efficiency, high sensitivity, high detection efficiency, and high timing resolution, SPADs have been deployed in various optical communication applications such as quantum key distribution [26, 52], deep space laser communications [53], gas well downhole monitoring systems [7], data transmission over plastic optical fibres [8], and underwater communications [54, 55]. So far, much effort has been devoted to optimising and improving their performance for communication purposes [9, 10, 56, 57] and still, there is broad room for

more improvements.

2.2.1 Operating Mechanism

SPADs are semiconductor devices with p-n junctions and operate based on a simple principle: if the reverse bias voltage, $V_{\rm bias}$, of the p-n junction is raised slightly above the breakdown voltage, $V_{\rm br}$, a very high electric field is produced. Hence, even a single carrier can trigger a strong avalanche, leading to a measurable current. The avalanche current rises rapidly to a steady level which primarily depends on the excess bias voltage, i.e. $V_{\rm ex} = V_{\rm bias} - V_{\rm br}$, the effective series resistance of the photodiode and the circuitry [21–24, 28].

The leading edge of the avalanche current is sensed by a discriminator and a synchronized output pulse is generated. While the bias voltage is above the breakdown level, the avalanche current continues to flow and the photodiode is not able to detect a subsequent photon. Reducing the bias voltage below the breakdown threshold, ceasing the current flow, and then raising the bias voltage above the breakdown level, is accomplished by an electronic circuit called the *quenching circuit*. In fact, the quenching circuit restores the SPAD to the operating conditions for detecting further photons. The quenching process typically lasts a few tens of nanoseconds. This recovery time is usually termed as the dead time [21–24, 28].

2.2.2 Figures of Merit

The key parameters for assessing the performance of SPAD PDs are as follows:

Dead Time

As discussed earlier, the dead time or recovery time, τ, is the time interval that follows the detection of a photon, during which the SPAD is unable to resolve a second photon. The type and length of the dead time depend strongly on the bias circuit and the counting electronics, rather than the photodiode element itself. The dead time causes some counting losses and limits the maximum count rate of the SPAD [27]. The effect of dead time on the performance of the SPAD, when used as an optical receiver, is the main focus of this thesis and is deeply studied in Chapters 3, 4, and 5.

Afterpulsing

An afterpulsing is a secondary avalanche event related to an earlier photon detection. Afterpulsing events are caused by carriers that get trapped during an avalanche breakdown and are released with a randomly fluctuating delay, when the SPAD is newly biased above its breakdown voltage. The mechanisms behind afterpulsing are well understood and the literature on the subject is extensive [19, 58]. This phenomenon is commonly described by a probability measure known as the *afterpulsing probability* which is defined as the probability that an afterpulsing event will happen after detection of a photon.

Because of afterpulsing, the measured number of detections is always higher than the actual number of detected photons. To suppress afterpulsing in the SPAD devices, τ can be deliberately lengthened to allow the trapped carriers to be released. In this way, the afterpulsing probability can be kept below a desired threshold, however, at the expense of a lower count rate.

Dark Counts

Similar to the dark current of PIN diodes and APDs, dark counts are the intrinsic noise of the SPADs. Dark counts are false detection events in the absence of any optical illumination and arise mostly due to thermally generated carriers and afterpulsing. Since the SPAD is highly sensitive, any carrier generated with no illumination can also produce the same current response as the signal photons, reducing the effective sensitivity of the device [26]. A probability measure is often used for reporting the effect of dark counts. The *dark count probability*, denoted by p_{dc}, is the probability that at least one dark carrier successfully triggers an avalanche and is approximated as [25]:

$$p_{\mathrm{dc}} = 1 - e^{-N_{\mathrm{dc}} p_{\mathrm{a}}}, \tag{2.25}$$

where N_{dc} is the average number of dark carriers in the multiplication region of the device and p_{a} is the avalanche probability, the probability that a carrier initiates an avalanche. The average avalanche triggering rate by dark counts is termed as the *dark count rate* and is denoted by R_{dc}. The minimum count rate of the SPAD is limited by R_{dc} which strongly depends on the SPAD active area and increases with the temperature and the excess bias voltage. The requirements of low dark count rates make the device fabrication very delicate [10].

Photon Detection Efficiency

Photon detection efficiency (PDE) is commonly defined as the overall probability of registering a count if a photon arrives at the active area of the SPAD. This depends on the SPAD quantum efficiency η, and the avalanche probability p_{a}. As such, PDE can be approximated as [34]:

$$\mathrm{PDE} = \eta \times p_{\mathrm{a}} \ . \tag{2.26}$$

For most well designed SPADs, η is quite high $(80 - 90\%)$ [59]. The avalanche probability, p_{a}, is generally specific to a particular device structure and increases with the excess bias voltage, since a higher electric field enhances the triggering probability [27].

Timing Jitter

The timing jitter is the statistical spread of the time interval between the photon arrival and the generation of an output electrical pulse. In fact, timing jitter represents the timing uncertainty due to the statistical nature of the impact ionization process. The jitter is typically reported as either the standard deviation or the full-width at half maximum (FWHM) of the corresponding distribution histogram. In any photon counting experiment, the maximum clock rate is determined by the timing jitter, which reduces as the excess bias voltage increases [27].

Crosstalk

Crosstalk is a phenomenon that takes place in SPAD arrays, when the avalanche in one SPAD triggers an undesired secondary avalanche in a neighbouring SPAD. There are two types of crosstalk: optical crosstalk and electrical crosstalk. In optical crosstalk, the secondary photons released by an avalanche elsewhere may cause avalanches. In fact, when one SPAD detects a photon, secondary photons may be emitted by the SPAD itself. These photons can be detected by adjacent SPADs, resulting in optical crosstalk. The optical crosstalk increases when the distance is reduced between array elements; hence, this phenomenon imposes a restriction on the array density. However, it can be effectively reduced by using optical shields between array elements. In electrical crosstalk, a carrier generated in one SPAD may trigger an avalanche elsewhere. The electrical crosstalk is strongly reduced by insulating the multiplication region of each SPAD [27].

Fill Factor

Fill factor (FF) of a SPAD array, is the ratio of its photosensitive area to its total area. Generally, FF is limited by the additional circuitry of the array. In low intensity conditions, FF plays an important role, as fewer photons arrive at the SPAD. One of the drawbacks of the SPADs integrated in CMOS technologies is their relatively poor FF [27, 60]. Prior to 2010, the FF was often less than 10% [9]. Recently, it has been improved through a number of techniques, e.g. in [60], a FFs of 57% is reported. However, this often comes at the expense of a significant crosstalk effect.

2.2.3 Quenching Circuits

Quenching circuits directly affect the photon counting performance of the SPAD due to the dead time they introduce. A slow quenching circuit limits the maximum count rate, or it may impair the timing response. It is therefore important to choose the quenching circuit most suitable to the desired application. For designing the quenching circuit and determining optimal operating conditions of the SPAD to ensure proper static and dynamic SPAD behaviour, detailed and accurate equivalent circuit models of the SPAD photodiode are essential [22, 61]. Such a model should precisely represent the transient behaviour of the SPAD element and its current-voltage characteristics [14, 62, 63]. In the last twenty years, quenching circuits have been vastly developed and their performance has remarkably been improved [20]. In the following, the main approaches in designing quenching circuits are discussed.

2.2.3.1 Passive Quenching SPADs

Passive quenching (PQ) is the simplest method to quench the SPAD avalanche current. A PQ circuit consists of a resistor, R_{q}, connected to the photodiode, as illustrated in Fig. 2.3. When there are no charge carriers in the depletion layer of the photodiode, the current across R_{q} is zero. Accordingly, the SPAD is biased with a voltage larger than its breakdown voltage ($V_{\mathrm{S}} = V_{\mathrm{br}} + V_{\mathrm{ex}}$) and is ready to operate. The absorption of a single photon can now initiate an avalanche breakdown. With the avalanche current flow, there will be a large voltage drop over the resistor, which will reduce the voltage across the SPAD and stop the avalanche (quenching stage). Then, the resistor R_{q} will recharge the SPAD and the voltage across the SPAD slowly increases from V_{br} to $V_{\mathrm{br}} + V_{\mathrm{ex}}$ (recharging stage). As long as V_{S} is less than a threshold

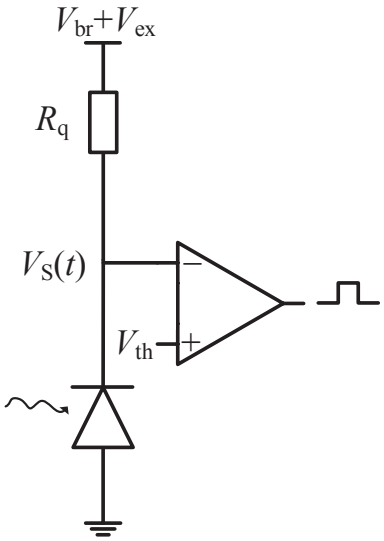

Figure 2.3: *Basic configuration of a PQ SPAD [20].*

value V_{th}, the SPAD is unable to detect any other photons, however, incident photons may still initiate weaker breakdowns, resulting in further voltage drops across the SPAD and prolonging the dead time. Once the SPAD is fully recharged and its voltage is above the breakdown level again, the circuit is ready for the detection of a new photon [14, 15, 20].

Fig. 2.4 shows an example voltage waveform for a PQ SPAD. With the arrival of the first photon, the SPAD voltage drops to the breakdown voltage V_{br}. The recharge process then starts and the SPAD voltage slowly increases. Before the SPAD voltage reaches the threshold voltage V_{th}, the second photon arrives and again V_{S} drops to V_{br}. As a consequence, the total duration of dead time is extended. Since the voltage is still lower than the threshold voltage, the second photon is not registered by the comparator. Once V_{S} exceeds V_{th}, the dead time finishes and the SPAD becomes operative again. The third incident photon is then successfully detected. The PQ SPAD is also identified as a paralyzable detector where any photon arriving during the dead time is not detected, but it extends the dead time [30, 31].

The dead time depends on the value of the quenching resistor R_{q} and the total parasitic capacitance seen by the SPAD. The resistor R_{q} should be very large to ensure reliable quenching of the avalanche breakdown. But the larger R_{q}, the slower the recharge process. In fact, the main drawback of the PQ SPAD is its slow quenching and recharging processes, hence, a relatively long dead time, which limits the maximum count rate. If a high count rate is

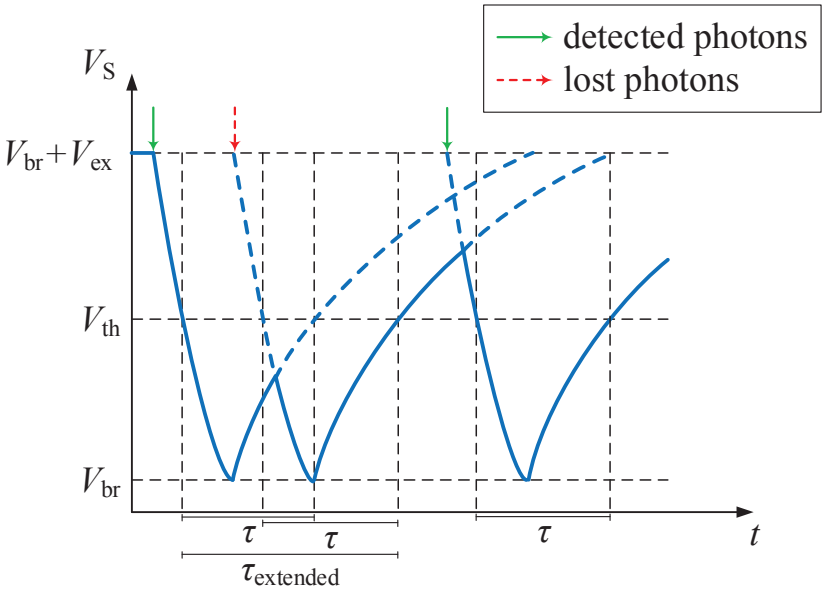

Figure 2.4: *An example voltage waveform for a PQ SPAD. The PQ SPAD device is a paralyzable photon detector. The duration of the dead time introduced by the quenching circuit is not constant, that is, any photon arrival occurring during the dead time is not counted, but it extends the dead time period [29].*

not required, then the PQ circuit is convenient, as it is robust, simple to implement and requires a minimum of power or area [14, 15, 20].

2.2.3.2 Active Quenching SPADs

Although PQ is a very simple and convenient method, it has the disadvantage of a relatively long dead time. To overcome this drawback of the PQ SPADs, active quenching (AQ) SPADs have been introduced [14,16,20]. In Fig. 2.5, an AQ circuit with a switching element is presented. In this circuit, R_q is very small compared to the ones typically used in PQ circuits. Once a photon is detected and an avalanche is triggered, the voltage across the SPAD is immediately reduced by closing the fast active switch, as shown in Fig. 2.5. The fast switch is a double-diffused metal-oxide-semiconductor (DMOS) field-effect transistor (FET), capable of withstanding the required voltage and of switching in nanosecond time from a low series resistance (on state) to a high series resistance (off state) and conversely. Such a fast switch is simple and compact and has low power dissipation, since the driver dissipates power only during the transitions [14,20]. According to Fig. 2.5, the closing of this switch reduces the voltage across the SPAD to a voltage below the breakdown voltage, $V_{br} - V_q$, hence, the avalanche is quenched. This is

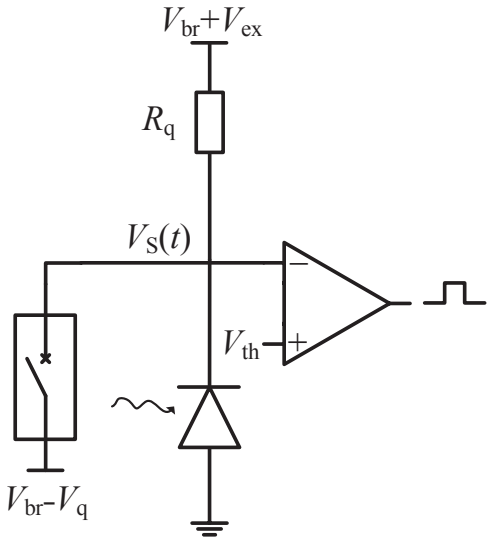

Figure 2.5: *Basic configuration of an AQ SPAD [20].*

to ensure complete termination of the avalanche current in the multiplication region, and to prevent the dead time being extended by any other photons. The switch is kept closed for a predetermined period (to minimize afterpulsing). As long as the switch remains closed, the voltage is below the breakdown level and no new photons can be detected. After the switch opens, the SPAD will be promptly recharged to the operating voltage, $V_{\mathrm{br}} + V_{\mathrm{ex}}$. Since R_{q} is small, the recharge process happens very fast. However, with such a small resistor the avalanche current is much larger [14, 16, 20].

More complicated AQ circuits take advantage of a feedback loop to control the bias voltage [14], where both the quenching and recharge processes are carried out very quickly using pulse generators. Compared with the PQ SPAD, the configuration of the AQ SPAD is more complex and requires more logic area and circuit power [14, 16, 20].

Fig. 2.6 shows an example of the voltage waveform for an AQ SPAD. It can be seen that when a photon arrives, the voltage of the AQ SPAD, V_{S}, drops from $V_{\mathrm{br}} + V_{\mathrm{ex}}$ to below V_{br} quickly. V_{S} is kept below the breakdown voltage for some time and is then increased to $V_{\mathrm{br}} + V_{\mathrm{ex}}$ again sharply. In this whole process, any photon arriving during the quenching or recharge processes is not able to trigger an avalanche and is therefore lost. Unlike the PQ SPAD, the dead time of the AQ SPAD is constant and is not extended by incoming photons. Thus, the AQ SPAD is identified as a nonparalyzable detector [29].

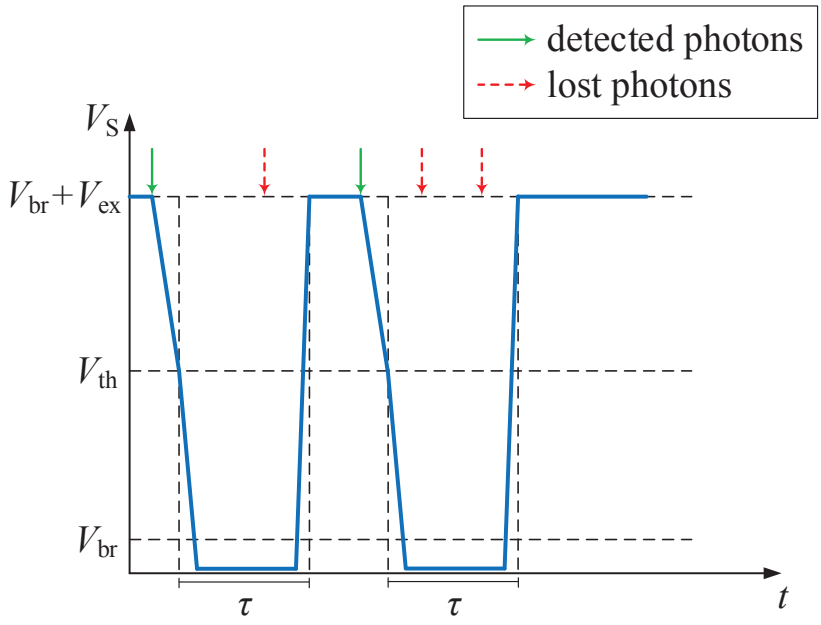

Figure 2.6: *An example voltage waveform for an AQ SPAD. The AQ SPAD device is a nonparalyzable photon detector. The duration of the dead time introduced by the quenching circuit is constant, that is, any photon arriving during the dead time is neither counted nor has any influence on the dead time duration [20].*

Although the actual quenching time might not be so short in AQ SPADs, the quenching transition and the recharge process are much faster than those in the PQ SPADs. This, along with the nonextendable dead time of the AQ SPADs lead to higher count rates and less counting losses, but at the expense of a higher complexity. In AQ SPADs, the avalanche photocurrent and the afterpulsing probability are higher. Also, AQ circuits generally occupy larger areas compared to PQ circuits, and this would reduce the FF in SPAD arrays [20].

2.2.3.3 Mixed Active/Passive Quenching SPADs

The quenching and recharge processes do not necessarily have to be both passive or both active. For satisfying specific application requirements, mixed circuits can be an effective approach to design simple and compact circuits. Mixed active/passive quenching circuits can combine the advantages of purely passive and purely active quenching circuits. For example, consider a circuit with passive quenching and active reset. In such a case, the SPAD is connected to both a large resistor and an active reset circuitry. When an avalanche is triggered, the avalanche current flows through the resistor, so the avalanche is initially quenched like in PQ circuits. Then, the

active circuitry soon senses the avalanche. It keeps the SPAD quenched for a specific dead time and then actively restores the bias voltage to the operating level [14]. Mixed quenching circuits typically feature a smaller parasitic capacitance and therefore a much smaller avalanche photocurrent, as in PQ circuits. They also offer a fast reset and a well-defined dead time, as in AQ circuits. However, the integration of the photodiode and both quenching parts significantly limits the FF in SPAD arrays, so integration is feasible for single SPADs or small size arrays [20].

2.3 Related Works

SPADs have recently found applications in OWC. The interest in this subject was initiated by the work [64] where MPPCs were proposed for OWC systems dealing with low light levels. The numerical results in [64] claimed that the MPPC can reach sensitivities of -70 dBm at 8.5 Mbits/s and -59 dBm at 140 Mbits/s, higher than the typical sensitivities of conventional APDs. Since then, there has been a growing interest in this topic, however, the literature is still scarce. Most of the related research articles are experimental studies and the theoretical studies on the subject are limited. In the following, the main contributions of these articles are highlighted.

2.3.1 Experimental Studies

Fisher *et al.* [9, 10], have implemented a reconfigurable SPAD array in 130 nm CMOS technology for photon counting in OWC. The 32×32 SPAD array is designed for on-off keying (OOK), pulse amplitude modulation (PAM) and pulse width modulation (PWM) and works in two different modes: AQ and PQ. It has a FF of 2.5%, a bandwidth of 100 MHz, a dead time of 5.9 ns for PQ and 10.5 ns for AQ mode, and a dark count rate of 2.5 kHz per SPAD. A maximum count rate of 58 GHz is observed, with a sensitivity of -31.7 dBm for a bit error ratio (BER) of 10^{-9}.

Chitnis *et al.* [8], have designed and fabricated a small array of 64 SPADs in 0.18 μm CMOS process and have tested it for OWC. The experimental results show that by using arrays of SPADs, less optical power is required at the receiver to achieve a target BER. In [65], same authors have presented the measurement results of a visible light communication (VLC) receiver consisting of a small array of 60 SPADs. The BER performance of an OOK system

with and without a decision feedback equaliser, is reported for various data rates and dead times. For a dead time of 10.8 ns, a data rate of 200 Mbits/s is achieved with OOK modulation and a decision feedback equaliser. In [56], a SPAD-based VLC receiver achieves a sensitivity of -64 dBm, a data rate of 100 kbits/s and a BER of 10^{-5} with PAM signalling. In [57], an optical link operating in indoor ambient lighting conditions is demonstrated which uses a SPAD array receiver with 4096 elements. The link operates at a 2 m distance at a data rate of 60 Mbits/s and a BER of 10^{-3} without lensing. The results suggest that the use of SPAD arrays can help to cope with strong background light conditions. In [54], a long distance SPAD-based VLC system with a red LED is demonstrated. Using a SPAD PD with a dead time of 20 ns, a data rate of 100 kbits/s and a BER of 1.22×10^{-3} is achieved at a distance of 333 m.

In [66, 67], the first attempt to determine when SPADs should be preferred to APDs is reported and the potential benefits of using SPADs, rather than APDs, in the presence of ambient light are quantified. The effects of dead time and the PDE on the sensitivity of the SPAD arrays are investigated. The measured link performances of two systems containing an APD and a large SPAD array (with PDE of only 8%) show that the SPAD-based receiver is more sensitive in the darkness, while the APD-based receiver is more sensitive in typical ambient light conditions. The simulation results in [67] suggest that a SPAD receiver with an improved PDE (e.g. 40%) is significantly more sensitive than the APD-based receiver even in the ambient light conditions. The experimental results with the large SPAD array also show that, when this large SPAD array is used as the receiver, the transmitted power needed to obtain a target data rate increases rapidly once the bit time becomes shorter than the width of the array's output pulses. The maximum OOK data rate at which this receiver can operate efficiently is therefore limited by the width of the output pulses.

In [68, 69], a fully integrated SPAD array receiver is fabricated in a 0.35 μm CMOS process. The array of four SPADs has a short dead time of 3.5 ns with an AQ circuit and can achieve data rates of up to 200 Mbits/s. A sensitivity of -43.8 dBm and a BER of 6.5×10^{-3} at 200 Mbits/s are reported.

2.3.2 Theoretical Studies

In [7], it is demonstrated for the first time that the problem of continuous downhole monitoring in the oil and gas industry can be effectively addressed by the use of a SPAD-based VLC system. In this article, a SPAD array is considered, and the error probability of an OOK

system is analysed for a 4 km long metal pipe. The authors in [70] have investigated the signal detection in SPAD-based VLC systems. A low-complexity receiver based on Anscombe root transformation and an energy-efficient one dimensional constellation are proposed for the signal detection over the Poisson channels. The authors have extended their methodology in [71, 72] to design optimal space constellations for SPAD-based multiple-input multiple-output (MIMO) OWC systems. They have also applied Anscombe root transformation to the conventional DC-biased optical OFDM (DCO-OFDM) to approximate the Poisson channels by Gaussian channels without significantly increasing the detection complexity [73]. In [74], an initial attempt has been made to assess the error performance of PAM in SPAD-based systems. In [75, 76] the performance of SPAD detectors in long distance VLC links for under water communication (UWC) is analysed considering the effect of the turbulence-induced fading resulting from air bubbles in addition to the combined effects of attenuation and scattering. In [77], a multiple LED parallel transmission scheme is proposed for an under water visible light communication (UWVLC) system with a single SPAD receiver. In [78–81], various receiver designs are proposed for SPAD-based systems with Poisson shot noise. The authors in [82] investigate the likelihood detection of pulse position modulation (PPM) signals for a photon counting array receiver in the presence of detector timing jitter.

In the aforementioned articles, i.e. [7, 70–82], the impact of SPAD dead time has not been considered and an ideal Poisson process is assumed for the photon counting process of the SPAD detector.

In [83] and [84], a SPAD-based orthogonal frequency division multiplexing (OFDM) system is presented and the nonlinear distortion due to the saturation of the SPAD receiver, as well as the BER performance of both DCO-OFDM and asymmetrically clipped optical OFDM (ACO-OFDM) are investigated.

In [85], the feasibility of employing SiPMs for signal detection in UWC systems is addressed. For a typical under water link, the link performance is evaluated and compared for SiPM- and APD-based receivers. The numerical results show that the link span can be increased by the SiPM-based receiver. A follow-up study is conducted in [55], where the practical considerations regarding the system implementation and the main drawbacks of SiPM devices are addressed. In particular, the limited transmission data rates and the non-linear distortion in relatively short ranges are pointed out.

Authors in [55, 83–85], have assumed a Poisson distribution with dead time modified mean value for the SPAD photon counting process.

In [86, 87], a novel optical transmission scheme is demonstrated which is suitable for OWC at ultra-low light levels. This method is inspired by time-correlated single photon counting (TCSPC) techniques often used for fluorescence lifetime imaging [51] and operates under the presence of both constant and modulated background noise. A 100 kbits/s link has been reported with a BER of less than 10^{-3} at a received power of 8.25 pW. The works of [86, 87] are fundamentally different as the data transmission is enabled by the encoding of data in the timing statistics of the received photons, rather than the number of received photons.

In [88, 89], a practical photon counting receiver in optical scattering communication (OSC) with finite sampling rate, paralyzable dead time, and electrical noise is characterized where it is shown that the dead time effect leads to sub-Poisson distribution for the number of recorded pulses. An approximate photocount distribution is derived in [88, 89], which is only applicable for extremely low photon rates.

In [90], the BER performance of a SPAD array optical receiver is presented. The model considers important nonidealities including dead time and the SPAD intrinsic parasitic effects and provides approximations to the error probability of OOK modulation for bit times equal to the dead time. The results show that the crosstalk makes the major contribution to the BER as compared to dark counts and afterpulsing. The analysis in this article does not consider the inter-slot interference (ISI) impairments arising from long dead times.

In [91], the bit error performance of a SPAD-based UWC system is evaluated considering the characteristics of the underwater channel and also the impact of SPAD dead time. In this article, our dead time-modified photocount distributions presented in [35] are adopted.

2.4 Summary

In this chapter, a short overview of OWC was given with focus on the photodetection process. The common PDs in OWC systems were reviewed. In particular, PIN diodes and APDs were referred to. The details of their physical mechanism of operation, noise properties and performance specifications in terms of gain, bandwidth and SNR were reported from literature. It was discussed that in photon-starving applications and long distance transmissions, where the optical signal may be received at levels below the sensitivity of PIN diodes and APDs, PDs with single-photon sensitivity, such as PMTs are required. The advantages and disadvantages of PMTs were addressed. Then, the SPAD detectors were brought into discussion as a promising replacement for the PMTs in OWC applications. A short review for the past and present applications of SPAD detectors was provided. Also, the operating mechanism and the main performance metrics and the quenching circuits used for resetting the SPAD PDs were reviewed. Finally, the related research articles were referred to.

Chapter 3
SPAD Photocount Statistics

While single-photon avalanche diodes (SPADs) are an active area of development, there is not enough theoretical analysis which would specify their photon counting performance limitations. The unavoidable dead time caused by the quenching circuit has a substantial impact on the photon counting performance of these photodetectors. From a communication theory point of view, the dead time-induced counting losses not only degrade the bit error ratio (BER) of a system, but also limit the achievable data rates. Particularly, in applications involving high photon rates and in high data rate optical wireless communication (OWC), the SPAD dead time causes significant data loss. Therefore, it is of great importance to accurately characterize the effect of dead time.

The *blocking probability* of single-photon detectors is a metric which has been widely addressed in the literature [32, 33]. It is defined as the probability that the detector becomes inoperative for some time after a detection event. Although, the blocking probability is a useful metric for assessing the photon counting performance of single-photon detectors, it does not provide a complete description of the shot noise. It is the photocount distribution that suffices and is required for the performance evaluation of any SPAD-based OWC system.

In the absence of dead time, the SPAD photocounts follow a Poisson distribution. Likewise, in the presence of dead time, a Poisson approximation is commonly used [7,55,70–85]. However, this approximation does not provide an accurate description of the counting process and leads to inaccurate and unrealistic results when evaluating the bit error performance of the SPAD-based OWC system.

In this chapter, a comprehensive analytical approach is presented for modelling the SPAD photon counting process. The mathematical framework is established based on the concepts of arrival processes and the renewal theory. Throughout this study, it is assumed that the sampling rate is very high compared to the dead time, so that the counting losses arising from finite sampling rates are negligible. The photocount statistics of an ideal SPAD without dead time, an active quenching (AQ) SPAD with a nonparalyzable dead time, a passive quenching (PQ) SPAD

with a paralyzable dead time and a mixed AQ/PQ SPAD are precisely modelled. The exact expressions for the probability mass function (PMF), the mean and the variance of photocounts are derived. This study reveals how the SPAD counting process deviates from a Poisson process due to the dead time.

Nonparalyzable and paralyzable dead time count rate models are two approximate expressions, well-known in literature, which provide estimations of the actual count rate of single-photon detectors [30, 31]. These two models have also been adopted for SPAD detectors and have been verified experimentally [29]. In this chapter, the exact expressions for the count rate of the AQ and PQ SPADs are also derived and it is shown that these models asymptotically approach the existing approximate count rate models.

Moreover, in this chapter, the counting statistics of SPAD arrays are studied and approximate expressions for their PMF, mean and variance are developed. It is shown that the impact of both AQ and PQ dead times is eliminated in a sufficiently large SPAD array.

All the analytical expressions derived in this chapter are verified by Monte Carlo simulations. These models are then used in Chapter 4 to assess the bit error performance of the SPAD-based OWC systems, and in Chapter 5 to obtain the information transfer rate of the SPAD receivers.

The rest of this chapter is organised as follows. In Section 3.1 the required background for establishing the mathematical framework is provided. In Section 3.2 the photon counting process of the ideal SPAD is addressed. The statistical modelling of the photon counting processes of the AQ SPAD, the PQ SPAD, the mixed AQ/PQ SPAD and the SPAD array is presented in Sections 3.3–3.6. Finally, a summary of the chapter is given in Section 3.7.

3.1 Preliminaries

In this section, the concept of *arrival processes* with emphasis on *Poisson processes* is reviewed. Some of the well-known results from the book by Snyder [92] are presented. Also, some of the principal elements and results in *renewal theory* are introduced, where the book by Cox [93] is closely followed. These mathematical tools are applied in Sections 3.2–3.6 for modelling the dead time-modified photocount distribution of SPAD receivers.

Figure 3.1: *Arrival and inter-arrival time sequences.*

3.1.1 Arrival Processes

An arrival process is a sequence of increasing random variables $0 < t_1 < t_2 < \cdots$, known as *arrival times* or *occurrence times*. The arrivals are also referred to as *incidents* or *events*. We denote this sequence by $\{t_i\}$ and assume that the process starts at time $t = 0$ and multiple arrivals can not occur simultaneously [94].

As illustrated in Fig. 3.1, the arrival process can be specified by two other stochastic processes. The first is the sequence of inter-arrival times, $w_1, w_2, \ldots$, which are positive random variables such that $w_1 = t_1$ and $w_i = t_i - t_{i-1}$ for $i > 1$ and $\Pr\{w_i \leq 0\} = 0$. Given the sequence $\{w_i\}$, the arrival time t_i is expressed as:

$$t_i = \sum_{j=1}^{i} w_j. \tag{3.1}$$

In order to characterize the arrival process by the sequence $\{t_i\}$, it is sufficient to determine the joint probability distribution of the subsequences $t_1, t_2, \ldots, t_k$ for all $k > 1$. Similarly, the joint probability distribution of $w_1, w_2, \ldots, w_k$ for all $k > 1$ is sufficient to specify the arrival process. When the inter-arrival times are independent and identically distributed (iid), it is usually easier to specify the joint distribution of $\{w_i\}$ than that of $\{t_i\}$ [94].

The second alternative for specifying an arrival process is by the counting process $K(t)$ corresponding to it. The random variable $K(t)$, is the number of events in the interval $(0, t]$. We denote this counting process by $\{K(t); t > 0\}$ and assume that $\Pr\{K(0) = 0\} = 1$, as arrivals occur at strictly positive times. For any given $t' > t$, denote the number of arrivals in the interval $(t - t']$ by $\widetilde{K}(t, t') = K(t') - K(t)$. For any given integer $i \geq 1$ and $t > 0$, the ith arrival time, t_i, and the counting random variable, $K(t)$, are related by:

$$\Pr\{t_i \leq t\} = \Pr\{K(t) \geq i\}. \tag{3.2}$$

Definition 1. *The counting process* $\{K(t); t > 0\}$ *has the stationary increment property, if* $\widetilde{K}(t, t')$ *has the same distribution function as* $K(t' - t)$ *for every* $t' > t$ *[92, 94].*

Definition 2. *The counting process* $\{K(t); t > 0\}$ *has the independent increment property, if the* i*-tuple of random variables* $K(t_1)$, $\widetilde{K}(t_1, t_2)$, $\ldots$, $\widetilde{K}(t_{i-1}, t_i)$ *are statistically independent, for every integer* $i > 0$ *and every* i*-tuple of times* $0 < t_1 < t_2 < \cdots < t_i$ *[92, 94].*

3.1.1.1 Poisson Processes

Poisson process is an example of arrival processes for which the inter-arrival times are iid random variables with exponential distribution; i.e., each random variable W_i has the probability density function (PDF) $f_{W_i}(w) = \lambda e^{-\lambda w}$ for $w \geq 0$ and is memoryless[1]. The parameter λ is the *rate* or *intensity* of the Poisson process and λt is the expected number of arrivals in the interval $(0, t]$ [92].

Homogeneous Poisson Processes

The Poisson processes are usually characterized by a constant arrival rate λ. In these cases, the Poisson process is termed as a *homogeneous* or *stationary* point process. Homogeneous Poisson processes have both of the stationary increment and the independent increment properties [92, 94]. Denote by $p^{(k)}(t_1, t_2, \ldots, t_k)$ the joint probability density for the first k arrival times t_1, t_2, $\ldots$, t_k. For a homogeneous Poisson process, $p^{(k)}(t_1, t_2, \ldots, t_k)$ is given by [92]:

$$p^{(k)}(t_1, t_2, \ldots, t_k) = \begin{cases} \lambda^k e^{-\lambda t_k}, & 0 < t_1 < t_2 < \cdots < t_k \\ 0, & \text{otherwise.} \end{cases} \tag{3.3}$$

Non-homogeneous Poisson Processes

Non-homogeneous Poisson processes have a time-varying arrival rate $\lambda(t)$ for $t \geq 0$. These processes have the independent increment property, however, they do not have the stationary increment property [92, 94]. For a non-homogeneous Poisson process, $p^{(k)}(t_1, t_2, \ldots, t_k)$ is

[1] A non-negative non-deterministic random variable X is memoryless if for every $x \geq 0$ and $\alpha \geq 0$,

$$\Pr\{X > x + \alpha\} = \Pr\{X > x\}\Pr\{X > \alpha\}.$$

given by [92]:

$$p^{(k)}(t_1, t_2, \ldots, t_k) = \begin{cases} \left(\prod_{i=1}^{k} \lambda(t_i)\right) \exp\left(-\int_0^{t_k} \lambda(\sigma) d\sigma\right), & 0 < t_1 < t_2 < \cdots < t_k \\ 0, & \text{otherwise.} \end{cases} \tag{3.4}$$

The above expression is used later in Section 3.3 for obtaining the photocount distribution of AQ single SPADs.

3.1.2 Renewal Theory

In the following, the concepts of *product density functions* and *renewal processes* are introduced.

3.1.2.1 Product Density Functions

Consider the counting process $\{K(t); t > 0\}$ with the arrival time sequence of $\{t_i\}$, $i = 1, 2, \ldots$. For this counting process, the random variable $dK(t)$ denotes the number of events in the small interval $(t, t + dt]$. A function $f_1(t)dt$ can be defined such that [93]:

$$f_1(t)dt = \mathbb{E}[dK(t)], \tag{3.5}$$

where $\mathbb{E}[dK(t)]$ represents the average number of events in the interval $(t, t+dt]$. Accordingly, the product of two random variables $dK(t_1)$ and $dK(t_2)$ can be defined as [93]:

$$f_2(t_1, t_2)dt_1dt_2 = \mathbb{E}[dK(t_1)dK(t_2)], \tag{3.6}$$

which is also equal to the joint probability of one arrival event in $(t_1, t_1+dt_1]$ and another arrival event in $(t_2, t_2 + dt_2]$. The function f_2 is called *a product density of order two*. Similarly, the product density function of order k, $f_k(t_1, t_2, \ldots, t_k)$, is defined as [93]:

$$f_k(t_1, t_2, \ldots, t_k)dt_1dt_2 \cdots dt_k = \mathbb{E}[dK(t_1) \cdots dK(t_k)], \tag{3.7}$$

where $f_k(t_1, t_2, \ldots, t_k)dt_1dt_2 \cdots dt_k$ represents the joint probability of one arrival event in the interval $(t_1, t_1 + dt_1]$, one in $(t_2, t_2 + dt_2]$, …, and one in $(t_k, t_k + dt_k]$.

Assuming a Poisson arrival process and provided that $0 < t_1 < t_2 < \cdots < t_k$, the following equation holds between the product density of order k and the product densities of order one [93]:

$$f_k(t_1, t_2, \ldots, t_k) = f_1(t_1) f_1(t_2 - t_1) \cdots f_1(t_k - t_{k-1}). \tag{3.8}$$

The above equation implies that an event is given at $t = 0$, and given this arrival event, the probability that an event occurs between t and $t+dt$ is determined by $f_1(t)dt$ and is independent of what happened before $t = 0$. This is a conventional assumption in most problems in renewal theory. For the SPAD, this assumption means that the SPAD is blocked at the beginning of the counting interval. We will proceed with our mathematical modellings under this assumption and will relax it at the end.

Define $p(k,t) = \Pr\{K(t) = k\}$. Thus, $p(k,t)$ denotes the probability of k detection events during the interval $(0,t]$, given one arrival at $t = 0$. The generating function (GF) corresponding to $p(k,t)$ is given by:

$$G(z,t) = \sum_{k=0}^{\infty} p(k,t) z^k. \tag{3.9}$$

The following property holds for $G(z,t)$ and the product density of order k [93]:

$$\left.\frac{\partial^k G(z,t)}{\partial z^k}\right|_{z=1} = \int_0^t \int_0^t \cdots \int_0^t f_k(t_1, t_2, \ldots, t_k)\, dt_1 dt_2 \cdots dt_k. \tag{3.10}$$

For a symmetrical f_k with respect to t_1, t_2, $\ldots$, t_k, (3.10) can be written as [93]:

$$\left.\frac{\partial^k G(z,t)}{\partial z^k}\right|_{z=1} = k! \int_0^t dt_k \int_0^{t_k} dt_{k-1} \ldots \int_0^{t_3} dt_2 \int_0^{t_2} f_1(t_1) f_1(t_2 - t_1) \cdots f_1(t_k - t_{k-1}) dt_1. \tag{3.11}$$

The following equation is concluded from (3.11):

$$\left.\frac{\partial G(z,t)}{\partial z}\right|_{z=1} = \int_0^t f_1(t_1) dt_1. \tag{3.12}$$

Now, let $F_1(s) = \int_0^\infty f_1(t) e^{-st} dt$ be the Laplace transform (LT) of the function $f_1(t)$ with respect to the variable t. The LT of (3.12) is obtained as:

$$g(z,s) = \frac{1}{s} \times \frac{1}{1 - (z-1)F_1(s)}, \tag{3.13}$$

where $g(z,s)$ is the LT of the function $G(z,t)$. Let also define $P(k,s)$ as the LT of the function $p(k,t)$. The following diagram summarizes how the four functions $p(k,t)$, $P(k,s)$, $G(z,t)$, and $g(z,s)$ are related:

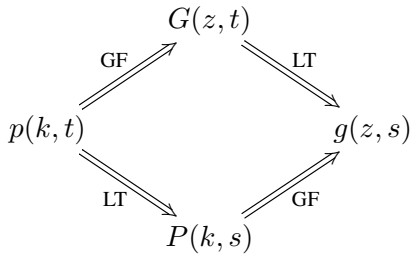

Since $g(z,s)$ is the GF of $P(k,s)$, according to (3.13), $P(k,s)$ can be obtained as [95]:

$$P(k,s) = \frac{1}{s} \times \frac{[F_1(s)]^k}{[1+F_1(s)]^{k+1}}. \tag{3.14}$$

Therefore, if $f_1(t)$ or $F_1(s)$ is known for a counting process, $P(k,s)$, and hence, $p(k,t)$ can be obtained using (3.14).

3.1.2.2 Renewal Processes

Definition 3. *A renewal process is an arrival process for which the inter-arrival times are iid random variables.*

Renewal processes are often described by a special type of integral equations known as *renewal equations*, which represent the regenerative nature of the process, that is, the property that the process restarts at each arrival time, independently of the past. In general, a renewal equation is of the form [93]:

$$B(t) = b(t) + \int_0^t B(t-t')dA(t'), \tag{3.15}$$

where $A(t)$ is the cumulative distribution function (CDF) of the inter-arrival times, such that $A(0) = 0$, $b(t)$ is a known function and $B(t)$ is an unknown function. The solution to this renewal equation, $B(t)$, is obtained conditioned on the time of the first event and can represent many quantities in the study of renewal processes [93].

If the counting process $\{K(t); t > 0\}$ is a renewal process, then a renewal equation can be constituted for obtaining $p(k,t)$. We make the assumption that there is an initial arrival at $t = 0$. This assumption helps us to make our later mathematical derivations tractable, as the

the properties of the renewal processes will be combined with the product density functions in which an event at $t = 0$ is a hidden assumption.

Denote by $\phi(t)$ the probability of no events in $(0, t]$, given one event at $t = 0$. Thus, $p(0, t) = \phi(t)$. It is also apparent that $A(t) = 1 - \phi(t)$. For $k \geq 1$, the following renewal equation can be considered:

$$p(k, t) = \int_0^t p(k-1, t-t')dA(t'). \tag{3.16}$$

In the above equation, $dA(t') = (-\partial\phi(t')/\partial t')dt'$ is the probability that the *next* event occurs between t' and $t' + dt'$, given the initial event at $t = 0$. Also, $p(k-1, t-t')dA(t')$ represents the probability of $k-1$ events in the interval (t', t) and one event at $t = t'$, given the event at $t = 0$. This clearly shows the regenerative nature of the renewal process, i.e., the counting process restarts at $t = t'$. By integrating over all admissible values of t', $p(k, t)$ is obtained. Therefore, for $k \geq 0$, the total integral equation for this renewal process can be written as:

$$p(k, t) = \int_0^t p(k-1, t-t')(-\frac{\partial\phi(t')}{\partial t'})dt' + \delta(k)\phi(t), \tag{3.17}$$

where $\delta(.)$ is the Dirac delta function and $\delta(k) = 1$ for $k = 0$ and 0 otherwise. The following equation holds for the GF corresponding to $p(k, t)$:

$$G(z, t) = \int_0^t z\, G(z, t-t')(-\frac{\partial\phi(t')}{\partial t'})dt' + \phi(t). \tag{3.18}$$

The LT of the above equation with respect to the variable t is given by:

$$g(z, s) = \frac{\Phi(s)}{1 + z(s\,\Phi(s) - 1)}\,, \tag{3.19}$$

where $\Phi(s)$ is the LT of $\phi(t)$. Since $g(z, s)$ is the GF of $P(k, s)$, according to (3.19), $P(k, s)$ is given by [95]:

$$P(k, s) = \Phi(s)(1 - s\,\Phi(s))^k. \tag{3.20}$$

Thus, if $\phi(t)$ or $\Phi(s)$ is known for a renewal counting process, $P(k, s)$, and hence, $p(k, t)$ can be obtained using (3.20).

The key results given in (3.14) and (3.20) are used later in Sections 3.3–3.5 for obtaining the

photocount distribution of AQ, PQ and mixed AQ/PQ single SPADs.

3.2 Ideal SPAD

Assume that the photons arrive at the surface of the SPAD detector according to a Poisson arrival process. For an ideal SPAD detector, the photocounts follow a Poisson distribution and the probability of detecting k photons during a time period of $(0, T_{\rm b}]$ is given by [1, 5, 42]:

$$p_0(k) = p(k,t)|_{t=T_{\rm b}} = \frac{(\lambda T_{\rm b})^k e^{-\lambda T_{\rm b}}}{k!}\,, \tag{3.21}$$

where the constant λ is the average photon arrival rate (in photons/s). Throughout this thesis, we may also use the notation $p_0(k;\lambda)$ to distinguish between various values of the parameter λ. The mean and variance of the photocounts over the observation time of $T_{\rm b}$ seconds are given by [1, 5, 42]:

$$\mu_0 = \sigma_0^2 = \lambda T_{\rm b}. \tag{3.22}$$

The photon arrival rate λ is related to the power of the optical signal by [1, 5, 42]:

$$\lambda = \frac{\eta P_{\rm s}}{h\nu}\,, \tag{3.23}$$

where η is the quantum efficiency of the SPAD; $P_{\rm s}$ denotes the power of the incident optical signal; h is the Planck constant; and ν represents the frequency of the optical signal.

3.3 AQ SPAD

In this section, the dead time-modified photocount distribution of an AQ SPAD is derived. Recall that in AQ SPADs, any photon arriving during the dead time is lost and has no influence on the dead time period. It is only after this dead time that the SPAD is able to detect a subsequent photon. Assume that the dead time is of length τ. If the SPAD is free at the beginning of the counting interval $(0, T_{\rm b}]$, the number of photocounts during this period can not exceed $k_{\max} = \lfloor T_{\rm b}/\tau \rfloor + 1$, where $\lfloor x \rfloor$ denotes the largest integer that is smaller than x. In the sequel, the AQ SPAD photocount distribution $p_K(k) = p(k,t)|_{t=T_{\rm b}}$ is obtained using two different approaches: Poisson processes and renewal processes.

3.3.1 Poisson Processes

Assume that t_1, t_2, …, t_k are the photon arrival times such that $0 < t_1 < t_2 < \cdots < t_k \leq T_\mathrm{b}$. Note that the probability of detecting $k > k_\mathrm{max}$ is zero. Therefore, $p_K(k) = 0$ for $k > k_\mathrm{max}$.

The AQ SPAD photon counting process is an inhomogeneous Poisson process with the joint probability density function $p^{(k)}(t_1, t_2, \ldots, t_k)$ given in (3.4). Therefore,

$$\begin{aligned} p^{(0)} &= e^{-\lambda T_\mathrm{b}} \\ p^{(1)}(t_1) &= \lambda e^{-\lambda(T_\mathrm{b}-\tau)} \\ &\vdots \\ p^{(k-1)}(t_1, t_2, \ldots, t_{k-1}) &= \lambda^{k-1} e^{-\lambda(T_\mathrm{b}-(k-1)\tau)}\ , \end{aligned} \tag{3.24}$$

where $t_i + \tau \leq t_{i+1}$ for $i = 1, 2, \ldots, k-1$. The kth arrival time, t_k, may or may not fall within the last τ seconds of the counting interval. Therefore, depending on t_k:

$$p^{(k)}(t_1, t_2, \ldots, t_k) = \begin{cases} \lambda^k e^{-\lambda(T_\mathrm{b}-k\tau)}, & t_k < T_\mathrm{b} - \tau \\ \lambda^k e^{-\lambda(t_k-(k-1)\tau)}, & t_k > T_\mathrm{b} - \tau. \end{cases} \tag{3.25}$$

For obtaining $p_K(k)$, the joint probability density function in (3.25) needs to be integrated over the region spanned by t_1, t_2, …, t_k. Region $\{\mathcal{R}\}$ is defined as the set of all possible values for arrival times t_1, t_2,…, t_k, and it can be divided into two subsets $\{\mathcal{R}_1\}$ and $\{\mathcal{R}_2\}$ such that $\{\mathcal{R}\} = \{\mathcal{R}_1\} \cup \{\mathcal{R}_2\}$. The subset $\{\mathcal{R}_1\}$ consists of all possible k-tuples for which the first case of (3.25) holds, meaning that the detection of all k photons is entirely contained in $(0, T_\mathrm{b}]$. For the k-tuples of $\{\mathcal{R}_2\}$, the second case of (3.25) holds and the dead time of the last photon (kth photon) extends out of $(0, T_\mathrm{b}]$. Therefore, the probability of detecting k photons in the interval $(0, T_\mathrm{b}]$ is given by:

$$p_K(k) = p_1(k) + p_2(k), \tag{3.26}$$

where,

$$p_1(k) = \int\limits_{\{\mathcal{R}_1\}} p^{(k)}(t_1, \ldots, t_k) dt_1 \cdots dt_k \tag{3.27a}$$

$$p_2(k) = \int\limits_{\{\mathcal{R}_2\}} p^{(k)}(t_1, \ldots, t_k) dt_1 \cdots dt_k \tag{3.27b}$$

The arrival time sequence $\{t_i\}$ belonging to the subset $\{\mathcal{R}_1\}$ should satisfy the following

inequalities:

$$\begin{aligned} 0 \leq\ & t_1 && \leq t_2 - \tau \\ \tau \leq\ & t_2 && \leq t_3 - \tau \\ & \vdots \\ (k-2)\tau \leq\ & t_{k-1} && \leq t_k - \tau \\ (k-1)\tau \leq\ & t_k && \leq T_\mathrm{b} - \tau. \end{aligned}$$

The integral in (3.27a) is calculated as (see Appendix A):

$$p_1(k) = \frac{\lambda^k (T_\mathrm{b} - k\tau)^k}{k!} e^{-\lambda(T_\mathrm{b} - k\tau)}. \tag{3.28}$$

For the subset $\{\mathcal{R}_2\}$, the arrival time sequence $\{t_i\}$ should satisfy the following inequalities:

$$\begin{aligned} 0 \leq\ & t_1 && \leq t_2 - \tau \\ \tau \leq\ & t_2 && \leq t_3 - \tau \\ & \vdots \\ (k-2)\tau \leq\ & t_{k-1} && \leq t_k - \tau \\ T_\mathrm{b} - \tau \leq\ & t_k && \leq T_\mathrm{b} \end{aligned}$$

Also, $p_2(k)$ in (3.27b) is given by (see Appendix A):

$$p_2(k) = \sum_{i=0}^{k-1} \frac{\lambda^i (T_\mathrm{b} - k\tau)^i}{i!} e^{-\lambda(T_\mathrm{b} - k\tau)} - \sum_{i=0}^{k-1} \frac{\lambda^i (T_\mathrm{b} - (k-1)\,\tau)^i}{i!} e^{-\lambda(T_\mathrm{b} - (k-1)\tau)}. \tag{3.29}$$

Define $\psi(i, \lambda) = \lambda^i e^{-\lambda}/i!$ and $\lambda_k = \lambda(T_\mathrm{b} - k\tau)$. Therefore:

$$p_K(k) = \sum_{i=0}^{k} \psi\left(i, \lambda_k\right) - \sum_{i=0}^{k-1} \psi\left(i, \lambda_{k-1}\right) \tag{3.30}$$

for $k \leq k_\mathrm{max}$. This expression provides the probability of counting k photons by an AQ SPAD with constant dead time τ. A similar approach has been previously used in [96], however, a wrong assumption has led to invalid expressions.

3.3.2 Renewal Processes

Recall from Section 3.1.2 that $\phi(t)$ is the probability of no photon detection event during the interval $(0, t]$, given an event at $t = 0$. Thus, for the AQ SPAD:

$$\phi(t) = \begin{cases} e^{-\lambda(t-\tau)}, & t > \tau \\ 1, & t < \tau. \end{cases} \tag{3.31}$$

The LT of $\phi(t)$ is given by:

$$\Phi(s) = \frac{1}{s} - \frac{\lambda e^{-\tau s}}{s(s+\lambda)}. \tag{3.32}$$

According to (3.20), $P(k, s)$ can be obtained as:

$$P(k,s) = \frac{1}{s}\left[\frac{\lambda^k e^{-k\tau s}}{(s+\lambda)^k} - \frac{\lambda^{k+1} e^{-(k+1)\tau s}}{(s+\lambda)^{k+1}}\right]. \tag{3.33}$$

The inverse LT from the above equation gives:

$$\begin{aligned} \frac{\partial p(k,t)}{\partial t} = {} & \frac{\lambda^k (t-k\tau)^{k-1}}{(k-1)!} e^{-\lambda(t-k\tau)} U(t-k\tau) \\ & - \frac{\lambda^{k+1}(t-(k+1)\tau)^k}{k!} e^{-\lambda(t-(k+1)\tau)} U(t-(k+1)\tau), \end{aligned} \tag{3.34}$$

where $U(t)$ is the unit step function:

$$U(t) = \begin{cases} 1, & t \geq 0 \\ 0, & t < 0. \end{cases}$$

Therefore (see Appendix A),

$$p(k,t) = \sum_{i=0}^{k} \frac{\lambda^i (t-(k+1)\tau)^i}{i!} e^{-\lambda(t-(k+1)\tau)} - \sum_{i=0}^{k-1} \frac{\lambda^i (t-k\tau)^i}{i!} e^{-\lambda(t-k\tau)}. \tag{3.35}$$

The expression for $p(k, t)$ in (3.35) is the probability of k photocounts in $(0, t]$, given one photon at $t = 0$. This means that the SPAD becomes free after $t = \tau$. Therefore, in order to relax this assumption, t can be replaced by $t + \tau$ in the above equation. Finally:

$$p_K(k) = p(k,t)|_{t=T_\mathrm{b}} = \sum_{i=0}^{k} \psi(i, \lambda_k) - \sum_{i=0}^{k-1} \psi(i, \lambda_{k-1}), \tag{3.36}$$

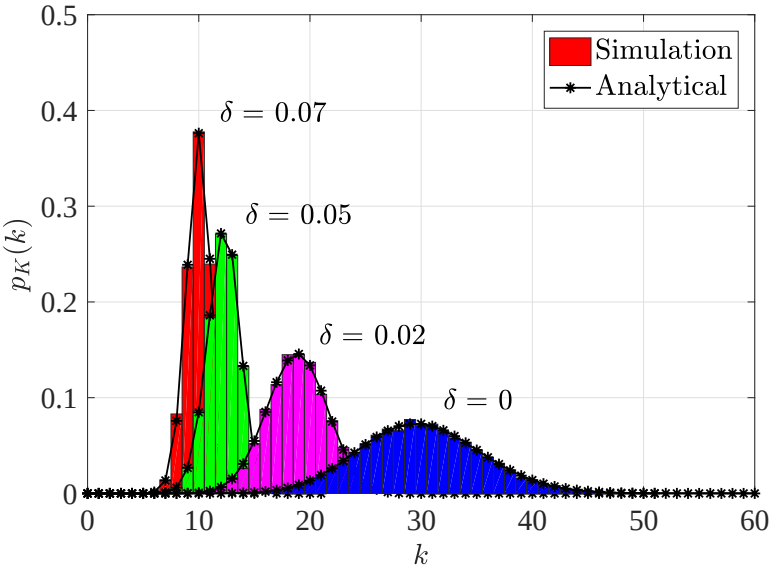

Figure 3.2: *PMF of AQ SPAD photocounts for $T_{\rm b} = 1$ μs, $\lambda = 3 \times 10^7$ photons/s and different values of δ (The solid line with marker represents a fitted curve for the discrete PMF).*

for $k \leq k_{\max}$. The above expression was previously derived in Section 3.3.1 using the concepts of Poisson processes.

The PMF obtained in in (3.30)/(3.36) is plotted in Fig. 3.2 and compared with the Monte Carlo simulation results for different values of dead time ratio, $\delta = \tau/T_{\rm b}$. For performing Monte Carlo simulations, within a time interval of $T_{\rm b}$ seconds, a Poisson arrival process with average rate of λ photons/s is generated which represents the photon arrival times at the SPAD receiver. Depending on the dead time duration, the total number of detected photons in this time interval is counted, and this test is repeated for 10^6 times (to achieve a high accuracy), so that the histograms in Fig. 3.2 are obtained based on the collected data. In this figure, a time interval of $T_{\rm b} = 1$ μs is considered and $\lambda = 3 \times 10^7$ photons/s. Also, $\delta = 0$, 0.02, 0.05 and 0.07 are considered. Note that for a SPAD without dead time, the photocount distribution is Poisson with mean $\lambda T_{\rm b}$ as discussed in Section 3.2. For the PMF expression in (3.30)/(3.36), some of the main properties are addressed as follows:

The Unitary Condition

As required for any valid distribution function, for the PMF in (3.36), the equality $\sum\limits_{k} p_K(k) = 1$ holds. Furthermore, it is easily seen that $\lim\limits_{\tau \to 0} p_K(k) = p_0(k)$, that is, when τ goes to zero, the

Poisson distribution of an ideal SPAD is recovered.

Mean and Variance

The mean and variance of the photocount distribution in (3.36) are given by (refer to Appendix C):

$$\mu_K = k_{\max} - \sum_{k=0}^{k_{\max}-1} \sum_{i=0}^{k} \psi(i, \lambda_k), \tag{3.37a}$$

$$\sigma_K^2 = \sum_{k=0}^{k_{\max}-1} \sum_{i=0}^{k} (2k_{\max} - 2k - 1)\psi(i, \lambda_k) - \left(\sum_{k=0}^{k_{\max}-1} \sum_{i=0}^{k} \psi(i, \lambda_k) \right)^2 . \tag{3.37b}$$

Again, as dead time goes to zero, the limiting relations $\lim_{\tau \to 0} \mu_K = \lambda T_{\mathrm{b}}$ and $\lim_{\tau \to 0} \sigma_K^2 = \lambda T_{\mathrm{b}}$ in (3.37a) and (3.37b) can be verified, where λT_{b} is the mean value of Poisson distribution corresponding to an ideal SPAD.

Fig. 3.3a presents μ_K and σ_K^2 for an AQ SPAD as functions of λ where they are compared to an ideal Poisson counting process. As shown, the difference between μ_K and σ_K^2 becomes more significant as λ increases. Let the ratio of the variance to mean be defined as:

$$\xi = \frac{\sigma_K^2}{\mu_K} . \tag{3.38}$$

Fig. 3.3b illustrates this ratio where it approaches to zero as λ goes to infinity, unlike the Poisson distribution where this ratio is equal to one for all values of λ.

Asymptotic Mean for Small τ/T_{b} Ratio

The exact mean value in (3.37a) can also be expressed as follows:

$$\mu_K = k_{\max} - \sum_{k=0}^{k_{\max}-1} \frac{\Gamma(k+1, \lambda_k)}{\Gamma(k+1)} , \tag{3.39}$$

where for a positive integer s, $\Gamma(s) = (s-1)!$ and $\Gamma(s, x) = e^{-x}(s-1)! \sum_{i=0}^{s-1} x^i/i!$ are the gamma and incomplete gamma functions, respectively [95]. Defining $\gamma(s, x) = \Gamma(s, x)/\Gamma(s)$,

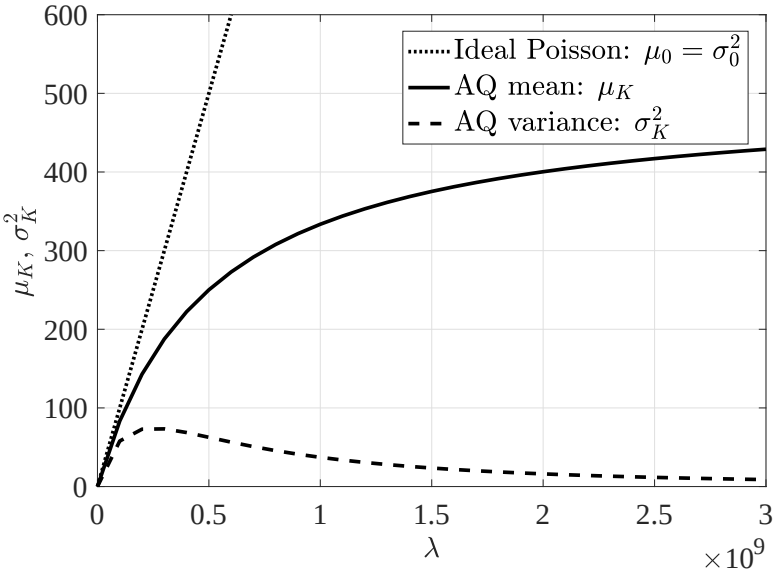

(a)

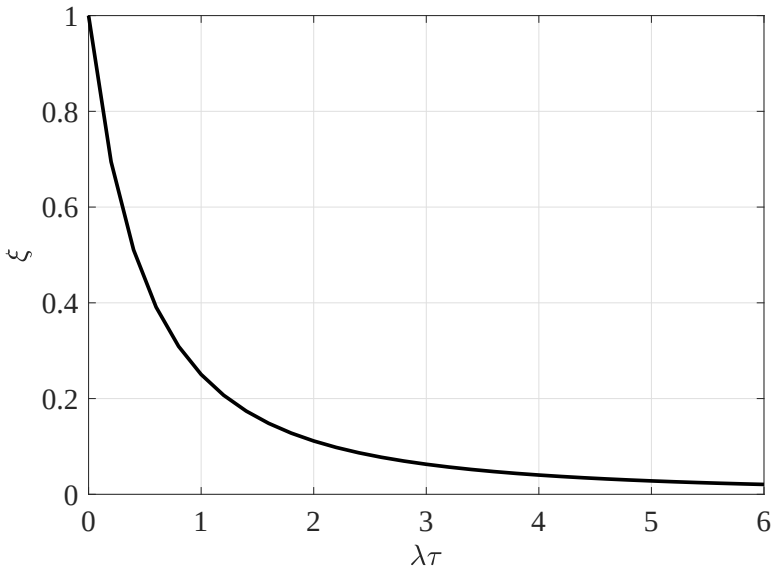

(b)

Figure 3.3: *Mean and variance of AQ SPAD photocounts with $T_\mathrm{b} = 1$ μs, $\tau = 2$ ns: (a) comparison of mean and variance with ideal Poisson distribution, (b) the variance to mean ratio.*

the following approximation holds for $\gamma(k+1, \lambda_k)$ when τ/T_b goes to zero [95]:

$$\gamma(k+1, \lambda_k) \approx \begin{cases} 1, & k+1 > \lambda_k \\ 0, & k+1 \leq \lambda_k \end{cases}$$

Therefore, $\gamma(k+1, \lambda_k)$ can be approximated as zero for $k+1 \leq \lambda T_{\rm b}/(1+\lambda\tau)$, and 1, otherwise. Applying the above approximation to (3.39) gives:

$$\lim_{\tau/T_{\rm b}\to 0} \mu_K = \frac{\lambda T_{\rm b}}{1+\lambda\tau}\cdot \tag{3.40}$$

The above expression has been derived in [97] through a different approach.

Effective Count Rate

The effective count rate of the SPAD detector is one of the most important practical considerations when it comes to high speed applications. The effective count rate is defined as the rate at which the SPAD can detect photons and is given by [31]:

$$\lambda' = \frac{\mu_K}{T_{\rm b}}\cdot \tag{3.41}$$

As the dead time incurs counting losses and degrades μ_K, λ' is also critically affected by the dead time. The effective count rate, λ', is always less than the photon arrival rate, λ. However, λ' does not grow boundlessly by increasing λ. Using (3.41) and the exact expression for μ_K derived in (3.37a), an exact analytical model for the count rate of the AQ SPAD can be obtained. In addition, using the approximate expression of μ_K derived in (3.40), an asymptotic count rate model is developed as:

$$\lambda' = \frac{\lambda}{1+\lambda\tau}\cdot \tag{3.42}$$

The above approximate model is well-known in the literature and has been verified through experiments [29–31].

In Fig. 3.4, the effective count rate of the AQ SPAD is evaluated for various dead time values and is also compared with Monte Carlo simulation results. In this figure, a normalized counting interval ($T_{\rm b} = 1$) and three different values for dead time ($\tau = 0.1$, 0.01, and 0.001) are considered. For each value of λ, random photon arrival times are generated as a Poisson process, and depending on the dead time duration, the registered photons are counted accordingly. Again, the Monte Carlo simulation consists of 10^6 runs. This number ensures a high accuracy and a perfect match with the analytical models. This figure demonstrates that the predictions of the analytical framework perfectly match with the simulation results.

According to Fig. 3.4, as λ increases, λ' also grows up to a *saturation* level, meaning that the

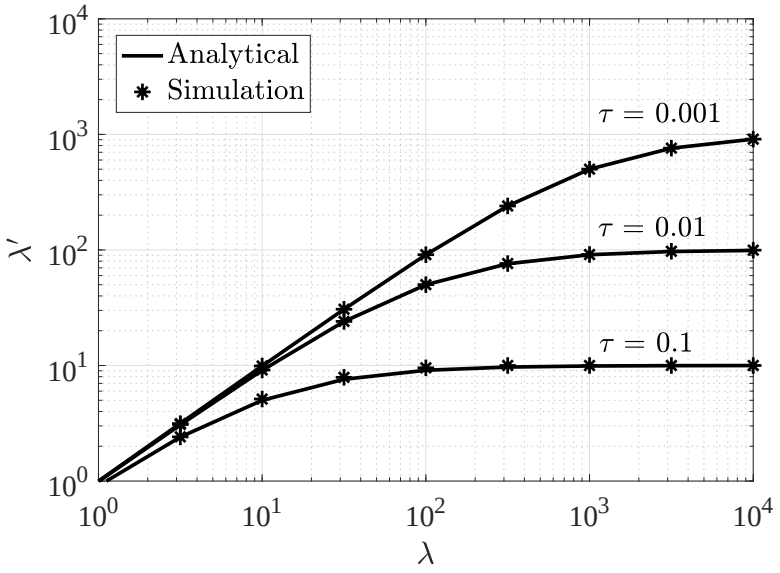

Figure 3.4: *Effective count rate of an AQ SPAD ($T_{\mathrm{b}} = 1$).*

SPAD is not able to reach count rates higher than this value. In addition, for a given photon arrival rate, longer dead times result in lower count rates and a lower saturation level. The count rate model in (3.42) predicts a saturation level of $1/\tau$ and this can be clearly observed in all the curves of Fig. 3.4, e.g. with $\tau = 0.1$, $\lambda'_{\mathrm{sat}} = 10$.

3.4 PQ SPAD

In this section, the dead time-modified photocount distribution of a PQ SPAD is derived. For PQ SPADs, any photon arrival event is followed by a dead time. Thus, the photons which arrive during the dead time of the previous photons extend the dead time duration.

Again, define $p(k,t)$ as the probability of k photocounts during the time interval $(0,t]$, given one detected photon at $t = 0$. The next photon arrives between t' and $t' + dt'$ with probability $\lambda e^{-\lambda t'} dt'$. If this photon arrives in $(0,\tau)$ it is not detected, but if it arrives after the dead time of the photon occurring at $t = 0$, it is counted. Therefore, the following renewal integral equation can be constituted:

$$p(k,t) = e^{-\lambda t}\delta(k) + \int_0^{\tau} \lambda e^{-\lambda t'} p(k, t-t')dt' + \int_{\tau}^{t} \lambda e^{-\lambda t'} p(k-1, t-t')dt'. \tag{3.43}$$

In the above renewal equation, the first term in the right-hand side accounts for the case where

no photon arrives at the SPAD. The second term is when the next photon arriving after $t = 0$ is lost, because it arrives during the dead time of the photon at $t = 0$. The last term represents the case where the next photon arrives after the dead time of the photon at $t = 0$ is finished, and therefore this photon is detected. The GF corresponding to $p(k, t)$ is given by:

$$G(z,t) = e^{-\lambda t} + \int_0^{\tau} \lambda e^{-\lambda t'} G(z, t - t')dt' + \int_{\tau}^{t} z\lambda e^{-\lambda t'} G(z - 1, t - t')dt', \tag{3.44}$$

Differentiating with respect to t gives:

$$\frac{\partial G(z,t)}{\partial t} = \lambda e^{-\lambda\tau}(z - 1)G(z, t - \tau). \tag{3.45}$$

According to (3.44), it is clear that $G(z, 0) = 1$, as $p(k, 0) = 1$ if $k = 0$, and 0 otherwise. Also, since no photon can be detected within the interval $(0, \tau)$, it can be concluded that if $0 \leq t < \tau$ then $G(z, t) = 1$. And, if k_0 be an integer such that $k_0\tau \leq t < (k_0 + 1)\tau$, then, $G(z, t - k_0\tau) = 1$. This requires $G(z, t)$ to be an upper semi-continuous function of t. Thus, the recurrence relation in (3.45) can be solved by iteration. Assume:

$$G(z,t) = \sum_{i=0}^{k_0} A_i(z)(t - i\tau)^i U(t - i\tau). \tag{3.46}$$

Substituting (3.46) into (3.45) gives:

$$\begin{aligned}
A_1(z) &= \lambda e^{-\lambda\tau}(z - 1)A_0(z) \\
2A_2(z) &= \lambda e^{-\lambda\tau}(z - 1)A_1(z) \\
3A_3(z) &= \lambda e^{-\lambda\tau}(z - 1)A_2(z) \\
&\vdots \\
k_0 A_{k_0}(z) &= \lambda e^{-\lambda\tau}(z - 1)A_{k_0-1}(z).
\end{aligned}$$

In addition, the boundary condition $G(z, 0) = 1$ directly leads to $A_0(z) = 1$ and the above equations result in:

$$A_i(z) = (z - 1)^i \times \frac{\lambda^i e^{-i\lambda\tau}}{i!} = \sum_{k=0}^{i} \binom{i}{k} z^k (-1)^{i-k} \times \frac{\lambda^i e^{-i\lambda\tau}}{i!}, \tag{3.47}$$

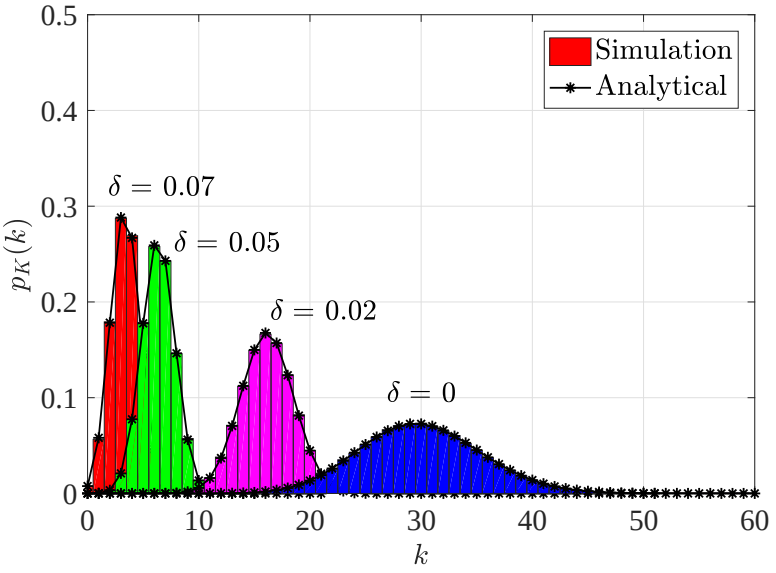

Figure 3.5: *PMF of PQ SPAD photocounts for $T_\mathrm{b} = 1$ μs, $\lambda = 3 \times 10^7$ photons/s and different values of δ (The solid line with marker represents a fitted curve for the discrete PMF).*

for $i > 0$. $G(z,t)$ is then obtained as:

$$\begin{aligned} G(z,t) &= \sum_{i=0}^{k_0} \sum_{k=0}^{i} \binom{i}{k} z^k (-1)^{i-k} \frac{\lambda^i e^{-i\lambda\tau}}{i!} (t - i\tau)^i U(t - i\tau) \\ &= \sum_{k=0}^{k_0} \sum_{i=k}^{k_0} \binom{i}{k} z^k (-1)^{i-k} \frac{\lambda^i e^{-i\lambda\tau}}{i!} (t - i\tau)^i U(t - i\tau). \end{aligned} \tag{3.48}$$

According to the definition of generating function $G(z,t)$ in (3.9), $p(k,t)$ is the coefficient of z^k in (3.48):

$$p(k,t) = \sum_{i=k}^{k_0} \binom{i}{k} (-1)^{i-k} \frac{\lambda^i e^{-i\lambda\tau}}{i!} (t - i\tau)^i U(t - i\tau). \tag{3.49}$$

The expression for $p(k,t)$ in (3.49) is the probability of k photocounts in $(0,t]$ given one photon arrival at $t = 0$. Unlike the case of AQ SPADs, relaxing the assumption of one photon at $t = 0$ is not straightforward, as the PQ SPAD does not necessarily become free at $t = \tau$. However, we resort to the same approach and replace t by $t+\tau$ in the above equation. For the dead time values and the photon rates considered here, this is a tight approximation. With the modification, k_0 is replaced by $k_0 + 1$. Therefore, the counting distribution of a PQ SPAD in the time interval

$(0, T_{\rm b}]$ is expressed as:

$$p_K(k) = p(k,t)|_{t=T_{\rm b}} = \sum_{i=k}^{k_{\max}} (-1)^{i-k} \binom{i}{k} \frac{\lambda^i (T_{\rm b} - (i-1)\tau)^i}{i!} e^{-i\lambda\tau}, \tag{3.50}$$

for $k \leq k_{\max}$ and $p_K(k) = 0$ for $k > k_{\max}$.

The PMF obtained in (3.50) is plotted in Fig. 3.5 and compared with the Monte Carlo simulation results for different values of $\delta = \tau/T_{\rm b}$. The approach for performing Monte Carlo simulations is similar to the one presented for AQ SPADs. In Fig. 3.5, a time interval of $T_{\rm b} = 1$ μs is considered and $\lambda = 3 \times 10^7$ photons/s. Also, $\delta = 0$, 0.02, 0.05, and 0.07 are assumed. Note that for a SPAD without dead time, the photocount distribution is Poisson with mean $\lambda T_{\rm b}$. For the PMF expression in (3.50), some of the main properties are addressed as follows:

The Unitary Condition

It can easily be verified that the unitary condition $\sum\limits_k p_K(k) = 1$ holds for the PMF in (3.50) and $\lim\limits_{\tau \to 0} p_K(k) = p_0(k)$, that is, when τ goes to zero, the PMF in (3.50) approaches the ideal Poisson distribution.

Mean and Variance

The mean and variance of the photocount distribution in (3.50) are derived as (refer to Appendix D):

$$\mu_K = \lambda e^{-\lambda\tau} T_{\rm b}, \tag{3.51a}$$

$$\sigma_K^2 = \lambda^2 e^{-2\lambda\tau}(\tau^2 - 2T_{\rm b}\tau) + \lambda e^{-\lambda\tau} T_{\rm b}. \tag{3.51b}$$

The expressions in (3.51) have been derived in [97] through a different approach. Similar to the AQ SPAD, the limiting relations $\lim\limits_{\tau \to 0} \mu_K = \lambda T_{\rm b}$ and $\lim\limits_{\tau \to 0} \sigma_K^2 = \lambda T_{\rm b}$ in (3.51a) and (3.51b) can be confirmed, where $\lambda T_{\rm b}$ is the mean value of the ideal Poisson distribution. Fig. 3.6a presents μ_K and σ_K^2 as functions of λ. The mean and variance are also compared to an ideal counting process where it is observed that unlike a Poisson process, μ_K and σ_K^2 can differ significantly. Fig. 3.6b illustrates the ratio ξ, as defined in (3.38) where the minimum occurs at $\lambda\tau = 1$ and the ξ approaches 1 when $\lambda\tau$ goes to infinity.

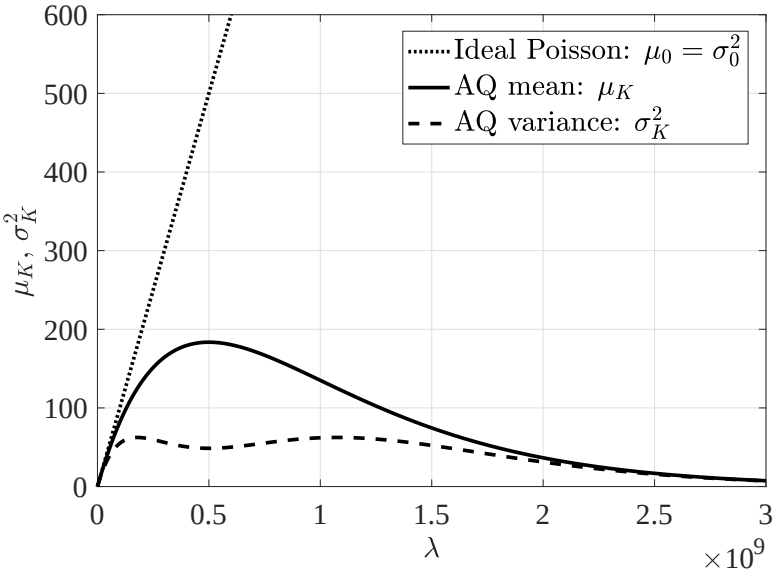

(a)

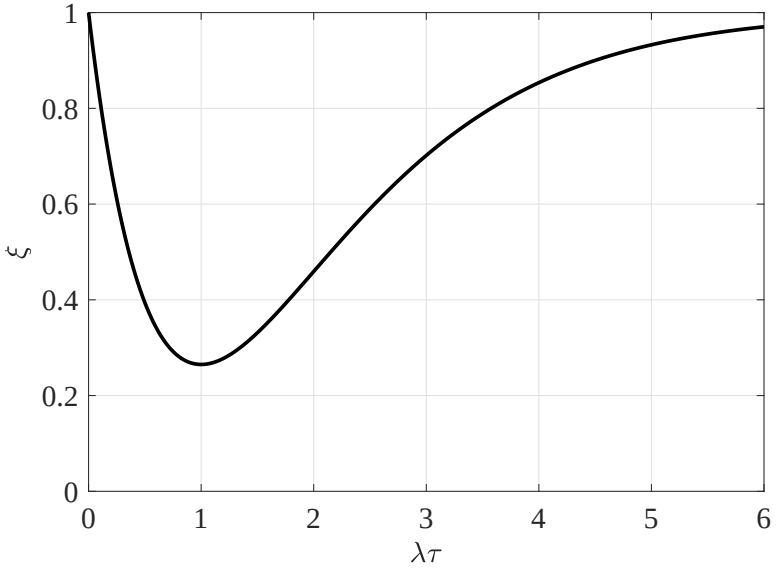

(b)

Figure 3.6: *Mean and variance of PQ SPAD photocounts with $T_\mathrm{b} = 1$ μs, $\tau = 2$ ns: (a) comparison of mean and variance with ideal Poisson distribution, (b) the variance to mean ratio.*

Effective Count Rate

Similar to the AQ SPAD, the effective count rate of the PQ SPAD is defined as:

$$\lambda' = \frac{\mu_K}{T_\mathrm{b}} \cdot \tag{3.52}$$

Therefore, based on (3.51a), the count rate of the PQ SPAD is given by:

$$\lambda' = \lambda e^{-\lambda\tau}. \tag{3.53}$$

The above expression specifies how λ' depends on τ and why it does not grow boundlessly by increasing λ. The count rate model of (3.53) is in line with the experimental results presented in [29], and this confirms the validity of our mathematical modelling.

In Fig. 3.7, the effective count rate of the PQ SPAD is evaluated and compared with Monte Carlo simulation results. In this figure, a normalized counting interval ($T_{\rm b} = 1$) and three different values for the dead time ($\tau = 0.1$, 0.01, and 0.001) are considered. According to Fig. 3.7, as λ increases, first λ' grows up to a *peak* saturation point and then decreases rapidly. Longer dead times result in lower count rates, an earlier saturation and a lower peak value. Referring to (3.53), the peak count rate is $\lambda'_{\rm sat} = 1/(e\tau)$ and it occurs at $\lambda = 1/\tau$. This can be clearly observed in all the curves of Fig. 3.7, e.g. with $\tau = 0.1$, $\lambda'_{\rm sat} \approx 3.7$.

In contrast to the AQ SPAD, which reaches a constant effective count rate after saturation, once the PQ SPAD reaches its maximum count rate, a further increase in the photon arrival rate will drastically degrade the photon counting performance and lead to reduced count rates. In fact, the maximum count rate of the PQ SPAD is only achieved at a specific photon arrival rate ($\lambda = 1/\tau$). Furthermore, this maximum count rate is lower than the saturation count rate of an AQ SPAD with the same τ. This is the reason why AQ SPADs are generally preferred over PQ SPADs.

3.5 Mixed AQ/PQ SPAD

In this section, the dead time-modified photocount distribution of a mixed AQ/PQ SPAD is derived. The AQ and PQ SPADs can be considered as special cases of this general hybrid receiver. Suppose that the detected and lost photons are followed by two different dead times, τ_1 and τ_2, respectively. Assuming different dead time values for detected and lost photons helps to clearly reflect distinct effects of paralyzable and nonparalyzable dead times on the total renewal process. Assume that $\tau_1 > \tau_2$. In addition, we assume a normalized photon arrival rate in the analytical derivations, for simplicity. The probability $\phi(t)$ that no photon is

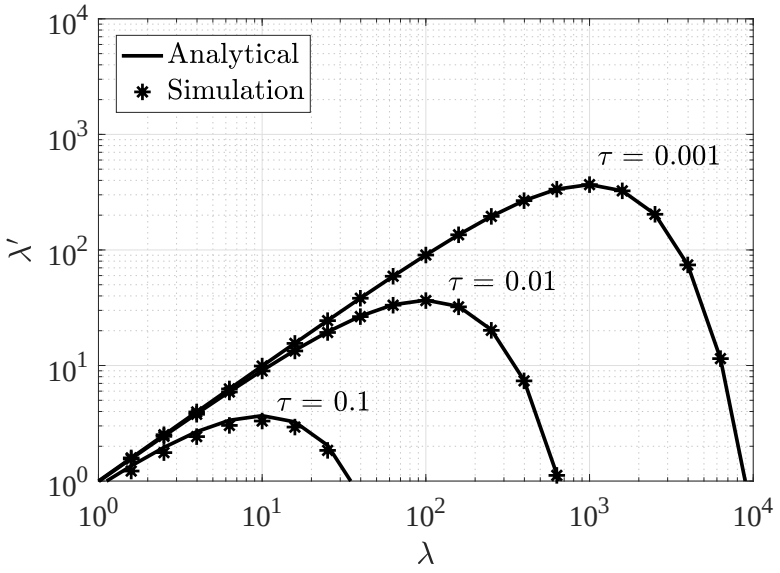

Figure 3.7: *Effective count rate of a PQ SPAD ($T_{\mathrm{b}} = 1$).*

detected up to time t, given that a photon is registered at $t = 0$, is:

$$\phi(t) = [U(t) - U(t - (\tau_1 - \tau_2))] + \phi^{\mathrm{p}}(t - (\tau_1 - \tau_2))U(t - (\tau_1 - \tau_2)). \tag{3.54}$$

In the above equation, the total probability of not detecting any photons is obtained as follows: The first term in the right-hand side of (3.54) expresses the condition that no photon is detected up to $t < \tau_1 - \tau_2$. If any photon arrives during time interval of $(0, \tau_1 - \tau_2)$, it is clearly lost and is followed by a dead time of length τ_2, and this dead time won't extend beyond the dead time of the registered photon at $t = 0$, i.e. τ_1. Thus, $\phi(t) = 1$ for $t < \tau_1 - \tau_2$. If any photon arrives after $\tau_1 - \tau_2$, the dead time will be extended beyond τ_1. It is then valid to assume that the detector is in paralyzable mode, where $\phi^{\mathrm{p}}(t - (\tau_1 - \tau_2))$ represents the probability that no photon is registered in time $t - (\tau_1 - \tau_2)$. Applying LT to (3.54) gives:

$$\Phi(s) = \frac{1}{s}(1 - e^{-s(\tau_1 - \tau_2)}) + e^{-s(\tau_1 - \tau_2)}\Phi^{\mathrm{p}}(s). \tag{3.55}$$

In order to obtain $\Phi^{\mathrm{p}}(s)$ and then $\Phi(s)$, the product density of the first order for the paralyzable mode is easily calculated as:

$$f_1^{\mathrm{p}}(t)dt = U(t - \tau_2)e^{-\tau_2}dt. \tag{3.56}$$

The above expression results from arguing that a photon is detected only if it arrives after the dead time of the photon at $t = 0$ ($t > \tau_2$) and it is also not preceded by any photon arrival event in time interval $(0, \tau_2)$. Thus:

$$F_1^{\mathrm{p}}(s) = \frac{1}{s} e^{-(s+1)\tau_2}. \tag{3.57}$$

$F_1^{\mathrm{p}}(s)$ and $\Phi^{\mathrm{p}}(s)$ are related through (3.14) and (3.20):

$$\Phi^{\mathrm{p}}(s) = \frac{1}{s} \times \frac{1}{1 + F_1^{\mathrm{p}}(s)}\,. \tag{3.58}$$

Therefore, (3.55), (3.57) and (3.58) result in:

$$F_1(s) = \frac{1}{s e^{s\tau_1+\tau_2} + e^{s(\tau_1-\tau_2)} - 1}\,. \tag{3.59}$$

The same result is obtained for $\tau_1 < \tau_2$ following exactly the same arguments. According to (3.14), for general values of τ_1 and τ_2, the following expression in is obtained for $P(k, s)$:

$$P(k,s) = \frac{1}{s}\left[\left(e^{s\tau_1+\tau_2} + e^{s(\tau_1-\tau_2)}\right)^{-k} - \left(e^{s\tau_1+\tau_2} + e^{s(\tau_1-\tau_2)}\right)^{-(k+1)}\right]. \tag{3.60}$$

The inverse LT then leads to:

$$\begin{aligned} p(k,t) &= \frac{1}{2\pi i}\int_{\alpha-i\infty}^{\alpha+i\infty}\left[\frac{1}{s}\left(e^{s\tau_1+\tau_2} + e^{s(\tau_1-\tau_2)}\right)^{-k} - \frac{1}{s}\left(e^{s\tau_1+\tau_2} + e^{s(\tau_1-\tau_2)}\right)^{-(k+1)}\right]e^{st}ds \\ &= \frac{1}{2\pi i}\int_{\alpha-i\infty}^{\alpha+i\infty}\sum_{r=0}^{\infty}\left[e^{-(k+r)\tau_2}(-1)^r\binom{k+r-1}{r}\frac{e^{s(t-k\tau_1-r\tau_2)}}{s^{k+r+1}}\right]ds \\ &\quad - \frac{1}{2\pi i}\int_{\alpha-i\infty}^{\alpha+i\infty}\sum_{r=0}^{\infty}\left[e^{-(k+r+1)\tau_2}(-1)^r\binom{k+r}{r}\frac{e^{s(t-(k+1)\tau_1-r\tau_2)}}{s^{k+r+2}}\right]ds. \end{aligned} \tag{3.61}$$

The following equality holds for $t > 0$ [95]:

$$\frac{1}{2\pi i}\int_{\alpha-i\infty}^{\alpha+i\infty}\frac{e^{st}}{s^k}\,ds = \frac{t^{k-1}}{(k-1)!}\,.$$

Thereby, the final expression for $p(k,t)$ is obtained as:

$$\begin{aligned} p(k,t) = &\sum_{r=0}^{K_1} (-1)^r \binom{k+r-1}{r} \frac{(t-k\tau_1-r\tau_2)^{k+r}}{(k+r)!} e^{-(k+r)\tau_2} \\ &- \sum_{r=0}^{K_2} (-1)^r \binom{k+r}{r} \frac{(t-(k+1)\tau_1-r\tau_2)^{k+r+1}}{(k+r+1)!} e^{-(k+r+1)\tau_2}, \end{aligned} \tag{3.62}$$

where K_1 and K_2 are integers such that:

$$\begin{aligned} \frac{t-k\tau_1}{\tau_2} - 1 < K_1 < \frac{t-k\tau_1}{\tau_2} \\ \frac{t-(k+1)\tau_1}{\tau_2} - 1 < K_2 < \frac{t-(k+1)\tau_1}{\tau_2}. \end{aligned}$$

When $\tau_1 \neq 0$ and $\tau_2 \neq 0$, $p(k,t)$ is given by a finite series. Particular cases include:

- With $\tau_1 = \tau_2 = 0$, the Poisson distribution for an ideal SPAD, given in (3.21), is obtained.
- With $\tau_2 = 0$, the photocount distribution for an AQ SPAD, given in (3.35), is obtained.
- With $\tau_1 = \tau_2$, the photocount distribution for a PQ SPAD, given in (3.49), is obtained.

3.6 SPAD Array

To eliminate the effect of dead time and to achieve higher count rates, an array of SPADs can be used. The output of a SPAD array is the aggregate number of all photons detected by individual SPADs over the same time interval. Other than the dead time of the single SPADs, the fill factor (FF) of the SPAD array affects the photocount distribution. Figure 3.8 illustrates the configuration of a rectangular SPAD array. The FF coefficient, C_{FF}, is equal to the ratio of the active area (the grey areas) to the total area of the array. Assume that the array consists of N_{array} single SPADs, and the photocounts of the array elements are statistically independent. Denoting by K_i the number of photocounts at the ith element, the output of the array is expressed as:

$$S = \sum_{i=1}^{N_{\mathrm{array}}} K_i. \tag{3.63}$$

In the absence of dead time, the random variables K_i are iid with Poisson distribution. However, when the dead time is present, K_i's follow the PMF expressions given in (3.36) or (3.50), for

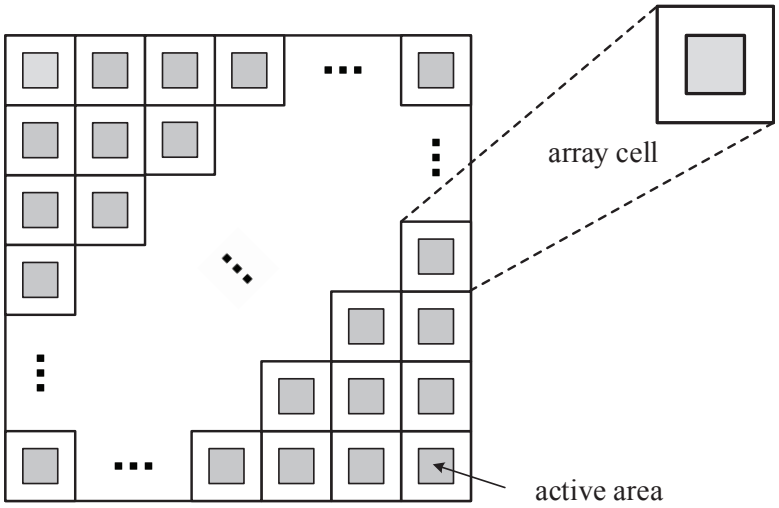

Figure 3.8: *Geometry of a SPAD array.*

AQ or PQ SPADs, respectively. Therefore, the PMF $p_K(k_i)$ for the ith element of the array can be rewritten with λ_i and τ_i denoting the average photon arrival rate and the dead time of the ith SPAD in the array, respectively. To take the effect of FF into account, λ_i in the PMF expression should be replaced by $C_{\mathrm{FF}}\lambda_i$.

If the number of array elements, N_{array}, is large, according to the central limit theorem (CLT), the dead time-modified photocount distribution of the SPAD array can be approximated by a Gaussian distribution, that is:

$$p_S(s) \sim \mathcal{N}(\mu_S, \sigma_S^2), \tag{3.64}$$

where,

$$\mu_S = \sum_{i=1}^{N_{\mathrm{array}}} \mu_i, \tag{3.65a}$$

$$\sigma_S^2 = \sum_{i=1}^{N_{\mathrm{array}}} \sigma_i^2. \tag{3.65b}$$

In (3.65), μ_i and σ_i^2 are the mean and variance of the photocount distribution of the ith SPAD in the array as previously derived in (3.37) and (3.51), for AQ and PQ SPADs, respectively.

The approximate counting distribution given in (3.64) is compared with the Monte Carlo simulation results in Fig. 3.9 for both AQ and PQ SPAD arrays. In these figures, ΛT_{b} is the average number of photons incident on the whole surface of the array in the counting interval of length T_{b}. When obtaining these results, it is assumed that all the array elements are identical

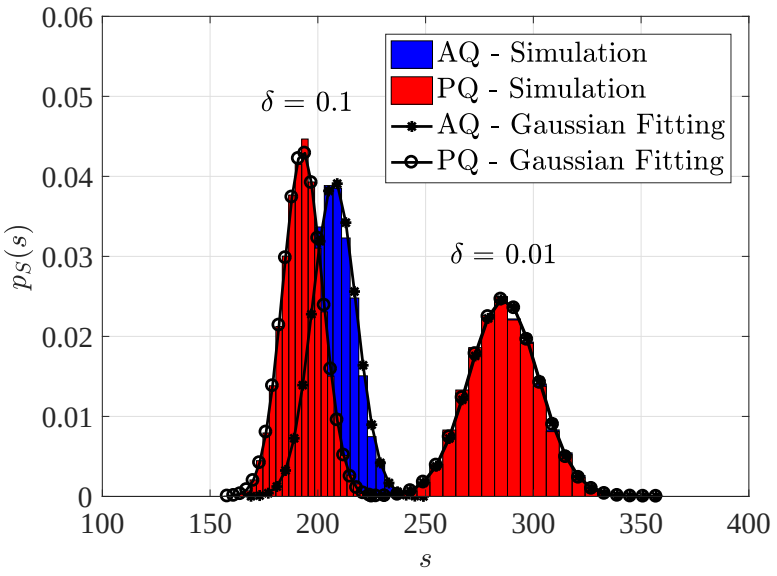

(a) $N_{\text{array}} = 64$

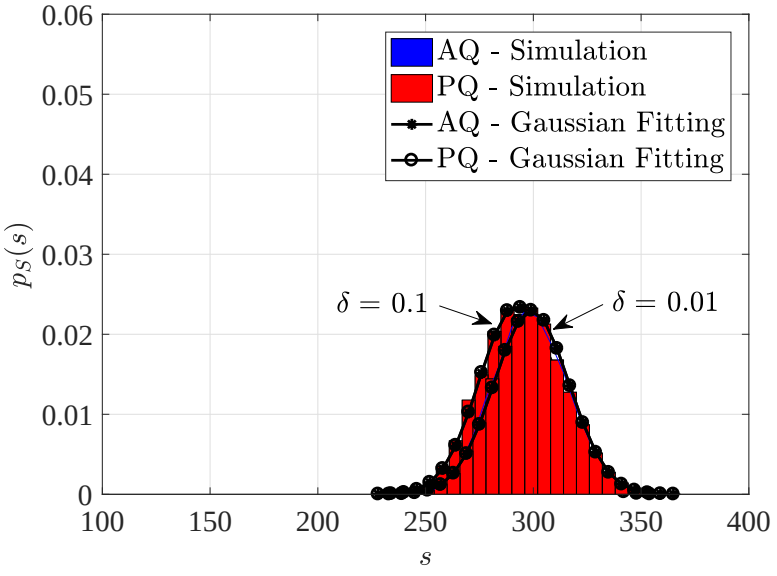

(b) $N_{\text{array}} = 1024$

Figure 3.9: *PMF of SPAD array photocounts with* $\Lambda T_{\text{b}} = 300$ *photons,* $C_{\text{FF}} = 1$ *(The solid lines with markers represent fitted curves for the discrete PMFs).*

(equal τ_i's) and the incident light beam has a uniform spatial distribution over the array surface (equal λ_i's), i.e. Λ is equally divided between the individual SPADs.

In Fig. 3.9a, arrays with 64 SPADs and in Fig. 3.9b, larger arrays with 1024 SPADs are considered. As shown, the Monte Carlo simulation results and the Gaussian approximations are perfectly matched and this confirms the validity of the approximation.

In Fig. 3.9a, it is observed that while for $\delta = 0.01$, the photocount histogram of the AQ SPAD array approximately matches that of the PQ SPAD array, the difference is still apparent for $\delta = 0.1$. However, according to Fig. 3.9b, the photon counting behaviour of the AQ and PQ SPAD arrays tends to match for larger array sizes, provided that the average number of photons per counting interval does not result in the saturation of the SPAD elements. It is also seen that for the same δ and ΛT_{b}, the array with 1024 SPADs has a higher mean value. This means that the counting losses arising from the dead time are mitigated to some extent if a larger array is used.

Effective Count Rate

The effective count rate of the SPAD array improves as the number of array elements increases. Assuming identical array elements and constant photon arrival rate, the count rate models of (3.42) and (3.53) can be modified for an array of N_{array} SPADs:

$$\Lambda'_{\mathrm{AQ}} = \frac{\Lambda}{1 + \dfrac{\Lambda\tau}{N_{\mathrm{array}}}}, \tag{3.66a}$$

$$\Lambda'_{\mathrm{PQ}} = \Lambda e^{-\dfrac{\Lambda\tau}{N_{\mathrm{array}}}}. \tag{3.66b}$$

The comparison between the above dead time-modified count rate models and the Monte Carlo simulations is given in Fig. 3.10. In this figure, the effective count rate of AQ and PQ SPAD arrays of two different sizes ($N_{\mathrm{array}} = 64$ and 1024) and three dead time values ($\tau = 0.1$, 0.01 and 0.001) are compared. According to these curves, the saturation and peak count rates are scaled by the size of the array compared to a single SPAD. Still, the dead time limits the maximum achievable count rate and determines the saturation level or peak value of the count rate curve, but the effect is shifted to higher photon rates. According to the expressions in (3.66) and Fig. 3.10, we can infer that with an array of N_{array} SPADs, the effective dead time reduces to τ/N_{array}.

Recall that in a SPAD array, the incident light intensity is divided between the array elements. It is then very unlikely that all the SPADs become inactive at the same time. Therefore, the array can detect a larger portion of the incident light intensity, i.e. a higher number of photons per counting interval. In addition, the dead time-induced counting losses decrease as the size of the

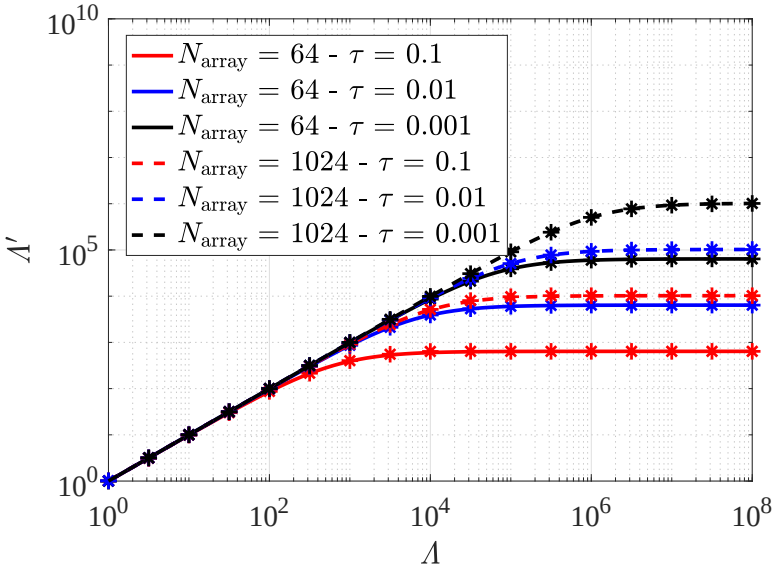

(a) AQ SPAD array

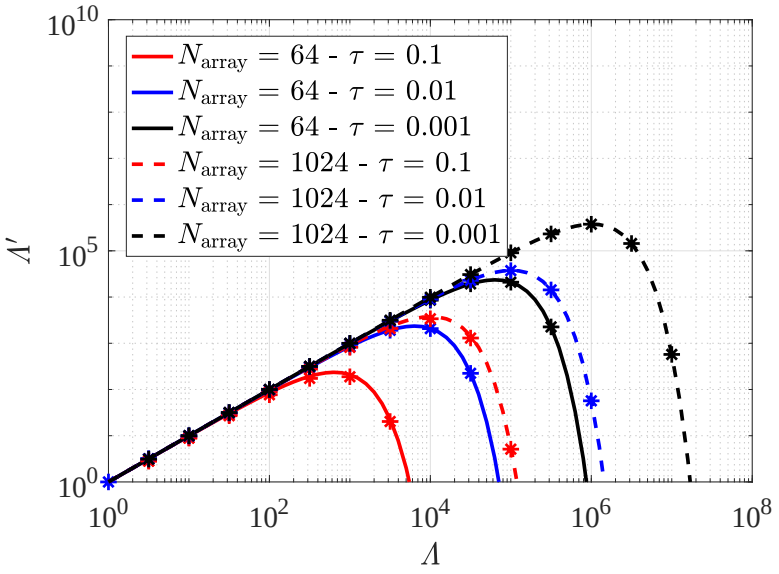

(b) PQ SPAD array

Figure 3.10: *Analytical (solid and dashed curves) and simulation (asterisks) results for effective count rate of SPAD arrays ($T_{\text{b}} = 1$ and $C_{\text{FF}} = 1$).*

array increases, such that in sufficiently large arrays AQ and PQ SPADs show a similar photon counting performance. This can be clearly observed in Figs. 3.9 and 3.10. Therefore, it can be concluded that using an array of SPADs makes it possible to reduce the effect of dead time and achieve higher counting rates. This means that SPAD arrays are more robust to dead time and can tolerate longer dead times, maintaining the required photon counting performance.

3.7 Summary

In this chapter, the photocount statistics of SPAD photodetectors were studied. The concepts of arrival processes and renewal processes were applied to investigate the impact of the detector dead time on the photon counting process of SPADs. Analytical expressions were derived for the PMF, mean, variance and count rate of the photocounts. The study was conducted for both single SPADs and SPAD arrays considering the effect of various dead time types imposed by AQ, PQ and mixed AQ/PQ circuits. It was shown that the commonly used Poisson distribution can not accurately describe the counting statistics of the SPAD detector with non-zero dead time. The dead time limits the maximum number of photons the SPAD can detect in the desired counting interval. Unlike the Poisson distribution with equal mean and variance, for the SPAD photocount distribution, the mean and variance are not equal and they do not change linearly with the incident photon rate. As the photon rate increases, the dead time counting losses increase and the moments deviate more from those of a Poisson distribution. Also, AQ and PQ single SPADs exhibit distinct photon counting behaviours, especially for longer dead times and/or in higher photon rates. The AQ single SPADs experience less counting losses and achieve higher count rates compared to the PQ single SPADs. In the SPAD arrays, the dead time losses are reduced. The effective dead time decreases with the size of the array and hence, the gap between the photon counting performance of the AQ and PQ SPADs almost disappears in sufficiently large arrays, in the photon rate range of interest.

This detailed statistical analysis was necessary to derive the later receiver performance evaluation results. As the next steps, the models developed in this chapter are to be used in Chapter 4 for assessing the bit error performance of the SPAD-based OWC systems, and in Chapter 5 for obtaining the information transfer rate of the SPAD receivers.

Chapter 4
SPAD-based Optical Systems

In recent years, single-photon avalanche diodes (SPADs) have drawn particular attention in the field of optical wireless communication (OWC), and this has led to a number of analytical and experimental studies among the scientific research community [8–10, 83]. Most of the existing studies appreciate the presence and impact of dead time on the overall performance of the systems and several studies and experiments suggest that the impact of dead time can be mitigated by employing arrays of SPADs [8, 65, 83]. However, there is a lack of an in-depth analysis and understanding of how exactly the dead time distorts the data reception and why systems consisting of SPAD arrays are more tolerant to dead time.

In this chapter, the effect of dead time on the bit error performance of a SPAD-based OWC system is investigated. The block diagram of this system is shown in Fig. 2.1. An ideal optical channel is considered here, as the aim is to purely focus on the receiver side. On-off keying (OOK) and binary pulse position modulation (BPPM) are the modulation schemes considered in this chapter. In these binary modulation schemes, each bit is sent individually by transmitting one of two optical pulses over an interval of length T_{b} seconds and the optical intensity modulated signal is transmitted by an optical source. In this system, the data rate is expressed as $R_{\mathrm{b}} = 1/T_{\mathrm{b}}$ bits/s. At the receiver side, direct detection (DD) is applied where the received optical signal is photodetected by the SPAD. During each bit interval, the number of photocounts is processed to decide which of two optical pulses is received, and then the transmitted bit is determined. In this photon counting system, the background noise counts and the SPAD dead time determine the bit error ratio (BER) of the system. All sources of noisy counts (arising from dark counts, afterpulsing, and ambient light) are referred to as background noise and are described by an additive Poisson noise model.

In the first part of this chapter, an OWC system consisting of an active quenching (AQ) or a passive quenching (PQ) single SPAD is considered. Assuming independent count statistics over different bit intervals, the photocount distributions derived in Chapter 3 are used for the bit error performance analysis. The results demonstrate that the SPAD dead time critically degrades the BER, especially in systems with PQ single SPADs.

In the second part of this chapter, the bit error performance of an OWC system with a SPAD array is investigated. Again, by assuming independent count statistics over different bit intervals and using the Gaussian photocount distributions derived in Chapter 3, the exact and approximate error probabilities of an OOK system are derived. The results depict that SPAD arrays are more robust to the dead time losses and larger arrays exhibit shorter effective dead times. It is also shown that the SPAD array can better cope with the background noise and requires much lower optical powers to achieve a target BER, compared with single SPADs.

The rest of this chapter is organised as follows. In Section 4.1, OWC systems with single SPAD receivers are studied. In Section 4.2, OWC systems with SPAD array receivers are addressed. A summary of the chapter is given in Section 4.3.

4.1 OWC Systems with Single SPAD Receivers

4.1.1 On-Off Keying (OOK)

OOK is a common modulation technique for intensity modulation and direct detection (IM/DD) systems, because of its bandwidth efficiency, easy implementation, simple receiver design, and cost effectiveness. In OOK, the information bits are transmitted through the intensity of light, where the presence of a pulse denotes a bit '1' and the absence of a pulse denotes a bit '0', during each bit interval.

Denote by $\lambda_{\rm s}$ and $\lambda_{\rm n}$ the photon rates from the signal and the background noise, respectively. Let $K_{\rm s} = \lambda_{\rm s} T_{\rm b}$ and $K_{\rm n} = \lambda_{\rm n} T_{\rm b}$ represent the average number of signal and background noise photons per bit interval $T_{\rm b}$, respectively. Define $p_{\rm n}(k)$ as the probability of detecting k photons in the bit interval, when '0' has been sent and $p_{\rm sn}(k)$ as the probability of detecting k photons, when '1' has been transmitted. Therefore:

$$\begin{aligned} p_{\rm n}(k) &= p_K(k;\lambda_{\rm n}), \\ p_{\rm sn}(k) &= p_K(k;\lambda_{\rm s}+\lambda_{\rm n}). \end{aligned} \tag{4.1}$$

where $p_K(k;\lambda)$ is the dead time-modified photocount distribution of an AQ/PQ single SPAD given in (3.36)/(3.50).

Hypothesis Testing

OOK demodulation is accomplished by a classical binary detection process: Let hypothesis "H_0" represent the case when a '0' is sent (noise only) and "H_1" represent the hypothesis that a '1' is transmitted (signal plus noise). The aim is to determine the optimum rule for deciding which hypothesis is true based on a single observation. This simple binary hypothesis testing problem is often formulated using the *Bayes criterion*, where the decision should be made according to the well-known likelihood ratio test to minimize the probability of error [98]. In this test, the likelihood ratio is defined as:

$$L(k) = \frac{\Pr\{k|H_1\}}{\Pr\{k|H_0\}} \underset{H_0}{\overset{H_1}{\gtrless}} 1, \tag{4.2}$$

where H_0 and H_1 are assumed to be equally probable, and $\Pr\{k|H_i\}$ is the probability of detecting k photons given that H_i is true. With this detection strategy, the probability of error for the case of equally likely bits is minimized [98].

For an ideal SPAD with Poisson statistics as discussed in Section 3.2, the likelihood ratio test of (4.2) is expressed as [1]:

$$L(k) = \frac{p_0(k;\lambda_\mathrm{s}+\lambda_\mathrm{n})}{p_0(k;\lambda_\mathrm{n})} = e^{-\lambda_\mathrm{s} T_\mathrm{b}} \left(\frac{\lambda_\mathrm{s}+\lambda_\mathrm{n}}{\lambda_\mathrm{n}}\right)^k \underset{H_0}{\overset{H_1}{\gtrless}} 1, \tag{4.3}$$

where $p_0(k;\lambda)$ was defined in (3.21). Taking the natural logarithm from both sides gives:

$$k \underset{H_0}{\overset{H_1}{\gtrless}} \frac{\lambda_\mathrm{s} T_\mathrm{b}}{\ln\left(1+\dfrac{\lambda_\mathrm{s}}{\lambda_\mathrm{n}}\right)}. \tag{4.4}$$

Therefore, the maximum likelihood test simplifies to a threshold test for an ideal SPAD [1].

For a SPAD detector with dead time, the likelihood ratio is given by:

$$L(k) = \frac{p_\mathrm{sn}(k)}{p_\mathrm{n}(k)} = \frac{p_K(k;\lambda_\mathrm{s}+\lambda_\mathrm{n})}{p_K(k;\lambda_\mathrm{n})} \underset{H_0}{\overset{H_1}{\gtrless}} 1. \tag{4.5}$$

The complicated mathematical expressions of $p_\mathrm{sn}(k)$ and $p_\mathrm{n}(k)$ (for both AQ and PQ single SPADs), makes the algebraic manipulation of $L(k)$ intractable. For given values of λ_s and λ_n, if $L(k)$ is monotonic with respect to k, the test in (4.5) is equivalent to a single threshold test, i.e. the maximum likelihood detection is achieved by a threshold comparison. But it

is even more challenging to check the monotonicity of $L(k)$ using finite differences (discrete derivatives). For an AQ SPAD with small dead time ratio ($\delta < 0.1$), an approximate photocount distribution can be provided (see Appendix B) and it can be proved that the above likelihood ratio test leads to a single threshold test (see Appendix E). For other cases, no such proof can be provided. However, we conjecture that the threshold detection is optimum in general. Our extensive numerical investigation of the monotonicity of $L(k)$ and the BER results in Section 4.1.3 strongly support this conjecture.

Probability of Error

With the maximum likelihood detection rule given in (4.5), the probability of error is expressed as:

$$P_{\mathrm{e}} = \frac{1}{2} \sum_{\{k:L(k)>1\}} p_{\mathrm{n}}(k) + \frac{1}{2} \sum_{\{k:L(k)\leq 1\}} p_{\mathrm{sn}}(k) \,. \tag{4.6}$$

Hereinafter, the threshold detection is adopted for the error probability calculations. The number of detected photons is compared with a threshold k_{th}. An error will occur if $k \leq k_{\mathrm{th}}$ when '1' is sent, or if $k > k_{\mathrm{th}}$ when '0' is sent. The probability of error for equally likely bits is then given by:

$$P_{\mathrm{e}} = \frac{1}{2} \sum_{k=k_{\mathrm{th}}+1}^{k_{\max}} p_{\mathrm{n}}(k) + \frac{1}{2} \sum_{k=0}^{k_{\mathrm{th}}} p_{\mathrm{sn}}(k) \,. \tag{4.7}$$

This equation holds for both AQ and PQ SPADs, however, for each case, the corresponding photocount distribution should be considered. The error probability, P_{e}, highly depends on k_{th}. The lowest probability of making an error occurs at the value of k_{th} where $dP_{\mathrm{e}}/dk_{\mathrm{th}} = 0$. It is in general challenging to obtain a closed-form expression for k_{th}. Nevertheless, for an AQ SPAD with $\tau \ll T_{\mathrm{b}}$, the optimum threshold k_{th} is derived as (see Appendix F):

$$k_{\mathrm{th}} = \frac{\lambda_{\mathrm{s}} T_{\mathrm{b}}}{\lambda_{\mathrm{s}}\tau + \ln\left(1 + \dfrac{\lambda_{\mathrm{s}}}{\lambda_{\mathrm{n}}}\right)}, \tag{4.8}$$

and the expression for P_{e} given in (4.7) simplifies to (see Appendices E and F):

$$P_{\mathrm{e}} = \frac{1}{2} - \frac{1}{2} \sum_{k=0}^{k_{\mathrm{th}}} \psi\left(k, \lambda_{\mathrm{n}}(T_{\mathrm{b}} - k_{\mathrm{th}}\tau)\right) + \frac{1}{2} \sum_{k=0}^{k_{\mathrm{th}}} \psi\left(k, (\lambda_{\mathrm{s}} + \lambda_{\mathrm{n}})(T_{\mathrm{b}} - k_{\mathrm{th}}\tau)\right). \tag{4.9}$$

4.1.2 Binary Pulse Position Modulation (BPPM)

The basic disadvantage of OOK signalling is that the average photon rates $\lambda_{\rm s}$ and $\lambda_{\rm n}$ must be known to optimally set the threshold. BPPM signalling avoids this difficulty by using pulse-to-pulse comparison for detection. In BPPM modulation, the optical pulse is sent in one of two adjacent time intervals, each of length $T_{\rm b}/2$ and then the output counts are compared over each half-bit interval. A '1' is sent as a pulse in the first half of the bit interval, and a '0' as a pulse in the second half. At the receiver side, the SPAD separately counts the number of photons over the two half-bit intervals which are then compared for bit decoding. Since the pulse slot is half of the bit interval, the receiver bandwidth must be higher than for the OOK system [1].

In BPPM, an error is made if the number of photocounts in the pulsed slot does not exceed that of the non-pulsed slot. Hence:

$$P_{\rm e} = \sum_{k_1=0}^{\infty} \sum_{k_2=k_1+1}^{\infty} p_{\rm sn}(k_1) p_{\rm n}(k_2) + \frac{1}{2} \sum_{k=0}^{\infty} p_{\rm sn}(k) p_{\rm n}(k). \tag{4.10}$$

The second term in (4.10) accounts for the possibility of equal counts in half-bit intervals, in which case a random choice will be made.

4.1.3 Numerical Results and Discussions

In the following, the bit error performance results are presented and the analytical/numerical results are compared with Monte Carlo simulation results. The BER results are plotted as a function of $\overline{K_{\rm s}}$ for various $\overline{K_{\rm n}}$ values and $\delta = \tau/T_{\rm b}$, where $\overline{K_{\rm s}}$ and $\overline{K_{\rm n}}$ are defined as the average $K_{\rm s}$ and $K_{\rm n}$ per bit interval, respectively. Therefore, for both OOK and BPPM, $\overline{K_{\rm s}} = 0.5\lambda_{\rm s}T_{\rm b}$ and $\overline{K_{\rm n}} = \lambda_{\rm n}T_{\rm b}$. In all the figures, $T_{\rm b} = 1$ μs is considered, unless stated otherwise. For performing the Monte Carlo simulations, a stream of 10^6 bits is randomly generated. Depending on the modulation scheme, in each time slot (bit interval in OOK and half-bit interval in BPPM), a Poisson process with rate $\lambda_{\rm n}$ (only noise) or $\lambda_{\rm s} + \lambda_{\rm n}$ (signal and noise) is simulated and the counting process is simulated according to the Monte Carlo methods presented in Chapter 3. Note that when the SPAD receiver is counting in consecutive intervals (as in OWC systems), the dead time of the last detected photon in each interval may overlap the next interval(s), so that the counting statistics of adjacent intervals become correlated. In OWC

systems, this can be considered as inter-slot interference (ISI). Throughout the calculations and simulations, it is assumed that the dead time is short relative to the bit intervals ($\tau \leq 0.1T_{\rm b}$) such that the ISI is negligible.

4.1.3.1 AQ SPAD

First, we graphically represent $L(k)$ or $\ln L(k)$ given in (4.5) in Fig. 4.1 to support the statement that *the threshold detection is optimum in the presence of dead time*. In this figure, $\ln L(k)$ is numerically calculated for admissible values of k. To have a better insight into the behaviour of the function $\ln L(k)$, different values of δ, $\lambda_{\rm s}$ and $\lambda_{\rm n}$ are considered. According to Figs. 4.1a–4.1f, it is observed that the function $\ln L(k)$ (and hence $L(k)$) is monotonically non-decreasing for various values of δ, $\lambda_{\rm s}$ and $\lambda_{\rm n}$. This monotonicity implies that for each triple of $(\delta, \lambda_{\rm s}, \lambda_{\rm n})$, there exists a unique integer $k_{\rm th}$, such that the test:

$$k \underset{H_0}{\overset{H_1}{\gtrless}} k_{\rm th}$$

is equivalent to the test given in (4.5). Therefore, the maximum likelihood (ML) detection rule reduces to a single threshold (TH) detection test.

The BER results for the AQ SPAD-based optical system with OOK modulation are provided in Fig. 4.2. In this figure, the error probability of OOK systems with ML detection and TH detection are compared with the Monte Carlo simulations, resulting in perfectly matching curves. The analytical calculations are based on the expressions given in (4.6) for the ML detection, and (4.8) and (4.9) for the TH detection. According to Figs. 4.2a and 4.2b, ML and TH detections show an excellent match for all cases, confirming that for the specified range of values in these figures, the ML detection and the TH detection are equivalent.

In Fig. 4.2a, $\delta = 0.001$ and 0.01 are assumed, while in Fig. 4.2b, the dead time ratio is $\delta = 0.1$. According to Fig. 4.2a, the BER depends strongly on the background noise level. For $\overline{K_{\rm n}} = 0$ and 2, the BER is slightly affected by the SPAD dead time. This becomes more significant when $\overline{K_{\rm n}}$ increases. Also, it is apparent that for a given $\overline{K_{\rm n}}$, a higher signal power is needed to maintain the system performance in the presence of a longer dead time. In other words, to achieve a particular BER, the larger δ is, the higher $\overline{K_{\rm s}}$ should be. It is observed in Fig. 4.2b that $\delta = 0.1$ degrades the system performance significantly and the SPAD is saturated with lower signal and/or background noise levels. In this case, $k_{\rm max}$ and $k_{\rm th}$ are small, and the ripples in

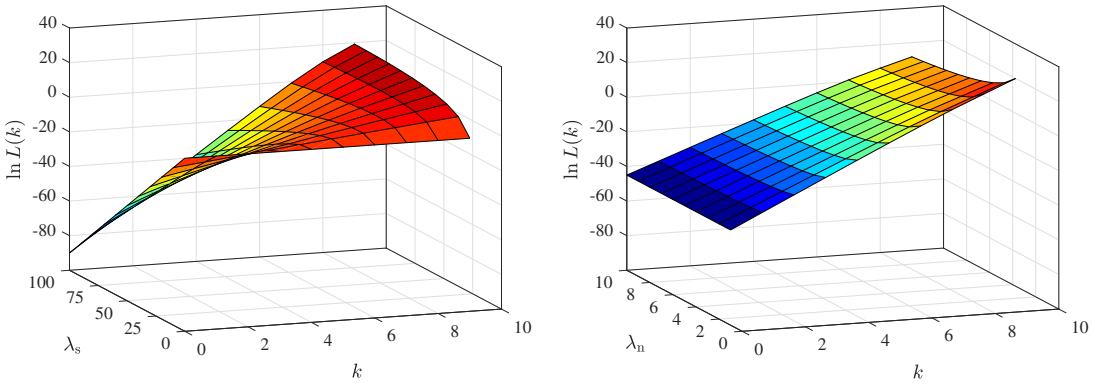

(a) $\lambda_{\mathrm{n}} = 1, \delta = 0.1$

(d) $\lambda_{\mathrm{s}} = 50, \delta = 0.1,$

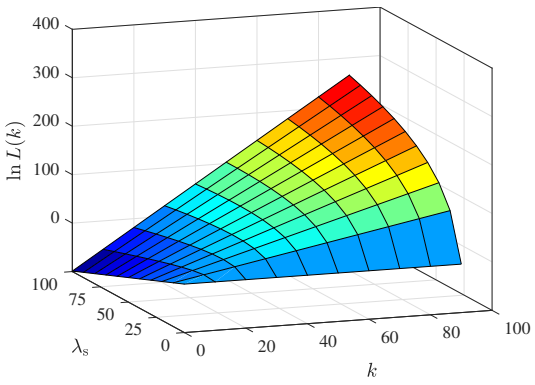

(b) $\lambda_{\mathrm{n}} = 1, \delta = 0.01$

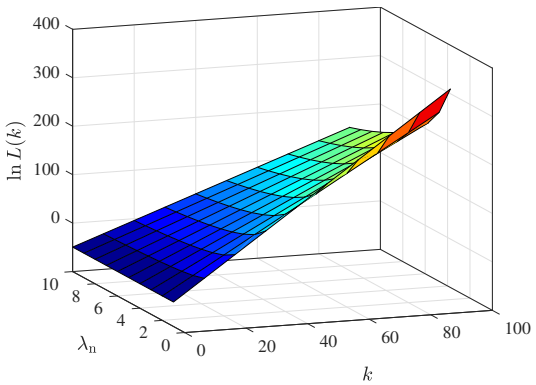

(e) $\lambda_{\mathrm{s}} = 50, \delta = 0.01$

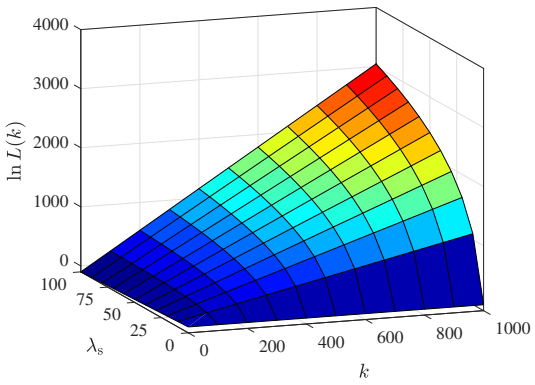

(c) $\lambda_{\mathrm{n}} = 1, \delta = 0.001$

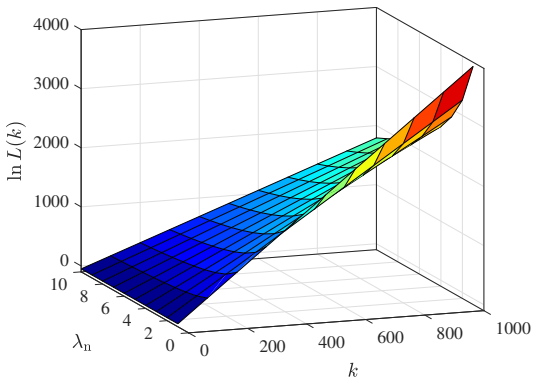

(f) $\lambda_{\mathrm{s}} = 50, \delta = 0.001$

Figure 4.1: *Log-likelihood ratio for the AQ SPAD ($T_{\mathrm{b}} = 1$).*

the BER curves are because of discrete threshold values. For the quantum-limited cases, i.e. $\overline{K_{\mathrm{n}}} = 0$ curves, the threshold k_{th} is zero and no ripples are observed.

Fig. 4.3 provides the BER results for an AQ SPAD-based optical system with BPPM modulation. It is observed that, in the absence of the background noise, the effect of dead time

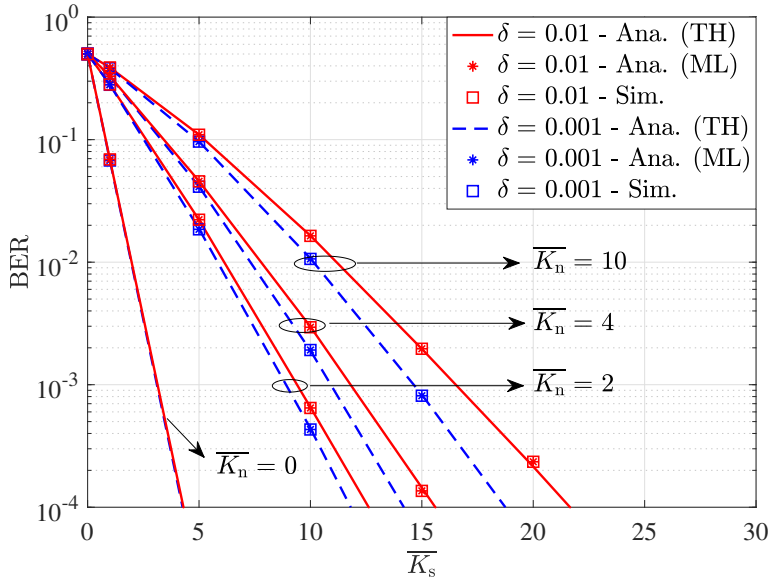

(a)

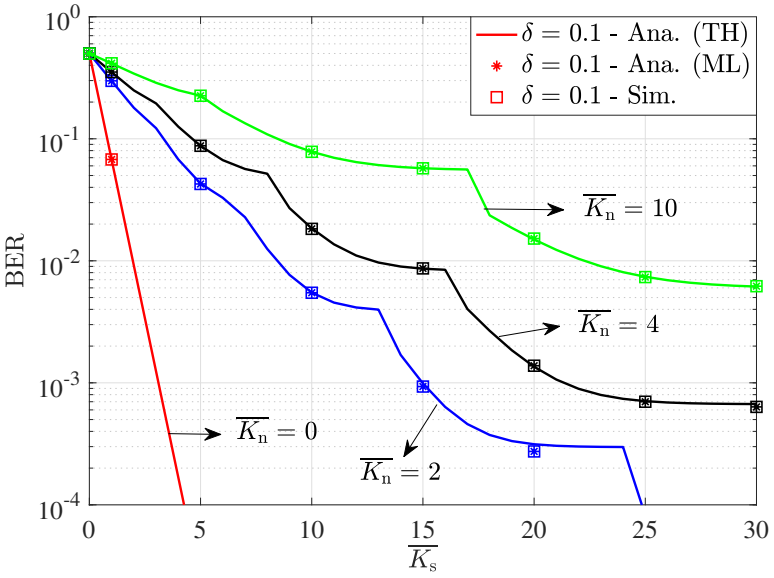

(b)

Figure 4.2: *OOK bit error performance of an AQ SPAD-based system: (a)* $\delta = 0.01, 0.001$ *and (b)* $\delta = 0.1$.

on BER is negligible for small values of $\overline{K_s}$, as in Fig. 4.3a. However, when the background noise is present, the BER becomes very sensitive to the dead time, such that higher dead time values lead to higher error probabilities. It should also be noted that, as seen in Fig. 4.3b, the BER severely degrades when $\delta = 0.1$. In this case, the SPAD becomes saturated with lower signal and/or background noise levels. Also, for stronger background noise levels, the

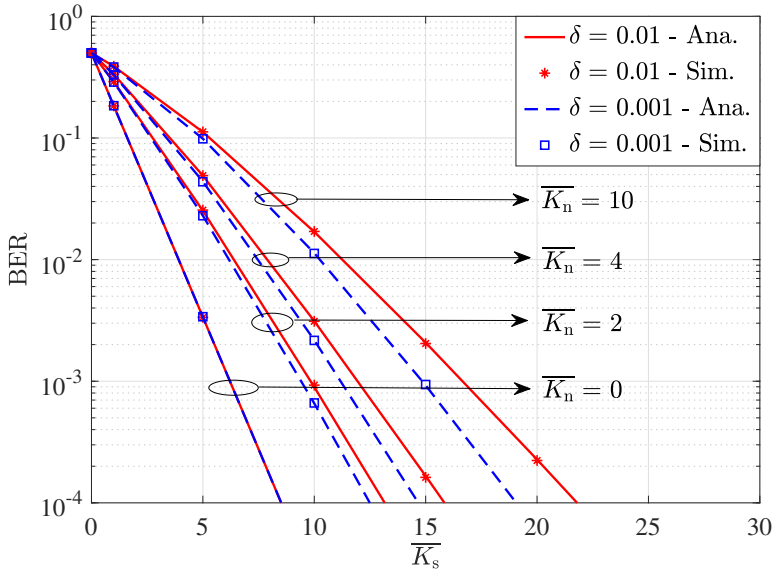

(a)

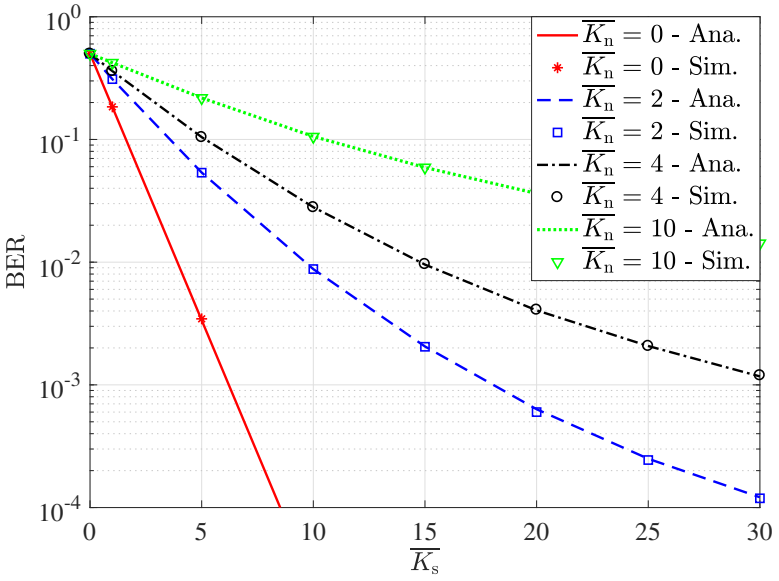

(b)

Figure 4.3: *BPPM bit error performance of an AQ SPAD-based system: (a)* $\delta = 0.01, 0.001$ *and (b)* $\delta = 0.1$.

saturation happens at lower signal levels.

Note that OOK uses pulses twice as long as BPPM, and therefore, has higher signal and background counts. Therefore, a fair comparison between OOK and BPPM systems can be made if the same average signal and background noise powers are assumed. For the systems

under consideration, average signal and background noise powers are directly proportional to $\overline{K_{\rm s}}$ and $\overline{K_{\rm n}}$, respectively. Thus, it is fair to compare the BER performance of the OOK and BPPM systems as presented in Figs. 4.2 and 4.3. Based on Fig. 4.2a and Fig. 4.3a, OOK and BPPM show almost similar performance when the background noise is present and the dead time ratio is very small. For larger dead time ratio ($\delta = 0.1$ as in Fig. 4.2b and Fig. 4.3b), in the presence of the background noise, the OOK system shows slightly better BER values. For ideal quantum-limited OOK and BPPM ($\overline{K_{\rm n}} = 0$) without any dead time counting losses, OOK has 3 dB better BER performance as discussed in [1]. As illustrated in Figs. 4.2 and 4.3, consistent results are achieved in the presence of dead time for the range of interest, since the effect of dead time is insignificant in the quantum-limited conditions.

4.1.3.2 PQ SPAD

In Fig. 4.4, the function $\ln L(k)$ given in (4.5) is graphically represented for the PQ SPAD for various values of δ, $\lambda_{\rm s}$, $\lambda_{\rm n}$ and all the admissible values of k. It is observed that the monotonicity direction of $\ln L(k)$ depends on $\lambda_{\rm s}$ and $\lambda_{\rm n}$. For example, keeping $\lambda_{\rm n}$ constant, at a specific value of $\lambda_{\rm s}$, the monotonicity of $\ln L(k)$ changes from monotonically non-decreasing to monotonically non-increasing. In Figs. 4.4a and 4.4d with $\delta = 0.1$, in the specified ranges of $\lambda_{\rm s}$ and $\lambda_{\rm n}$, the change in the monotonicity direction of $\ln L(k)$ is observed. Since the monotonicity of the function is guaranteed for each specific value of $\lambda_{\rm s}$ and $\lambda_{\rm n}$, still a single threshold test is effective. However, care must be taken in probability of error calculations. According to Figs. 4.4b–4.4c and Figs. 4.4e–4.4f, with $\delta = 0.001$ and 0.01, for the specified ranges of $\lambda_{\rm s}$ and $\lambda_{\rm n}$, the function $\ln L(k)$ (and hence $L(k)$) is monotonically non-decreasing, and therefore the maximum likelihood detection can be achieved by a single threshold detection test.

Fig. 4.5 demonstrates the BER curves of a PQ SPAD-based system with OOK modulation. In this figure, the error probability with the ML detection, given in (4.6), and the error probability with the TH detection, given in (4.7), are numerically evaluated and compared with the simulation results. The threshold value is also obtained numerically. It is again observed that the ML and TH detection rules yield perfectly matching curves, confirming that these two detection schemes are equivalent in the range of interest.

Similar to the BER results of the the AQ SPAD, three different values of δ are considered here. In Fig. 4.5a, $\delta = 0.001$ and $\delta = 0.01$ are assumed, and in Fig. 4.5b the dead time ratio is equal to 0.1. Again, $\delta = 0.1$ severely degrades the error performance and results in SPAD saturation.

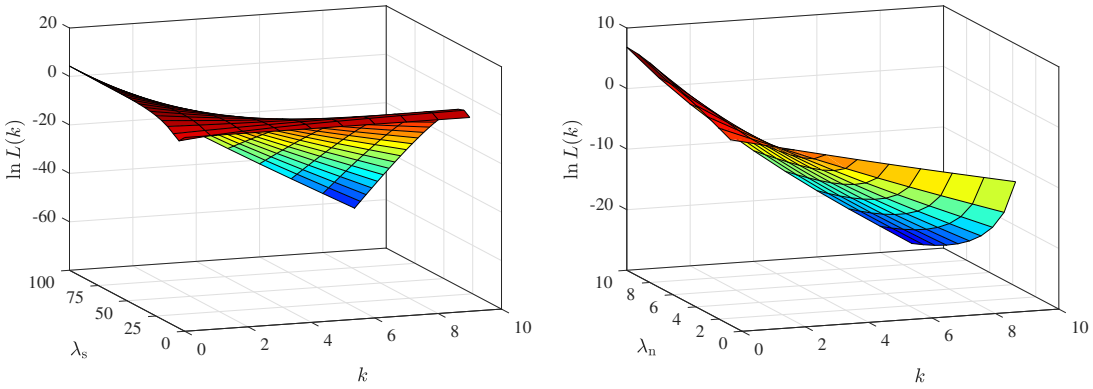

(a) $\lambda_{\mathrm{n}} = 1, \delta = 0.1$

(d) $\lambda_{\mathrm{s}} = 50, \delta = 0.1$

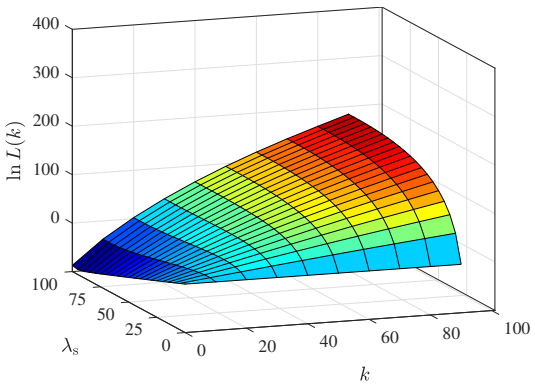

(b) $\lambda_{\mathrm{n}} = 1, \delta = 0.01$

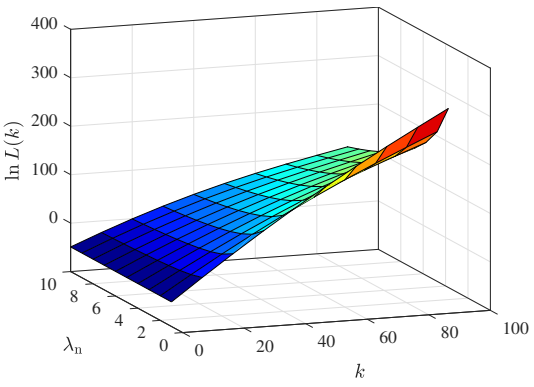

(e) $\lambda_{\mathrm{s}} = 50, \delta = 0.01$

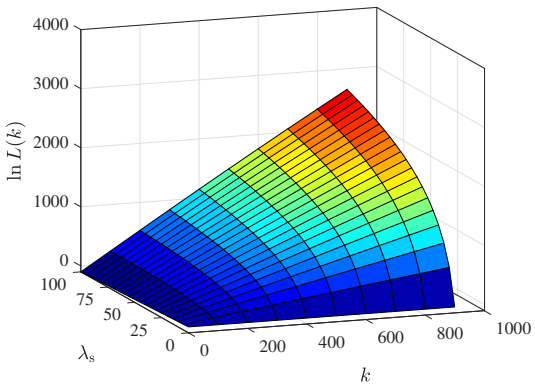

(c) $\lambda_{\mathrm{n}} = 1, \delta = 0.001$

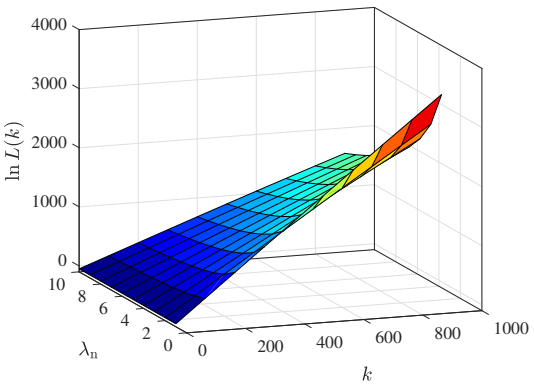

(f) $\lambda_{\mathrm{s}} = 50, \delta = 0.001$

Figure 4.4: *Log-likelihood ratio for the PQ SPAD ($T_{\mathrm{b}} = 1$).*

Recall from (3.53) that the maximum count rate of the PQ SPAD occurs at the point $\lambda = 1/\tau$. The lowest BER also occurs at this point. Therefore, in each BER curve, the lowest BER happens at $\lambda_{\mathrm{s}} + \lambda_{\mathrm{n}} = 1/\tau$ or equivalently $K_{\mathrm{s}} + K_{\mathrm{n}} = 1/\delta$. This is clearly seen in Fig. 4.5b, e.g. for $\overline{K_{\mathrm{n}}} = 0$, the minimum occurs at $\overline{K_{\mathrm{s}}} = 5$. After this point, the counting losses due to the

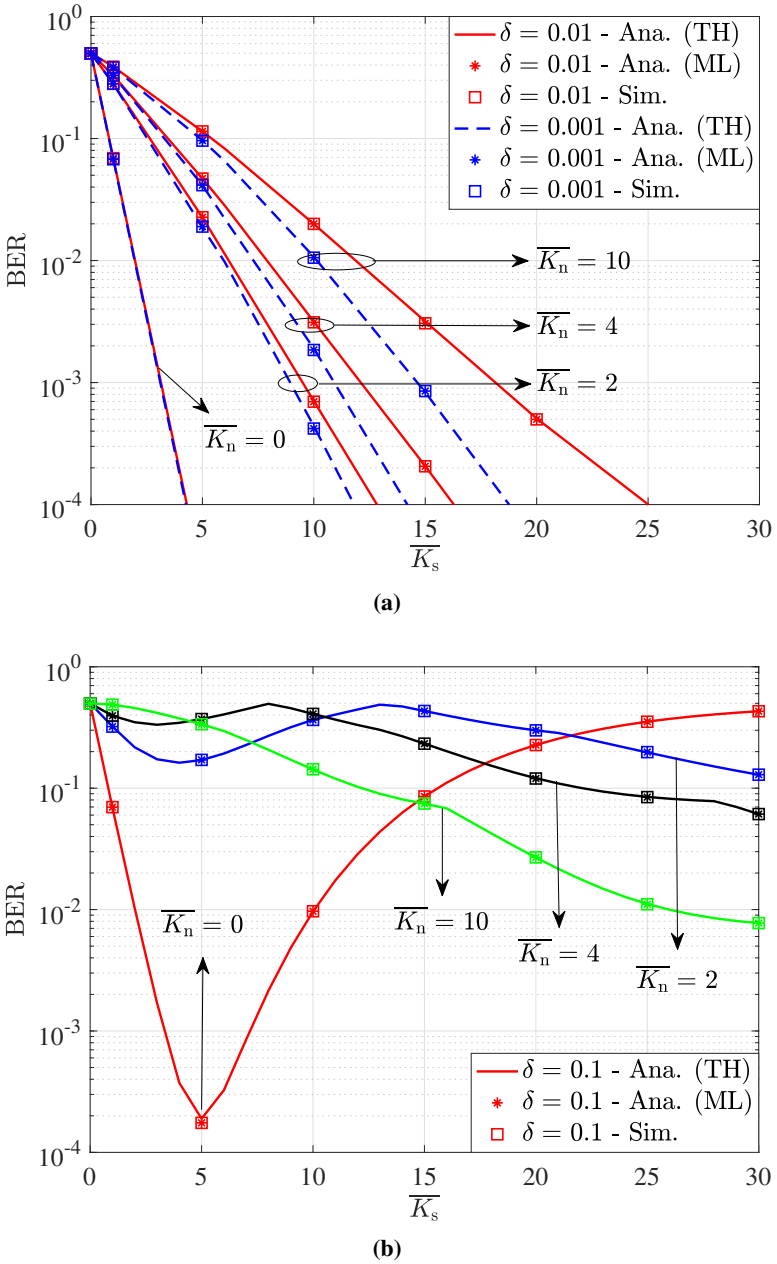

Figure 4.5: *OOK bit error performance of a PQ SPAD-based system: (a)* $\delta = 0.01, 0.001$ *and (b)* $\delta = 0.1$.

dead time drastically increase. So the BER increases until the paralysis behaviour (see Fig. 3.7) causes the average photon count of the pulsed slots to become lower than that of the non-pulsed slots. Our extensive numerical calculations show that at this latter point, the monotonicity of the likelihood ratio function $L(k)$, given in (4.5) changes from monotonically non-decreasing to monotonically non-increasing. In such cases, keeping the definition of the hypotheses H_0

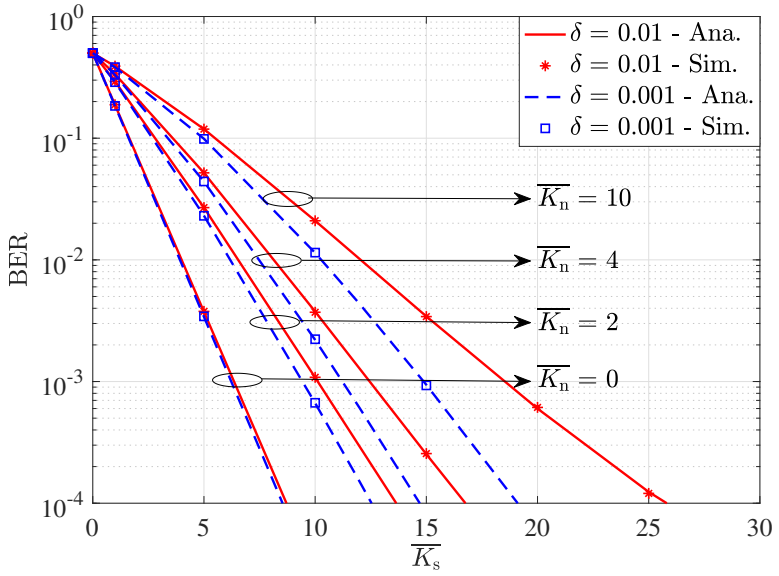

(a)

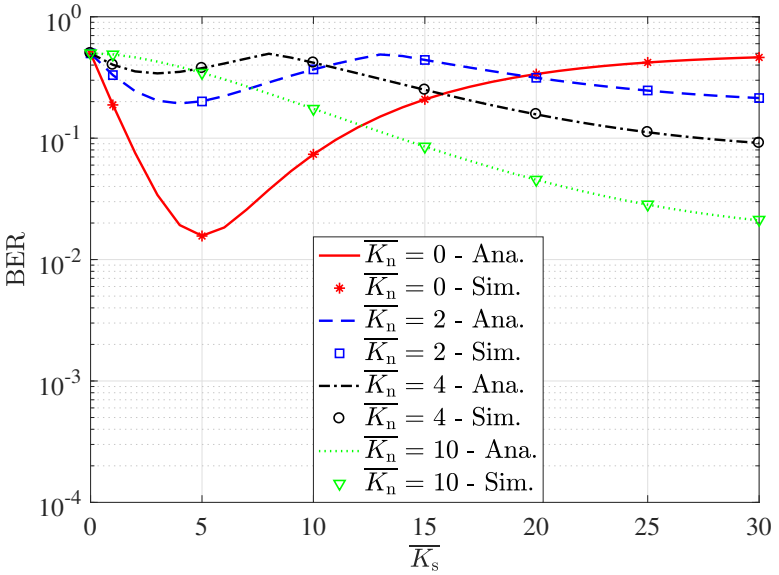

(b)

Figure 4.6: *BPPM bit error performance of a PQ SPAD-based system: (a)* $\delta = 0.01, 0.001$ *and (b)* $\delta = 0.1$.

and H_1 as before, the direction of the likelihood ratio test presented in (4.5) should be reversed and the error probability expressions should be modified accordingly. This has been done for obtaining the results of Fig. 4.5b.

The error probability of a PQ SPAD-based optical system with BPPM, given in (4.10), is in the

form of discrete summations, and therefore can be calculated numerically. Fig. 4.6 shows some plots of the BER results for this system. Similar to the previous cases, in the absence of the background noise, the effect of dead time on the BER is negligible. However, if the background noise is present, the dead time degrades the BER. Again, it is seen that the error performance is severely affected by larger dead time ratios ($\delta = 0.1$) and the lowest BER occurs at the maximum count rate, as predicted.

4.1.3.3 AQ SPAD vs. PQ SPAD

As stated earlier, when using PQ SPADs, any photon arriving during the dead time is not detected but is assumed to extend the dead time period, while for AQ SPADs, any photon arriving during the dead time is neither counted nor has any influence on the dead time duration. Thus, assuming the same dead time duration, in a bit interval of length T_{b}, the average number of photocounts by an AQ SPAD is generally higher than that of a PQ SPAD. This can be observed from Figs. 3.2 and 3.5. Furthermore, this behaviour directly affects the BER performance. When the dead time duration only is one order of magnitude lower than the bit interval ($\delta = 0.1$), the difference of AQ and PQ SPADs is perceptible, as observed in Fig. 4.2b and Fig. 4.5b for OOK modulation or in Fig. 4.3b and Fig. 4.6b for BPPM. For the AQ SPAD, increasing the signal photon rate (or the signal count) results in the saturation and the BER will reach a constant value. However, for the PQ SPAD, by increasing the signal photon rate (or the signal count), the BER decreases until the SPAD reaches its maximum count rate. At this point, the lowest possible BER is achieved and higher signal counts degrade the bit error performance.

4.1.3.4 Applicability of Gaussian and Poisson Approximations

The probability mass function (PMF) of the SPAD photocounts is commonly approximated by a Poisson distribution [7, 83, 84]. In order to investigate the accuracy of this approximation, in Fig. 4.7, the OOK error probabilities of both AQ and PQ SPAD-based OWC systems, given in (4.7), are evaluated and compared with when the photocount distribution is approximated by a Poisson distribution through moment matching, i.e., the rate parameter of the approximated Poisson distribution is calculated from (3.42) and (3.53), rather than using an ideal Poisson model which does not take into account the effect of dead time in any wise. In Figs. 4.7a and 4.7b, $\delta = 0.01$ is assumed, and as can be seen, for both AQ and PQ SPADs, there is a considerable gap between the exact BER values and the approximate results, especially for

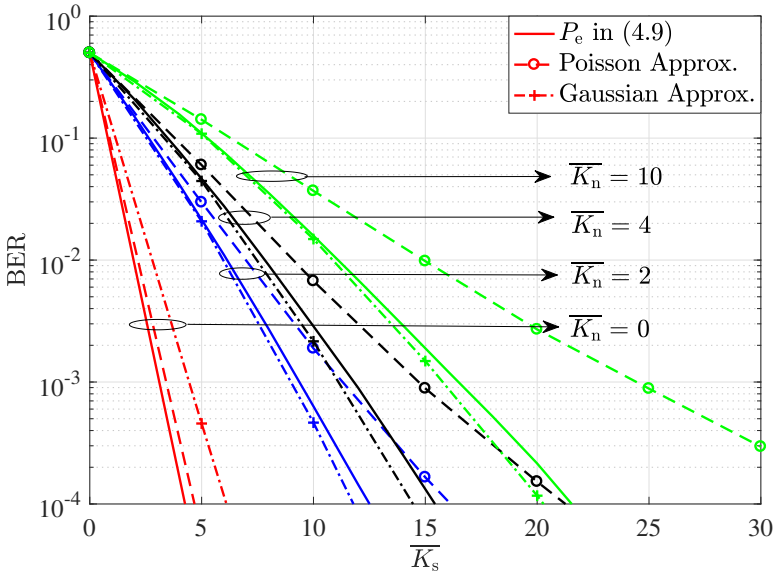

(a) AQ

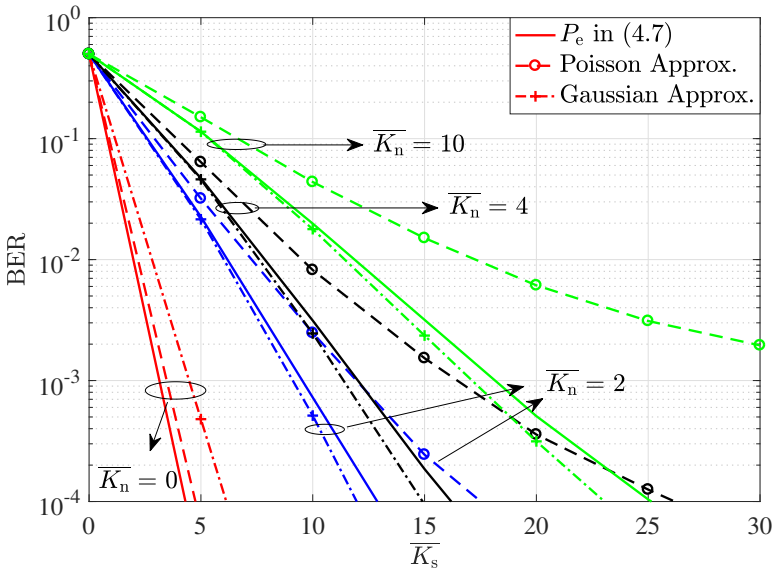

(b) PQ

Figure 4.7: *OOK BER performance of (a) AQ, and (b) PQ SPAD-based systems, considering the exact SPAD photocount distribution, the Poisson approximation, and the Gaussian approximation.*

higher values of $\overline{K_n}$.

To have a better insight, the AQ and PQ SPAD photocount distributions have also been approximated by a Gaussian distribution in Fig. 4.7, using a similar moment matching approach. The mean and variance of the Gaussian distribution are approximated as in (3.37)

for the AQ SPAD, and as in (3.51) for the PQ SPAD. Although the Gaussian approximation shows higher accuracy compared with the Poisson approximation, the differences are still noticeable. Note that by increasing the dead time ratio, the accuracy of these approximations will be more degraded. By comparing the results of these approximations for AQ and PQ SPADs, it is observed that the approximations show slightly higher accuracy for AQ SPADs, and the reason is that the counting losses due to the paralyzable dead time are generally higher than that of the nonparalyzable dead time. According to these observations, the use of Poisson or Gaussian approximations does not provide enough accuracy for assessing the bit error performance of OWC systems, and this highlights the importance of our statistical modelling for a precise error analysis for potential optical communication applications.

4.2 OWC Systems with SPAD Array Receivers

As seen in Figs. 4.2–4.6, the BER of SPAD-based OWC systems strongly depends on the value of dead time such that, for example, $\delta = 0.1$ results in BER $\geq 10^{-3}$. Several studies and experiments suggest that the impact of dead time can be mitigated by employing arrays of SPADs [8–10, 65, 83]. Also, the use of SPAD arrays helps to cope with strong background radiation [57]. In the following, the SPAD array photocount distribution derived in Chapter 3 is applied to analyse the bit error performance of an OWC system with a SPAD array. Notice that AQ SPAD arrays are considered as the baseline scenario in this section, as they generally outperform PQ SPAD arrays, if the array is not large and exhibit almost the same performance, if the array is sufficiently large.

4.2.1 On-Off Keying (OOK)

Denote the signal and background noise photon rates per SPAD by $\lambda_{\rm s}$ and $\lambda_{\rm n}$, respectively. Thus, $K_{\rm s} = \lambda_{\rm s} T_{\rm b}$ and $K_{\rm n} = \lambda_{\rm n} T_{\rm b}$ are the corresponding average number of photons per bit interval for each array element. Assuming that the signal and noise intensities have a uniform spatial distribution over the array area, we have:

$$\begin{aligned} \Lambda_{\rm s} &= N_{\rm array} \lambda_{\rm s}, \\ \Lambda_{\rm n} &= N_{\rm array} \lambda_{\rm n}, \end{aligned} \tag{4.11}$$

where $\Lambda_{\rm s}$ and $\Lambda_{\rm n}$ are the average signal and background noise photon rates for the whole array. Similarly, $K_{\rm s}^{\rm a} = N_{\rm array}K_{\rm s}$ and $K_{\rm n}^{\rm a} = N_{\rm array}K_{\rm n}$ are the corresponding average aggregate number of photons per bit interval.

Let $p_{\rm n}(s)$ and $p_{\rm sn}(s)$ denote the probabilities of s photocounts when '0' or '1' are transmitted, respectively. Thus:

$$\begin{aligned} p_{\rm n}(s) &= p_S(s;\Lambda_{\rm n}), \\ p_{\rm sn}(s) &= p_S(s;\Lambda_{\rm s}+\Lambda_{\rm n}), \end{aligned} \tag{4.12}$$

where $p_S(s;\Lambda)$ is the dead time-modified photocount distribution of a SPAD array given in (3.64).

Hypothesis Testing

Recall from Section 4.1, the classical binary detection problem with two hypothesises "H_0" and "H_1". The receiver attempts to determine the correct bit based upon a single observation of the aggregate number of array photocounts over each bit interval. The likelihood ratio test is defined as:

$$L(s) = \frac{p_{\rm sn}(s)}{p_{\rm n}(s)} \underset{H_0}{\overset{H_1}{\gtrless}} 1 \tag{4.13}$$

where $p_{\rm sn}(s)$ and $p_{\rm n}(s)$ were defined in (4.12) and are Gaussian distributed according to (3.64). Thus, let $p_{\rm sn}(s) \sim \mathcal{N}(\mu_{\rm sn},\sigma_{\rm sn}^2)$ and $p_{\rm n}(s) \sim \mathcal{N}(\mu_{\rm n},\sigma_{\rm n}^2)$. The above likelihood ratio test then simplifies to a single threshold test with the optimum threshold given by (see Appendix G):

$$s_{\rm th} = \frac{\dfrac{\mu_{\rm n}}{\sigma_{\rm n}^2} - \dfrac{\mu_{\rm sn}}{\sigma_{\rm sn}^2} + \sqrt{\left(\dfrac{\mu_{\rm n}}{\sigma_{\rm n}^2} - \dfrac{\mu_{\rm sn}}{\sigma_{\rm sn}^2}\right)^2 - \left(\dfrac{1}{\sigma_{\rm n}^2} - \dfrac{1}{\sigma_{\rm sn}^2}\right)\left(\dfrac{\mu_{\rm n}^2}{\sigma_{\rm n}^2} - \dfrac{\mu_{\rm sn}^2}{\sigma_{\rm sn}^2} + 2\ln\dfrac{\sigma_{\rm n}}{\sigma_{\rm sn}}\right)}}{\dfrac{1}{\sigma_{\rm n}^2} - \dfrac{1}{\sigma_{\rm sn}^2}}. \tag{4.14}$$

This threshold can be further approximated as (see Appendix G):

$$s_{\rm th} = \frac{\mu_{\rm sn}\sigma_{\rm n} + \mu_{\rm n}\sigma_{\rm sn}}{\sigma_{\rm n} + \sigma_{\rm sn}}. \tag{4.15}$$

Note that this threshold depends on $\mu_{\rm n}$, $\mu_{\rm sn}$, $\sigma_{\rm n}$, and $\sigma_{\rm sn}$ which are all functions of $\Lambda_{\rm s}$ and $\Lambda_{\rm n}$. A technical challenge with OOK systems is that for determining $s_{\rm th}$, $\Lambda_{\rm s}$ and $\Lambda_{\rm n}$ must be known exactly.

Probability of Error

In OOK demodulation, the number of array photocounts is compared with the threshold $s_{\rm th}$ provided in (4.14). With this threshold, the minimum error probability is ensured. An error will occur if $s \leq s_{\rm th}$ for a bit '1', or if $s > s_{\rm th}$ for a bit '0'. The probability of error for equally likely bits is [1]:

$$P_{\rm e} = \frac{1}{2} \sum_{s=\lfloor s_{\rm th} \rfloor + 1}^{\infty} p_{\rm n}(s) + \frac{1}{2} \sum_{s=0}^{\lfloor s_{\rm th} \rfloor} p_{\rm sn}(s). \tag{4.16}$$

$P_{\rm e}$ can be approximated as:

$$\begin{aligned} P_{\rm e} &\cong \frac{1}{2} \int_{s_{\rm th}}^{\infty} p_{\rm n}(s)\, ds \;\; + \frac{1}{2} \int_{0}^{s_{\rm th}} p_{\rm sn}(s)\, ds \\ &= \frac{1}{2}\, {\rm Q}\left(\frac{s_{\rm th} - \mu_{\rm n}}{\sigma_{\rm n}} \right) + \frac{1}{2}\, {\rm Q}\left(\frac{\mu_{\rm sn} - s_{\rm th}}{\sigma_{\rm sn}} \right), \end{aligned} \tag{4.17}$$

where, ${\rm Q}(x) = 1/\sqrt{2\pi} \int_x^{\infty} \exp(-\alpha^2/2)\, d\alpha$ is the Q-function. With the approximate threshold given in (4.15), $P_{\rm e}$ further simplifies to:

$$P_{\rm e} \cong {\rm Q}\left(\frac{\mu_{\rm sn} - \mu_{\rm n}}{\sigma_{\rm sn} + \sigma_{\rm n}} \right). \tag{4.18}$$

The above approximate error probability suggests that $P_{\rm e}$ depends only on $\mu_{\rm sn} - \mu_{\rm n}$. Therefore, any contribution to both $\mu_{\rm sn}$ and $\mu_{\rm n}$, such as from dark counts, would not effect the $\mu_{\rm sn} - \mu_{\rm n}$ term, this will, however, contribute to the variances. Defining the signal-to-noise ratio (SNR) as:

$${\rm SNR} = \frac{(\mu_{\rm sn} - \mu_{\rm n})^2}{(\sigma_{\rm sn} + \sigma_{\rm n})^2}, \tag{4.19}$$

$P_{\rm e}$ can also be written as:

$$P_{\rm e} = {\rm Q}\left(\sqrt{\rm SNR} \right). \tag{4.20}$$

4.2.2 Numerical Results and Discussions

In the following, the bit error performance results of the OWC systems with SPAD arrays are presented. The results are focused on AQ SPAD arrays, as they generally outperform PQ SPAD arrays, albeit in larger array sizes, the performance gap tends to become insignificant. Throughout the calculations and simulations, it is assumed that the array elements are identical. In all the figures, $T = 1$ μs and $C_{\rm FF} = 1$ are considered and the BER results are reported as a

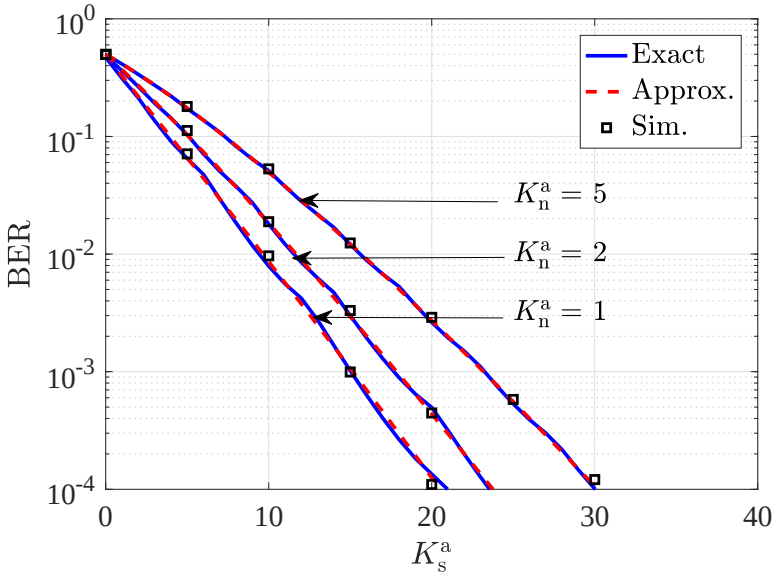

Figure 4.8: *OOK BER performance with a SPAD array of* $N_{\mathrm{array}} = 64$ *and* $\delta = 0.1$.

function of $K_{\mathrm{s}}^{\mathrm{a}}$ or $K_{\mathrm{n}}^{\mathrm{a}}$ or δ for different array sizes.

In Fig. 4.8, the exact error probability given in (4.16) is numerically evaluated and compared with the approximate error probability of (4.18) and also the Monte Carlo simulation results for an array of 64 SPADs with a dead time ratio of $\delta = 0.1$. Although, the discrete threshold values cause some ripples in the curves, (4.18) can well approximate the error probability. Hereinafter, the approximate error probability expression given in (4.18) is adopted for the BER calculations.

4.2.2.1 ISI

As discussed in Chapter 3, the SPAD arrays are expected to be more robust to dead time losses. Therefore, in this section, longer dead times are also considered. However, care must be taken regarding the ISI impairments. While, the primary effect of the SPAD dead time is to cause some counting losses in each interval, its secondary effect is to incur counting losses in the neighbouring intervals. From a communication theory perspective, this can be regarded as the ISI effect. Therefore, ISI is an outcome of the photon counting process of the SPAD receiver. So far, all the analytical modellings have focused on the primary effect of the SPAD dead time and the secondary effect has not been taken into account. It has been assumed that the dead time is short enough compared to the counting interval ($\tau \leq 0.1T_{\mathrm{b}}$), so that the counting

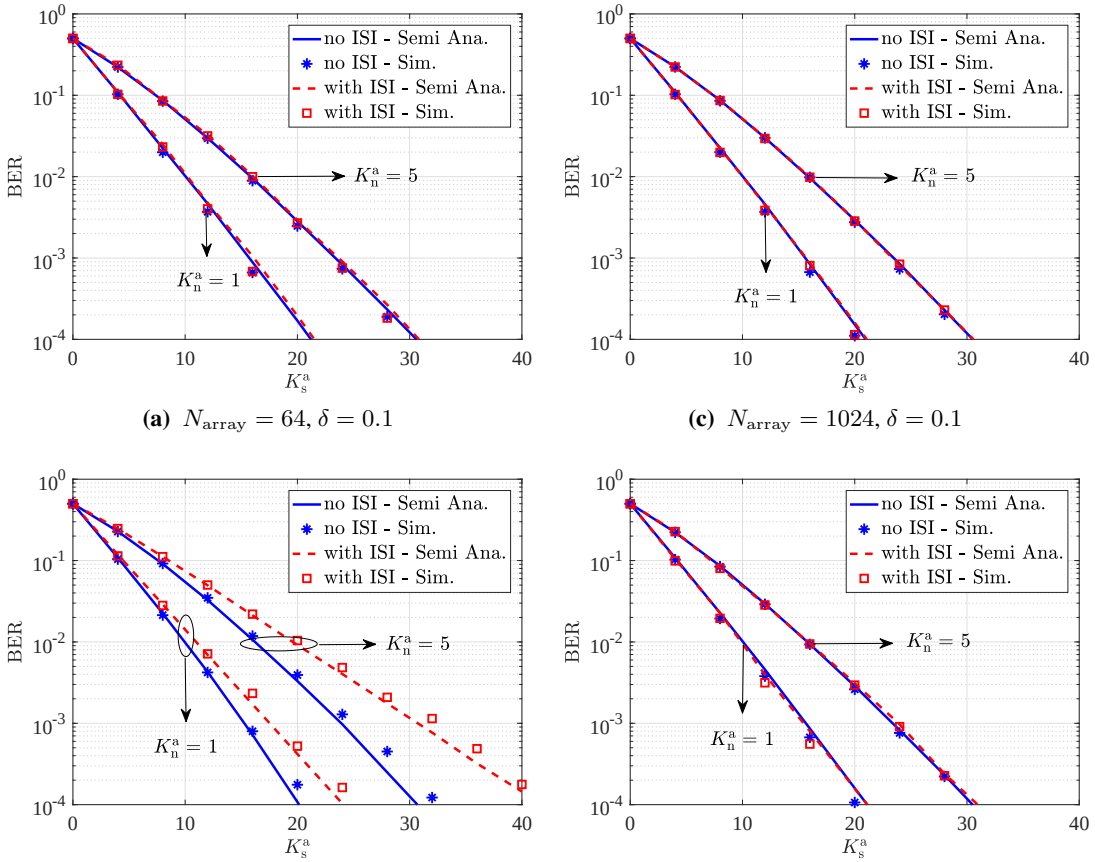

(a) $N_{\text{array}} = 64$, $\delta = 0.1$ **(c)** $N_{\text{array}} = 1024$, $\delta = 0.1$

(b) $N_{\text{array}} = 64$, $\delta = 1$ **(d)** $N_{\text{array}} = 1024$, $\delta = 1$

Figure 4.9: *The effect of ISI on the BER results.*

processes of the neighbouring intervals are disjoint and the ISI is negligible. However, the ISI effect is noticeable for longer dead times. In such cases, the single SPAD photocount statistics should be modified accordingly. Nevertheless, the complicated photon counting behaviour of the single SPADs, makes this mathematical analysis intractable. Therefore, for longer dead times ($\tau > 0.1T_{\text{b}}$), we resort to Monte Carlo simulations to obtain the ISI-modified PMF, mean and variance of the AQ and PQ single SPADs. These modified photocount statistics are then applied to obtain those of the SPAD arrays. In all the numerical and simulation results of this section, the ISI effect is considered, unless stated otherwise. In order to obtain the ISI-modified photocount distribution of the single SPADs through Monte Carlo simulations, when generating a Poisson arrival process and recording the number of photocounts according to the dead time effects, the arrival time of the first photon in each counting interval is compared with the arrival time of the last photocount in the previous interval to see whether the first photon is lost or not. In scenarios with long dead times or high photon rates, this effect is noticeable.

Fig. 4.9 presents the effect of ISI on the BER of two arrays with 64 and 1024 SPADs. For each array two cases are considered, a short dead time ($\delta = 0.1$) and a long dead time ($\delta = 1$). As predicted, for $\delta = 0.1$, the ISI is negligible in both arrays. However, the long dead time of $\delta = 1$ results in significant ISI impairment for the array of size $N_{\text{array}} = 64$, while the array of 1024 SPADs is very robust to the ISI. These results indicate that large arrays can suppress the ISI effectively. Nonetheless, note that the ISI is stronger in higher photon rates. If the photon rate is very high, such that all the SPADs in a large array are saturated, then even the large array may not be able to alleviate the adverse impact of ISI. This case does not take place for the photon rate regimes considered in this thesis.

4.2.2.2 Array Size

In Fig. 4.10, the BER of three SPAD arrays with $N_{\text{array}} = 16$, 64, and 1024 are compared for $\delta = 0.1$ and $\delta = 1$. To make a fair comparison, it is assumed that the total sensitive area of the arrays is equal. Therefore, the average number of signal counts or background noise counts per bit interval is the same for all three arrays. Please note that with this assumption, each SPAD in the array of 1024 SPADs receives less signal and background noise levels compared to each SPAD in the array of 64 elements. According to Fig. 4.10a, all arrays perform the same for $K_{\text{n}}^{\text{a}} = 1$, while for $K_{\text{n}}^{\text{a}} = 5$ arrays with 64 and 1024 elements slightly outperform the array of 16 SPADs. For $\delta = 1$ as in Fig. 4.10b, arrays with larger sizes show better error performance for various average background noise levels.

4.2.2.3 Dead Time

Fig. 4.11 shows the effect of dead time on the average number of photons per bit time (i.e. K_{s}^{a}) required by the SPAD array to achieve a particular BER for OOK modulation. In this figure the BER $= 10^{-3}$ contours are displayed as a function of δ and K_{s}^{a} for a single SPAD and three different array sizes. The average background noise count level is $K_{\text{n}}^{\text{a}} = 1$ in Fig. 4.11a and $K_{\text{n}}^{\text{a}} = 5$ in Fig. 4.11b.

The counting losses due to the dead time are mitigated to some extent when several SPADs operate in parallel inside an array. It is very unlikely that all the SPADs of an array become inactive at the same time. In low photon rate regimes, if the dead time is short (compared to the bit interval), the use of large size SPAD arrays does not offer considerable performance

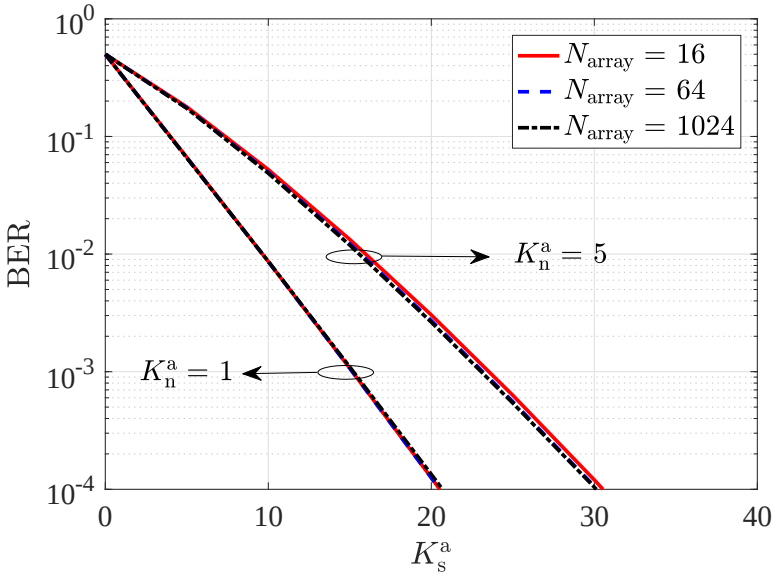

(a) $\delta = 0.1$

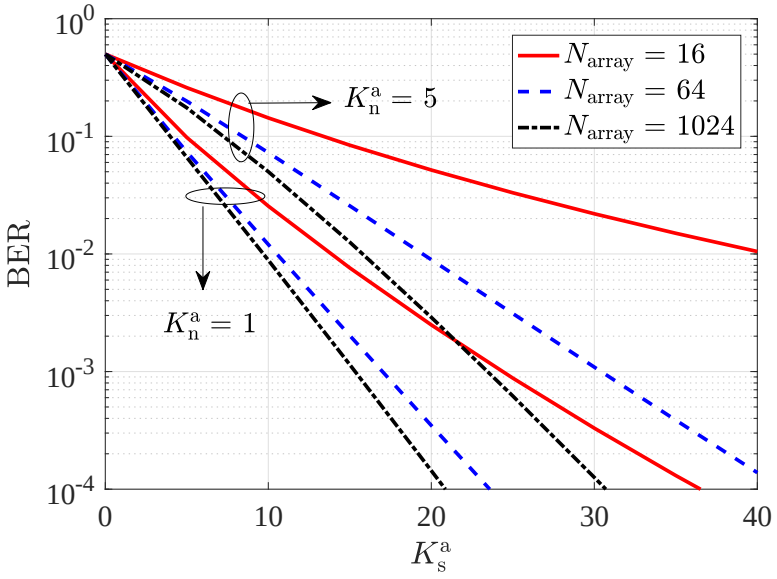

(b) $\delta = 1$

Figure 4.10: *BER results of SPAD array receivers with (a)* $\delta = 0.1$ *and (b)* $\delta = 1$.

improvements. In high photon rate regimes, or in the case of long dead times, larger array sizes are required. In such cases, smaller arrays may not achieve the target BER even in higher SNRs, as increasing the optical power leads to the saturation of the SPAD array. According to Fig. 4.11a, for shorter dead time durations ($\delta < 0.5$), all three arrays provide BER $\leq 10^{-3}$ with $K_s^a \approx 16$. However, for longer dead times ($\delta > 0.5$), larger arrays require fewer number of photons, i.e. lower optical power, to achieve BER $= 10^{-3}$. For instance, for $N_{array} = 16$,

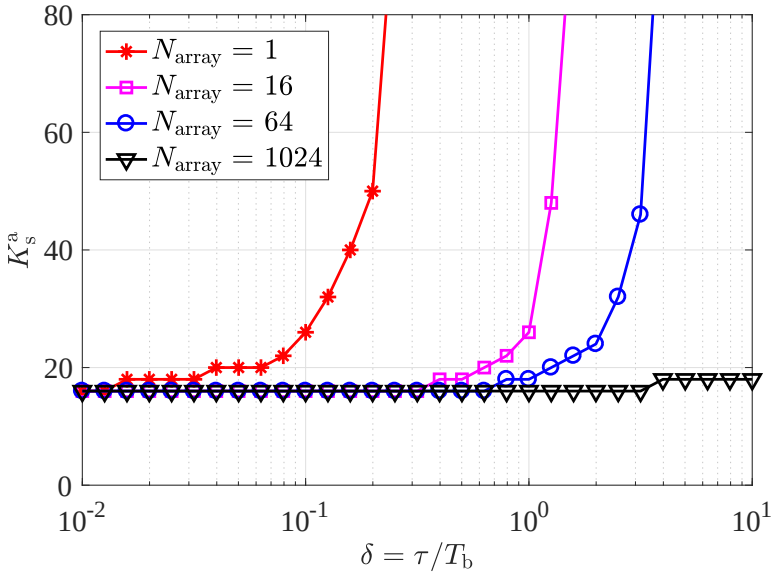

(a) $K_{\mathrm{n}}^{\mathrm{a}} = 1$

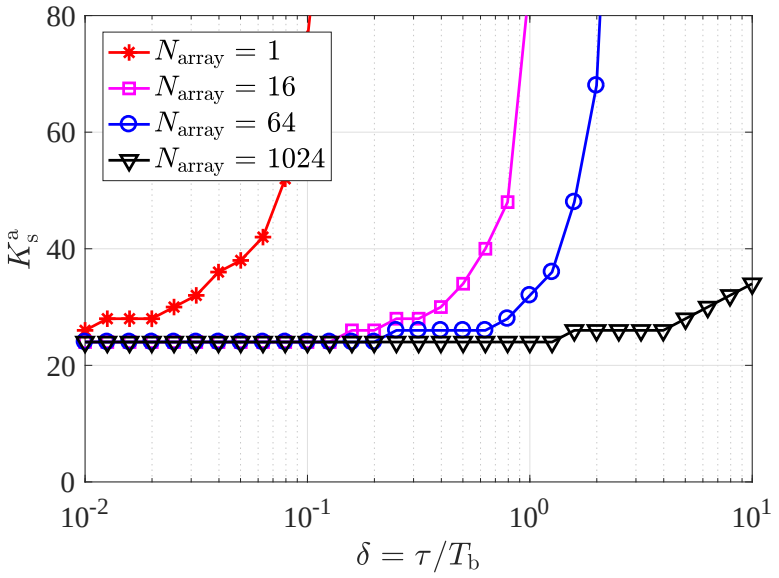

(b) $K_{\mathrm{n}}^{\mathrm{a}} = 5$

Figure 4.11: *The BER* $= 10^{-3}$ *contours as a function of the dead time ratio and the average number of photons per bit time required by the SPAD array.*

if $\delta < 1$, the target BER can be achieved with $K_{\mathrm{s}}^{\mathrm{a}} < 30$. As the dead time increases, many of the arriving photons get lost and $K_{\mathrm{s}}^{\mathrm{a}}$ increases very rapidly, such that $K_{\mathrm{s}}^{\mathrm{a}} > 80$ is required for $\delta > 1$. This sharp increase in $K_{\mathrm{s}}^{\mathrm{a}}$ is due to the saturation of the SPAD array. With $N_{\mathrm{array}} = 1024$ the limiting effect of dead time is almost eliminated, such that regardless of the value of δ, BER $= 10^{-3}$ is guaranteed with $K_{\mathrm{s}}^{\mathrm{a}} < 20$. Note that depending on the background noise level,

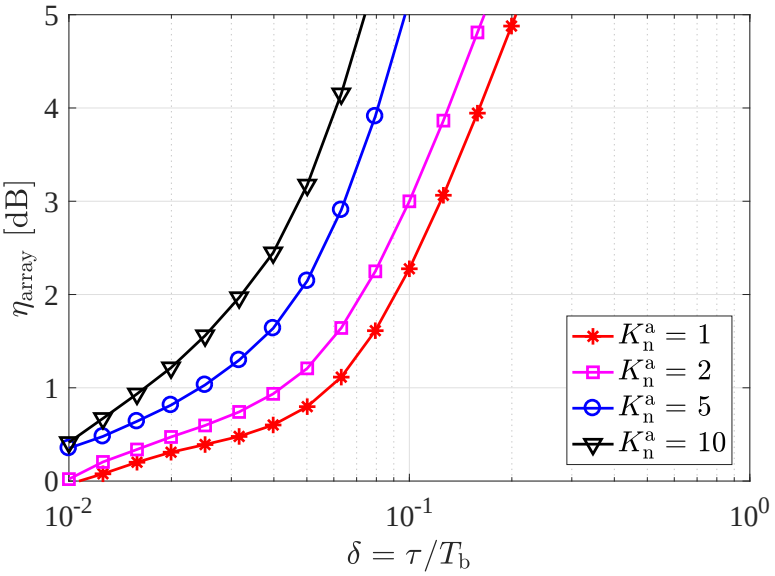

Figure 4.12: *Power gain of a SPAD array of* $N_{\text{array}} = 1024$ *for* $\text{BER} = 10^{-3}$.

the target BER may not be achieved at all; e.g. as in Fig. 4.11a, for $N_{\text{array}} = 64$ and $\delta > 4$.

Consider a target BER of 10^{-3} and denote by η_{array} the ratio of required K_{s} for a single SPAD to the required K_{s}^{a} for a SPAD array. This ratio can be interpreted as the power gain of the SPAD array compared to the single SPAD for achieving the target BER of 10^{-3}:

$$\eta_{\text{array}}\Big|_{\text{BER}=10^{-3}} = \frac{K_{\text{s}}}{K_{\text{s}}^{\text{a}}}\,. \tag{4.21}$$

Note that the total active area of the array is assumed to be the same as that of the single SPAD. Thus, it is fair to say that the SPAD array requires less power to achieve a target BER. Fig. 4.12 depicts η_{array} for the array of 1024 SPADs. To obtain some of the curves in this figure, minor data extrapolation has been applied.

4.2.2.4 Background Noise

In Fig. 4.13, the required K_{s}^{a} for achieving some target BERs is plotted as a function of K_{n}^{a} for $N_{\text{array}} = 64$ and 1024. According to this figure, the minimum required K_{s}^{a} to achieve the target BER is constant for $K_{\text{n}}^{\text{a}} \leq 10^{-2}$. However, for $K_{\text{n}}^{\text{a}} > 10^{-2}$, the required K_{s}^{a} grows as K_{n}^{a} increases. For $N_{\text{array}} = 64$, as shown in Fig. 4.13a, a higher K_{s}^{a} is needed to maintain the system performance in the presence of dead time. However, for $N_{\text{array}} = 1024$ (see Fig. 4.13b) the effect of dead time is negligible even for larger values of K_{n}^{a}.

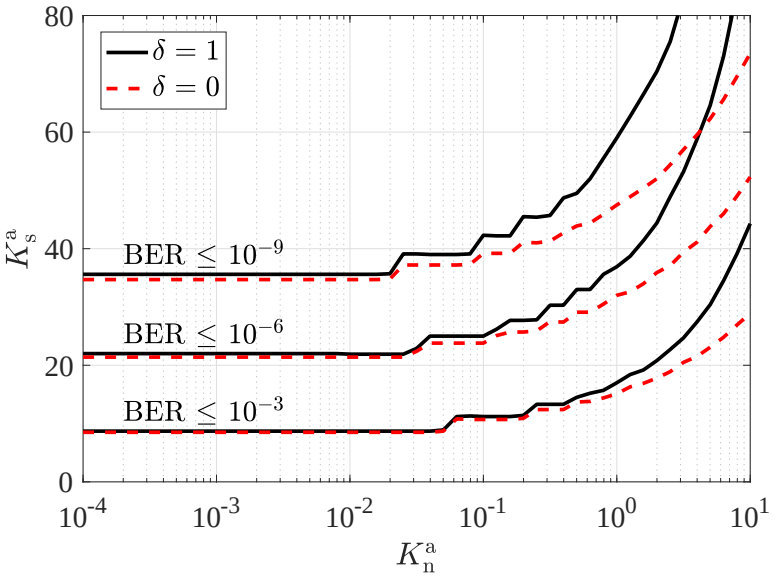

(a) $N_{\mathrm{array}} = 64$

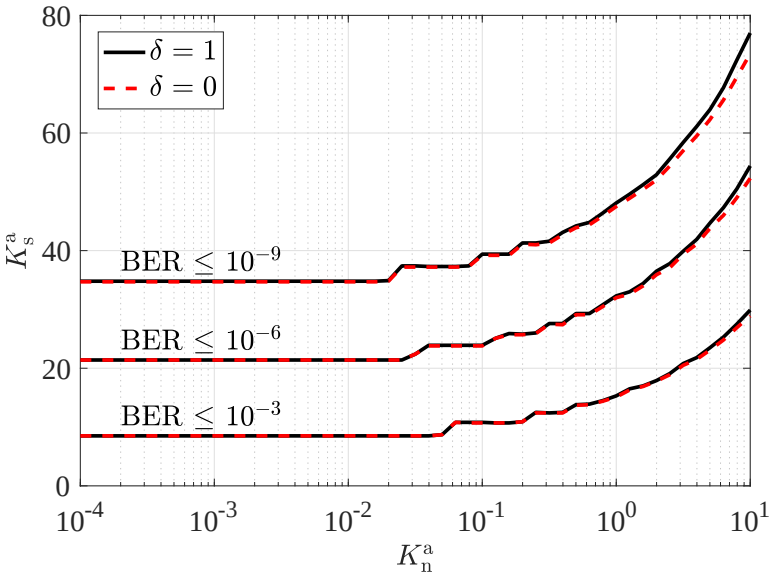

(b) $N_{\mathrm{array}} = 1024$

Figure 4.13: *The BER contours as a function of the average number of signal counts per bit time and average background counts per bit time.*

4.3 Summary

In this chapter, the effect of dead time on the bit error performance of SPAD-based OWC systems were investigated. A data rate of 1 Mbits/s was assumed. In the first study, OWC systems with single AQ or PQ SPADs and dead time ratios of $\delta = 0.001$, 0.01, and 0.1 were considered. A theoretical study was conducted to obtain the error probability of OOK and BPPM binary modulation schemes. Assuming negligible ISI (for $\delta \leq 0.1$) and hence, independent count statistics over different bit intervals, the photocount distributions derived in Chapter 3 were used for the bit error performance analysis. All the analytical derivations were supported by Monte Carlo simulation results. It was found that the dead time distorted count statistics result in higher bit error rates. With the binary modulation schemes, if $\delta \leq 0.01$, BER values of less than 10^{-3} were achieved, however, $\delta = 0.1$ critically degraded the bit error performance of both AQ and PQ single SPADs. Nevertheless, the impact of dead time was negligible in quantum-limited conditions. The results demonstrated that with a longer dead time, a higher signal intensity is required to maintain the system performance, e.g. in the AQ SPAD-based OWC system, assuming OOK modulation and constant average background noise of $\overline{K_{\mathrm{n}}} = 2$, for a BER value of 10^{-4}, the reduction of dead time by one order of magnitude led to almost 3 dB improvement in the average signal count. The improvement was about 3.8 dB for BPPM. It was shown that PQ SPAD-based OWC systems with $\delta = 0.1$ can not achieve BER values lower than 10^{-3}. In general, for longer dead times, AQ SPADs significantly outperform PQ SPADs. For shorter dead times, AQ SPADs still provide slightly better bit error performance. The SPAD photocount distribution was also approximated by Gaussian and Poisson distributions which are commonly used in the literature. It was concluded that these approximate distributions can not provide enough accuracy in the performance analysis of SPAD-based OWC systems.

In the second study, OWC systems with SPAD arrays and dead time ratios of $\delta = 0.1$ and 1 were considered. The focus was on AQ SPAD arrays, as they generally outperform PQ SPAD arrays. It was verified that the dead time ratio of $\delta = 0.1$ is small enough to ensure negligible ISI. Then, by assuming independent count statistics over different bit intervals and using the Gaussian photocount distributions derived in Chapter 3, the exact and approximate error probabilities of an OOK system were derived. Simulations were carried out to verify the analytically predicted bit error probabilities. For $\delta = 1$, the ISI-modified Gaussian photocount distributions were obtained through Monte Carlo simulations and then were applied for the

performance analysis. With $\delta = 1$, the ISI was noticeable for $N_{\text{array}} = 64$, while it was negligible for $N_{\text{array}} = 1024$. It was then concluded that larger arrays can suppress the ISI effectively. The performance results also showed that compared with a single SPAD of the same sensitive area, the SPAD array was more robust to dead time. The SPAD array could tolerate longer dead time durations maintaining the system performance and required less signal power to achieve the same probability of error.

Chapter 5
Information Transfer Rate of SPAD Receivers

In Chapter 4, the reliability performance of single-photon avalanche diode (SPAD) receivers for optical wireless communication (OWC) applications was specified by system error probabilities. Another key performance metric is the maximum achievable data rate of the system. In SPAD-based systems, the transmission data rate needs to be chosen in such a way that a reliable photon counting performance is ensured for the SPAD receiver. In particular, the factor which limits the maximum data rate in SPAD-based communication systems, is dead time.

If the SPAD is assumed as a communication channel, then the limiting effect of dead time can be assessed by the *input-output information transfer rate* of the corresponding channel. In this context, the relevance of the *channel capacity* as a performance metric is clear. As long as the information transfer rate through the SPAD channel is less than its capacity, it is possible to make the error probability arbitrarily small with proper modulation and coding schemes.

In this chapter, the information transfer rate and the capacity of SPAD receivers in the presence of dead time is investigated. Recall from Chapter 4 that the SPAD dead time not only results in counting losses in each time interval, but also leads to inter-slot interference (ISI) distortion. When the ISI is negligible, the SPAD can be considered as a discrete memoryless channel (DMC). However, with the ISI, the SPAD channel is not memoryless and falls into the category of finite-state channels (FSCs) [99].

The capacity analysis of FSCs with general input distributions is mathematically intractable in general [100–103]. Therefore, in this chapter, the capacity analysis is conducted for two special cases of binary and pulse amplitude modulation (PAM) signalling. Even for these simplified cases, obtaining the capacity of the SPAD channel is still cumbersome and hence, lower and upper bounds on the capacity are developed instead. In particular, two auxiliary DMCs are proposed which provide an upper and a lower bound on the SPAD channel capacity.

First, the binary signalling scheme is considered and the analysis is conducted for active quenching (AQ) single SPADs. The bounds are derived for two cases of hard decision (HD) and soft decision (SD) outputs. Then, the information rates of AQ SPAD arrays with PAM signalling are analysed. A discrete-time Gaussian channel model with input-dependent mean and variance is assumed for the auxiliary DMC channels. Using a numerical algorithm, the capacity of the auxiliary channels, subject to peak and average power constraints, are acquired. Over a range of parameter values for which the lower and upper bounds are very tight, the capacity of the SPAD array channel is characterized by its bounds. As such, the auxiliary DMC models are adopted as a benchmark to study the properties of the capacity-achieving input distributions. The channel capacity and the capacity-achieving input distributions, subject to peak and average power constraints, are then presented for several array sizes, dead time values and background count levels.

The rest of this chapter is organised as follows. In Section 5.1, the relevant background from information theory is provided. Section 5.2 provides the SPAD channel model and discusses the choice of auxiliary channels for bounding the SPAD channel capacity. The capacity analysis of AQ single SPAD with binary signalling is conducted in Section 5.3. The analysis for AQ SPAD array and PAM signalling is provided in Section 5.4. A summary of the chapter is given in Section 5.5.

5.1 Preliminaries

In this section, some of the well-known results in information theory, that are needed in this chapter, are summarized. Hereinafter, the book by Cover and Thomas [104] is followed very closely.

Definition 4. *The entropy of a discrete random variable X with probability mass function (PMF) $p_X(x)$ is given by:*

$$H(X) \triangleq -\sum_{x} p_X(x)\log_2 p_X(x). \tag{5.1}$$

Definition 5. *The entropy of a discrete random variable Y conditioned on a discrete random*

variable X is given by:

$$H(Y|X) \triangleq -\sum_{x,y} p_{XY}(x,y)\log_2 p_{Y|X}(y|x). \tag{5.2}$$

where $p_{XY}(x,y)$ is the joint probability of the random variables X and Y, and $p_{Y|X}(y|x)$ is the conditional probability of Y given X.

Differential entropies and conditional differential entropies of continuous random variables are defined by replacing the summation with an integration. They are denoted by $h(X)$ and $h(Y|X)$, respectively.

Definition 6. *The entropy rate of a stochastic process $\mathcal{X}$ is defined by:*

$$H(\mathcal{X}) \triangleq \lim_{L\to\infty} \frac{1}{L} H(X_1, X_2, \ldots, X_L) \tag{5.3}$$

when the limit exists. The right-hand side expression is the per-symbol entropy rate.

Proposition 7. *If $\{X_1, X_2, \ldots, X_L\}$ is a sequence of independent and identically distributed (iid) random variables, then:*

$$H(\mathcal{X}) = H(X). \tag{5.4}$$

5.1.1 Discrete Memoryless Channels (DMCs)

A DMC consists of two finite alphabet sets $\mathcal{A}_\mathrm{x}$ and $\mathcal{A}_\mathrm{y}$ and a PMF $p_{Y|X}(y|x)$, such that for every x and y, $p_{Y|X}(y|x) > 0$, and for every $x \in \mathcal{A}_\mathrm{x}$, $\sum_y p_{Y|X}(y|x) = 1$. The PMF $p_{Y|X}(y|x)$ is termed as the *forward channel law*, X is the input and Y is the output of the channel.

Let $\{X_1, X_2, \ldots, X_L\}$ and $\{Y_1, Y_2, \ldots, Y_L\}$ be the ensembles of input and output sequences of length L, respectively. Further, let $\{x_1, x_2, \ldots, x_L\}$ $\forall x_i \in \mathcal{A}_\mathrm{x}$ be an arbitrary sequence of L inputs and $\{y_1, y_2, \ldots, y_L\}$ $\forall y_i \in \mathcal{A}_\mathrm{y}$ be the corresponding output sequence. In a DMC, the following equation holds:

$$\Pr\{y_i|x_1, x_2, \ldots, x_i, y_1, y_2, \ldots, y_{i-1}\} = p_{Y|X}(y_i|x_i) \tag{5.5}$$

for $i = 1, 2, \ldots, L$. The above equation represents the memoryless property of the DMC. Note that $p_{Y|X}(\cdot|\cdot)$ may depend on i, i.e., the channel may be time-varying.

Definition 8. *The mutual information between the input X and output Y of a DMC with the input distribution $p_X(x)$ and the forward channel law $p_{Y|X}(y|x)$ is defined as:*

$$\begin{aligned} I(X;Y) &\triangleq \sum_{x,y} p_{XY}(x,y)\log_2\frac{p_{XY}(x,y)}{p_X(x)p_Y(y)} \\ &\triangleq \sum_{x,y} p_X(x)p_{Y|X}(y|x)\log_2\frac{p_{Y|X}(y|x)}{p_Y(y)} \end{aligned} \tag{5.6}$$

where $p_Y(y)$ is the channel output distribution defined as:

$$p_Y(y) \triangleq \sum_x p_X(x)p_{Y|X}(y|x), \quad \forall y \in \mathcal{A}_\mathrm{y}. \tag{5.7}$$

The mutual information can also be written as:

$$I(X;Y) = H(X) - H(X|Y) = H(Y) - H(Y|X). \tag{5.8}$$

For continuous random variables, differential entropies are used. For a DMC, $H(Y)$ is a concave and $H(Y|X)$ is a linear function of the input probability distribution $p_X(x)$. Hence, the mutual information of a DMC is a concave function of the input probability distribution $p_X(x)$ [99, 102, 104].

Definition 9. *The capacity of a DMC is defined as the maximum mutual information between the input X and the output Y:*

$$C \triangleq \max_{p_X} I(X;Y), \tag{5.9}$$

with $p_X(x) \geq 0\ \forall x \in \mathcal{A}_\mathrm{x}$ and $\sum_x p_X(x) = 1$. Any $p_X(x)$ that maximizes (5.9) is called a capacity-achieving input distribution. Note that this maximization does not necessarily lead to a unique distribution.

In general, there is no analytical solution for computing the channel capacity. For DMCs, the Blahut-Arimoto algorithm [105, 106] is an elegant iterative algorithm to determine the capacity-achieving input distribution and to compute the capacity.

5.1.2 Discrete Channels with Memory

In this class of channels, the outputs y_i are in general no longer independent events given the input sequence. This means that (5.5), the condition for a channel to be memoryless, does not hold for these channels; the discrete channel is then said to have *memory*. In these channels, errors typically occur in clusters and are signal dependent. The characterization of channels with memory is in general more difficult than DMCs. Ideally, such a characterization should be mathematically tractable and should accurately represent the properties of the channel memory.

Definition 10. *The information rate between the input process $\mathcal{X} = \{X_1, X_2, \dots\}$ and the output process $\mathcal{Y} = \{Y_1, Y_2, \dots\}$ of a discrete-time channel with memory is given in the limit as:*

$$I(\mathcal{X};\mathcal{Y}) \triangleq \lim_{L\to\infty} \frac{1}{L} I(X_1, X_2, \cdots, X_L; Y_1, Y_2, \cdots, Y_L), \tag{5.10}$$

when the limit exists.

There are a number of variations of the channels with memory in the literature [100, 101]. However, in many cases of practical interest, the computation of (5.10) is complex or even intractable. Analytical simplifications of (5.10) are usually not available, even if the input symbols X_i are iid. The complexity of the direct numerical computation of:

$$I(L) \triangleq \frac{1}{L} I(X_1, X_2, \cdots, X_L; Y_1, Y_2, \cdots, Y_L), \tag{5.11}$$

is exponential in L, but the sequence $I(1)$, $I(2)$, $I(3)$, ...converges rather slowly even for channels with small memory [102, 103].

Definition 11. *The capacity of a channel with memory, with the input process $\mathcal{X}$ and the output process $\mathcal{Y}$ is defined by:*

$$C \triangleq \lim_{L\to\infty} \max_{p_{X^L}} \frac{1}{L} I(X_1, X_2, \cdots, X_L; Y_1, Y_2, \cdots, Y_L), \tag{5.12}$$

In [99], Gallager defined a class of the channels with memory known as FSCs. A FSC is a discrete-time channel for which the distribution of the channel output depends on both the channel input and the underlying channel state. This allows the channel output to depend implicitly on previous inputs and outputs via the channel state. Each FSC consists of an input process $\mathcal{X}$, a nonobservable state process $\mathcal{S}$, and an observable output process $\mathcal{Y}$. The

Gallager's definition of FSCs is as follows:

Definition 12. *The output at time i of a FSC is statistically independent of the state at time i, given the state at time $i-1$ and the input at time i:*

$$\Pr\{y_i, s_i|x_i, s_{i-1}\} = \Pr\{y_i|x_i, s_{i-1}\}\Pr\{s_i|x_i, s_{i-1}\}, \tag{5.13}$$

where x_i, s_i and y_i are the input, the channel state and the output at time i, respectively.

5.2 SPAD Channel Model

Recall from Chapter 4 that in OWC systems, the SPAD dead time has two effects on the photon counting process. The primary effect is to cause some counting losses in each time interval. The secondary effect is incurring counting losses in the neighbouring intervals, i.e. the ISI distortion. Both effects limit the maximum achievable data rate through increasing the error probability. A realistic model for the SPAD channel (whether single or array) should therefore consider both effects.

The ISI occurs if the dead time of the last detected photon in one interval overlaps with the next time slot. This leads to a temporal inactivity of the SPAD at the beginning of the time interval, thereby distorting the output (the number of photocounts). Without ISI, the photocount statistics of neighbouring time slots are independent. In such a case, the SPAD channel is memoryless and therefore can be modelled as a DMC [99]. With ISI, however, the memoryless property is lost and the neighbouring time slots become correlated. In this case, the SPAD can be assumed as a FSC [99] for which the information rate given in (5.10) determines the achievable rate of reliable communication through the SPAD channel for a specific input distribution. The channel capacity is the supremum of this information rate over all admissible input distributions.

For tractability, it is assumed that the input random variables are iid. This simplifying assumption is widely used in the literature [107, 108]. With this assumption, the resulting information rate will be a lower bound of the expression in (5.10). But with a slight abuse of notation, it is reported as the "information transfer rate" in this chapter. Despite this simplification, calculating the capacity of (5.12) for the SPAD channel is still intractable and hence, we resort to limiting the focus to binary and PAM signalling schemes and establishing lower and upper bounds on the capacity.

In this study, the bounds are inspired by [102, 103, 107, 108]. For each bound, an auxiliary channel model is adopted that somehow approximates the actual SPAD channel. The accuracy of this approximation affects the tightness, but not the validity of the bounds.

5.2.1 Upper Bound

For the upper bound, the auxiliary channel is an ISI-less DMC [102, 107, 108]. More precisely, a DMC which is only subject to the primary effect of dead time. Hence, the PMF expressions developed in Chapter 3 can be used in this case. Hereinafter, this channel is referred to as DMC_1.

5.2.2 Lower Bound

Similarly, for the lower bound, the auxiliary channel DMC_2 is considered. In this DMC, there is an output power degradation that rises due to the memory introduced by the ISI [102, 107, 108]. For the SPAD receiver, this power degradation should be accounted for in the forward channel law, i.e. the photocount distributions. Since the analytical expressions of the ISI-modified photocount distributions are not available, the required PMFs are obtained through Monte Carlo methods. To this end, considering both of the dead time effects, the photon counting process of the SPAD is simulated. The process is allowed to operate for enough time (e.g. 10^6 consecutive counting intervals) to reach the so-called *equilibrium* conditions.[1] Once in equilibrium, the photocount distribution of consecutive intervals are independent. And the steady state photocount distribution can be used for the lower bound calculations [108].

In the following sections, the capacity analysis is conducted for two case studies: i) the AQ single SPAD channel with binary signalling, and ii) the AQ SPAD array channel with PAM signalling. In each study, the capacity of the auxiliary DMCs are analysed and bounds on the SPAD channel capacity are developed.

[1] According to [39], the SPAD photon counting process can be described by a hidden Markov process with stationarity and ergodicity properties. Therefore, it has a unique stationary distribution regardless of the initial state distributions. The stationary distribution is also known as the *equilibrium* or *steady state* distribution.

5.3 Information Rates of AQ Single SPAD with Binary Signalling

5.3.1 Capacity Analysis for DMCs

In the binary signalling scheme, the input X takes the value 1 when a signal is present, and 0 otherwise. Let $p_X(1) = q$ and $p_X(0) = 1 - q$. In addition, let $p_{\mathrm{n}}(k)$ and $p_{\mathrm{sn}}(k)$ be the probabilities of k photocounts in a detection interval of length T when '0' or '1' is sent, respectively. Two categories can be realised depending on the receiver output: SD and HD. In SD, the output is equal to the number of photocounts. In HD, the output takes only two values, '0' and '1', as determined by a likelihood ratio test.

5.3.1.1 Soft Decision

In this case, the output Y is equal to the number of photocounts in the counting interval where Y can take all non-negative integer values 0, 1, 2, ..., $k_{\max}$. Therefore, it follows that:

$$\begin{aligned} p_{Y|X}(k|0) &= p_{\mathrm{n}}(k), \\ p_{Y|X}(k|1) &= p_{\mathrm{sn}}(k). \end{aligned} \tag{5.14}$$

According to (5.6), the mutual information $I(X;Y)$ is given by:

$$I(X;Y) = \sum_k \left[(1-q) p_{\mathrm{n}}(k) \log_2 \frac{p_{\mathrm{n}}(k)}{p_Y(k)} + q p_{\mathrm{sn}}(k) \log_2 \frac{p_{\mathrm{sn}}(k)}{p_Y(k)} \right], \tag{5.15}$$

Using (5.7) and (5.14), the marginal PMF $p_Y(k)$ is expressed as:

$$p_Y(k) = (1-q) p_{\mathrm{n}}(k) + q p_{\mathrm{sn}}(k). \tag{5.16}$$

With (5.15) and (5.16), $I(X;Y)$ can be numerically calculated for any given value of q. Then, the channel capacity C can be obtained according to (5.9). Since the SD capacity is expressed as a function of the forward channel law $p_{Y|X}(y|x)$, it is a function of dead time, and the average signal and background noise counts.

5.3.1.2 Hard Decision

In this case, the output Y takes only two values, 0 and 1, as determined by a likelihood ratio test. The conditional probability, $p_{Y|X}(y|x)$, for the four possible combinations of the binary input-output pair, (x, y), is calculated as:

$$p_{Y|X}(0|0) = \Pr\{k \leq k_{\rm th}|0\} = \sum_{k=0}^{k_{\rm th}} p_{\rm n}(k), \tag{5.17a}$$

$$p_{Y|X}(1|0) = 1 - p_{Y|X}(0|0), \tag{5.17b}$$

$$p_{Y|X}(0|1) = \Pr\{k \leq k_{\rm th}|1\} = \sum_{k=0}^{k_{\rm th}} p_{\rm sn}(k), \tag{5.17c}$$

$$p_{Y|X}(1|1) = 1 - p_{Y|X}(0|1), \tag{5.17d}$$

where $k_{\rm th}$ denotes the optimum threshold for the maximum likelihood detection and has been derived for the AQ single SPAD in Appendix F. Also, the marginal PMF $p_Y(y)$ is given by:

$$p_Y(0) = (1-q)\sum_{k=0}^{k_{\rm th}} p_{\rm n}(k) + q\sum_{k=0}^{k_{\rm th}} p_{\rm sn}(k), \tag{5.18a}$$

$$p_Y(1) = (1-q)\left(1 - \sum_{k=0}^{k_{\rm th}} p_{\rm n}(k)\right) + q\left(1 - \sum_{k=0}^{k_{\rm th}} p_{\rm sn}(k)\right). \tag{5.18b}$$

Based on (5.6), (5.17) and (5.18), the mutual information is then calculated. Note that, $p_{Y|X}(y|x)$ in (5.17) is a function of *a priori* probability q, since it depends on $k_{\rm th}$ which is a function of q.

5.3.2 Bounds on the Capacity of AQ Single SPAD

Define the DMC_1 as:

$$\begin{aligned} p_{\rm n}(k) &= p_K(k; \lambda_{\rm n}), \\ p_{\rm sn}(k) &= p_K(k; \lambda_{\rm s} + \lambda_{\rm n}), \end{aligned} \tag{5.19}$$

where $p_K(k;\lambda)$ is the dead time-modified photocount distribution of an AQ single SPAD given in (3.36), without ISI impairments. Also, define the DMC_2 as:

$$\begin{aligned} p_{\mathrm{n}}(k) &= \tilde{p}_K(k;\lambda_{\mathrm{n}}), \\ p_{\mathrm{sn}}(k) &= \tilde{p}_K(k;\lambda_{\mathrm{s}}+\lambda_{\mathrm{n}}), \end{aligned} \tag{5.20}$$

where $\tilde{p}_K(k;\lambda)$ is the dead time and ISI-modified stationary photocount distribution of an AQ single SPAD, as discussed in Section 5.2.2. Let $I_{\mathrm{U}}^{\mathrm{SD}}$ and $I_{\mathrm{U}}^{\mathrm{HD}}$ be the SD and HD mutual informations of the DMC_1 and $I_{\mathrm{L}}^{\mathrm{SD}}$ and $I_{\mathrm{L}}^{\mathrm{HD}}$, those of the DMC_2. Therefore:

$$I_{\mathrm{L}}^{\mathrm{SD}} \leq C^{\mathrm{SD}} \leq I_{\mathrm{U}}^{\mathrm{SD}}, \tag{5.21}$$

$$I_{\mathrm{L}}^{\mathrm{HD}} \leq C^{\mathrm{HD}} \leq I_{\mathrm{U}}^{\mathrm{HD}}, \tag{5.22}$$

where C^{SD} and C^{HD} are the SD and HD capacities of the AQ single SPAD, respectively.

5.3.3 Numerical Results and Discussions

In this section, some numerical results on the bounds and the capacity of AQ single SPADs are provided. In particular, the effects of three parameters are investigated: K_{s}, K_{n}, and δ. In each figure, the bounds or the capacity are presented as functions of one of these parameters while the two others remain fixed. In order to optimize the operating conditions and the structure of a SPAD receiver to achieve its maximum information transfer rate, the effect of these parameters should be treated simultaneously.

In Fig. 5.1, the upper and lower bounds on the SD and HD capacities of the AQ single SPAD are shown as functions of the average signal count, K_{s}. In this figure, a dead time ratio of $\delta = 0.1$ and average background noise counts of $K_{\mathrm{n}} = 0$, 5 and 10 are assumed. The SD and HD capacities of an ideal SPAD with $\delta = 0$ are also provided as benchmarks.

Fig. 5.1a shows that in the quantum-limited condition of $K_{\mathrm{n}} = 0$, the bounds are perfectly matching and the SD and HD cases overlap. In addition, the dead time has no impact on the capacity of the SPAD channel in quantum-limited conditions. It can be observed in Figs. 5.1b and 5.1c that when $K_{\mathrm{n}} > 0$, the SD and HD capacities are no longer the same and soft outputs offer higher information rates compared with the hard outputs. According to Figs. 5.1b and 5.1c, for the SD (HD) case, $I_{\mathrm{U}}^{\mathrm{SD}}$ ($I_{\mathrm{U}}^{\mathrm{HD}}$) with $\delta = 0.1$ is lower than C^{SD} (C^{HD}) with $\delta = 0$

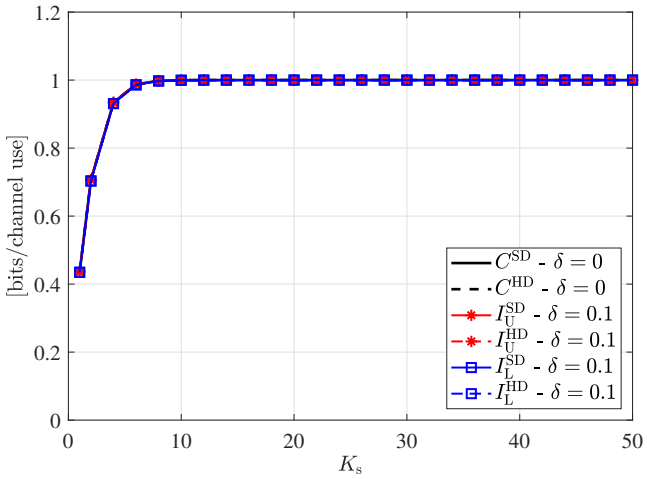

(a) $K_n = 0$

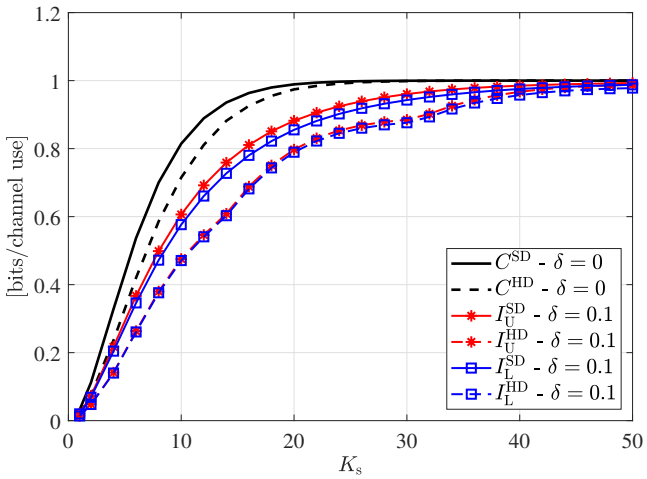

(b) $K_n = 5$

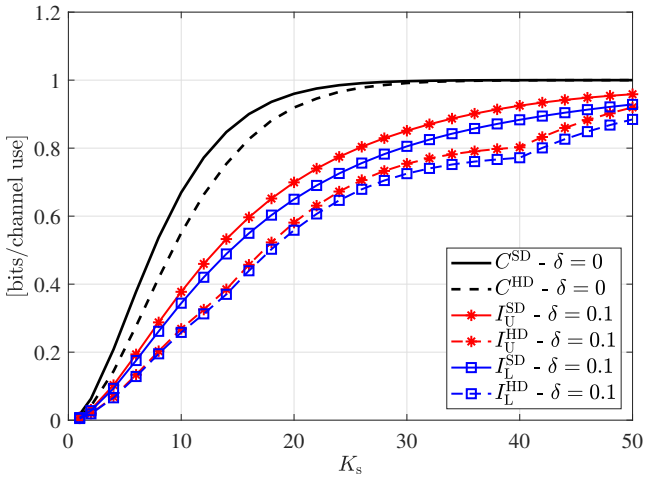

(c) $K_n = 10$

Figure 5.1: *Bounds on the capacity of AQ single SPAD as functions of* K_s.

for the whole range of K_{s} values. This is also observed in the lower bounds. Thus, in the presence of dead time, both bounds are decreased. As a results, the information rates, and hence, the capacity of a SPAD with $\delta = 0.1$ are less than those of an ideal SPAD with $\delta = 0$.

Figs. 5.1 also illustrates that higher average signal counts lead to higher capacity values for both SD and HD cases. However, the capacity cannot exceed 1 bits/channel use. The minimum K_{s} required for achieving this capacity depends on δ and K_{n}. For example, with $\delta = 0.1$ and $K_{\mathrm{n}} = 5$, the SD capacity reaches the maximum value of 1 for $K_{\mathrm{s}} \geq 40$, and the limiting effect of dead time vanishes. This happens at a higher K_{s} if a higher K_{n} is considered (see Fig. 5.1c). In addition, if δ is smaller, this capacity is achieved at lower signal levels. This trend suggests that by choosing a proper signal intensity in practice, the information transfer rate of the single SPAD receiver can be maximized.

For the range of signal and background noise levels shown in Fig. 5.1, the upper and lower bounds are tight in both SD and HD cases. Note that for smaller dead time ratios, e.g. $\delta = 0.01$ or 0.001, the bounds would be even tighter. Therefore, it can be concluded that for $\delta \leq 0.1$ and the range of parameters considered here, the ISI is insignificant for both SD and HD cases. As such, the AQ single SPAD can be assumed as a DMC. In the sequel, this assumption is used for obtaining the rest of the results.

Fig. 5.2 presents the mutual information, $I(X;Y)$, of the AQ single SPAD as a function of *a priori* probability, q, for both SD and HD categories. The red solid curves represent the SPAD channel with soft outputs, and the blue dashed curves represent the SPAD channel with hard outputs. In Fig. 5.2a the effect of average signal count, K_{s}, is displayed for $K_{\mathrm{s}} = 5$, 15, 30, with an average background noise count of $K_{\mathrm{n}} = 5$ and a dead time ratio of $\delta = 0.02$. In Fig. 5.2b the effect of K_{n} is illustrated for $K_{\mathrm{n}} = 1$ and 10, assuming $K_{\mathrm{s}} = 20$ and $\delta = 0.02$. In Fig. 5.2c the effect of dead time ratio is presented for $\delta = 0$ and 0.1, assuming $K_{\mathrm{s}} = 15$ and $K_{\mathrm{n}} = 5$. These results indicate that the mutual information decreases with decreasing average signal counts (see Fig. 5.2a), increasing average background noise count (see Fig. 5.2b), and increasing dead time (see Fig. 5.2c). It is observed that the peak value of each curve which represents the channel capacity, occurs at or near $q = 0.5$ in most cases.

An obvious distinction between the two types is that the HD exhibits discontinuities in the $I(X;Y)$ curves. This is due to the discrete nature of the decision threshold k_{th} which jumps from one integer to the next at certain values of q. Furthermore, as mentioned earlier, the SD

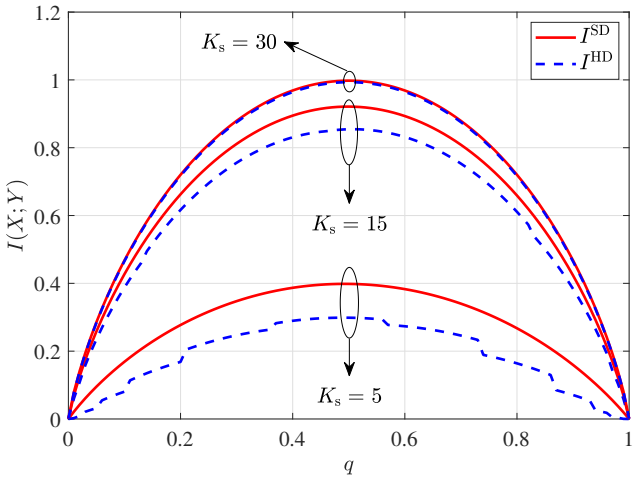

(a) $\delta = 0.02$, $K_n = 5$

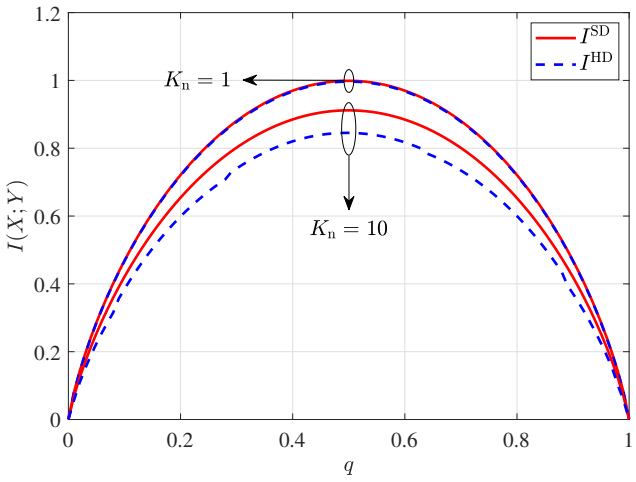

(b) $\delta = 0.02$, $K_s = 20$

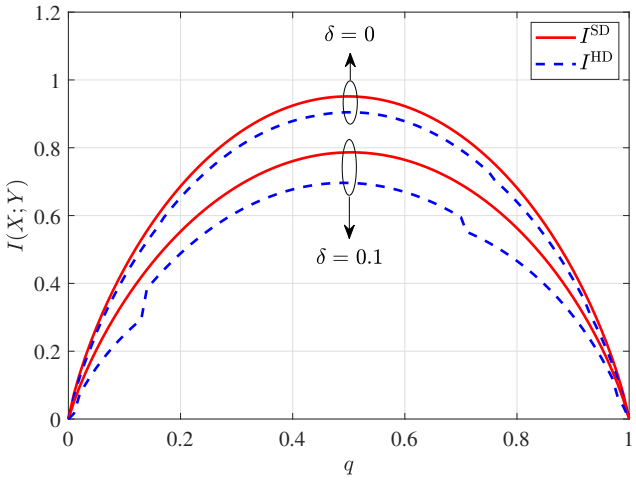

(c) $K_s = 15$, $K_n = 5$

Figure 5.2: *Mutual information, $I(X;Y)$, versus a priori signal probability, q.*

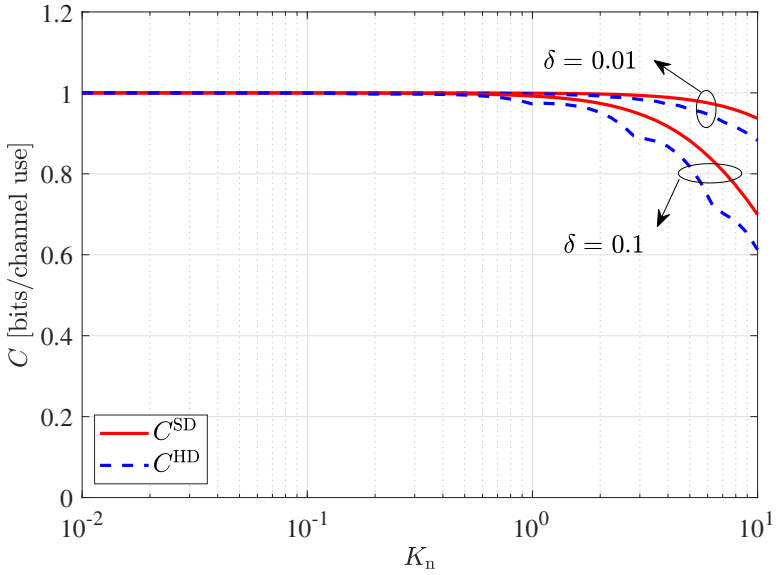

Figure 5.3: *Capacity of AQ single SPAD as a function of* K_{n} *for* $K_{\mathrm{s}} = 20$.

provides a higher mutual information compared with the HD, thereby always having a higher capacity than the HD case. This is because the slot photocounts provide additional information in the SD case.

Since both the input and the output take the values 0 and 1, a hard output SPAD receiver can be considered as an asymmetric binary channel with varying error transition probability, i.e. $p_{Y|X}(1|0)$ and $p_{Y|X}(0|1)$. Therefore, the channel capacity can not exceed 1.

The effect of background noise counts is shown in Fig. 5.3 for $K_{\mathrm{s}} = 20$ and $\delta = 0.1, 0.01$. According to this figure, for larger values of δ, the limiting effect of the background noise appears in smaller values of K_{n}. In other words, with larger values of δ the capacity becomes more sensitive to background noise. This can also be interpreted as follows: keeping the average background noise count below an optimum value (1 for the SD and 0.1 for the HD according to Fig. 5.3), will help to overcome the limiting effect of dead time on the capacity.

In Fig. 5.4, the capacity curves are plotted versus δ for $K_{\mathrm{s}} = 10, 20, 50$ and $K_{\mathrm{n}} = 5$. As seen in this figure, with higher signal levels ($K_{\mathrm{s}} = 50$), the SPAD achieves $C^{\mathrm{SD}} = 1$ for $\delta \leq 0.1$ and $C^{\mathrm{HD}} = 1$ with $\delta \leq 0.07$. With lower signal levels ($K_{\mathrm{s}} = 10$), the capacity becomes more sensitive to the dead time such that for $\delta > 0.01$, C^{SD} and C^{HD} decrease significantly.

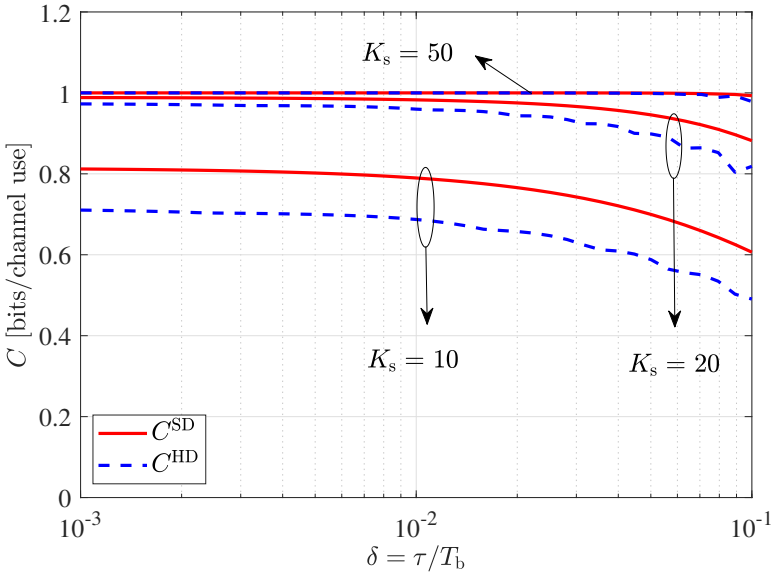

Figure 5.4: *Capacity of AQ single SPAD as a function of δ for $K_n = 5$.*

5.4 Information Rates of AQ SPAD Array with PAM Signalling

5.4.1 Capacity Analysis for DMCs

In the PAM signalling scheme, the intensity of the input signal, Λ_s, can vary between discrete time slots while remaining constant within each time interval. The channel input X is the average number of incident photons in a time interval of length T. Therefore, X is proportional to the incident light intensity and is non-negative. The channel output Y is the number of photocounts in each time interval, corrupted by background counts, N, with an intensity of Λ_n.

According to the discussions in Section 3.6, where the photocount distribution of the SPAD array was modelled by a Gaussian distribution, a *discrete-time Gaussian channel* is considered here. Therefore, the channel model for the auxiliary channels can be expressed as $Y = S(X + N)$, where X, N and Y denote the random variables for the channel input, noise and channel output, respectively. $S(\cdot)$ represents the number of photocounts which implicitly depends on the intensity of the optical signal, and hence the channel input X. Furthermore, $S(X + N)$ is Gaussian distributed with mean $\mu_S(X + N)$ and variance $\sigma_S^2(X + N)$. Accordingly,

$$p_{Y|X}(y|x) = \frac{1}{\sqrt{2\pi\sigma_S^2(x+n)}} \exp \frac{-(y - \mu_S(x+n))^2}{2\sigma_S^2(x+n)}, \tag{5.23}$$

where $x \in \mathbb{R}^+$ and $y \in \mathbb{Z}^+$. Due to practical considerations and device limitations, such as the saturation of SPAD receivers at high intensities, the input signal is subject to peak and average power constraints. Also, since X is proportional to the light intensity, the constraints are directly imposed on X. In addition, X should be non-negative. Thus,

$$0 \leq X \leq \mathcal{A}, \tag{5.24a}$$

$$\mathbb{E}[X] \leq \mathcal{E}, \tag{5.24b}$$

where $\mathcal{A}$ and $\mathcal{E}$ are the peak and average power, respectively. Without loss of generality, it is assumed that $0 \leq \mathcal{E} \leq \mathcal{A}$ and A is finite.

For the channel model in (5.23), $\mu_S(x+n)$ and $\sigma_S^2(x+n)$ are *signal-dependent*, unlike the classical Gaussian channels [109]. Such a class of Gaussian channels whose conditional output distribution given the channel input is Gaussian with input-dependent mean and variance are termed as conditionally Gaussian (CG) channels [110] or additive Gaussian signal-dependent noise (AGSDN) channels [111]. Although the properties of such channels have been studied in the literature, their capacity is not yet known [110, 111]. Nevertheless, it is well known that subject to peak and average power constraints, the channel capacity is achievable and the capacity-achieving distribution is unique and discrete with a finite number of mass points for finite A and $\mathcal{E}$. In what follows, some of the findings in the aforementioned reference articles are adopted to study the capacity of auxiliary DMCs.

Assume an input distribution defined over constellation $\psi_x = \{x_1, x_2, \ldots, x_b\}$, where $0 \leq x_1 < x_2 < \cdots < x_b \leq \mathcal{A}$, with probability distribution $\psi_p = \{p_1, p_2, \ldots, p_b\}$. Let P_X denote the corresponding cumulative distribution function (CDF), that is:

$$dP_X = p_1\delta(x - x_1) + p_2\delta(x - x_2) + \cdots + p_b\delta(x - x_b). \tag{5.25}$$

Also, let $\mathcal{P}_X$ be the set of all input distributions satisfying the constraints defined in (5.24):

$$\mathcal{P}_X \triangleq \left\{ P_X : \int_0^{\mathcal{A}} dP_X = 1, \mathbb{E}[X] \leq \mathcal{E} \right\}. \tag{5.26}$$

For each P_X, denote the corresponding distribution of Y by $p_Y(y; P_X)$, the marginal entropy of Y by $H(Y; P_X)$, the conditional entropy of Y given X by $H(Y|X; P_X)$, and the mutual

information between Y and X by $I(P_X)$. Recall from Section 5.1:

$$\begin{aligned} p_Y(y;P_X) &= \int_x p_{Y|X}(y|x)dP_X \\ H(Y;P_X) &= -\sum_y p_Y(y;P_X)\log_2 p_Y(y;P_X) \\ H(Y|X;P_X) &= \frac{1}{2}\int_x \log_2[2\pi e\sigma^2(x+n)]\; dP_X \\ I(P_X) &= H(Y;P_X) - H(Y|X;P_X) \\ &= \int_x \left[\sum_y p_{Y|X}(y|x)\log_2\frac{p_{Y|X}(y|x)}{p_Y(y;P_X)}\right] dP_X \end{aligned} \tag{5.27}$$

And the channel capacity is:

$$C = \max_{P_X\in\mathcal{P}_X} I(P_X)\;. \tag{5.28}$$

Let the capacity-achieving values of ψ_x, ψ_p, and P_X subject to constraints $\mathcal{A}$ and $\mathcal{E}$, be denoted by $\psi_x^*(\mathcal{A},\mathcal{E})$, $\psi_p^*(\mathcal{A},\mathcal{E})$, and $P_X^*(\mathcal{A},\mathcal{E})$, respectively. In the following, some of the main properties of the capacity-achieving distribution are summarized.

- *Existence and uniqueness*: There exists a unique probability measure P_X^* satisfying the bounded-input and average power constraints which maximizes $I(P_X)$ [110, Theorem 1].
- *Necessary and sufficient condition*: P_X^* is capacity-achieving if and only if there exists $\alpha \geq 0$ such that for all $x \in [0,\mathcal{A}]$ [110, Theorem 2]:

$$Q(x;P_X^*) - I(P_X^*) - \frac{1}{2}\log_2[2\pi e\sigma^2(x+n)] - \alpha(x-\mathcal{E}) \leq 0, \tag{5.29}$$

  where

$$Q(x;P_X) = -\sum_y p_{Y|X}(y|x)\log_2 p_Y(y;P_X). \tag{5.30}$$

- *Discreteness*: The capacity-achieving distribution, P_X^*, is discrete and consists of a finite set of mass points [110, Theorem 3].
- *Mass point at zero*: The capacity-achieving distribution always contains a mass point located at zero [110, Corollary 3]. That is, $0 \in \psi_x^*(\mathcal{A},\mathcal{E})$. Therefore,

$$\alpha = \frac{1}{\mathcal{E}}\left[I(P_X^*) - Q(0;P_X^*) + \frac{1}{2}\log_2[2\pi e\sigma^2(n)]\right]. \tag{5.31}$$

Algorithm 1 Search algorithm for finding the capacity-achieving input distribution.

Input: $\mathcal{A}, \mathcal{E}$
Output: C, P_X^*
1: **procedure** CAPACITY($\mathcal{A}, \mathcal{E}$)
2: $b \leftarrow 2$
3: Solve (5.28) such that $\|\psi_x\| = b$.
4: Determine $\alpha^{(b)}$ according to (5.31).
5: **if** $\alpha^{(b)} < 0$ **then**
6: $b \leftarrow b + 1$
7: **go to** 3
8: **end if**
9: **if** (5.29) holds for all $x \in [0, \mathcal{A}]$ **then**
10: **return** C and P_X^*
11: **else**
12: $b \leftarrow b + 1$
13: **go to** 3
14: **end if**
15: **end procedure**

Although the above properties of the capacity-achieving distributions for the CG channels are known, closed-form analytical expressions are unknown in general. Therefore, numerical methods are applied in order to compute the capacity and capacity-achieving distributions for the SPAD array channel. The optimal input distribution and the capacity of the DMCs can be obtained via the algorithm presented in Algorithm 1.

In Algorithm 1, the inputs are $\mathcal{A}$ and $\mathcal{E}$. The algorithm initializes with a binary distribution ($b = 2$). In each iteration, first the optimal P_X which maximizes $I(P_X)$ is obtained using the method presented in [109]. Since a mass point at $x = 0$ always exits, $\alpha^{(b)}$ is determined using (5.31). Failure of the necessary condition $\alpha^{(b)} > 0$ indicates that this P_X is not optimal and the current number of mass points, b, is not sufficient. Thus, the number of mass points should be increased by one, and the distribution function P_X which maximizes the information rate (subject to constraints) should be determined again. If $\alpha^{(b)} > 0$, then the necessary and sufficient condition in (5.29) is tested. If it is satisfied, then P_X is the capacity-achieving probability measure. Otherwise, b is increased by one and the procedure is repeated.

5.4.2 Bounds on the Capacity of SPAD Array

Consider the auxiliary channel DMC_1 for which:

$$\begin{aligned} \mu(x+n) &= \mu_S(\Lambda + \Lambda_\mathrm{n}), \\ \sigma^2(x+n) &= \sigma_S^2(\Lambda + \Lambda_\mathrm{n}), \end{aligned} \tag{5.32}$$

where μ_S and σ_S^2 are the dead time-modified mean and variance of the photocount distribution of a SPAD array given in (3.65). The above expressions does not take the effect of ISI impairments into account. Similarly, consider DMC_2 with:

$$\begin{aligned} \mu(x+n) &= \tilde{\mu}_S(\Lambda + \Lambda_\mathrm{n}), \\ \sigma^2(x+n) &= \tilde{\sigma}_S^2(\Lambda + \Lambda_\mathrm{n}), \end{aligned} \tag{5.33}$$

where $\tilde{\mu}_S$ and $\tilde{\sigma}_S^2$ are the dead time and ISI-modified mean and variance of the stationary photocount distribution of a SPAD array and are obtained based on Monte Carlo methods. Denote by I_U, I_L and I the mutual informations of the DMC_1, DMC_2 and the SPAD channel, respectively. Also, let the corresponding capacities be denoted by C_U, C_L and C. Therefore:

$$I_\mathrm{L} \leq C \leq I_\mathrm{U}. \tag{5.34}$$

5.4.3 Numerical Results and Discussions

In the following, some numerical results are provided for the above capacity analysis. As stated earlier in this section, the mean and variance of the SPAD array photocounts and both of the DMC channels are signal-dependent due to the dead time. Therefore, dead time is the parameter which determines the degree of signal dependency.

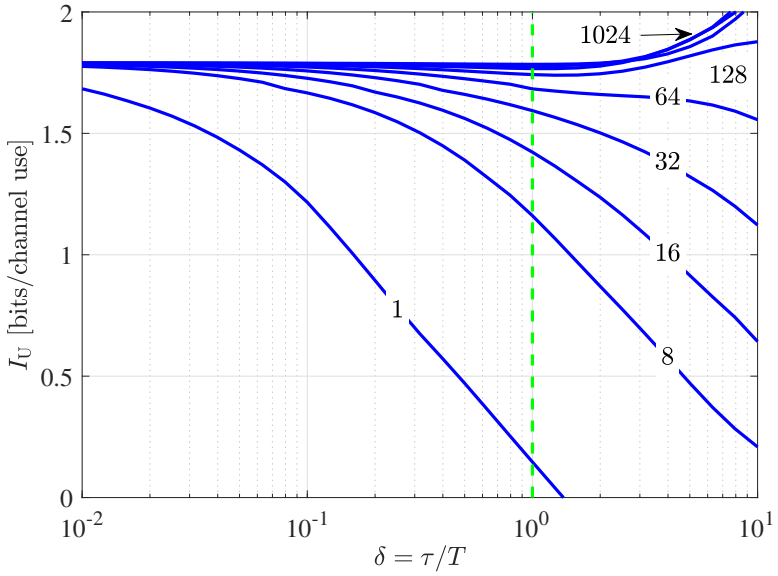

(a) Upper bounds

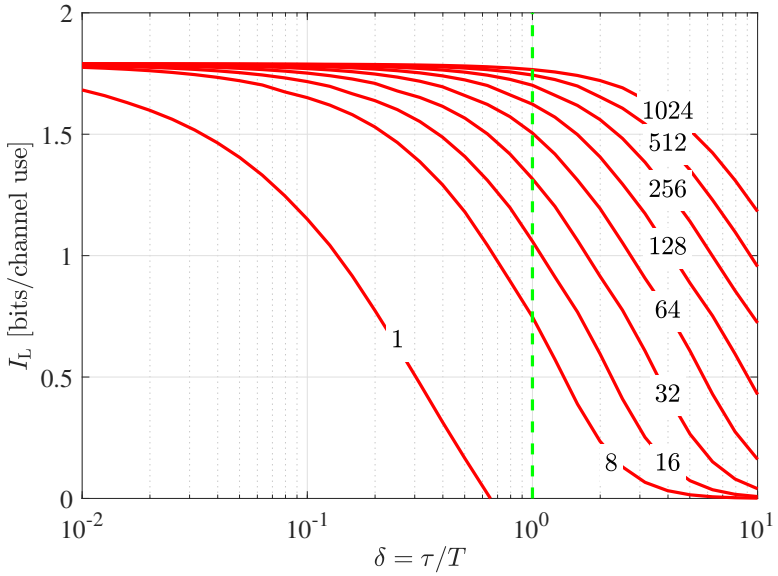

(b) Lower bounds

Figure 5.5: *Bounds on the capacity of SPAD array for several array sizes:* $\mathcal{A} = 50$, $\mathcal{E} = 20$ *and* $K_{\mathrm{n}}^{\mathrm{a}} = 5$.

Fig. 5.5 illustrates the bounds on the SPAD array channel capacity as a function of dead time ratio δ for $A = 50$, $\mathcal{E} = 20$, $K_{\mathrm{n}}^{\mathrm{a}} = 5$, and various array sizes. The range of interest is $\delta \leq 1$. For $\delta \leq 0.1$, the bounds are tight for all the array sizes. They remain tight for $0.1 < \delta \leq 1$ if $N_{\mathrm{array}} \geq 256$.

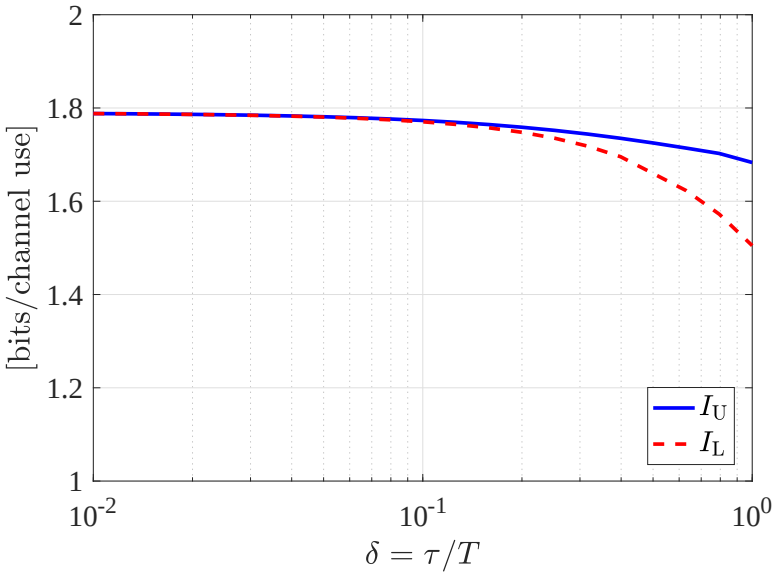

(a) $N_{\mathrm{array}} = 64$

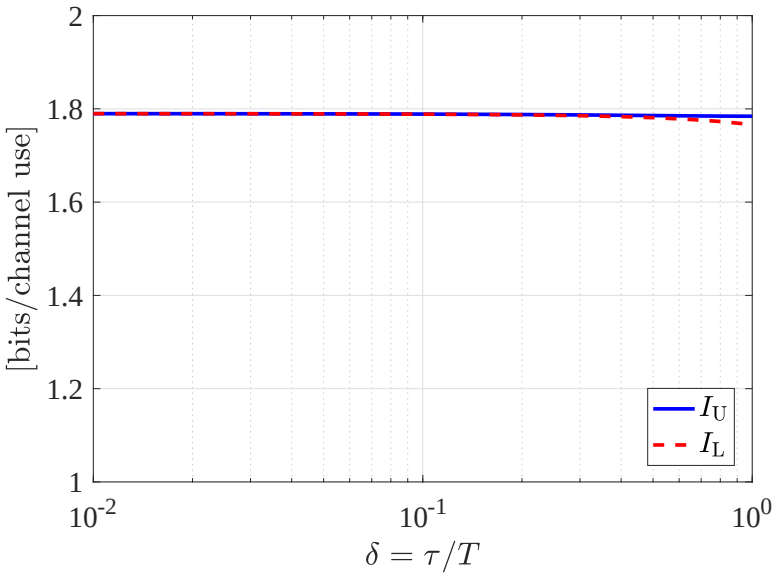

(b) $N_{\mathrm{array}} = 1024$

Figure 5.6: *Bounds on the capacity:* $\mathcal{A} = 50$, $\mathcal{E} = 20$ *and* $K_{\mathrm{n}}^{\mathrm{a}} = 5$.

For comparison purposes, the upper and lower bounds of $N_{\mathrm{array}} = 64$ and 1024 are extracted from Fig. 5.5 and are shown in Fig. 5.6.

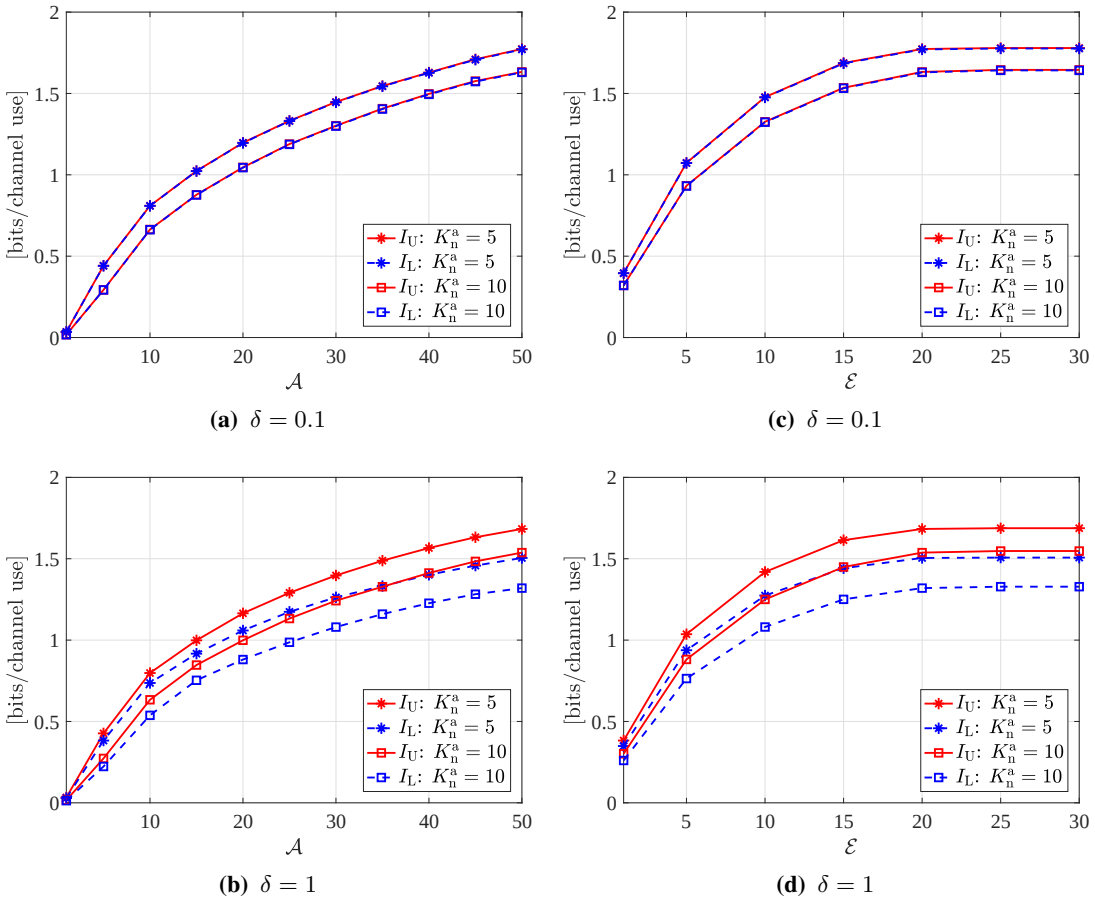

(a) $\delta = 0.1$ **(c)** $\delta = 0.1$

(b) $\delta = 1$ **(d)** $\delta = 1$

Figure 5.7: *Bounds on the capacity of SPAD array for* $N_{\mathrm{array}} = 64$*: (a),(b)* $\mathcal{E} = 20$*; (c),(d)* $\mathcal{A} = 50$.

Fig. 5.7 shows the upper and the lower bounds (the capacities of the DMC auxiliary channels) for $N_{\mathrm{array}} = 64$, as a function of the peak power constraint, $\mathcal{A}$, in Figs. 5.7a and 5.7b, and as a function of the average power constraint, $\mathcal{E}$, in Figs. 5.7c and 5.7d. In these figures, two different background noise levels ($K_{\mathrm{n}}^{\mathrm{a}} = 5$ and 10) and two dead time ratios ($\delta = 0.1$ and 1) are considered. From Figs. 5.7a and 5.7c, it is seen that for $\delta = 0.1$, the bounds are tight, confirming the negligible effect of ISI. However, according to Figs. 5.7b and 5.7d, with $\delta = 1$, the ISI is apparent, leading to a gap between the bounds.

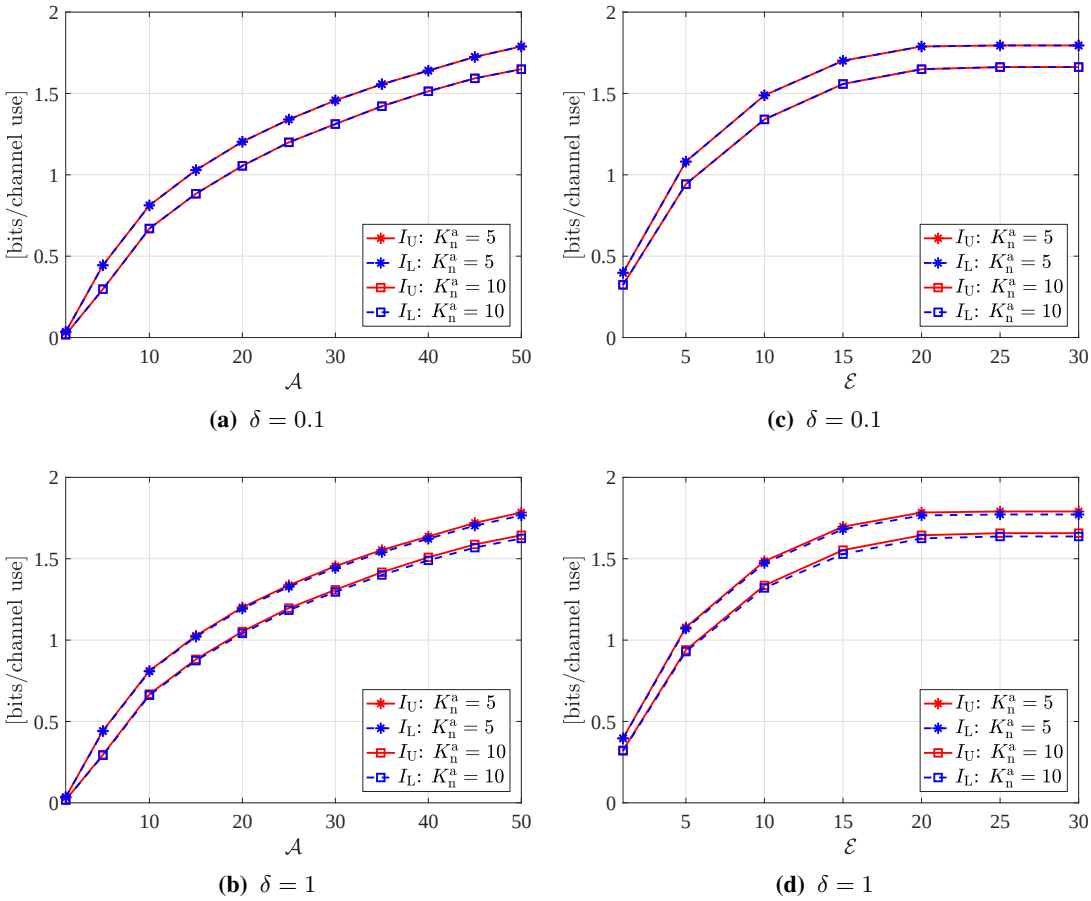

(a) $\delta = 0.1$ **(c)** $\delta = 0.1$

(b) $\delta = 1$ **(d)** $\delta = 1$

Figure 5.8: *Bounds on the capacity of SPAD array for* $N_{\mathrm{array}} = 1024$*: (a),(b)* $\mathcal{E} = 20$*; (c),(d)* $\mathcal{A} = 50$*.*

In Fig. 5.8, the bounds are provided for the array of $N_{\mathrm{array}} = 1024$ considering two different background noise levels and dead time ratios. As observed in this figure, the bounds are remarkably tight for $N_{\mathrm{array}} = 1024$ for all the presented parameter values. According to our extensive numerical investigation of the bounds, the following conclusions can be drawn; the capacity of:

- the SPAD array of $N_{\mathrm{array}} = 64$ with $\delta \leq 0.1$,
- the SPAD array of $N_{\mathrm{array}} = 1024$ with $\delta \leq 1$,

can be accurately approximated by their bounds. This means that in these cases, the SPAD array can be well approximated by the auxiliary DMCs. Figs. 5.6– 5.8 also support these statements. In the following numerical results, this approximation is used and the effect of different parameters on the capacity and the capacity-achieving input distribution are investigated.

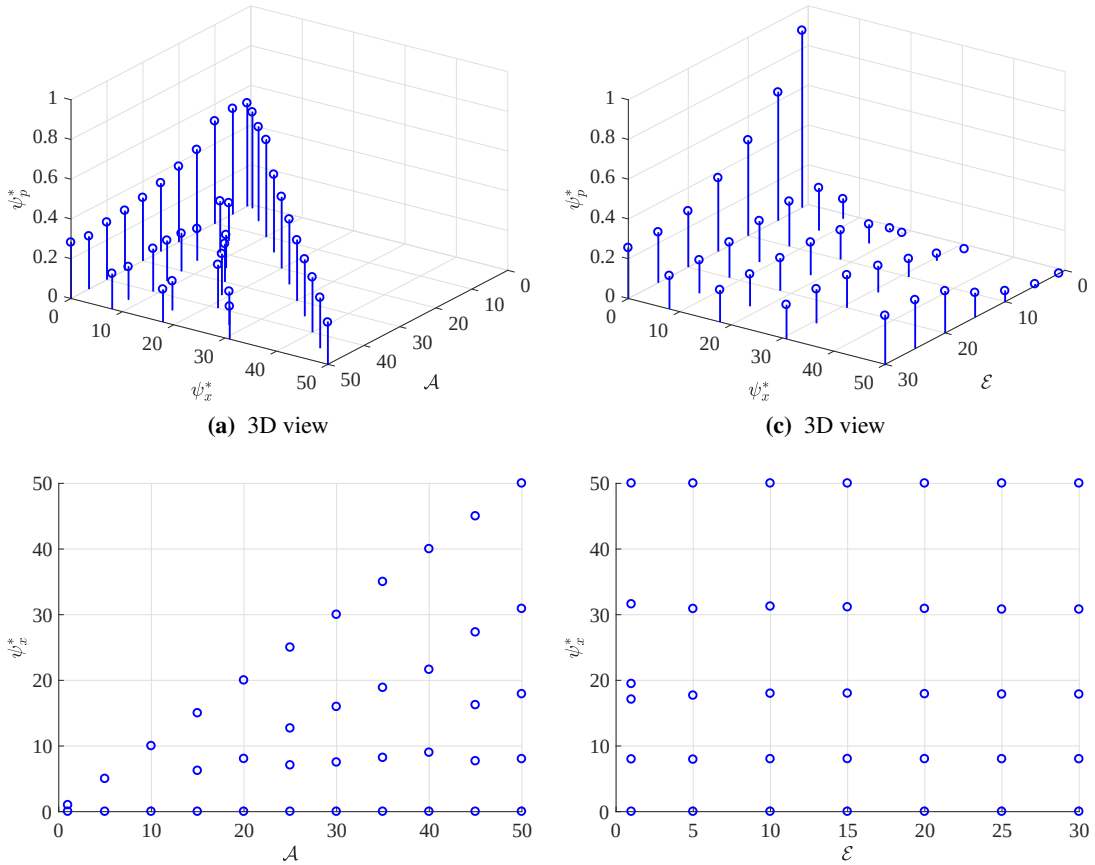

(a) 3D view **(c)** 3D view

(b) top view **(d)** top view

Figure 5.9: *SPAD array capacity-achieving distributions for* $N_{\text{array}} = 64$*,* $\delta = 0.1$ *and* $K_{\text{n}}^{\text{a}} = 5$*: (a),(b)* $\mathcal{E} = 20$*; (c),(d)* $\mathcal{A} = 50$*.*

In Fig. 5.9 the effect of peak power constraint, $\mathcal{A}$, and the average power constraint, $\mathcal{E}$, on the optimal mass points (ψ_x^*) and the corresponding probability measure (ψ_p^*) is presented for the array of 64 SPADs. In these figures, the parameters δ and K_{n}^{a} are assumed to remain fixed as $\delta = 0.1$ and $K_{\text{n}}^{\text{a}} = 5$. Similarly, in Fig. 5.10, ψ_x^* and ψ_p^* are provided for an array of 1024 SPADs with $\delta = 1$ and $K_{\text{n}}^{\text{a}} = 10$.

In Fig. 5.11 the effect of dead time on ψ_x^* and ψ_p^* is shown for the array of $N_{\text{array}} = 1024$. From Figs. 5.9– 5.11, the following remarks are deduced:

- The capacity-achieving measure (ψ_x^*, ψ_p^*) contains two mass points at $x = 0$ and $x = \mathcal{A}$, for all the parameter values. In [110], it is proved that $x = 0$ is always a mass point of (ψ_x^*, ψ_p^*). However, it is not proved whether $x = \mathcal{A}$ is also a mass point in general.
- As $\mathcal{A}$ increases, more mass points are required for achieving the capacity. In the

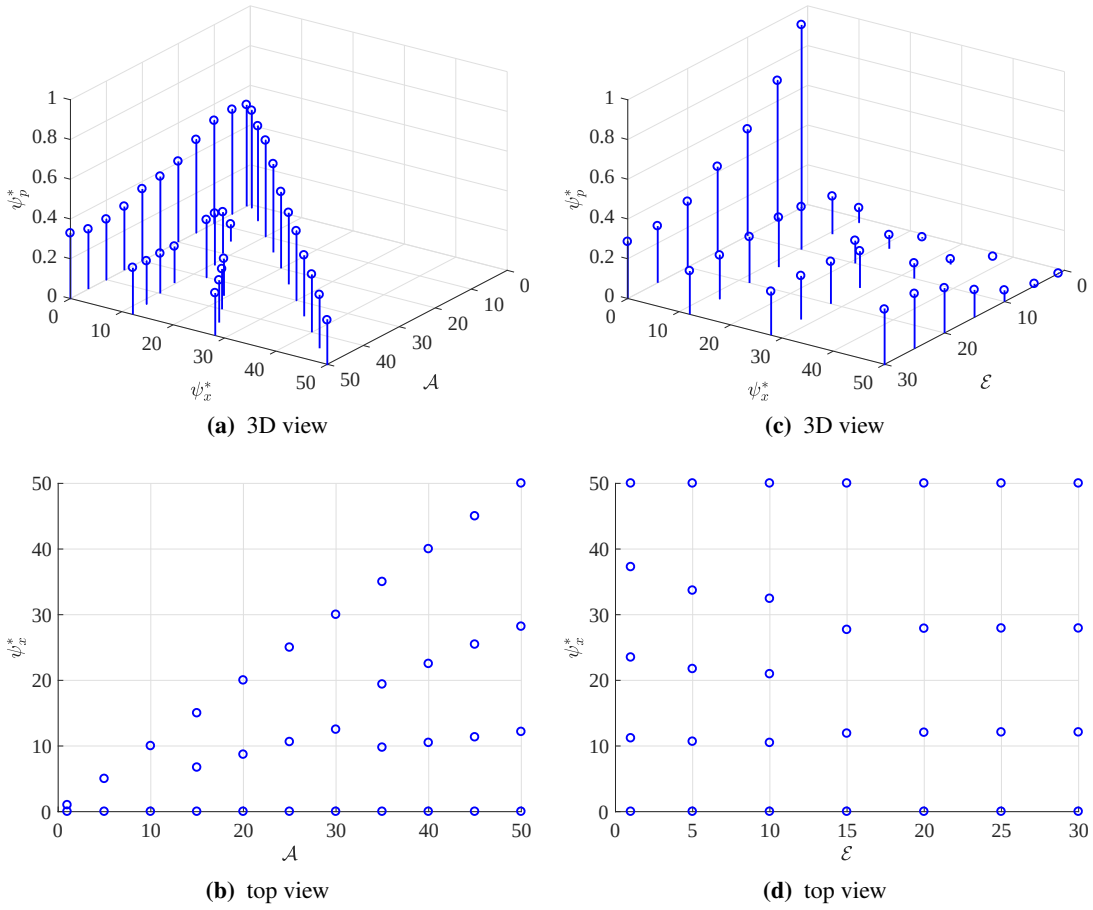

(a) 3D view **(c)** 3D view

(b) top view **(d)** top view

Figure 5.10: *SPAD array capacity-achieving distributions for* $N_{\text{array}} = 1024$*,* $\delta = 1$ *and* $K_{\text{n}}^{\text{a}} = 10$*: (a),(b)* $\mathcal{E} = 20$*; (c),(d)* $\mathcal{A} = 50$*.*

presented range of parameters, the variance of the signal-dependent noise term is almost a linear function of the signal power. As a result, for higher values of $\mathcal{A}$, the average signal-dependent noise power is higher; hence, a signalling scheme with a larger constellation size is more favourable.

- As $\mathcal{E}$ increases, the capacity also increases almost until $\mathcal{E} \approx 0.5\mathcal{A}$. After this point, the channel capacity remains constant.

Another important observation is that for $N_{\text{array}} = 1024$, if $\delta \leq 1$, the capacity-achieving measure (ψ_x^*, ψ_p^*) does not depend on δ (see Fig. 5.11). This means that in this large array the impact of dead time is effectively cancelled. As a numerical example, assuming a typical dead time of 10 ns, using a PAM signalling scheme with 5 levels, this array can achieve the capacity of 1.8 bits/channel use or equivalently a maximum data rate of 180 Mbits/s with $\mathcal{A} = 50$ and $\mathcal{E} = 20$.

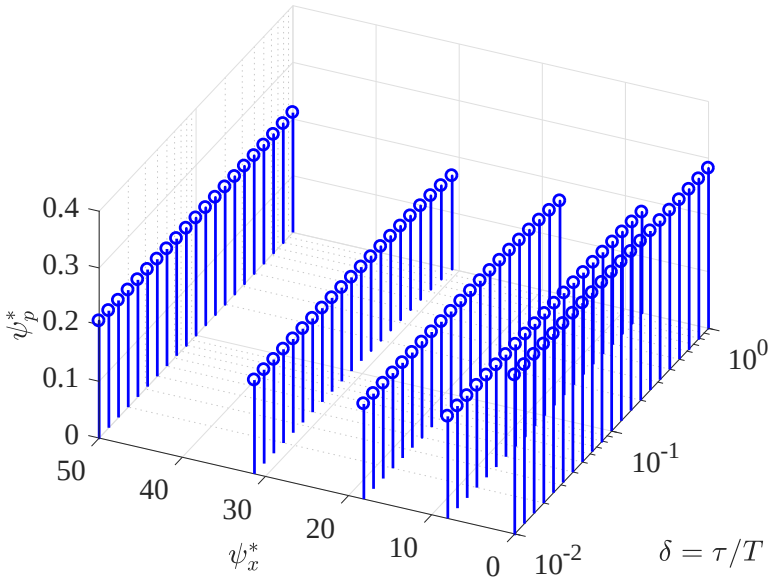

(a)

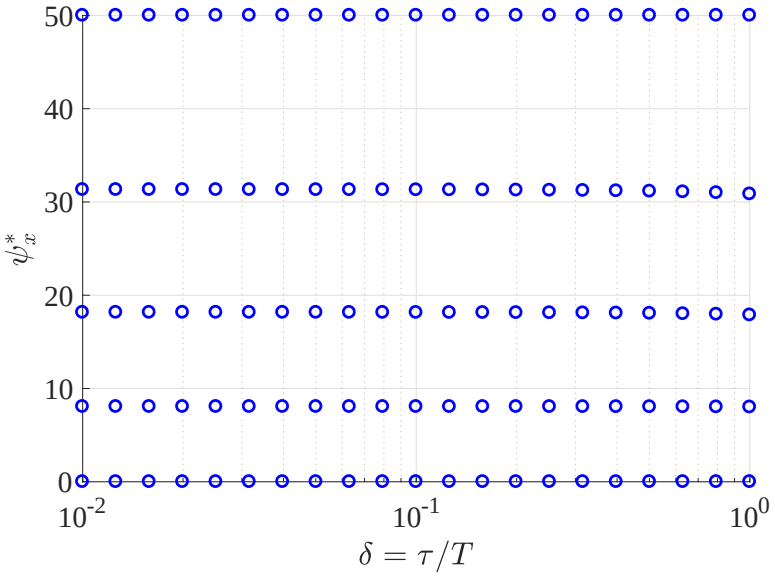

(b)

Figure 5.11: *SPAD array capacity-achieving distributions for* $N_{\text{array}} = 1024$, $\mathcal{A} = 50$, $\mathcal{E} = 20$ *and* $K_{\text{n}}^{\text{a}} = 5$.

5.5 Summary

In this chapter the information transfer rate of SPAD receivers was studied. The SPAD was modelled as a communication channel with finite memory and the information rates with binary and PAM signalling schemes were analysed. Two auxiliary channels were used for establishing upper and lower bounds on the capacity.

The analysis of the binary signalling was conducted for AQ single SPADs. The mathematical expressions for the mutual information of the auxiliary channels were derived and the bounds on the capacity of the SPAD channel were obtained. For the single SPADs with dead time ratios $\delta \leq 0.1$, the bounds were very tight for a wide range of signal and background noise levels, showing that the dead time induced-ISI was negligible for $\delta \leq 0.1$. Therefore, the capacity of the AQ single SPAD could be tightly approximated by those of the auxiliary channels. The results showed that with lower signal levels, the capacity becomes more sensitive to the dead time losses. Also, keeping the average background noise count below an optimum value will help to overcome the limiting effect of dead time on the capacity.

The analysis of the PAM signalling was carried out for the AQ SPAD arrays. A discrete-time Gaussian channel model with input-dependent mean and variance was adopted for the auxiliary channels. Using a numerical algorithm, the capacity of the auxiliary channels, subject to average and peak power constraints was evaluated, and the bounds on the capacity of the SPAD array were established. The numerical results were provided for $\delta = 0.1$, 1 and $N_{\text{array}} = 64$, 1024. For $N_{\text{array}} = 1024$, the bounds were very tight for both $\delta = 0.1$ and $\delta = 1$ over a wide range of signal and background count levels. This, again confirmed that in larger arrays the ISI was insignificant. Thus, the SPAD array of $N_{\text{array}} = 1024$ could be well approximated as a memoryless channel. As such, it was found that for a large array, the channel capacity, subject to the average and peak power constraints, is achievable. The capacity-achieving distribution is discrete, consists of a finite set of mass points, and always contains a mass point at zero.

Chapter 6
Conclusions and Future Research

In this thesis, the general objective was to investigate the application of single-photon avalanche diode (SPAD) photodetectors (PDs) for optical wireless communication (OWC). A series of fundamental studies related to the impact of SPAD dead time were presented. To the best of the author's knowledge, this is the first comprehensive study in this context. The contribution of this thesis was threefold: First, a novel analytical method was proposed for modelling the statistical photon counting behaviour of SPADs in the presence of different types of dead time. This method was used to obtain the photocount distributions for active quenching (AQ) and passive quenching (PQ) single SPADs and SPAD arrays. Second, the effect of dead time on the error performance of SPAD-based OWC systems were deeply analysed. Finally, the effect of dead time on the information transfer rate of SPADs were studied through an information theoretic approach.

6.1 Summary

In Chapter 2, a short overview of the OWC was given, with a focus on the photodetection process, the main task of optical PDs. The common PDs used in OWC systems were reviewed. In particular, positive-intrinsic-negative (PIN) diodes and avalanche photodiodes (APDs) were referred to. The details of their physical mechanism of operation, noise properties and performance specifications in terms of gain, bandwidth and signal-to-noise ratio (SNR) were reported from the literature. It was discussed that in photon starving applications and long distance transmissions, where the optical signal may be received at levels below the sensitivity of PIN diodes and APDs, photodetectors with single-photon sensitivity, such as photomultiplier tubes (PMTs) are required. The advantages and disadvantages of PMTs were addressed. Then, the SPAD PDs were brought into discussion as a promising replacement for the PMTs in OWC applications. A short overview of the past and present applications of the SPADs was provided. Also, the operating principle and the main performance metrics of the SPAD receivers were reviewed. Active and passive quenching circuits, used for resetting the

SPAD PDs, were introduced. It was highlighted that these quenching circuits directly affect the photon counting performance of the SPAD receivers due to the dead time they introduce for the recovery process. The background presented in this chapter was required for a better understanding of the fundamental differences between the conventional PDs and the SPADs and conducting the research in this thesis.

In Chapter 3, a novel statistical model for the SPAD photon counting process in the presence of dead time was presented. The mathematical analysis was based on the concepts of arrival processes and renewal processes. Exact expressions were derived for the probability mass function (PMF), mean, variance and the count rate of the SPAD photocounts. The study was conducted for both single SPADs and SPAD arrays and expounded the effect of various dead time types imposed by AQ, PQ and mixed AQ/PQ circuits. In contrast to the commonly used Poisson distribution, the new expressions accurately took the effect of dead time into account. The proposed expressions for the mean of AQ and PQ single SPAD photocounts precisely predicted the SPAD effective count rates and were in line with the experimental data available in the literature. The mathematical models derived in Chapter 3 were the foundation of the studies in the subsequent chapters of this thesis.

In Chapter 4, the bit error performance of the SPAD-based OWC systems was analysed. In these systems, not only the primary counting losses arising from dead time were degrading the link performance, but also an inter-slot interference (ISI) distortion was realized. This ISI was due to the overlap of dead times of the previous interval(s). In this study, two scenarios were considered: OWC systems with single AQ or PQ SPAD receivers, and OWC systems with AQ SPAD array receivers. A data rate of 1 Mbits/s with binary modulation schemes (on-off keying (OOK) and binary pulse position modulation (BPPM)) was considered.

In the first scenario, a theoretical study was undertaken for deriving the error probability of OOK and BPPM schemes. Dead time ratios of $\delta = 0.001$, 0.01, and 0.1 were considered for which the ISI effect was insignificant. Assuming independent count statistics over different bit intervals, the photocount distributions derived in Chapter 3 were used for the bit error performance analysis. Analytical and simulation results were provided for several dead time ratios and background noise levels. It was verified that the dead time degrades the bit error performance of the system. While with $\delta \leq 0.01$, bit error ratios (BERs) of less than 10^{-3} could be attained, $\delta = 0.1$ critically degraded the BER, such that the systems with PQ single SPADs could not reach BER values better than 10^{-2}, unless in quantum-limited conditions. In

the AQ SPAD-based OWC system, with OOK modulation and constant average background noise of $\overline{K_{\mathrm{n}}} = 2$, for a BER value of 10^{-4}, the reduction of dead time by one order of magnitude led to almost 3 dB improvement in the average signal count. The improvement was about 3.8 dB for BPPM. In general, with longer dead times, higher signal intensities were required for achieving a target BER. It was also found that in quantum-limited OWC systems, the effect of dead time becomes negligible. The results showed that OWC systems with AQ single SPADs generally outperform those with PQ single SPADs in terms of error probability. Compared with the proposed photocount distributions, the Gaussian and Poisson distributions commonly used in the literature were shown to be inaccurate in the performance analysis of OWC systems. This in turn highlights the importance of this statistical modelling for a precise error analysis of potential OWC applications.

In the second scenario, the focus was on AQ SPAD arrays and the bit error performance of an OOK system was analysed. For two dead time ratios of $\delta = 0.1$ and 1 and two different array sizes ($N_{\mathrm{array}} = 64$ and 1024), the impact of ISI on the BER of the system was investigated. The results showed that for $\delta = 0.1$, the impact of ISI was negligible in both arrays. However, for $\delta = 1$, the ISI was noticeable in the smaller array. The ISI-modified Gaussian photocount distributions were obtained through Monte Carlo simulations and then were applied for the performance analysis. The performance results demonstrated that the SPAD array was more robust to the background noise and could tolerate longer dead times maintaining the system performance. Compared with a single SPAD of the same sensitive area, the SPAD array required less signal power to achieve a target BER. For instance, a SPAD array of size $N_{\mathrm{array}} = 1024$ provided a power gain of 3 dB compared to a single SPAD, for achieving BER$= 10^{-3}$ with $\delta = 0.1$ and $K_{\mathrm{n}}^{\mathrm{a}} = 2$.

A follow-up study was presented in Chapter 5 to investigate the impact of dead time on the information rate of the SPAD receiver. The SPAD was modelled as a communication channel with a finite memory arising from the dead time-induced ISI distortions. Since the capacity analysis of the memory channels with general input distributions was mathematically intractable, two special cases of binary and pulse amplitude modulation (PAM) signalling were considered. Even for these simplified cases, calculating the capacity of the SPAD channel was still cumbersome and hence, lower and upper bounds on the capacity were developed instead. To establish each bound, an auxiliary channel model was proposed and used. For the upper bound, the auxiliary channel was an ISI-less discrete memoryless channel (DMC) with the

primary dead time-induced counting losses. For this channel, the photocount distributions of Chapter 3 were adopted. For the lower bound, the auxiliary channel was a DMC with the primary counting losses and an additional source of counting losses due to the ISI. For the photocount distribution of this channel, the stationary state distribution of the SPAD channel with ISI was used, which was obtained through Monte Carlo simulations.

The capacity analysis of the binary signalling was conducted for AQ single SPADs. The mathematical expressions for the mutual information of the auxiliary channels were derived and the bounds on the capacity of the SPAD channel were obtained. For single SPADs with dead time ratios $\delta \leq 0.1$, the bounds were very tight for a wide range of signal and background noise levels, showing that the ISI effect was negligible for $\delta \leq 0.1$. Therefore, the capacity of the AQ single SPAD could be tightly approximated by those of the auxiliary channels. It was concluded that with lower signal levels, the capacity becomes more sensitive to the dead time losses. Also, keeping the average background noise count below an optimum value will help to overcome the limiting effect of dead time on the capacity.

The capacity analysis of the PAM signalling was carried out for AQ SPAD arrays. The same auxiliary channels were used. In this case, a discrete-time Gaussian channel model with input-dependent mean and variance was adopted for the auxiliary channels. Using a numerical algorithm, the capacity of the auxiliary channels, subject to average and peak power constraints was evaluated, and hence, the bounds on the capacity of the SPAD array were established. The numerical results were provided for $\delta = 0.1, 1$ and $N_{\text{array}} = 64, 1024$. For $N_{\text{array}} = 1024$, the bounds were very tight for both $\delta = 0.1$ and $\delta = 1$ over a wide range of signal and background noise levels. This, again confirmed that in larger arrays the ISI was insignificant. Thus, the SPAD array of $N_{\text{array}} = 1024$ could be well approximated as a memoryless channel. As such, it was found that for a large array, the channel capacity, subject to the average and peak power constraints, is achievable. The capacity-achieving distribution is discrete, consists of a finite set of mass points, and always contains a mass point at zero.

The results of this analysis can be used for the theoretical optimization of the device structure and operating conditions to maximize the achievable data rate.

6.2 Key Findings

This thesis has provided new insights into the application of SPAD detectors for OWC. It reveals a fundamental limit of the SPAD detectors which is dead time. The new findings of this research lead to a better comprehension of the dead time effects.

The proposed mathematical models for the SPAD photon counting process under the limits of dead time, allow an accurate description of SPAD blocking losses. These models are particularly required for maximum likelihood detection analysis and assessing the performance of any SPAD-based OWC system in terms of error probability or data rate. The capacity and capacity-achieving distributions of SPADs can be used for designing efficient modulation schemes, and optimizing the device structure and operating conditions to maximize the achievable data rate. These results can also serve as a benchmark for evaluating the efficiency of practical SPAD-based optical systems.

The research presented in this thesis highlights a trade-off between the SPAD photon counting performance and the data rates of OWC systems; in high data rates the existence of dead time causes significant counting losses and thus, significant data loss. Commercially available SPAD devices have dead times in the range of a few nanoseconds to tens of nanoseconds. With binary modulation schemes and an AQ single SPAD of dead time τ, the data rate can not exceed $1/\tau$. For a PQ single SPAD, the limit is even lower than $1/\tau$. As a numerical example, assume an AQ single SPAD with a dead time of 10 ns. For a data rate of 100 Mbits/s, the bit interval equals to the dead time, that is 1 bit of information per photon. However, at this data rate, the error performance is not reliable. The capacity results of Chapter 5 ensure that this AQ single SPAD can achieve a maximum data rate of 10 Mbits/s with a reliable error performance, given the best operating conditions. Instead, for an AQ SPAD array of 1024 elements, the maximum achievable data rate is 100 Mbits/s, again given the best operating conditions. It can then be concluded that the commercially available single SPAD devices can achieve a reliable performance with a maximum data rate of a few Mbits/s. This is up to a few hundreds of Mbits/s for the case of large SPAD arrays.

The data rate can be improved to some extent with the help of advanced modulation techniques; but, the inherent limitation of dead time remains. To achieve data rates in the range of Gbits/s, SPAD devices with much shorter dead times are required. SPADs are still a relatively immature technology, thus, in this current stage, they are suitable for scenarios in which the high data rate

is not a mandatory requirement. With further technological advances, they may become capable of targeting higher data rates.

6.3 Limitations and Future Work

There is much work yet to be done in this topic. A number of findings and limitations in this work inspire potential future research directions, which are important for the further development of SPAD-based OWC.

In the analysis presented in Chapter 3, the impact of dead time has been addressed. However, a number of other factors, such as afterpulsing and timing jitter have not been considered. Afterpulsing leads to false detection events. The literature on afterpulsing is extensive. The available models of afterpulsing can be combined with the analytical expressions of this thesis to obtain a more realistic model for describing the SPAD photon counting process. Several practical studies have also been devoted to investigate the timing jitter phenomenon, however, there is a lack of proper analytical models for it. Timing jitter essentially perturbs the timing resolution of the SPADs. It is generally shorter than the dead time and thus, results in less counting losses compared to the dead time. However, in high data rates, it plays a significant role. Future research can consider the joint impact of dead time, timing jitter and afterpulsing. This will give insights into the actual photon counting performance of SPAD receivers in practice.

In Chapter 3, an idealised assumption had to be made so that the analysis can be tractable. It was assumed that the SPAD is free at the beginning of each counting interval. Despite this simplifying assumption, the mathematical derivations were still cumbersome. This assumption relates to the ISI impairments when the SPAD is counting in consecutive intervals. In Chapters 4 and 5, it is was observed that for relatively short dead times, this assumption had no noticeable effect on the results. However, for larger dead times, it led to underestimated error probabilities and also overestimated channel capacities. For such cases, the ISI-modified photocount distribution of the SPAD receiver was obtained through Monte Carlo simulations. The statistical modelling of this ISI effect can be the subject of future research.

Moreover, in Chapter 4, only the bit error performance of binary signalling schemes were studied. The investigation of higher order modulation schemes is also of great importance. In such schemes, the ISI effect becomes even more significant. This again necessitates modifying

the SPAD photocount distributions in consideration of ISI. As such, the capacity of SPAD receivers can be estimated with higher accuracies using the mathematical tools available for finite-state channels (FSCs). Then, optimized modulation schemes can be designed to improve the link performance and to achieve higher data rates.

Another possible direction for future research is to consider sequence detection schemes to account for the dead time induced channel memory. Designing maximum-likelihood sequence detection (MLSD) schemes will help to improve the total error performance of the system. Furthermore, the performance analyses conducted in Chapter 4 were only focused on the receiver photon counting performance. The characteristics of the transmitter and the optical channel were not addressed. For specific applications such free space optics (FSO), visible light communication (VLC) or under water communication (UWC), the corresponding light propagation characteristics can be incorporated with the receiver model developed in this thesis to perform a comprehensive performance evaluation of the end-to-end SPAD-based system.

Here, at the University of Edinburgh, efforts are underway to improve the structure of the SPAD devices in order to decrease the dead time duration, and also to implement SPAD arrays for mitigating the effect of dead time. Our research group is mainly focusing on the area of OWC and our interest lies in utilizing SPAD receivers in this area. Experimental works are in progress to validate the proposed analytical models in this current thesis. Further measurements will be carried out to characterize the ISI impairments so as to design proper modulation and coding techniques to attain the maximum potential of the SPAD receivers in OWC applications.

Appendix A
Mathematical Derivations

A.1 Integral in (3.27a)

The integral in (3.27a) is calculated as follows:

$$\begin{aligned} p_1(k) &= \int\limits_{\{\mathcal{R}_1\}} p^{(k)}(t_1, t_2, \cdots, t_k) dt_1 dt_2 \cdots dt_k \\ &= \int\limits_{t_k=(k-1)\tau}^{T_\mathrm{b}-\tau} \cdots \int\limits_{t_2=\tau}^{t_3-\tau} \int\limits_{t_1=0}^{t_2-\tau} \lambda^k e^{-\lambda(T_\mathrm{b}-k\tau)} dt_1 dt_2 \cdots dt_k \\ &= \lambda^k e^{-\lambda(T_\mathrm{b}-k\tau)} \int\limits_{t_k=(k-1)\tau}^{T_\mathrm{b}-\tau} \cdots \int\limits_{t_2=\tau}^{t_3-\tau} \int\limits_{t_1=0}^{t_2-\tau} dt_1 dt_2 \cdots dt_k \\ &= \lambda^k e^{-\lambda(T_\mathrm{b}-k\tau)} \int\limits_{t_k=(k-1)\tau}^{T_\mathrm{b}-\tau} I_{k-1}(t_k) dt_k, \end{aligned} \tag{A.1}$$

where $I_{k-1}(t_k)$ is a $(k-1)$-tuple integral and is readily solved by recursion:

$$I_{k-1}(t_k) = \frac{(t_k - (k-1)\tau)^{k-1}}{(k-1)!}\,. \tag{A.2}$$

Using (A.2), $p_1(k)$ is obtained:

$$p_1(k) = \frac{\lambda^k (T_\mathrm{b} - k\tau)^k}{k!} e^{-\lambda(T_\mathrm{b}-k\tau)}. \tag{A.3}$$

A.2 Integral in (3.27b)

The integral in (3.27b) is evaluated as detailed below:

$$\begin{aligned} p_2(k) &= \int\limits_{\{\mathcal{R}_2\}} p^{(k)}(t_1, t_2, \ldots, t_{k-1}, t_k) dt_1 \cdots dt_k \\ &= \int\limits_{t_k=T_\mathrm{b}-\tau}^{T_\mathrm{b}} \int\limits_{t_{k-1}=(k-2)\tau}^{t_k-\tau} \cdots \int\limits_{t_2=\tau}^{t_3-\tau} \int\limits_{t_1=0}^{t_2-\tau} \lambda^k e^{-\lambda(t_k-(k-1)\tau)} dt_1 \cdots dt_k \\ &= \lambda^k e^{\lambda(k-1)\tau} \int\limits_{t_k=T_\mathrm{b}-\tau}^{T_\mathrm{b}} e^{-\lambda t_k} I_{k-1}(t_k) dt_k, \end{aligned} \tag{A.4}$$

where $I_{k-1}(t_k)$ is given in (A.2). Now, let's proceed with the final integral left to obtain $p_2(k)$. Define:

$$S_{m-1} = \int\limits_{T_\mathrm{b}-\tau}^{T_\mathrm{b}} \frac{(x-(k-1)\tau)^{m-1}}{(m-1)!} e^{-\lambda x} dx. \tag{A.5}$$

An integration by parts gives:

$$\begin{aligned} S_{m-1} = &-\frac{1}{\lambda} \times \frac{(T_\mathrm{b}-(k-1)\tau)^{m-1}}{(m-1)!} e^{-\lambda T_\mathrm{b}} \\ &+\frac{1}{\lambda} \times \frac{(T_\mathrm{b}-k\tau)^{m-1}}{(m-1)!} e^{-\lambda(T_\mathrm{b}-\tau)} \\ &+\frac{1}{\lambda} \times \int\limits_{T_\mathrm{b}-\tau}^{T_\mathrm{b}} \frac{(x-(k-1)\tau)^{m-2}}{(m-2)!} e^{-\lambda x} dx. \end{aligned} \tag{A.6}$$

Now define:

$$A_m = \frac{(T_\mathrm{b}-(k-1)\tau)^m}{m!} e^{-\lambda T_\mathrm{b}} - \frac{(T_\mathrm{b}-k\tau)^m}{m!} e^{-\lambda(T_\mathrm{b}-\tau)}, \tag{A.7}$$

Thus, S_{m-1} given in (A.6) can be expressed as:

$$S_{m-1} = -\frac{1}{\lambda} A_{m-1} + \frac{1}{\lambda} S_{m-2}, \tag{A.8}$$

Solving the above recursive equation for S_{m-1} gives:

$$\begin{aligned}
S_{m-1} =& -\sum_{i=1}^{m-1} \frac{A_j}{\lambda^{m-i}} + \frac{S_0}{\lambda^{m-1}} \\
=& -\sum_{i=1}^{m-1} \frac{1}{\lambda^{m-i}} \times \frac{(T_\mathrm{b}-(k-1)\tau)^i}{i!} e^{-\lambda T_\mathrm{b}} + \sum_{i=1}^{m-1} \frac{1}{\lambda^{m-i}} \times \frac{(T_\mathrm{b}-k\tau)^i}{i!} e^{-\lambda(T_\mathrm{b}-\tau)} \\
& - \frac{1}{\lambda^m}(e^{-\lambda T_\mathrm{b}} - e^{-\lambda(T_\mathrm{b}-\tau)}) \\
=& -\frac{1}{\lambda^m} \times \sum_{i=0}^{m-1} \frac{\lambda^i (T_\mathrm{b}-(k-1)\tau)^i}{m!} e^{-\lambda T_\mathrm{b}} + \frac{1}{\lambda^m} \times \sum_{i=0}^{m-1} \frac{\lambda^i (T_\mathrm{b}-k\tau)^i}{m!} e^{-\lambda(T_\mathrm{b}-\tau)}
\end{aligned} \tag{A.9}$$

Finally, according to (A.4):

$$\begin{aligned}
p_2(k) =& \lambda^k e^{\lambda(k-1)\tau} \times S_{k-1} \\
=& \sum_{i=0}^{k-1} \frac{\lambda^i (T_\mathrm{b}-k\tau)^i}{m!} e^{-\lambda(T_\mathrm{b}-k\tau)} - \sum_{i=0}^{k-1} \frac{\lambda^i (T_\mathrm{b}-(k-1)\tau)^i}{m!} e^{-\lambda(T_\mathrm{b}-(k-1)\tau)}
\end{aligned} \tag{A.10}$$

A.3 Solving (3.34)

From (3.34), $p(k,t)$ can be derived as follows:

$$\begin{aligned}
p(k,t) =& \int_{k\tau}^{t} \frac{\lambda^k (t'-k\tau)^{k-1}}{(k-1)!} e^{-\lambda(t'-k\tau)} dt' - \int_{(k+1)\tau}^{t} \frac{\lambda^{k+1}(t'-(k+1)\tau)^k}{k!} e^{-\lambda(t'-(k+1)\tau)} dt' \\
=& \int_{0}^{t-k\tau} \frac{\lambda^k (t')^{k-1}}{(k-1)!} e^{-\lambda t'} dt' - \int_{0}^{t-(k+1)\tau} \frac{\lambda^{k+1}(t')^k}{k!} e^{-\lambda t'} dt'
\end{aligned} \tag{A.11}$$

With an approach similar to the one used for (A.5), the above integral is evaluated. Thus:

$$p(k,t) = \sum_{i=0}^{k} \frac{\lambda^i (t-(k+1)\tau)^i}{i!} e^{-\lambda(t-(k+1)\tau)} - \sum_{i=0}^{k-1} \frac{\lambda^i (t-k\tau)^i}{i!} e^{-\lambda(t-k\tau)} \tag{A.12}$$

Appendix B
An Asymptotic Expression for AQ PMF

The PMF in (3.36) can be rewritten as:

$$\begin{aligned} p_K(k) &= \sum_{i=0}^{k} \psi(i,\lambda_k) - \sum_{i=0}^{k-1} \psi(i,\lambda_{k-1}) \\ &= \psi(k,\lambda_k) + \sum_{i=0}^{k-1} \left[\psi(i,\lambda_k) - \psi(i,\lambda_{k-1})\right] \\ &= \psi(k,\lambda_k) + \sum_{i=0}^{k-1} \psi(i,\lambda_k) \left[1 - \left(\frac{T_\mathrm{b} - (k-1)\tau}{T_\mathrm{b} - k\tau}\right)^i e^{-\lambda\tau}\right] . \end{aligned} \tag{B.1}$$

Define A and B as follows:

$$A = \sum_{i=0}^{k-1} \psi(i,\lambda_k) \underbrace{\left[1 - \left(\frac{T_\mathrm{b} - (k-1)\tau}{T_\mathrm{b} - k\tau}\right)^i e^{-\lambda\tau}\right]}_{B} .$$

Two asymptotic cases can be considered:

- Large λ ($\lambda \gg 1$): The limiting relation $\lim_{t\to\infty} t^\alpha e^{-t} = 0$ results in $\lim_{\lambda\to\infty} A = 0$.
- Small δ ($\tau \ll T_\mathrm{b}$): Since $\lim_{\delta\to 0} B = 0$ and $\psi(k,\lambda_k)$ is finite, $\lim_{\delta\to 0} A = 0$ is concluded.

Therefore, for the above two cases, the following approximation can be adopted:

$$p_K(k) \approx \psi(k,\lambda_k) . \tag{B.2}$$

Appendix C
Mean and Variance of AQ PMF

By definition, the mean value of the distribution in (3.36) is:

$$\begin{aligned}\mu_K &= \sum_{k=0}^{k_{\max}} k p_K(k) \\ &= \sum_{k=0}^{k_{\max}} k \times \left\{ \sum_{i=0}^{k} \psi(i,\lambda_k) - \sum_{i=0}^{k-1} \psi(i,\lambda_{k-1}) \right\}. \end{aligned} \tag{C.1}$$

Replacing $k-1$ by k in the summation index of the second term in the right-hand side of the previous expression gives:

$$\begin{aligned}\mu_K &= \sum_{k=0}^{k_{\max}} \sum_{i=0}^{k} k\psi(i,\lambda_k) - \sum_{k=0}^{k_{\max}-1} \sum_{i=0}^{k} (k+1)\psi(i,\lambda_k) \\ &= \sum_{i=0}^{k_{\max}} k_{\max}\psi(i,\lambda_{k_{\max}}) - \sum_{k=0}^{k_{\max}-1} \sum_{i=0}^{k} \psi(i,\lambda_k) \\ &\approx k_{\max} - \sum_{k=0}^{k_{\max}-1} \sum_{i=0}^{k} \psi(i,\lambda_k). \end{aligned} \tag{C.2}$$

where the approximation $\sum_{i=0}^{k_{\max}} \psi(i,\lambda_{k_{\max}}) \approx 1$ is used. The above expression for μ_K in (C.2) can be further simplified to:

$$\mu_K = \sum_{k=0}^{k_{\max}-1} \sum_{i=k+1}^{\infty} \psi(i,\lambda_k), \tag{C.3}$$

Next, the limit of this expression for $\tau \to 0$ or $k_{\max} \to \infty$ is taken. Although it follows directly from $\lim_{\tau\to 0} p_K(k) = p_0(k)$ that $\lim_{\tau\to 0} \mu_K = \lambda T_{\mathrm{b}}$, a direct proof can also be obtained in the following way; the right-hand side of (C.3) is a double series whose terms can be ordered

in an infinite matrix:

$$e^{-\lambda T_\mathrm{b}} \times \begin{bmatrix} 0 & \frac{(\lambda T_\mathrm{b})^1}{1!} & \frac{(\lambda T_\mathrm{b})^2}{2!} & \dots & \frac{(\lambda T_\mathrm{b})^m}{m!} & \dots \\ 0 & 0 & \frac{(\lambda T_\mathrm{b})^2}{2!} & \dots & \frac{(\lambda T_\mathrm{b})^m}{m!} & \dots \\ 0 & 0 & 0 & \dots & \frac{(\lambda T_\mathrm{b})^m}{m!} & \dots \\ \vdots & \vdots & \vdots & \ddots & \vdots & \\ 0 & 0 & 0 & \dots & \frac{(\lambda T_\mathrm{b})^m}{m!} & \dots \\ \vdots & \vdots & \vdots & & \vdots & \ddots \end{bmatrix}$$

The rows and columns of the above matrix are indexed by summation indices of (C.3), k and i, respectively. Summation of the first m rows of this matrix gives:

$$\begin{aligned} S_m &= e^{-\lambda T_\mathrm{b}} \times \left[\sum_{i=0}^{m} i \times \frac{(\lambda T_\mathrm{b})^i}{i!} + m \times \sum_{i=m+1}^{\infty} \frac{(\lambda T_\mathrm{b})^i}{i!} \right] \\ &= e^{-\lambda T_\mathrm{b}} \times \left[(\lambda T_\mathrm{b}) \times \sum_{i=0}^{m-1} \frac{(\lambda T_\mathrm{b})^i}{i!} + m \times \sum_{i=0}^{\infty} \frac{(\lambda T_\mathrm{b})^i}{i!} - m \times \sum_{i=0}^{m} \frac{(\lambda T_\mathrm{b})^i}{i!} \right]. \end{aligned} \tag{C.4}$$

As m goes to infinity, the summation of the second and third terms clearly goes to zero. Furthermore, using the Taylor series expression $\lim\limits_{m\to\infty} \sum\limits_{i=0}^{m-1} (\lambda T_\mathrm{b})^i/i! = e^{\lambda T_\mathrm{b}}$:

$$\lim_{\tau\to 0} \mu_K = \lim_{m\to\infty} S_m = \lambda T_\mathrm{b}. \tag{C.5}$$

With an approach similar to the one used for deriving μ_K, the variance of the distribution in (3.36) can be obtained as:

$$\sigma_K^2 = \sum_{k=0}^{k_\mathrm{max}-1} \sum_{i=0}^{k} (2k_\mathrm{max} - 2k - 1)\psi(i, \lambda_k) - \left(\sum_{k=0}^{k_\mathrm{max}-1} \sum_{i=0}^{k} \psi(i, \lambda_k) \right)^2. \tag{C.6}$$

The limiting relation $\lim\limits_{\tau\to 0} \sigma_K^2 = \lambda T_\mathrm{b}$ can also be verified, where the product λT_b is the variance of the original Poisson distribution.

Appendix D
Mean and Variance of PQ PMF

According to (3.9) and (3.50), the generating function $G(z,t)$ and its derivatives are given by:

$$\begin{aligned} G(z,T_\mathrm{b}) &= \sum_{k=0}^{k_\mathrm{max}} p_K(k) z^k \\ &= \sum_{i=0}^{k_\mathrm{max}} (z-1)^i \frac{\lambda^i (T_\mathrm{b}-(i-1)\tau)^i}{i!} e^{-i\lambda\tau}, \end{aligned} \tag{D.1}$$

$$\begin{aligned} \frac{\partial G(z,T_\mathrm{b})}{\partial z} &= \sum_{k=0}^{k_\mathrm{max}} k p_K(k) z^{k-1} \\ &= \sum_{i=1}^{k_\mathrm{max}} i(z-1)^{i-1} \frac{\lambda^i (T_\mathrm{b}-(i-1)\tau)^i}{i!} e^{-i\lambda\tau}, \end{aligned} \tag{D.2}$$

$$\begin{aligned} \frac{\partial^2 G(z,T_\mathrm{b})}{\partial z^2} &= \sum_{k=0}^{k_\mathrm{max}} k(k-1) p_K(k) z^{k-2} \\ &= \sum_{i=2}^{k_\mathrm{max}} i(i-1)(z-1)^{i-2} \frac{\lambda^i (T_\mathrm{b}-(i-1)\tau)^i}{i!} e^{-i\lambda\tau}. \end{aligned} \tag{D.3}$$

Therefore, the mean and variance of the PQ PMF in (3.50) are derived as:

$$\mu_K = \sum_{k=0}^{k_\mathrm{max}} k p_K(k) = \left. \frac{\partial G(z,T_\mathrm{b})}{\partial z} \right|_{z=1} = \lambda e^{-\lambda\tau} T_\mathrm{b}. \tag{D.4a}$$

$$\begin{aligned} \sigma_K^2 &= \sum_{k=0}^{k_\mathrm{max}} k^2 p_K(k) - \left(\sum_{k=0}^{k_\mathrm{max}} k p_K(k) \right)^2 \\ &= \left. \left[\frac{\partial^2 G(z,T_\mathrm{b})}{\partial z^2} + \frac{\partial G(z,T_\mathrm{b})}{\partial z} - \left(\frac{\partial G(z,T_\mathrm{b})}{\partial z} \right)^2 \right] \right|_{z=1} \\ &= \lambda^2 e^{-2\lambda\tau} (\tau^2 - 2T_\mathrm{b}\tau) + \lambda e^{-\lambda\tau} T_\mathrm{b}. \end{aligned} \tag{D.4b}$$

Finally, the limiting expressions $\lim_{\tau\to 0} \mu_K = \lambda T_\mathrm{b}$ and $\lim_{\tau\to 0} \sigma_K^2 = \lambda T_\mathrm{b}$ are verified.

Appendix E
Special Property of AQ PMF in Threshold Detection

Assuming $k_{\rm th} < k_{\max}$, the probability of counting at most $k_{\rm th}$ photons is calculated as:

$$\begin{aligned}
\sum_{k=0}^{k_{\rm th}} p_K(k) &= \sum_{k=0}^{k_{\rm th}} \left[\sum_{i=0}^{k} \psi(i,\lambda_k) - \sum_{i=0}^{k-1} \psi(i,\lambda_{k-1}) \right] \\
&\overset{(*)}{=} \sum_{i=0}^{k_{\rm th}} \sum_{k=i}^{k_{\rm th}} \psi(i,\lambda_k) - \sum_{i=0}^{k_{\rm th}-1} \sum_{k=i+1}^{k_{\rm th}} \psi(i,\lambda_{k-1}) \\
&\overset{(**)}{=} \psi(k_{\rm th},\lambda_{k_{\rm th}}) + \sum_{i=0}^{k_{\rm th}-1} \left[\sum_{k=i}^{k_{\rm th}} \psi(i,\lambda_k) - \sum_{k'=i}^{k_{\rm th}-1} \psi(i,\lambda_{k'}) \right] \\
&= \psi(k_{\rm th},\lambda_{k_{\rm th}}) + \sum_{i=0}^{k_{\rm th}-1} \psi(i,\lambda_{k_{\rm th}}) \\
&= \sum_{i=0}^{k_{\rm th}} \psi(i,\lambda_{k_{\rm th}}),
\end{aligned} \tag{E.1}$$

where in $(*)$ the order of summations is changed and for $(**)$ a change of variable $k' = k-1$ is used. According to (E.1), for an AQ SPAD receiver with the dead time τ, the probability of counting up to $k_{\rm th}$ photons in a bit interval of length $T_{\rm b}$, is the same as that of:

- an ideal single-photon detector with the same quantum efficiency, but counting photons during an interval of length $T_{\rm b} - k_{\rm th}\tau$.
- an ideal single-photon detector with the quantum efficiency reduced by the factor $(1 - \frac{k_{\rm th}\tau}{T_{\rm b}})$ and counting photons during an interval of length $T_{\rm b}$.

The above result significantly simplifies the error probability calculations for the AQ SPADs.

Appendix F
Optimum Threshold for AQ Single SPAD

With the approximate PMF given in (B.2), the likelihood ratio test in (4.5) reduces to:

$$L(k) = \frac{\psi(k, \lambda_k^{\mathrm{sn}})}{\psi(k, \lambda_k^{\mathrm{n}})} \underset{H_0}{\overset{H_1}{\gtrless}} 1, \tag{F.1}$$

where $\lambda_k^{\mathrm{n}} = \lambda_{\mathrm{n}}(T_{\mathrm{b}} - k\tau)$ and $\lambda_k^{\mathrm{sn}} = (\lambda_{\mathrm{s}} + \lambda_{\mathrm{n}})(T_{\mathrm{b}} - k\tau)$. Substituting $\psi(i, \lambda) = \lambda^i e^{-\lambda}/i!$ gives:

$$L(k) = e^{-\lambda_{\mathrm{s}}(T_{\mathrm{b}} - k\tau)} \left(\frac{\lambda_{\mathrm{s}} + \lambda_{\mathrm{n}}}{\lambda_{\mathrm{n}}} \right)^k \underset{H_0}{\overset{H_1}{\gtrless}} 1. \tag{F.2}$$

Taking the natural logarithm from both sides gives:

$$k \underset{H_0}{\overset{H_1}{\gtrless}} \frac{\lambda_{\mathrm{s}} T_{\mathrm{b}}}{\lambda_{\mathrm{s}}\tau + \ln\left(1 + \dfrac{\lambda_{\mathrm{s}}}{\lambda_{\mathrm{n}}}\right)}. \tag{F.3}$$

Therefore, for an AQ SPAD, the maximum likelihood detection simplifies to a threshold detection for short dead times or in low photon rate regimes.

The optimum threshold in (F.3) can also be derived through minimizing the probability of error given in (4.7) through solving $dP_{\mathrm{e}}/dk_{\mathrm{th}} = 0$. For an AQ SPAD, it is shown that (see Appendix E):

$$\sum_{k=0}^{k_{\mathrm{th}}} p_K(k) = \sum_{i=0}^{k_{\mathrm{th}}} \psi(i, \lambda_{k_{\mathrm{th}}}).$$

Therefore, (4.7) can be rewritten as:

$$P_{\mathrm{e}} = \frac{1}{2}\left(1 - \sum_{i=0}^{k_{\mathrm{th}}} \psi(i, \lambda_{k_{\mathrm{th}}}^{\mathrm{n}})\right) + \frac{1}{2}\sum_{i=0}^{k_{\mathrm{th}}} \psi(i, \lambda_{k_{\mathrm{th}}}^{\mathrm{sn}}). \tag{F.4}$$

The rule of differentiating summations is given by [1]:

$$\frac{d}{dx}\left[\sum_{k=0}^{x} f\left(k\right)\right] = f\left(x\right). \tag{F.5}$$

Using (F.5), the equation $dP_{\mathrm{e}}/dk_{\mathrm{th}} = 0$ can be solved for finding the optimum threshold value. For the asymptotic cases of $\lambda_{\mathrm{n}} \gg 1$ or $\tau \ll T_{\mathrm{b}}$, $dP_{\mathrm{e}}/dk_{\mathrm{th}} = 0$ leads to:

$$\psi(k_{\mathrm{th}}, \lambda_{k_{\mathrm{th}}}^{\mathrm{n}}) = \psi(k_{\mathrm{th}}, \lambda_{k_{\mathrm{th}}}^{\mathrm{sn}}). \tag{F.6}$$

Substituting $\psi(i, \lambda) = \lambda^i e^{-\lambda}/i!$ gives:

$$\left(\frac{\lambda_{\mathrm{n}}}{\lambda_{\mathrm{s}} + \lambda_{\mathrm{n}}}\right)^{k_{\mathrm{th}}} = e^{-\lambda_{\mathrm{s}}(T_{\mathrm{b}} - k_{\mathrm{th}}\tau)}\ .$$

Taking the natural logarithm of both sides results in:

$$k_{\mathrm{th}} \ln\left(\frac{\lambda_{\mathrm{n}}}{\lambda_{\mathrm{s}} + \lambda_{\mathrm{n}}}\right) = -\lambda_{\mathrm{s}} T_{\mathrm{b}} + k_{\mathrm{th}} \lambda_{\mathrm{s}} \tau.$$

Therefore, the threshold value, k_{th}, which minimizes P_{e} of an AQ SPAD, occurs at:

$$k_{\mathrm{th}} = \frac{\lambda_{\mathrm{s}} T_{\mathrm{b}}}{\lambda_{\mathrm{s}}\tau + \ln\left(1 + \dfrac{\lambda_{\mathrm{s}}}{\lambda_{\mathrm{n}}}\right)}. \tag{F.7}$$

Appendix G
Optimum Threshold for SPAD Array

According to (4.13), the likelihood ratio is defined as:

$$L(s) = \frac{p_{\mathrm{sn}}(s)}{p_{\mathrm{n}}(s)} \underset{H_0}{\overset{H_1}{\gtrless}} 1,$$

where $p_{\mathrm{sn}}(s) \sim \mathcal{N}(\mu_{\mathrm{sn}}, \sigma^2_{\mathrm{sn}})$ and $p_{\mathrm{n}}(s) \sim \mathcal{N}(\mu_{\mathrm{n}}, \sigma^2_{\mathrm{n}})$ are the approximate probability mass functions (PMFs) for the SPAD array photocounts. Substituting the Gaussian expressions for $p_{\mathrm{sn}}(s)$ and $p_{\mathrm{n}}(s)$ in the above likelihood ratio test gives:

$$\begin{aligned} L(s) &= \frac{\frac{1}{\sqrt{2\pi\sigma^2_{\mathrm{sn}}}} \exp\left(-\frac{(s-\mu_{\mathrm{sn}})^2}{2\sigma^2_{\mathrm{sn}}}\right)}{\frac{1}{\sqrt{2\pi\sigma^2_{\mathrm{n}}}} \exp\left(-\frac{(s-\mu_{\mathrm{n}})^2}{2\sigma^2_{\mathrm{n}}}\right)} \\ &= \frac{\sigma_{\mathrm{n}}}{\sigma_{\mathrm{sn}}} \exp\left(s^2\left(\frac{1}{2\sigma^2_{\mathrm{n}}} - \frac{1}{2\sigma^2_{\mathrm{sn}}}\right) - s\left(\frac{\mu_{\mathrm{n}}}{\sigma^2_{\mathrm{n}}} - \frac{\mu_{\mathrm{sn}}}{\sigma^2_{\mathrm{sn}}}\right) + \left(\frac{\mu^2_{\mathrm{n}}}{2\sigma^2_{\mathrm{n}}} - \frac{\mu^2_{\mathrm{sn}}}{2\sigma^2_{\mathrm{sn}}}\right)\right). \end{aligned} \tag{G.1}$$

Taking the natural logarithm results in the following inequality:

$$s^2\left(\frac{1}{2\sigma^2_{\mathrm{n}}} - \frac{1}{2\sigma^2_{\mathrm{sn}}}\right) - s\left(\frac{\mu_{\mathrm{n}}}{\sigma^2_{\mathrm{n}}} - \frac{\mu_{\mathrm{sn}}}{\sigma^2_{\mathrm{sn}}}\right) + \left(\frac{\mu^2_{\mathrm{n}}}{2\sigma^2_{\mathrm{n}}} - \frac{\mu^2_{\mathrm{sn}}}{2\sigma^2_{\mathrm{sn}}}\right) \underset{H_0}{\overset{H_1}{\gtrless}} \ln\frac{\sigma_{\mathrm{sn}}}{\sigma_{\mathrm{n}}}. \tag{G.2}$$

This is a polynomial inequality of degree 2 and is easily solved as:

$$s \underset{H_0}{\overset{H_1}{\gtrless}} s_{\mathrm{th}} \tag{G.3}$$

where $s_{\mathrm{th}} \geq 0$ and is given by:

$$s_{\mathrm{th}} = \frac{\frac{\mu_{\mathrm{n}}}{\sigma^2_{\mathrm{n}}} - \frac{\mu_{\mathrm{sn}}}{\sigma^2_{\mathrm{sn}}} + \sqrt{\left(\frac{\mu_{\mathrm{n}}}{\sigma^2_{\mathrm{n}}} - \frac{\mu_{\mathrm{sn}}}{\sigma^2_{\mathrm{sn}}}\right)^2 - \left(\frac{1}{\sigma^2_{\mathrm{n}}} - \frac{1}{\sigma^2_{\mathrm{sn}}}\right)\left(\frac{\mu^2_{\mathrm{n}}}{\sigma^2_{\mathrm{n}}} - \frac{\mu^2_{\mathrm{sn}}}{\sigma^2_{\mathrm{sn}}} + 2\ln\frac{\sigma_{\mathrm{n}}}{\sigma_{\mathrm{sn}}}\right)}}{\frac{1}{\sigma^2_{\mathrm{n}}} - \frac{1}{\sigma^2_{\mathrm{sn}}}}. \tag{G.4}$$

The threshold value in (G.4) can be further approximated as:

$$s_{\mathrm{th}} = \frac{\mu_{\mathrm{sn}}\sigma_{\mathrm{n}} + \mu_{\mathrm{n}}\sigma_{\mathrm{sn}}}{\sigma_{\mathrm{n}} + \sigma_{\mathrm{sn}}} \,. \tag{G.5}$$

Appendix H
Publications

H.1 Conference Papers

E. Sarbazi and H. Haas, "Detection Statistics and Error Performance of SPAD-based Optical Receivers," in *Proc. IEEE 26th Ann. Int. Symp. Personal, Indoor, and Mobile Radio Communications*, (Hong Kong, China), pp. 830834, Sept. 2015.

E. Sarbazi, M. Safari, and H. Haas,"Photon Detection Characteristics and Error Performance of SPAD Array Optical Receivers," in *Proc. IEEE 4th Int. Workshop on Optical Wireless Communications*, (Istanbul, Turkey), pp. 132136, Sept. 2015.

E. Sarbazi, M. Safari, and H. Haas, "On the Information Transfer Rate of SPAD Receivers for Optical Wireless Communications," in *Proc. IEEE Global Communications Conf.*, (Washington, DC, USA), pp. 16, Dec. 2016.

E. Sarbazi, M. Safari, and H. Haas, "The Impact of Long Dead Time on the Photocount Distribution of SPAD Receivers," in *Proc. IEEE Global Communications Conf.*, (Abu Dhabi, UAE), pp. 16, Dec. 2018.

H.2 Journal Papers

E. Sarbazi, M. Safari, and H. Haas, "Statistical Modeling of Single-Photon Avalanche Diode Receivers for Optical Wireless Communications," *IEEE Trans. Commun.*, vol. 66, no. 9, pp. 40434058, Apr. 2018.

E. Sarbazi, M. Safari, and H. Haas, "On the Capacity and Error Performance of SPAD Array Optical Receivers," *Submitted*.

2015 IEEE 26th International Symposium on Personal, Indoor and Mobile Radio Communications - (PIMRC): Fundamentals and PHY

Detection Statistics and Error Performance of SPAD-based Optical Receivers

Elham Sarbazi and Harald Haas
Li-Fi Research and Development Centre, Institute for Digital Communications
The University of Edinburgh, Edinburgh, EH9 3JL, UK.
Email: {e.sarbazi, h.haas}@ed.ac.uk

***Abstract*—This paper presents the characterization of single photon avalanche diodes (SPADs) for optical communication applications. SPAD-based optical receivers can provide a significantly improved single-photon detection sensitivity compared with conventional photodiodes. However, an undesirable dead time introduced by the quenching circuit decreases the performance of these receivers. Using a precise analysis, we show that in the presence of dead time, the photon arrival process does not follow a Poisson process. Also, the effective count rate is evaluated and shown to depend critically on dead time. The effect of SPAD dead time on the error performance of an on-off keying (OOK) modulation optical communication system is also investigated. It is shown that, when background counts due to dark current and afterpulsing are small, the performance degradation of the SPAD-based receiver due to dead time losses is negligible. However, for systems with considerable background counts, the bit error rate (BER) degrades rapidly with increasing dead time.**

***Keywords*—Single Photon Avalanche Diode (SPAD), photon counting, optical receivers, on-off keying (OOK).**

I. Introduction

The state-of-the-art photodetectors, avalanche photodiodes (APDs), are susceptible to circuit gain-dependent excess noise which limits their maximum gain. However, APDs can be used in the so-called 'Geiger mode' in which the extremely high gain allows single photon events to be detected effectively and single-photon detection sensitivity can be improved. In Geiger mode, the diode is biased beyond its breakdown voltage and the absorption of a single photon will then initiate an avalanche of charge carriers, which can easily be detected. However, after each photon detection event, the APD needs to be quenched to recover from the excess charge carriers. This quenching process introduces a finite recovery time, known as the 'dead time', during which the device does not respond to another incident photon.

Geiger-mode APDs, also termed as single-photon avalanche diodes (SPADs), have been successfully employed in a number of applications, including three-dimensional imaging [1], quantum key distribution [2] and deep space laser communications [3]. Recently, SPADs have been proposed for use in optical communication applications [4], [5], and in particular, for some visible light communication (VLC) applications where long distance transmission requires highly sensitive receivers capable of detecting a single photon. For example, the potential application of SPADs can be in the gas extraction industry, or in downhole monitoring communication systems [6].

However, to the best of our knowledge, a comprehensive study of the characteristics of SPAD receivers has not yet been published. In this paper a detailed analysis of detection statistics and the main characteristics of SPAD-based optical receivers are presented. In particular, analytical modelling and simulation results are provided which predict the performance of a SPAD-based receiver.

The rest of the paper is organized as follows. The photocount statistics of a SPAD receiver are discussed in Section II, and how the actual count statistics deviate from the Poisson process in the presence of detector dead time is explained. We develop a mathematical model for the dead time modified count probability and employ Monte Carlo methods to verify the validity of the analytical models. In Section III, the major constraints which limit the achievable count rate of SPAD receivers are addressed. Available count rate models in literature are adopted and confirmed to be applicable to SPAD receivers through Monte Carlo simulations. The mathematical count probability derived in Section II is then used in Section IV to predict the error performance of an on-off keying (OOK) modulation optical system. Finally, concluding remarks are given in Section V.

II. Photocount Statistics

In the absence of SPAD dead time, the detection of photon arrival events can be modeled as a Poisson arrival process for which the probability of detecting k photons over a time period of $[0, T_{\rm b})$ is given by:

$$p_0(k; \lambda T_{\rm b}) = \frac{(\lambda T_{\rm b})^k e^{-\lambda T_{\rm b}}}{k!} , \quad (1)$$

where the constant λ is the average photon arrival rate, hence, $\lambda T_{\rm b}$ is the average number of photons arriving at the SPAD during the observation time of $T_{\rm b}$ seconds. The photocount rate λ is related to the power of the optical signal by:

$$\lambda = \frac{\eta_{QE} P_s}{h\nu} , \quad (2)$$

where η_{QE} is the quantum efficiency of the SPAD; P_s denotes the power of the incident optical signal; h is the Planck's constant; and ν represents the frequency of the optical signal.

When the SPAD dead time is considered, the actual count statistics can be very different from the photon arrival statistics and the photon counts are no longer Poisson distributed. Any incident photons which arrive after the initial photon event and before the end of the quenching process, go undetected. In this study, a SPAD detector with constant dead time is considered which cannot record counts for a time interval of fixed duration, $T_{\rm d}$, immediately following the registration of a count. It is assumed that the SPAD is ready to operate at the beginning of the counting interval of $[0, T_{\rm b})$. Therefore, the maximum observable count during this period is $k_{\max} = \lfloor \delta \rfloor + 1$, where $\delta = T_{\rm b}/T_{\rm d}$ and $\lfloor x \rfloor$ denotes the largest integer that is smaller than x. The probability of k photons being detected during the time interval of $[0, T_{\rm b})$ where $k \leq k_{\max}$ is computed here.

978-1-4673-6782-0/15/$31.00 ©2015 IEEE

2015 IEEE 26th International Symposium on Personal, Indoor and Mobile Radio Communications - (PIMRC): Fundamentals and PHY

Assume that $k < k_{\max}$. Let the time of arrival of photons be denoted by $t_1, t_2, ..., t_k$ where $0 \le t_1 \le t_2 \le ... \le t_k < T_\mathrm{b}$. The sample function density on the interval $[0, T_\mathrm{b})$ for this counting process is $p(t_1, t_2, ..., t_k, K = k; \lambda, T_\mathrm{b}, T_\mathrm{d})$, which can be treated as an ideal counting process affected by dead time. Hereinafter, for simplicity of notations, the sample function density is denoted by $p(t_1, t_2, ..., t_k, K = k)$ which can be calculated as [7]:

$$\begin{aligned} p(K=0) &= e^{-\lambda T_\mathrm{b}} \\ p(t_1, K=1) &= \lambda e^{-\lambda(T_\mathrm{b}-T_\mathrm{d})} \\ &\vdots \\ p(t_1, t_2, ..., t_{k-1}, K=k-1) &= \lambda^{k-1} e^{-\lambda(T_\mathrm{b}-(k-1)T_\mathrm{d})}. \end{aligned} \tag{3}$$

where $t_i + T_\mathrm{d} \le t_{i+1}$ for $i = 1, 2, ..., k-1$. The kth arrival time, t_k, may or may not fall within the last T_d seconds of the counting time T_b. Therefore, depending on t_k:

$$p(t_1, t_2, ..., t_k, K=k) = \begin{cases} \lambda^k e^{-\lambda(T_\mathrm{b}-kT_\mathrm{d})}, & t_k < T_\mathrm{b} - T_\mathrm{d} \\ \lambda^k e^{-\lambda(t_k-(k-1)T_\mathrm{d})}, & t_k > T_\mathrm{b} - T_\mathrm{d}. \end{cases} \tag{4}$$

In order to obtain the probability of receiving k photons over the period $[0, T_\mathrm{b})$, the probability density in (4) needs to be integrated over the region spanned by t_1, t_2, ..., t_k. Region $\{R\}$ is defined as the set of all possible values for arrival times t_1, t_2,..., t_k, and it can be divided into two subsets $\{R_1\}$ and $\{R_2\}$ such that, $\{R\} = \{R_1\} \cup \{R_2\}$, where $\{R_1\}$ consists of all possible k-tuples which hold the first case of (4), meaning that the detection of all k photons are entirely contained in $[0, T_\mathrm{b})$, while k-tuples of $\{R_2\}$ hold the second case of (4) and the dead time of the SPAD after detecting the last (kth) photon extends out of $[0, T_\mathrm{b})$. Therefore, the probability of detecting k photons in the interval $[0, T_\mathrm{b})$ is given by:

$$p_K(k) = p_1(k) + p_2(k) \,, \tag{5}$$

where,

$$\begin{aligned} p_1(k) &= \int\limits_{\{R_1\}} p(t_1, ..., t_k, K=k) dt_k ... dt_1 \\ p_2(k) &= \int\limits_{\{R_2\}} p(t_1, ..., t_k, K=k) dt_1 ... dt_k \end{aligned} \tag{6}$$

The photon arrival times $t_1, t_2, ..., t_k$ belonging to subset $\{R_1\}$ must satisfy the following inequalities,

$$\begin{aligned} 0 \le\ & t_1 \ \le T_\mathrm{b} - kT_\mathrm{d} \\ t_1 + T_\mathrm{d} \le\ & t_2 \ \le T_\mathrm{b} - (k-1)T_\mathrm{d} \\ &\vdots \\ t_{k-1} + T_\mathrm{d} \le\ & t_k \ \le T_\mathrm{b} - T_\mathrm{d} \,. \end{aligned}$$

The first integral in (6) can be calculated as:

$$p_1(k) = \frac{(\lambda(T_\mathrm{b} - kT_\mathrm{d}))^k}{k!} e^{-\lambda(T_\mathrm{b}-kT_\mathrm{d})} \,. \tag{7}$$

For the subset $\{R_2\}$, the detecting times t_1, t_2, ..., t_k of photons must satisfy the following inequalities:

$$\begin{aligned} T_\mathrm{b} - T_\mathrm{d} \le\ & t_k \ \le T_\mathrm{b} \\ (k-2)T_\mathrm{d} \le\ & t_{k-1} \le t_k - T_\mathrm{d} \\ &\vdots \\ 0 \le\ & t_1 \ \le t_2 - T_\mathrm{d} \,. \end{aligned}$$

and,

$$\begin{aligned} p_2(k) = &\sum_{i=0}^{k-1} \frac{\lambda^i (T_\mathrm{b} - kT_\mathrm{d})^i}{i!} e^{-\lambda(T_\mathrm{b}-kT_\mathrm{d})} \\ &- \sum_{i=0}^{k-1} \frac{\lambda^i (T_\mathrm{b} - (k-1)\,T_\mathrm{d})^i}{i!} e^{-\lambda(T_\mathrm{b}-(k-1)T_\mathrm{d})} \,. \end{aligned} \tag{8}$$

Therefore:

$$\begin{aligned} p_K(k) = &\sum_{i=0}^{k} \psi\left(i, \lambda\left(T_\mathrm{b} - kT_\mathrm{d}\right)\right) \\ &- \sum_{i=0}^{k-1} \psi\left(i, \lambda\left(T_\mathrm{b} - (k-1)\,T_\mathrm{d}\right)\right) \,, \end{aligned} \tag{9}$$

where $\psi(x, y) = y^x e^{-y}/x!$ is used for simplicity.

Consider the case where $k = k_{\max}$. In this case, the dead time of last detected photon ends outside the interval $[0, T_\mathrm{b})$, then:

$$p(t_1, t_2, ..., t_k, K=k) = \lambda^k e^{-\lambda(t_k-(k-1)T_\mathrm{d})} \,, \tag{10}$$

$$p_K(k) = \int\limits_{\{R'\}} p(t_1, ..., t_k, K=k) dt_1 ... dt_k \,, \tag{11}$$

where the domain of integration $\{R'\}$ is defined by the following inequalities:

$$\begin{aligned} (k-1)T_\mathrm{d} \le\ & t_k \ \le T_\mathrm{b} \\ (k-2)T_\mathrm{d} \le\ & t_{k-1} \le t_k - T_\mathrm{d} \\ &\vdots \\ T_\mathrm{d} \le\ & t_2 \ \le t_3 - T_\mathrm{d} \\ 0 \le\ & t_1 \ \le t_2 - T_\mathrm{d} \,. \end{aligned}$$

The integral in (11) is then calculated as:

$$p_K(k) = 1 - \sum_{i=0}^{k-1} \psi\left(i, \lambda\left(T_\mathrm{b} - (k-1)\,T_\mathrm{d}\right)\right) . \tag{12}$$

$$p_K(k) = \begin{cases} \sum\limits_{i=0}^{k} \psi(i, \lambda(T_\mathrm{b} - kT_\mathrm{d})) - \sum\limits_{i=0}^{k-1} \psi(i, \lambda(T_\mathrm{b} - (k-1)T_\mathrm{d})) & k < k_{\max} \\ 1 - \sum\limits_{i=0}^{k-1} \psi(i, \lambda(T_\mathrm{b} - (k-1)T_\mathrm{d})) & k = k_{\max} \\ 0 & k > k_{\max} \end{cases} \tag{13}$$

2015 IEEE 26th International Symposium on Personal, Indoor and Mobile Radio Communications - (PIMRC): Fundamentals and PHY

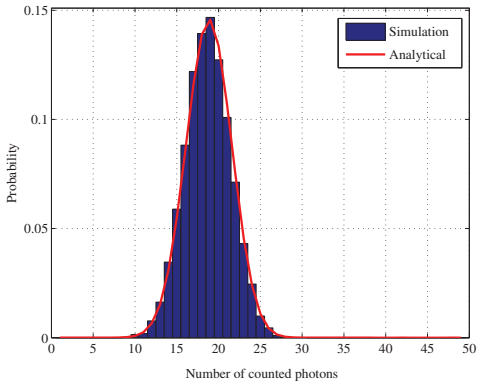

Figure 1. Probability distribution of SPAD photocounts for $T_{\rm b} = 1$ μs, $\lambda = 3 \times 10^7$ photon/s and $\delta = 0.02$.

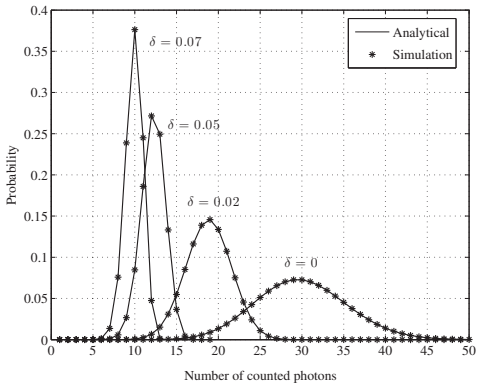

Figure 2. Probability distribution of SPAD photocounts for $T_{\rm b} = 1$ μs, $\lambda = 3 \times 10^7$ photon/s and different values of δ.

It is therefore concluded that the probability of counting k photons by a SPAD with fixed dead time $T_{\rm d}$ is given by (13). The probability mass function (PMF) obtained in (13) is plotted in Fig. 1 and compared with the Monte Carlo simulation results. In Fig. 2, the PMF is plotted for different values of $\delta = T_{\rm d}/T_{\rm b}$. Note that for a receiver with no dead time, the photocount distribution is Poisson with mean $\lambda T_{\rm b}$. In the presence of dead time, the PMF is shifted towards the lower end as shown in Fig. 2. Furthermore, the probability density is zero for $k > k_{\max}$.

III. Effective Count Rate

In all counting systems there are a number of practical constraints which limit the minimum and/or maximum achievable count rate. In the case of SPAD-based devices, background noise and dead time losses are the two main limiting factors. While dead time gives restrictions on the highest measurable count rate, noise causes the limitation in the low count rate region. The maximum count rate of commercial SPADs is restricted to a few MHz, due to the slow recharging process after a detection event, and it is also affected by afterpulsing, which is an additional source of counting errors and refers to avalanche events that originate from the emission of carriers that were trapped in the multiplication region during previous avalanche events.

SPADs can be considered as a new generation of Geiger-Muller (GM) detectors which have been widely studied in published research [8] and various models for their achievable count rates have been developed which take into account the effects of dead time losses [9]. Regarding dead time losses, a SPAD is quite similar to GM counters except the noise effect is different; unlike GM counters, the background noise, an intrinsic characteristic of SPADs, is due to the thermal generation, not an external source of counts.

Detailed studies for GM counters have identified two idealized models for dead time modified count rate, the paralyzable and the nonparalyzable dead time models [8]. These models can also be used for SPAD detectors, provided that all the device characteristics concerning noise and afterpulsing are taken into account.

In a nonparalyzable SPAD, any photon arriving during the dead time is neither counted nor has any influence on the dead time duration; while for the paralyzable case, any photon arrival occurring during the dead time is not counted but is assumed to extend the dead time period. In these two cases the relationship between the true counting rate (i.e. photon rate), λ, and the effective count rate (i.e. observed rate), λ', is given by [8]:

$$\begin{aligned} \text{paralyzable}: &\quad \lambda' = \lambda e^{-\lambda T_{\rm p}}\,, \\ \text{nonparalyzable}: &\quad \lambda' = \frac{\lambda}{1+\lambda T_{\rm nonp}}\,, \end{aligned} \tag{14}$$

where $T_{\rm p}$ and $T_{\rm nonp}$ are the paralyzable and nonparalyzable dead times, respectively. In addition, assuming a time interval of $T_{\rm b}$ seconds, the maximum predicted count rate for the nonparalyzable case would be $1/T_{\rm nonp}$, which is also called 'saturation count rate', meaning that a SPAD is not able to reach count rates higher than this value. For the paralyzable case, however, the peak count rate would be lower than $1/T_{\rm p}$, because each photon arriving during dead time, prolongs the dead time duration.

Note that two approaches can be followed to recover the SPAD after a successful detection: passive quenching and active quenching. In general, passive quenched circuits show a paralyzable dead time behavior, whereas active quenching generates a short nonparalyzable dead time [10].

The comparison between the Monte Carlo simulations and the above dead time modified count rate models for a single SPAD, for a count interval of $T_{\rm b} = 1$ μs is given in Fig. 3. These Monte Carlo simulations demonstrate that the predictions of the analytical framework perfectly match with the simulation results. The nonparalyzable case reaches the theoretical saturation count rate of $1/T_{\rm nonp}$ and the peak count rate of the paralyzable type occurs at $1/(eT_{\rm p})$, accurately predicted by the paralyzable model.

In Fig. 4, the effect of SPAD dead time on the achievable count rate is investigated. As shown, for a given photon rate, when the dead time is increased, the achievable count rate decreases and both paralyzable and nonparalyzable SPADs will reach a lower peak or saturation count rate.

2015 IEEE 26th International Symposium on Personal, Indoor and Mobile Radio Communications - (PIMRC): Fundamentals and PHY

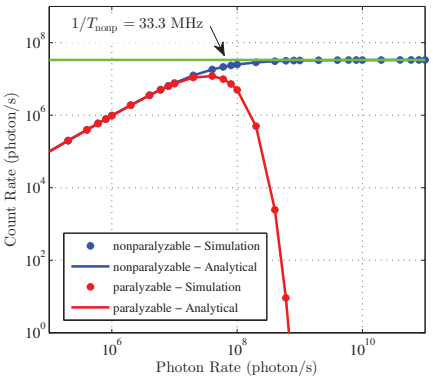

Figure 3. Effective count rate comparison of nonparalyzable and paralyzable SPAD receivers with respect to photon rate ($T_{\text{nonp}} = T_{\text{p}} = 30$ ns).

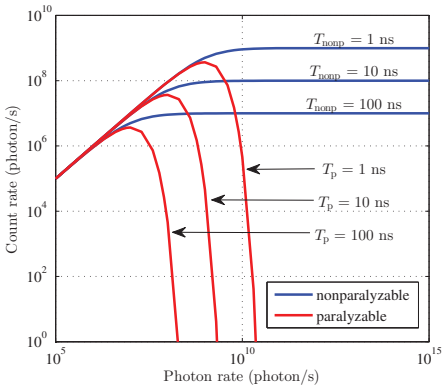

Figure 4. Effective count rate comparison of nonparalyzable and paralyzable SPAD receivers for different dead time values.

IV. Performance Evaluation

SPADs can be used as photon counting receivers in optical communication systems. In a photon counting receiver the dominant noise source is the background counts which mainly arises from dark counts, afterpulsing and ambient light, and will determine the achievable BER. However, the dead time is another limiting factor for the performance of any SPAD-based receiver. In the following, the effect of background counts and the dead time on the performance of a SPAD-based receiver is investigated and the bit error probability for OOK modulation is provided. In OOK modulation each bit is transmitted by either pulsing the light source on or off during each bit time interval, say T_{b} seconds long, so that one data bit is sent every T_{b} seconds. Hence the system transmits at the bit rate $R_{\text{b}} = 1/T_{\text{b}}$.

Assuming that λ_{s} and λ_{n} are the average photon rates from source and background noise, respectively, $K_{\text{s}} = \lambda_{\text{s}} T_{\text{b}}$ and $K_{\text{n}} = \lambda_{\text{n}} T_{\text{b}}$ are the contributions to the average count from the signal and background noise per bit interval T_{b}. When a "0" bit is transmitted, the average number of photons impinged on the SPAD per bit time interval is K_{n}, and when a "1" bit is transmitted, the average number of received photons per bit time interval is $K_{\text{s}} + K_{\text{n}}$. Therefore, according to (13), $p_{\text{n}}(k)$ and $p_{\text{sn}}(k)$, the probability that exactly k photons are counted by the SPAD in the counting interval of T_{b} seconds, when "0" or "1" are sent, respectively, are given by:

$$\begin{aligned} p_{\text{n}}(k) &= p_K(k; \lambda_{\text{n}}, T_{\text{b}}, T_{\text{d}}) \,, \\ p_{\text{sn}}(k) &= p_K(k; \lambda_{\text{s}} + \lambda_{\text{n}}, T_{\text{b}}, T_{\text{d}}) \,. \end{aligned} \tag{15}$$

In this system, decoding is simply achieved by a threshold comparison. The number of counted photons is compared with a threshold m_{T}. A decoding error will occur if $k \leq m_{\text{T}}$ when a "1" bit is sent, or if $k > m_{\text{T}}$, when a "0" bit is sent. Hence the probability of error for equally likely bits is:

$$P_e = \frac{1}{2} \Pr\{k > m_{\text{T}} | 0\} + \frac{1}{2} \Pr\{k \leq m_{\text{T}} | 1\} \,. \tag{16}$$

Considering the dead time modified count probabilities in (15):

$$P_e = \frac{1}{2} \sum_{k=m_{\text{T}}+1}^{\infty} p_{\text{n}}(k) + \frac{1}{2} \sum_{k=0}^{m_{\text{T}}} p_{\text{sn}}(k) \,. \tag{17}$$

In (17), the upper limit of the first summation can be replaced by $k_{\max}$. The error probability, P_e, highly depends on m_{T} which can be selected to yield the lowest probability of making an error. This occurs at the value of m_{T} where $dP_e/dm_{\text{T}} = 0$. Using the definition of incomplete gamma function and the rules of differentiating summations [11]:

$$\begin{aligned} \frac{d}{dx}\left[\sum_{k=0}^{x} f(k)\right] &= f(x) \,, \\ \frac{d}{dx}\left[\sum_{k=x}^{n} f(k)\right] &= -f(x-1) \,, \end{aligned} \tag{18}$$

it can be shown that the threshold value m_{T} which minimizes P_e occurs when the following equation holds:

$$\begin{aligned} &\Gamma(m_{\text{T}}, K_4) - \Gamma(m_{\text{T}}, K_2) \\ &\qquad = \frac{\Gamma(m_{\text{T}}+1, K_3) - \Gamma(m_{\text{T}}+1, K_1)}{m_{\text{T}}} \,, \end{aligned} \tag{19}$$

where $K_1 = \lambda_{\text{n}}(T_{\text{b}} - m_{\text{T}} T_{\text{d}})$, $K_2 = \lambda_{\text{n}}(T_{\text{b}} - (m_{\text{T}} - 1)T_{\text{d}})$, $K_3 = (\lambda_{\text{s}} + \lambda_{\text{n}})(T_{\text{b}} - m_{\text{T}} T_{\text{d}})$, and $K_4 = (\lambda_{\text{s}} + \lambda_{\text{n}})(T_{\text{b}} - (m_{\text{T}} - 1)T_{\text{d}})$ have been used for simplicity of representing the equation. This equation can be solved numerically to obtain m_{T}.

The probability of error given in (17) is evaluated and compared with simulation results in Fig. 5, using the threshold obtained in (19). Independent count statistics are assumed for each transmitted bit and $T_{\text{b}} = 1$ μs is further assumed. In this figure, BER is plotted as a function of K_{s} for different values of K_{n} and δ. As demonstrated, Monte Carlo simulations and analytical calculations result in perfectly matching curves. Also note that the threshold depends on the average number of received photons from both source and background noise, and this highlights a technical challenge with the OOK systems, as K_{s} and K_{n} must be known exactly to optimally set the

2015 IEEE 26th International Symposium on Personal, Indoor and Mobile Radio Communications - (PIMRC): Fundamentals and PHY

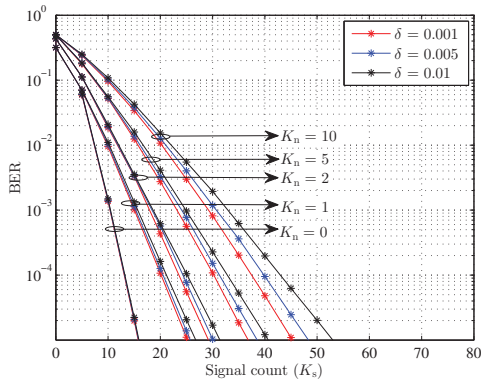

Figure 5. Analytical (solid curves) and simulation (asterisks) BER results of a SPAD-based receiver for different values of δ and K_n.

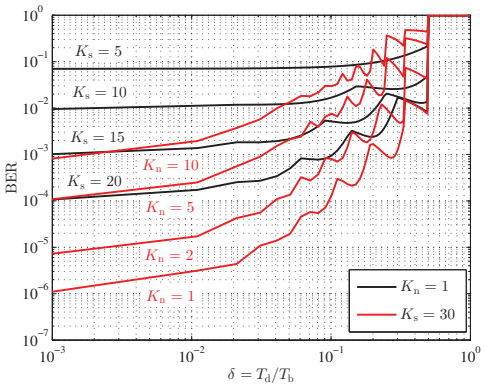

Figure 6. Probability of bit error versus SPAD dead time ratio with different background counts for OOK modulation.

threshold.

Note that the performance of the SPAD-based receivers depends strongly on the background count statistics. For SPADs with no background noise, the effect of dead time on BER is negligible for small values of K_s as in Fig. 5. However, when background noise is present, the performance becomes very sensitive to the dead time. According to Fig. 5, even for $K_n = 1$, the performance is sensitive to the SPAD dead time, and this becomes more apparent, when K_n increases. Also, it is apparent that for a given K_n, a higher signal power is needed to maintain the system performance in the presence of detector dead time. In other words, to achieve a particular BER, the larger δ is, the higher K_s should be.

In Fig. 6, BER is plotted as a function of δ. As shown, when $K_n = 1$ and for different values of K_s (black curves), at small values of δ, the effect of dead time on the BER is almost negligible. As the dead time increases, however, the BER starts to increase and a slight distortion is observed. This increasing trend of BER with respect to δ is more significant for larger values of K_s, and as K_s increases, the distortion in the BER curve occurs at a lower value of δ. As shown in Fig. 6, for $K_s = 30$ and different values of K_n (red curves), as the dead time increases, the BER starts to increase, and $\delta > 0.03$ results in a significant distortion in the BER curves.

V. Conclusion

In this paper, a comprehensive study of SPAD-based optical receivers is conducted and the effect of SPAD dead time on the photon counting process and maximum achievable count rate is investigated. It is shown that, unlike conventional photodetectors for which the detection process can be well approximated by a Poisson arrival process, SPAD count statistics are affected by its dead time, and the number of detected photons over a fixed time interval does not follow a Poisson distribution. In addition, the error performance of an OOK modulation optical system is derived in terms of SPAD dead time and background counts. It is shown that the distorted count statistics result in a higher bit error rates, and a higher signal intensity is required to maintain system performance.

Acknowledgment

Professor Harald Haas acknowledges support by the UK Engineering and Physical Sciences Research Council (EPSRC) under Grant EP/K008757/1.

References

[1] C. Niclass, A. Rochas, P. A. Besse, and E. Charbon, "Design and Characterization of a CMOS 3-D Image Sensor Based on Single Photon Avalanche Diodes," *IEEE Journal of Solid-State Circuits*, vol. 40, no. 9, pp. 1847–1854, Sept. 2005.

[2] A. Tosi, F. Zappa, and S. Cova, "Single-Photon Detectors for Practical Quantum Cryptography," in *SPIE Electro-Optical Remote Sensing, Photonic Technologies, and Applications VI*, vol. 8542, Edinburgh, United Kingdom, Nov. 19 2012, p. 8.

[3] P. I. Hopman *et al.*, "An End-to-End Demonstration of a Receiver Array Based Free-Space Photon Counting Communications Link," in *Proc. SPIE Free-Space Laser Communications VI, SPIE Optics and Photonics*, vol. 6304, San Diego, California, USA, Aug. 13 2006, p. 13.

[4] D. Chitnis and S. Collins, "A SPAD-Based Photon Detecting System for Optical Communications," *Journal of Lightwave Technology*, vol. 32, no. 10, pp. 2028–2034, May 2014.

[5] E. Fisher, I. Underwood, and R. Henderson, "A Reconfigurable Single-Photon-Counting Integrating Receiver for Optical Communications," *IEEE Journal of Solid-State Circuits*, vol. 48, no. 7, pp. 1638–1650, Jul. 2013.

[6] Y. Li *et al.*, "Single Photon Avalanche Diode (SPAD) VLC System and Application to Downhole Monitoring," in *IEEE Global Communications Conference (GLOBECOM)*, San Diego, California, USA, Dec. 8–12 2014, pp. 2108–2113.

[7] D. L. Snyder and M. I. Miller, *Random Point Processes in Time and Space*, 2nd ed., ser. Springer Texts in Electrical Engineering, J. B. Thomas, Ed. Wiley, 1991.

[8] S. H. Lee and R. P. Gardner, "A New GM Counter Dead Time Model," *Applied Radiation and Isotopes*, vol. 53, no. 4, pp. 731–737, Nov. 2000.

[9] J. H. Lee, I. J. Kim, and H. D. Choi, "On the Dead Time Problem of a GM Counter," *Applied Radiation and Isotopes*, vol. 67, no. 6, pp. 1094–1098, Jun. 2009.

[10] A. Eisele *et al.*, "185 MHz Count Rate, 139 dB Dynamic Range Single-Photon Avalanche Diode with Active Quenching Circuit in 130 nm CMOS Technology," in *International Image Sensor Workshop (IISW)*, Japan, Jun. 14 2011, pp. 278–281.

[11] R. M. Gagliardi and S. Karp, *Optical Communications*, 2nd ed. John Wiley, 1995.

2015 4th International Workshop on Optical Wireless Communications (IWOW)

Photon Detection Characteristics and Error Performance of SPAD Array Optical Receivers

Elham Sarbazi, Majid Safari and Harald Haas
Li-Fi Research and Development Centre, Institute for Digital Communications
The University of Edinburgh, Edinburgh, EH9 3JL, UK.
Email: {e.sarbazi, majid.safari, h.haas}@ed.ac.uk

***Abstract*—In this paper a novel photon counting receiver for optical communication applications is proposed. The proposed receiver is a single photon avalanche diode (SPAD) array which can provide a significantly improved detection sensitivity compared to conventional photodiodes. First, the detection statistics and main characteristics of a single SPAD receiver is presented, and the effects of the SPAD dead time, which is introduced by the quenching process, on the counting probability and effective count rate are studied. The approach is then extended to account for SPAD arrays. Using a Gaussian approximation, the counting distribution of a large size SPAD array is derived and effective count rate of arrays with different sizes is evaluated and compared. It is found that even in SPAD arrays, dead time still has a significant role in the maximum achievable count rate, and the fill factor of the array greatly affects the performance and count rate and has to be carefully dealt with. The impact of SPAD background counts and fill factor on the error performance of an on-off keying (OOK) modulation optical communication system is also investigated. It is shown that the bit error rate (BER) depends critically on back ground counts and improves with increasing fill factor.**

***Keywords*—Single Photon Avalanche Diode (SPAD), SPAD arrays, photon counting, optical receivers, on-off keying (OOK).**

I. Introduction

Visible light communications (VLC) has recently been an area of interest, and new devices have been proposed as potential transmitters and/or receivers for VLC systems. There has been significant progress towards the realization of optical receivers fully integrated with the standard digital CMOS technology. Recent trends towards integrated CMOS high-speed optical receivers have specially employed avalanche photodiodes (APDs), but the maximum achievable gain of an APD is limited due to low sensitivity and the gain-dependent excess noise. This requires the use of intricate high gain transimpedance amplifiers (TIAs), limiting amplifiers (LA) and adaptive equalizers.

To address these challenges, APDs can be used in the so-called 'Geiger mode' as single photon avalanche diodes (SPADs). In Geiger mode, the SPAD is biased beyond its breakdown voltage. As a result, due to the high electric field, the absorption of a single photon will initiate an avalanche of charge carriers which leads to a large internal gain. The extremely high gain allows single photon events to be detected effectively and single-photon detection sensitivity can then be improved. However, after each photon detection event, the SPAD needs to be quenched to recover from the excess charge carriers. This quenching process introduces a finite recovery time, known as the 'dead time', during which the device does not respond to another incident photon. Two approaches can be followed to recover the SPAD after a successful detection: passive quenching and active quenching. In general, passively quenched circuits show an extended or paralyzable dead time behavior, whereas active quenching generates a short constant or nonparalyzable dead time. In a SPAD device with nonparalyzable deadtime, any photon arriving during the dead time is neither counted nor has any influence on the dead time duration; while for the paralyzable case, any photon arrival occurring during the dead time is not counted but is assumed to extend the dead time period [1].

Various types of SPADs have been successfully employed in a number of applications, including three-dimensional imaging [2], quantum key distribution [3], and deep space laser communications [4]. The high sensitivity and time resolution of SPADs have recently highlighted the potential of employing SPADs as photon counting receivers for VLC systems [5]–[8]. They can be used with the long term aim of power efficient and highly sensitive receivers and are particularly attractive because they are able to closely approach quantum-limited sensitivity in the detection of weak optical signals in long distance communications, such as in the gas extraction industry, or in downhole monitoring systems [9].

Nevertheless, to the best of authors' knowledge, there is limited published research on the detection statistics of SPAD receivers in literature. In [10], we presented a thorough characterization and detailed analysis of detection statistics of a single SPAD with nonparalyzable dead time, operating as an optical receiver. In this paper, we extend our previous approach and characterize an array of SPADs for optical communication applications. In particular, analytical modelling and simulation results are provided which predict the performance of a SPAD-based array receiver. Throughout this paper, a SPAD device with a nonparalyzable dead time is considered.

The rest of the paper is organized as follows. The photo-count statistics and count rate of a single SPAD and a SPAD array are discussed in Section II, and how the count statistics and effective count rate are affected by SPAD dead time is explained. An approximate mathematical model for the count probability of a SPAD array is developed and Monte Carlo methods are employed to verify the validity of the analytical models. Furthermore, the major constraints which limit the achievable count rate of SPAD receivers are addressed. The mathematical counting distribution of the SPAD array derived in Section II is then used in Section III to predict the error performance of an on-off keying (OOK) modulation optical system. Finally, concluding remarks are given in Section IV.

978-1-4673-7726-3/15/$31.00 ©2015IEEE

2015 4th International Workshop on Optical Wireless Communications (IWOW)

II. PHOTOCOUNT STATISTICS

A. Single SPAD

1) Probability Mass Function (PMF): In the absence of SPAD dead time, the detection of photon arrival events can be modeled as a Poisson arrival process for which the probability of detecting k photons over a time period of $[0, T_{\rm b})$ is given by:

$$p_0(k; \lambda T_{\rm b}) = \frac{(\lambda T_{\rm b})^k e^{-\lambda T_{\rm b}}}{k!} , \tag{1}$$

where the constant λ is the average photon arrival rate, hence, $\lambda T_{\rm b}$ is the average number of photons arriving at the SPAD during the observation time of $T_{\rm b}$ seconds. The photocount rate λ is related to the power of the optical signal by:

$$\lambda = \frac{\eta_{\rm QE} P_{\rm s}}{h\nu} , \tag{2}$$

where $\eta_{\rm QE}$ is the quantum efficiency of SPAD; $P_{\rm s}$ denotes the power of the incident optical signal; h is the Planck's constant; and ν represents the frequency of the optical signal.

When the SPAD dead time is considered, however, the actual count statistics can be very different from the photon arrival statistics and the photon counts are no longer Poisson distributed. Any incident photons which arrive after the initial photon event and before the end of the quenching process, go undetected. In this study, a SPAD detector with constant dead time is considered which cannot record counts for a time interval of fixed duration, τ, immediately following the registration of a count. It is assumed that SPAD is ready to operate at the beginning of the counting interval of $[0, T_{\rm b})$. Therefore, the maximum observable count during this period is $k_{\max} = \lfloor \delta \rfloor + 1$, where $\delta = T_{\rm b}/\tau$ and $\lfloor x \rfloor$ denotes the largest integer that is smaller than x. In [10], the detection statistics of a single SPAD was investigated and it was shown that the probability of k photons being detected during the time interval of $[0, T_{\rm b})$ is given by [10]:

$$p_K(k) = \begin{cases} \sum\limits_{i=0}^{k} \psi(i, \lambda_k) - \sum\limits_{i=0}^{k-1} \psi(i, \lambda_{k-1}) & k < k_{\max} \\ 1 - \sum\limits_{i=0}^{k-1} \psi(i, \lambda_{k-1}) & k = k_{\max} \\ 0 & k > k_{\max} \end{cases} \tag{3}$$

where $\lambda_k = \lambda(T_{\rm b} - k\tau)$, $\lambda_{k-1} = \lambda(T_{\rm b} - (k-1)\tau)$ and the function $\psi(i, \lambda)$ is defined as:

$$\psi(i, \lambda) = \frac{\lambda^i e^{-\lambda}}{i!} . \tag{4}$$

2) First and second moments: The mean and variance of the photocount distribution in (3) are:

$$\mu_K = k_{\max} - \sum_{k=0}^{k_{\max}-1} \sum_{i=0}^{k} \psi(i, \lambda_k), \tag{5}$$

$$\sigma_K^2 = \sum_{k=0}^{k_{\max}-1} \sum_{i=0}^{k} (2k_{\max} - 2k - 1)\psi(i, \lambda_k) - \left(\sum_{k=0}^{k_{\max}-1} \sum_{i=0}^{k} \psi(i, \lambda_k) \right)^2 . \tag{6}$$

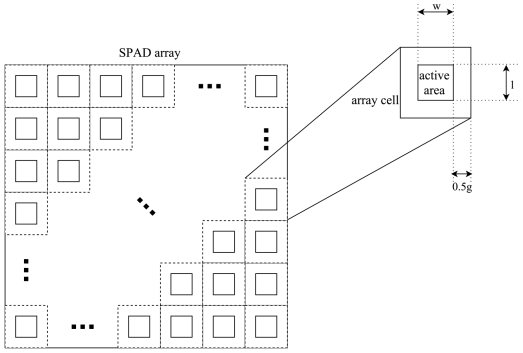

Figure 1. Geometry of a SPAD array.

It can readily be verified that as dead time goes to zero, the PMF in (3) approaches the ideal Poisson distribution. In such a case, the limiting relations $\lim_{\tau \to 0} \mu_K = \lambda T_{\rm b}$ and $\lim_{\tau \to 0} \sigma_K^2 = \lambda T_{\rm b}$ in (5) and (6) can also be confirmed, where $\lambda T_{\rm b}$ is the mean value of the ideal Poisson distribution.

3) Approximation of PMF for large mean counts: In the case where the mean count is large, it can be shown that the count distribution of (3) may be approximated as

$$p_K(k) \approx \psi(k, \lambda_k), \tag{7}$$

for $k \leq k_{\max}$.

4) Effective count rate: In a SPAD-based receiver, background noise and dead time losses limit the minimum and/or maximum achievable count rate. While dead time gives restrictions on the highest measurable count rate, noise is the limitation in the low count rate region. The maximum count rate of commercial SPADs is restricted to a few MHz, due to the slow recharging process, also called 'quenching process', after a detection event, and it is also affected by afterpulsing, which is an additional source of counting errors and refers to avalanche events that originate from the emission of carriers that were trapped in the multiplication region during previous avalanche events.

SPADs can be considered as a new generation of Geiger-Muller (GM) detectors which have been widely studied in published research [11], [12]. Provided that all the device characteristics concerning noise and afterpulsing are taken into account, a SPAD with constant dead time can be treated as a *nonparalyzable* GM counter, in which any photon arriving during the dead time is neither counted nor has any influence on the dead time duration. According to the nonparalyzable dead time count rate model, the relationship between the true counting rate (i.e. photon rate), λ, and the effective count rate (i.e. observed rate), λ', is given by [11]:

$$\lambda' = \frac{\lambda}{1 + \lambda \tau_{\rm nonp}} , \tag{8}$$

where $\tau_{\rm nonp}$ is the nonparalyzable dead time. Note that assuming a time interval of $T_{\rm b}$ seconds, the maximum predicted count rate for the nonparalyzable case would be $1/\tau_{\rm nonp}$, which is termed 'saturation count rate', meaning that a SPAD is not able to reach count rates higher than this value.

B. SPAD Array

To increase the capacity of the photon counts, an array of SPADs may be considered which outputs the superposition of the photon counts from the individual SPADs. Other than the dead time of the single SPADs, the Fill Factor (FF) of the SPAD array affects the photocount distribution. FF is defined as the ratio of the SPAD total active area to the total array area and it represents the probability that the incoming photons hit the active area.

Figure 1 illustrates the configuration of a rectangular SPAD array consisting of $R \times C$ single SPADs as the cell element of the array. The FF coefficient of this array is given by:

$$C_{\mathrm{FF}} = \frac{lw}{(l+g)(w+g)}. \tag{9}$$

Array elements are indexed with the subscripts mn, where $1 \leq m \leq R$ and $1 \leq n \leq C$, to denote their position within the array.

1) Probability distribution, mean and variance: In the absence of dead time, Poisson counting process will be observed at each element of the array. However, when dead time is present and the effect of FF is considered, the PMF in (3) can be rewritten for the mnth element of the array as $p_K(k_{mn})$ with parameters

$$k_{\max,mn} = \left\lfloor \frac{T_{\mathrm{b}}}{\tau_{mn}} \right\rfloor + 1 \, ,$$
$$\lambda'_{k_{mn}} = C_{\mathrm{FF}} \lambda_{mn} (T_{\mathrm{b}} - k_{mn}\tau_{mn}) \, ,$$

where λ_{mn} is the average photon arrival rate at mnth SPAD and τ_{mn} is the dead time of the mnth element.

Assuming independent statistics for each SPAD in the array, the joint sample function density of the SPAD array can be described as:

$$\Pr(\mathbf{n}) = \prod_{m=1}^{R} \prod_{n=1}^{C} p_K(k_{mn}), \tag{10}$$

where $\mathbf{n} \equiv [k_{11}, k_{12}, ..., k_{R(C-1)}, k_{RC}]$.

Considering independent random variables, K_{mn}, as the number of photon counts at mnth element of the array, a new random variable can be defined as:

$$X = \sum_{m=1}^{R} \sum_{n=1}^{C} K_{mn}, \tag{11}$$

Therefore, the probability distribution of X is expressed as:

$$p_X(x) = \sum_{k_{11}} \sum_{k_{12}} ... \sum_{k_{R(C-1)}} \Pr(\mathbf{n}'), \tag{13}$$

where $\mathbf{n}' \equiv [k_{11}, k_{12}, ..., k_{R(C-1)}, x - \sum_{m=1}^{R} \sum_{n=1}^{C-1} k_{mn}]$.

It is in general challenging to obtain a closed-form expression for (13), nevertheless, an approximate expression for $p_X(x)$ can be obtained when the number of array elements is large. In that case, according to Central Limit Theorem (CLT), the dead time modified counting distribution of a SPAD array can be approximated by a Gaussian distribution:

$$p_X(x) \sim \mathcal{N}(\mu_X, \sigma_X^2), \tag{14}$$

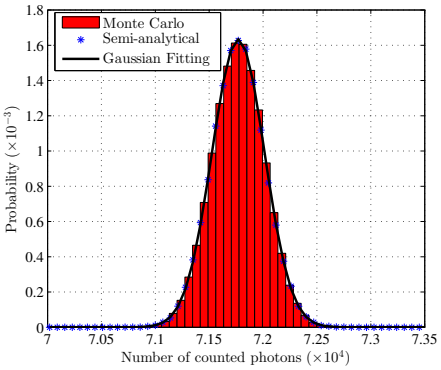

Figure 2. Probability distribution of a 64×64 SPAD array photocounts for $T_{\mathrm{b}} = 1$ μs, $\lambda = 3 \times 10^7$ photon/s, $C_{\mathrm{FF}} = 0.64$ and $\delta = 0.005$.

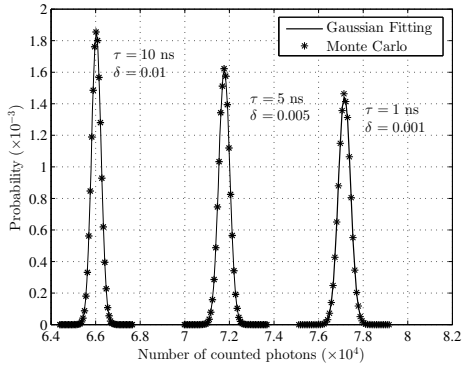

Figure 3. Probability distribution of a 64×64 SPAD array photocounts for $T_{\mathrm{b}} = 1$ μs, $\lambda = 3 \times 10^7$ photon/s, $C_{\mathrm{FF}} = 0.64$ and different values of δ.

where,

$$\mu_X = \sum_{m=1}^{R} \sum_{n=1}^{C} \mu_{mn},$$
$$\sigma_X^2 = \sum_{m=1}^{R} \sum_{n=1}^{C} \sigma_{mn}^2.$$

Here, μ_{mn} and σ_{mn}^2 are the mean and variance of the photocount distribution of the mnth SPAD in the array.

The exact counting distribution in (13), calculated using numerical methods, and the approximate counting distribution obtained in (14) are plotted in Fig. 2 and compared with the Monte Carlo simulation results. In Fig. 3, (14) is plotted for different values of $\delta = \tau / T_{\mathrm{b}}$. As shown, the Monte Carlo simulation results and the Gaussian approximation are perfectly matched and this confirms the validity of the approximation approach. Also note that as the dead time increases, both the mean and variance of the photon counts decrease and this is in total agreement with the analytical approximations.

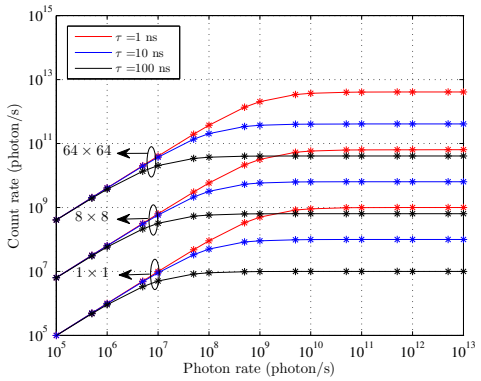

Figure 4. Analytical (solid curves) and simulation (asterisks) results for effective count rate of different SPAD arrays with $C_{\rm FF} = 0.64$ for various dead time values.

Furthermore, note that throughout this paper, in all simulation results, practical values for SPAD parameters are assumed which are all adoped from [6] and [7].

2) Effective count rate: For a SPAD array, the achievable count rate is expected to be improved as the number of array elements increases. Assuming identical array elements and constant photon arrival rate, the nonparalyzable count rate model in (8) can be modified for a SPAD array of size $R \times C$ elements as:

$$\lambda' = \frac{\lambda RC}{1 + \lambda \tau_{\rm nonp}} \ , \tag{15}$$

The comparison between the Monte Carlo simulations and the above dead time modified count rate model for a SPAD array, is given in Fig. 4 where the observed count rate for arrays of different sizes are compared. According to these curves, the saturation count rates are scaled by the size of array compared to a single SPAD. Also note that the dead time has a significant effect on the maximum achievable count rate and it determines the saturation level of the count rate.

III. Performance Evaluation

SPADs can be used as photon counting receivers in optical communication systems. In a photon counting receiver the dominant noise source is the background counts which mainly arises from dark counts, afterpulsing and ambient light, and will determine the achievable BER. However, the dead time is another limiting factor for the performance of any SPAD-based receiver. In the following, the effect of background counts and the dead time on the performance of a SPAD-based receiver is investigated and the bit error probability for OOK modulation is provided.

In OOK modulation each bit is transmitted by either pulsing the light source on or off during each bit time interval, say $T_{\rm b}$ seconds duration, so that one data bit is sent every $T_{\rm b}$ seconds. Hence the system transmits at the bit rate $R_{\rm b} = 1/T_{\rm b}$.

Assuming $\lambda_{\rm s}$ and $\lambda_{\rm n}$ as the average photon arrival rates from source and background noise, respectively, $K_{\rm s} = \lambda_{\rm s} T_{\rm b}$ and $K_{\rm n} = \lambda_{\rm n} T_{\rm b}$ are the contributions to the average count from the signal and background noise counts per bit interval $T_{\rm b}$ for each array element. When a "0" bit is transmitted, the average number of photons impinged on each single SPAD per bit time interval is $K_{\rm n}$, and when a "1" bit is transmitted, the average number of received photons per bit time interval is $K_{\rm s} + K_{\rm n}$. Therefore, according to (13), $p_0(x)$ and $p_1(x)$, the probability that exactly x photons are counted by the SPAD array in the counting interval of $T_{\rm b}$ seconds, when "0" or "1" are sent, respectively, are given by:

$$\begin{aligned} p_0(x) &= p_X(x; \lambda_{\rm n}) \ , \\ p_1(x) &= p_X(x; \lambda_{\rm s} + \lambda_{\rm n}) \ . \end{aligned} \tag{16}$$

In this system, decoding is simply achieved by a threshold comparison. The number of counted photons is compared with a threshold $x_{\rm T}$. A decoding error will occur if $x \le x_{\rm T}$ when a "1" bit is sent, or if $x > x_{\rm T}$, when a "0" bit is sent. Hence the probability of error for equally likely bits is [13]:

$$P_e = \frac{1}{2}{\rm Pr}\left\{x > x_{\rm T} | 0\right\} + \frac{1}{2}{\rm Pr}\left\{x \le x_{\rm T} | 1\right\} \ . \tag{17}$$

Considering the count probabilities in (16):

$$P_e = \frac{1}{2} \sum_{x=x_{\rm T}+1}^{\infty} p_0\left(x\right) + \frac{1}{2} \sum_{x=0}^{x_{\rm T}} p_1\left(x\right) \ . \tag{18}$$

In order to calculate the probability of error in (18), the Gaussian approximation in (14) can be applied to $p_0(x)$ and $p_1(x)$ so that $p_0(x) \sim \mathcal{N}(\mu_0, \sigma_0^2)$ and $p_1(x) \sim \mathcal{N}(\mu_1, \sigma_1^2)$. Note that the array size is assumed to be sufficiently large, hence, this approximation is valid. Therefore, P_e can be approximated as:

$$\begin{aligned} P_e &\cong \frac{1}{2} \int_{x_{\rm T}}^{\infty} p_0(x)\, dx \quad + \frac{1}{2} \int_{0}^{x_{\rm T}} p_1(x)\, dx \\ &= \frac{1}{2} Q\left(\frac{x_{\rm T} - \mu_0}{\sigma_0}\right) + \frac{1}{2} Q\left(\frac{\mu_1 - x_{\rm T}}{\sigma_1}\right) . \end{aligned} \tag{19}$$

where, $Q(x) = 1/\sqrt{2\pi} \int_x^{\infty} \exp(-\alpha^2/2)\, d\alpha$ is the Q-function. The error probability, P_e, highly depends on $x_{\rm T}$ which can be selected to yield the lowest probability of occurring an error. This occurs at the value of $x_{\rm T}$ where $dP_e/dx_{\rm T} = 0$. It can be shown that the threshold value $x_{\rm T}$ which minimizes P_e is given by (20) which can be further approximated as:

$$x_{\rm T} = \frac{\mu_1 \sigma_0 + \mu_0 \sigma_1}{\sigma_0 + \sigma_1} \ . \tag{21}$$

When this threshold is used, the resulting P_e in (19) is simplified to:

$$P_e \cong Q\left(\frac{\mu_1 - \mu_0}{\sigma_1 + \sigma_0}\right) . \tag{22}$$

$$x_{\rm T} = \frac{\frac{\mu_0}{\sigma_0^2} - \frac{\mu_1}{\sigma_1^2} + \sqrt{\left(\frac{\mu_0}{\sigma_0^2} - \frac{\mu_1}{\sigma_1^2}\right)^2 - \left(\frac{1}{\sigma_0^2} - \frac{1}{\sigma_1^2}\right)\left\{\left(\frac{\mu_0^2}{\sigma_0^2} - \frac{\mu_1^2}{\sigma_1^2}\right) + 2\ln\left(\frac{\sigma_0}{\sigma_1}\right)\right\}}}{\frac{1}{\sigma_0^2} - \frac{1}{\sigma_1^2}} \ , \tag{20}$$

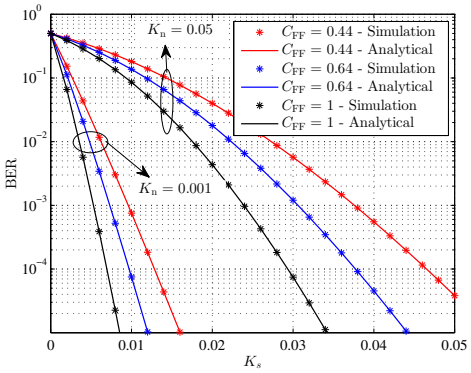

Figure 5. Analytical (solid curves) and simulation (asterisks) BER results of a 64×64 SPAD array receiver for different values of C_{FF} and K_{n} ($T_{\mathrm{b}} = 1$ μs and $\tau = 1$ ns).

Note that with the assumption of a Gaussian distribution, P_e depends only on the difference of the photodetected mean values. Thus any contribution to both means, such as from dark current or background noise, would not effect the $\mu_1 - \mu_0$ term, these will however contribute to the variances. Defining the signal-to-noise-ratio (*SNR*) as:

$$SNR = \frac{(\mu_1 - \mu_0)^2}{(\sigma_1 + \sigma_0)^2} \tag{23}$$

P_e can also be written as:

$$P_e = Q\left(\sqrt{SNR}\right). \tag{24}$$

The probability of error given in (22) is evaluated and compared with simulation results in Fig. 5, using the threshold obtained in (21). Independent count statistics are assumed for each transmitted bit, and it is assumed that the array elements are identical and $T_{\mathrm{b}} = 1$ μs. In this figure, BER is plotted as a function of K_{s} for different values of K_{n} and C_{FF}. As shown, Monte Carlo simulations and analytical models result in perfectly matching curves. Also note that the threshold depends on the average number of received photons from both the source and background noise, and this highlights a technical challenge with the OOK system, as λ_{s} and λ_{n} must be known exactly to optimally set the threshold.

According to this figure, it can also be concluded that the array FF has an important role in the performance of a SPAD-based array receiver where the increase in the array FF improves the system performance.

IV. Conclusion

In this paper, a comprehensive study of SPAD-based optical receivers is conducted. The detection statistics and main characteristics of single SPAD and SPAD array receivers are discussed and it is shown that, the counting distribution of a large size SPAD array can be well approximated by Gaussian distribution. The effects of SPAD dead time and array fill factor on the photon counting process and the maximum achievable count rate is also investigated. In addition, the error performance of an OOK modulation optical system is studied and it is concluded that as the background counts increase, a higher signal power is needed to maintain the system performance.

Acknowledgment

Professor Harald Haas acknowledges support by the UK Engineering and Physical Sciences Research Council (EPSRC) under Grant EP/K008757/1.

References

[1] A. Eisele, R. Henderson, B. Schmidtke, T. Funk, L. Grant, J. Richardson, and W. Freude, "185 MHz Count Rate, 139 dB Dynamic Range Single-Photon Avalanche Diode with Active Quenching Circuit in 130 nm CMOS Technology," in *International Image Sensor Workshop (IISW)*, Japan, Jun. 14 2011, pp. 278–281.

[2] C. Niclass, A. Rochas, P. A. Besse, and E. Charbon, "Design and Characterization of a CMOS 3-D Image Sensor Based on Single Photon Avalanche Diodes," *IEEE Journal of Solid-State Circuits*, vol. 40, no. 9, pp. 1847–1854, Sept. 2005.

[3] A. Tosi, F. Zappa, and S. Cova, "Single-Photon Detectors for Practical Quantum Cryptography," in *SPIE Electro-Optical Remote Sensing, Photonic Technologies, and Applications VI*, vol. 8542, Edinburgh, United Kingdom, Nov. 19 2012, p. 8.

[4] P. I. Hopman, P. W. Boettcher, L. M. Candell, J. B. Glettler, R. Shoup, and G. Zogbi, "An End-to-End Demonstration of a Receiver Array Based Free-Space Photon Counting Communications Link," in *Proc. SPIE Free-Space Laser Communications VI, SPIE Optics and Photonics*, vol. 6304, San Diego, California, USA, Aug. 13 2006, p. 13.

[5] D. Chitnis and S. Collins, "A SPAD-Based Photon Detecting System for Optical Communications," *Journal of Lightwave Technology*, vol. 32, no. 10, pp. 2028–2034, May 2014.

[6] E. Fisher, I. Underwood, and R. Henderson, "A Reconfigurable 14-bit 60GPhoton/s Single-Photon Receiver for Visible Light Communications," in *2012 Proceedings of the ESSCIRC (ESSCIRC)*, Sept. 2012, pp. 85–88.

[7] ——, "A Reconfigurable Single-Photon-Counting Integrating Receiver for Optical Communications," *IEEE Journal of Solid-State Circuits*, vol. 48, no. 7, pp. 1638–1650, Jul. 2013.

[8] Y. Li, M. Safari, R. Henderson, and H. Haas, "Optical OFDM With Single-Photon Avalanche Diode," *IEEE Photonics Technology Letters*, vol. 27, no. 9, pp. 943–946, May 2015.

[9] Y. Li *et al.*, "Single Photon Avalanche Diode (SPAD) VLC System and Application to Downhole Monitoring," in *IEEE Global Communications Conference (GLOBECOM)*, San Diego, California, USA, Dec. 8–12 2014, pp. 2108–2113.

[10] E. Sarbazi and H. Haas, "Detection Statistics and Error Performance of SPAD-based Optical Receivers," in *26th Annual International Symposium on Personal, Indoor, and Mobile Radio Communications*, Hong Kong, China, Aug. 30 2015.

[11] S. H. Lee and R. P. Gardner, "A New GM Counter Dead Time Model," *Applied Radiation and Isotopes*, vol. 53, no. 4, pp. 731–737, Nov. 2000.

[12] J. H. Lee, I. J. Kim, and H. D. Choi, "On the Dead Time Problem of a GM Counter," *Applied Radiation and Isotopes*, vol. 67, no. 6, pp. 1094–1098, Jun. 2009.

[13] R. M. Gagliardi and S. Karp, *Optical Communications*, 2nd ed. John Wiley, 1995.

On the Information Transfer Rate of SPAD Receivers for Optical Wireless Communications

Elham Sarbazi, Majid Safari and Harald Haas
Li-Fi Research and Development Centre, Institute for Digital Communications
The University of Edinburgh, Edinburgh, EH9 3JL, UK.
Email: {e.sarbazi, majid.safari, h.haas}@ed.ac.uk

***Abstract*—In this paper, the information rate of single photon avalanche diode (SPAD) receivers with active quenching circuits for optical communication systems is studied. The SPAD receiver is modeled as a discrete memoryless channel (DMC), and the information transfer rate is studied using an information theoretic approach. To assess the input-output information transfer rate of the SPAD optical receiver, a channel capacity metric is proposed which is a function of several parameters including average signal photon count, SPAD dead time, and SPAD average background counts. The proposed metric can be used for theoretical optimization of the device structure and operating conditions. Performance results are presented based on the proposed metric.**

***Index Terms*—Single Photon Avalanche Diode (SPAD), active quenching, photon counting, dead time, channel capacity.**

I. Introduction

Single Photon Avalanche Diodes (SPADs) are gaining interest in the field of optical wireless communications (OWC) owing to their high power efficiency, high sensitivity, high detection efficiency, and high timing resolution [1]–[3]. SPADs are able to closely approach quantum-limited sensitivity in the detection of weak optical signals and this has recently highlighted the potential of employing them in applications where long distance transmission requires highly sensitive receivers capable of detecting a single photon [4], [5].

SPADs are semiconductor devices with p-n junctions and are operated in avalanche breakdown photon counting mode, also termed as 'Geiger mode'. In Geiger mode, the p-n junction is biased above the breakdown voltage such that individual photons trigger an avalanche breakdown. The avalanche breakdown results in a strong output current spike which is then individually counted [6]. Every time an avalanche breakdown occurs, the output current has to be quenched by lowering the bias voltage down to or below breakdown voltage to stop the avalanche event, and in order to detect a subsequent photon, the bias voltage must be raised again. This is accomplished by a suitable electronic circuit known as 'quenching circuit'. During the quenching process, SPAD is unresponsive for a circuit specific 'dead time'. Two approaches can be followed to design a quenching circuit: passive quenching (PQ) and active quenching (AQ). The configurations of PQ and AQ circuits are presented in [7]. In general, PQ SPADs are identified as paralyzable detectors where any photon arrival occurring during the dead time is not counted but is assumed to extend the dead time period; while in an AQ SPAD device, the duration of the dead time introduced by the quenching process is constant, that is, any photon arriving during the dead time is neither counted nor has any influence on the dead time duration. Thus AQ SPADs are defined as nonparalyzable detectors and generally have higher count rates than PQ SPADs [7].

Quenching circuits directly affect the performance of the device because of the dead time they introduce for the recovering process. The relatively long dead time due to the slow recovery process, limits counting rates, and results in a considerable count loss relative to an ideal dead time-free photon counting detector, however second order effects such as afterpulsing, prevent arbitrarily short dead time. The dead time of commercially available SPAD receivers vary in the range of a few nanoseconds to tens of nanoseconds, causing significant losses for communication links with slot widths of the same order. This has motivated recent studies on characterizing losses due to the SPAD dead time [8], [9]. Furthermore, while dead time confines the highest measurable count rate, background noise limits the low count rates.

To date, there has been extensive work on designing SPAD receivers for a number of applications including three-dimensional imaging [10], quantum key distribution [11], and deep space laser communications [12], and much effort has been devoted to optimizing the SPAD key performance metrics (e.g. detection efficiency, dead time, dark count rate, timing jitter, etc.) to improve its performance for communication purposes [1], [2], [4], [13]. In all the aforementioned articles, the impact of SPAD dead time and dark current on the performance of the systems have been experimentally explored and it is reported that due to these non-idealities the output rate is limited. Currently, efforts are underway to integrate SPAD elements directly with quenching circuitry using standard digital CMOS technology. Aiming to achieve higher output rates for optical communication applications, SPAD arrays fully integrated with the CMOS technology have been implemented. Nevertheless, highest achievable data rates are still restricted to a few tens of MHz. The effect of dead time can be mitigated by improving the performance of active quenching circuits and by device multiplexing techniques. For example in [2], a reconfigurable 32×32 SPAD array receiver integrated in standard 130 nm CMOS is presented for optical links and the properties of the receiver for optical communications are investigated, and a data rate of 100 MHz is reported.

While SPAD detectors remain an active area of develop-

ment, there does not exist enough theoretical analysis which would specify the performance limitations of these receivers. In [8], we studied the effect of dead time on the photocount statistics of a single SPAD receiver where the probability of detection and the error probability in an optical communication system were analyzed. Also, in [9], the counting distribution and count rate of SPAD arrays were discussed. The aim of this study is to investigate how the maximum achievable information transfer rate of a SPAD receiver is limited by non-ideal behavior of an AQ circuit.

The rest of this paper is organized as follows. In Section II, a brief review of SPAD photocounting statistics in the presence of dead time is given, and the impact of dead time on the maximum achievable count rate of the SPAD receiver is discussed. In Section III, the modeling of a SPAD device as a discrete memoryless channel (DMC) with binary inputs is presented, and the channel capacity metric is introduced to assess the information transfer rate of the SPAD receiver. In Section IV, the numerical results are presented, and discussions on the effect of various parameters on the information transfer rate of the SPAD receiver are provided. Finally, concluding remarks are given in Section V.

II. SPAD Counting Statistics

In the following, the key statistical characteristics of AQ SPADs are summarized:

1) Probability Mass Function (PMF): In the absence of SPAD dead time, the detection of photon arrival events can be modeled as a Poisson arrival process for which the probability of detecting k photons over a time period of $[0, T_{\rm b})$ is given by [14], [15]:

$$p_0(k;\lambda) = \frac{(\lambda T_{\rm b})^k e^{-\lambda T_{\rm b}}}{k!} \ , \tag{1}$$

where the constant λ is the average photon arrival rate (in photons/sec), and hence, $\lambda T_{\rm b}$ is the average number of photons arriving at the SPAD during the observation time of $T_{\rm b}$ seconds. The photocount rate λ is related to the optical signal power by [14], [15]:

$$\lambda = \frac{\eta_{\rm QE} P_{\rm s}}{h\nu} \ , \tag{2}$$

where $\eta_{\rm QE}$ is the quantum efficiency of SPAD; $P_{\rm s}$ denotes the incident optical signal power; h is the Planck's constant; and ν represents the optical signal frequency.

When the SPAD dead time is considered, however, the photon counts are no longer Poisson distributed. Assuming that the SPAD detector is ready to operate at the beginning of the counting interval, the maximum observable counts during this period is $k_{\max} = \lfloor T_{\rm b}/\tau \rfloor + 1$, where τ is the dead time and $\lfloor x \rfloor$ denotes the largest integer that is smaller than x. In [8], it was shown that the probability of k photons being detected during the time interval of $[0, T_{\rm b})$ is given by:

$$p_K(k;\lambda) = \begin{cases} \sum\limits_{i=0}^{k} \psi(i,\lambda_k) - \sum\limits_{i=0}^{k-1} \psi(i,\lambda_{k-1}) & k < k_{\max} \\ 1 - \sum\limits_{i=0}^{k-1} \psi(i,\lambda_{k-1}) & k = k_{\max} \\ 0 & k > k_{\max} \end{cases} \tag{3}$$

where $\lambda_k = \lambda(T_{\rm b} - k\tau)$; and the function $\psi(.)$ is defined as:

$$\psi(i,\lambda) = \frac{\lambda^i e^{-\lambda}}{i!} \ . \tag{4}$$

2) First and second moments: The mean and variance of the photocount distribution in (3) are derived as:

$$\mu_K = k_{\max} - \sum_{k=0}^{k_{\max}-1} \sum_{i=0}^{k} \psi(i,\lambda_k), \tag{5}$$

$$\begin{aligned} \sigma_K^2 = & \sum_{k=0}^{k_{\max}-1} \sum_{i=0}^{k} (2k_{\max} - 2k - 1)\psi(i,\lambda_k) \\ & - \left(\sum_{k=0}^{k_{\max}-1} \sum_{i=0}^{k} \psi(i,\lambda_k) \right)^2 . \end{aligned} \tag{6}$$

It can be verified that as dead time goes to zero, the PMF in (3) approaches the ideal Poisson distribution. In such a case, the limiting relations $\lim_{\tau\to 0} \mu_K = \lambda T_{\rm b}$ and $\lim_{\tau\to 0} \sigma_K^2 = \lambda T_{\rm b}$ can also be confirmed, where $\lambda T_{\rm b}$ is the mean of the ideal Poisson distribution.

3) Effective count rate: For a SPAD detector, background counts and dead time losses limit the minimum and maximum achievable count rates. While dead time puts restrictions on the highest measurable count rate, background noise limits the lowest count rate. The maximum count rate of commercial SPADs is restricted to a few MHz, and the main reason of this low bandwidth response is the slow quenching process after a detection event. There is another source of counting errors called afterpulsing, and it refers to avalanche events that originate from the emission of carriers trapped in the multiplication region during previous avalanche events. The afterpulsing phenomenon, prevent arbitrarily short dead time, and hence, limits the maximum achievable count rate indirectly.

According to the nonparalyzable dead time model for single-photon detectors, the relationship between the actual count rate (i.e., incoming photon rate), λ, and the effective count rate (i.e., observed rate), λ', is given by [16], [17]:

$$\lambda' = \frac{\lambda}{1 + \lambda\tau} \ , \tag{7}$$

where τ is the nonparalyzable dead time for an AQ SPAD. Note that, the maximum predicted count rate would be equal to $1/\tau$, assuming a time interval of $T_{\rm b}$ seconds. This is termed as 'saturation count rate', which means that an AQ SPAD is not able to reach count rates higher than this value.

III. Channel Capacity

The reliability performance of SPAD receivers is specified by the error and detection probabilities. The maximum achievable data rate is another key metric to characterize SPAD receivers, and this determines whether or not it is suitable for optical communication systems. To address this question, the SPAD detector can be assumed as a communication channel, and in this case the channel capacity would be the appropriate metric to assess the input-output information transfer rate of the SPAD receiver. In this context, the relevance of the channel capacity as a performance metric is clear. As long as the transfer rate of information through the SPAD device is less than the SPAD capacity, it is possible to make the error probability arbitrarily small with proper modulation and coding. In the following, the capacity of the SPAD receiver as a communication channel is investigated.

A. Discrete Memoryless Channel (DMC)

Here, the SPAD receiver is modeled as a DMC which comprises a finite input alphabet $\mathcal{X} = \{x_1, x_2, ..., x_N\}$, and a finite output alphabet $\mathcal{Y} = \{y_1, y_2, ..., y_M\}$. Let $p_X(x_i)$ be the probability that the input X takes the value x_i, for $i = 1, 2, ..., N$, and let $p_Y(y_j)$ be the probability that the output Y takes the value y_j, for $j = 1, 2, ..., M$. Define $p_{XY}(x_i, y_j)$ as the joint probability of the random variables X and Y evaluated for x_i and y_j, and also define $p_{Y|X}(y_j|x_i)$ as the conditional probability, which expresses the probability of observing the output symbol y_j given the input symbol x_i. The mutual information $I(x_i; y_j)$ between the events $X = x_i$ and $Y = y_j$ is given by [18], [19]:

$$\begin{aligned} I(x_i; y_j) &= \log\left[p_{Y|X}(y_j|x_i)\right] - \log\left[p_Y(y_j)\right] \\ &= \log\left[\frac{p_{Y|X}(y_j|x_i)}{p_Y(y_j)}\right], \end{aligned} \tag{8}$$

where the logarithm is taken to the base 2. The average mutual information between the input X and the output Y is then:

$$I(X;Y) = \sum_{x_i}\sum_{y_j} p_{XY}(x_i, y_j) \log\left[\frac{p_{Y|X}(y_j|x_i)}{p_Y(y_j)}\right], \tag{9}$$

which can be rewritten for simplicity as:

$$\begin{aligned} I(X;Y) &= \sum_x \sum_y p_{XY}(x,y) \log\left[\frac{p_{Y|X}(y|x)}{p_Y(y)}\right] \\ &= \sum_x \sum_y p_X(x) p_{Y|X}(y|x) \log\left[\frac{p_{Y|X}(y|x)}{p_Y(y)}\right], \end{aligned} \tag{10}$$

where x and y represent the values of the random variables X and Y. Also, the marginal PMF $p_Y(y)$ is given by:

$$p_Y(y) = \sum_x p_X(x) p_{Y|X}(y|x)\,. \tag{11}$$

Therefore, if the conditional probability $p_{Y|X}(y|x)$ is given for the channel, $I(X;Y)$ in (10) can be maximized with respect to $p_X(x)$ to obtain the channel capacity as:

$$C = \max_{p_X(x)} I(X;Y)\,. \tag{12}$$

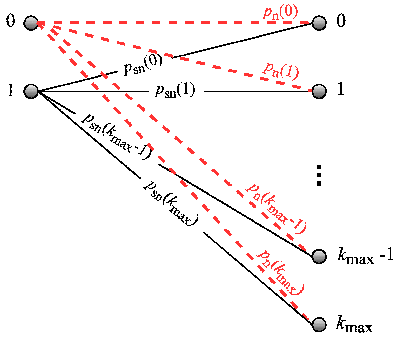

(a) Soft Decisions

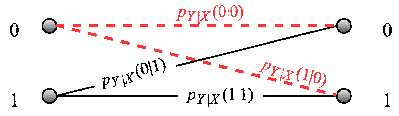

(b) Hard Decisions

Fig. 1. DMC modeling of a SPAD receiver.

Assuming a binary signaling case for the SPAD receiver, the input X takes the value 1 when a signal is present, and 0 when there is no incoming photon. Two categories may be considered depending on the SPAD output and the type of information provided to the decoder by the SPAD receiver:

1) The SPAD receiver makes no explicit symbol decision, but passes on the slot counts directly to the decoder. This process is termed as "soft decision". The soft decision capacity is expressed as a function of the channel conditional probability $p_{Y|X}(y|x)$.
2) The SPAD is designed such that it makes estimates of each input symbol, passing on these estimates to the decoder. This process is termed as "hard decision". The "hard decision" capacity is expressed as a function of the probability of symbol errors.

Fig. 1 shows the DMC model for the SPAD receiver with soft and hard outputs. In the following, the soft and hard decision capacities for the SPAD receiver with dead time are discussed.

B. Soft Decision Capacity

Define λ_s as the average incoming signal photon rate. Note that the SPAD receiver has an internal source of Poisson distributed noise, due to background counts such as dark counts and afterpulsing. Let the average photon rate from the background noise be denoted by λ_n. Therefore, when $X = 0$, the average number of photons in the time interval $[0, T_b)$ is $K_n = \lambda_n T_b$, and if $X = 1$, the average number of received photons is $K_s + K_n = (\lambda_s + \lambda_n)T_b$. According to (3), the

probabilities that exactly k photons are counted by the SPAD receiver in the counting interval of $T_{\rm b}$ seconds, denoted as $p_{\rm n}(k)$ and $p_{\rm sn}(k)$, for the corresponding input values of $X = 0$ and $X = 1$, are given by:

$$\begin{aligned} p_{\rm n}(k) &= p_K(k;\lambda_{\rm n}) \ , \\ p_{\rm sn}(k) &= p_K(k;\lambda_{\rm s}+\lambda_{\rm n}) \ . \end{aligned} \tag{13}$$

For the soft decision case, the output of the SPAD receiver, Y, is equal to the number of counts registered during the counting interval of $[0, T_{\rm b})$; thus Y can take all non-negative integer values 0, 1, 2, ..., $k_{\max}$. Furthermore, it follows that:

$$\begin{aligned} p_{Y|X}(y|0) &= p_{\rm n}(k) \ , \\ p_{Y|X}(y|1) &= p_{\rm sn}(k) \ . \end{aligned} \tag{14}$$

Assuming $p_X(x=1) = q$ and $p_X(x=0) = 1-q$, the average mutual information $I(X,Y)$ given in (10) is expressed as:

$$\begin{aligned} I(X;Y) = \sum_{k=0}^{k_{\max}} \Bigg\{ & (1-q)\, p_{\rm n}(k) \log\left[\frac{p_{\rm n}(k)}{p_Y(k)}\right] \\ & + q\, p_{\rm sn}(k) \log\left[\frac{p_{\rm sn}(k)}{p_Y(k)}\right] \Bigg\} \ , \end{aligned} \tag{15}$$

where $p_Y(k)$ is given using (11) as:

$$p_Y(k) = (1-q)\, p_{\rm n}(k) + q\, p_{\rm sn}(k) \ . \tag{16}$$

With (15) and (16), $I(X;Y)$ can be calculated for any given value of q, and thus the channel capacity C can be found using (12). For the SPAD receiver considered here, the channel capacity is a function of source statistics, SPAD dead time, and average signal and background counts.

C. Hard Decision Capacity

In this case, the output Y may take only two values, 0 and 1, as determined by a likelihood-ratio test. Thus, the conditional probabilities, $p_{Y|X}(y|x)$, for the four possible combinations of the binary input-output pair, (x, y), can be calculated as:

$$p_{Y|X}(0|0) = \Pr\{k \le k_{\rm TH} | x = 0\} = \sum_{k=0}^{k_{\rm TH}} p_{\rm n}(k), \tag{17}$$

$$p_{Y|X}(1|0) = 1 - p_{Y|X}(0|0), \tag{18}$$

$$p_{Y|X}(0|1) = \Pr\{k \le k_{\rm TH} | x = 1\} = \sum_{k=0}^{k_{\rm TH}} p_{\rm sn}(k), \tag{19}$$

$$p_{Y|X}(1|1) = 1 - p_{Y|X}(0|1), \tag{20}$$

where $k_{\rm TH}$ denotes the optimum threshold for maximum likelihood detection, which is given by:

$$k_{\rm TH} = \frac{K_{\rm s} + \ln\left(\frac{1-q}{q}\right)}{K_{\rm s}\delta + \ln\left(1 + \frac{K_{\rm s}}{K_{\rm n}}\right)} \ , \tag{21}$$

and $\delta = \tau/T_{\rm b}$ is the dead time ratio. Based on (17)–(20), and using (10), the average mutual information is calculated as:

$$\begin{aligned} I(X;Y) = \sum_{y=0}^{1} \Bigg\{ & (1-q)\, p_{Y|X}(y|0) \log\left[\frac{p_{Y|X}(y|0)}{p_Y(y)}\right] \\ & + q\, p_{Y|X}(y|1) \log\left[\frac{p_{Y|X}(y|1)}{p_Y(y)}\right] \Bigg\} \ . \end{aligned} \tag{22}$$

Note that, $p_{Y|X}(y|x)$ in (22) is a function of *a priori* probability q, since it depends on $k_{\rm TH}$, and $k_{\rm TH}$ given in (21) is a function of q.

IV. Numerical Results

Figs. 2–4 present performance results for the average mutual information, $I(X;Y)$, of the SPAD receiver as a function of *a priori* probability, q, for both soft decision and hard decision categories, based on (15) and (22) from Section III. The solid curves refer to the SPAD receiver with soft decision output, and the dashed curves represent the SPAD receiver with hard decision output. In Fig. 2 the effect of average signal count, $K_{\rm s}$, is studied for $K_{\rm s} = 5$, 15, 30, with an average background count of $K_{\rm n} = 10$ and a dead time ratio of $\delta = 0.05$. In Fig. 3 the effect of average background count, $K_{\rm n}$, is studied for $K_{\rm n} = 5$, 10, assuming $K_{\rm s} = 20$ and $\delta = 0.05$. In Fig. 4 the effect of the dead time ratio is studied for $\delta = 0$, 0.05, 0.1, assuming $K_{\rm s} = 20$ and $K_{\rm n} = 10$. These results indicate that, the average mutual information decreases with decreasing signal mean (see Fig. 2), increasing background counts mean (see Fig. 3), and increasing dead time (see Fig. 4). It is observed that the peak value of each curve which represents the channel capacity, occurs at or near $q = 0.5$ in most cases.

An obvious distinction between the two types of SPAD receivers is that the hard decision SPAD exhibits discontinuities in the $I(X;Y)$ curves. This is because of discrete nature of the decision threshold $k_{\rm TH}$ which jumps from one integer to the next at certain values of q. Furthermore, SPAD receivers with soft outputs result in higher average mutual information compared with the receivers with hard outputs. Thus, the hard decision SPAD gives a lower capacity than the SPAD receiver with soft outputs in all cases. This is because the slot counts provide additional information to the decoder in the soft decision case. Since both input and output take the values 0 and 1, a hard output SPAD receiver may be considered as an asymmetric binary channel with varying error transition probability, i.e. $p_{Y|X}(1|0)$ and $p_{Y|X}(0|1)$. Therefore, the channel capacity would not exceed 1.

Figs. 5–7 provide performance results for soft and hard decision capacities of the SPAD receiver, based on (15) and (22) from Section III. In Fig. 5, it is shown how the capacity is affected by the average signal count, $K_{\rm s}$. In this figure, an average background count of $K_{\rm n} = 10$ and two dead time ratios of $\delta = 0.1$, 0.001 are assumed. As shown in Fig. 2, higher average signal counts result in higher capacity values for both soft decision and hard decision cases. However, the capacity cannot exceed 1 and the minimum average signal count required for achieving the maximum capacity depends

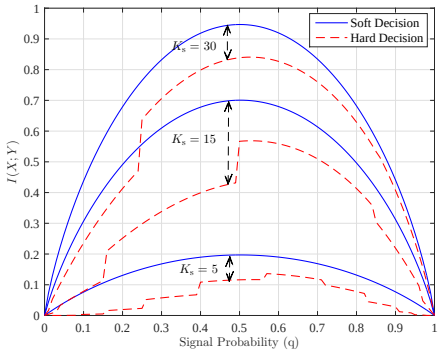

Fig. 2. Average mutual information, $I(X;Y)$, versus *a priori* signal probability, q, with $\delta = 0.05$, $K_\mathrm{n} = 10$.

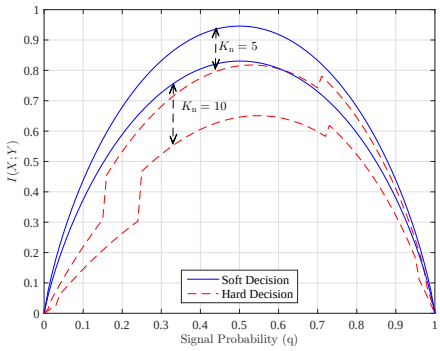

Fig. 3. Average mutual information, $I(X;Y)$, versus *a priori* signal probability, q, with $\delta = 0.05$, $K_\mathrm{s} = 20$.

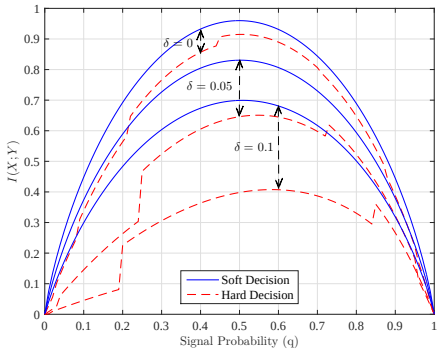

Fig. 4. Average mutual information, $I(X;Y)$, versus *a priori* signal probability, q, with $K_\mathrm{s} = 20$, $K_\mathrm{n} = 10$.

on the dead time of the receiver. Also, it can be observed from this figure that when $\delta = 0.001$, for $K_\mathrm{s} \geq 20$, the proposed capacity metric reaches it maximum value of 1 for both hard and soft decision cases and the limiting effect of dead time vanishes. This happens at a higher value ($K_\mathrm{s} \geq 100$) when larger dead time ratio ($\delta = 0.1$) is considered. This trend suggests that by choosing a proper incoming photon rate in practice, the information capacity of the SPAD receiver can be maximized.

The effect of SPAD background counts is shown in Fig. 6 where $K_\mathrm{s} = 100$ and $\delta = 0.1, 0.001$. According to this figure, when $\delta = 0.001$, background counts with mean counts lower than 100 have a negligible impact on the capacity. However, as the average background count increases, the capacity is severely limited. For larger values of the dead time ratio, the limiting effect of background counts appears in lower values of mean background count. Again, it is seen that higher values of dead time ratio lead to a larger gap between the soft decision and the hard decision capacities. Furthermore, this figure depicts that if the dead time ratio is small ($\delta = 0.001$), keeping the average background count lower than 110 photons/s, will help overcome the limiting effect of dead time on the capacity. However, for larger dead time ratio values such as $\delta = 0.1$, the maximum capacity is achieved only if $K_\mathrm{n} \leq 4$ for hard decision case and $K_\mathrm{n} \leq 10$ for soft decision case.

In Fig. 7, the capacity curves are plotted as a function of dead time ratio where $K_\mathrm{n} = 1$ and $K_\mathrm{s} = 10, 100$ are considered. As seen in this figure, dead time ratio values larger than 0.1 severely degrade the capacity. Hence, it is of greatest importance to keep dead time as small as possible.

Figs. 5–7 are presenting capacity results as a function of three parameters: K_s, K_n, and δ. In each figure, the effect of one parameter is studied while the two other parameters are fixed. In order to optimize the operating conditions and structure of a SPAD receiver to achieve maximum capacity, the effect of these parameters should be treated simultaneously.

V. Conclusions

In this study, the input-output information transfer rate of AQ SPAD receivers is investigated. The AQ SPAD receiver is modeled as a DMC with binary inputs, and a channel capacity metric is proposed to study the effect of SPAD dead time and background counts on the SPAD information transfer rate for both soft decision and hard decision categories. It is identified that soft decision outputs improve the capacity compared with the hard decision case. The proposed channel capacity metric is suitable for theoretical optimization of the device structure and operating conditions to maximize the achievable data rate. Future research will consider the effects of afterpulsing and timing jitter on the capacity of SPAD receivers, which may provide valuable insights into the fundamental limits of SPAD receivers for optical communication systems.

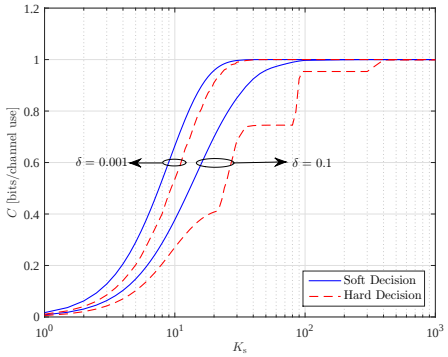

Fig. 5. Capacity of the SPAD receiver as a function of average signal count, K_s, with $K_\mathrm{n} = 10$ and $\delta = 0.1$, and 0.001.

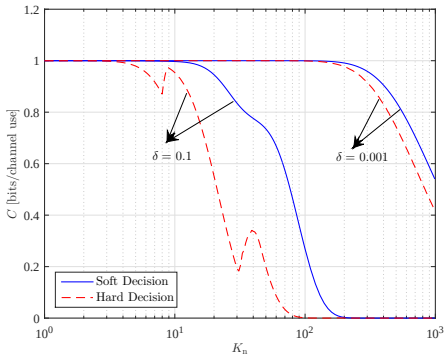

Fig. 6. Capacity of the SPAD receiver as a function of average background count, K_n, with $K_\mathrm{s} = 100$ and $\delta = 0.1$, and 0.001.

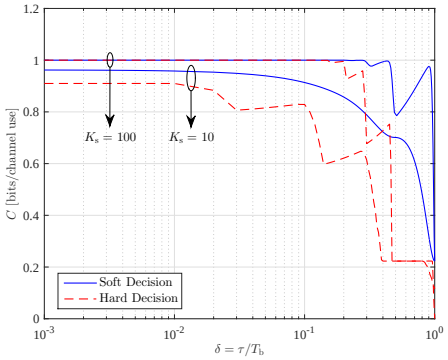

Fig. 7. Capacity of the SPAD receiver as a function of dead time ratio, δ, with $K_\mathrm{n} = 1$ and K_s =10, and 100.

ACKNOWLEDGMENT

Professor Harald Haas acknowledges support by the UK Engineering and Physical Sciences Research Council (EPSRC) under Grant EP/K008757/1.

REFERENCES

[1] D. Chitnis and S. Collins, "A SPAD-Based Photon Detecting System for Optical Communications," *J. Lightw. Technol.*, vol. 32, no. 10, pp. 2028–2034, May 2014.

[2] E. Fisher, I. Underwood, and R. Henderson, "A Reconfigurable Single-Photon-Counting Integrating Receiver for Optical Communications," *IEEE J. Solid-State Circuits*, vol. 48, no. 7, pp. 1638–1650, Jul. 2013.

[3] Y. Li, M. Safari, R. Henderson, and H. Haas, "Optical OFDM with Single-Photon Avalanche Diode," *IEEE Photonics Technol. Lett.*, vol. 27, no. 9, pp. 943–946, May 2015.

[4] E. Fisher, I. Underwood, and R. Henderson, "A Reconfigurable 14-bit 60GPhoton/s Single-Photon Receiver for Visible Light Communications," in *Proc. European Solid-State Circuits Conf.*, Bordeaux, France, 2012, pp. 85–88.

[5] Y. Li *et al.*, "Single Photon Avalanche Diode (SPAD) VLC System and Application to Downhole Monitoring," in *Proc. IEEE Global Commun. Conf.*, San Diego, CA, 2014, pp. 2108–2113.

[6] A. Spinelli and A. Lacaita, "Physics and Numerical Simulation of Single Photon Avalanche Diodes," *IEEE Trans. Electron Devices*, vol. 44, no. 11, pp. 1931–1943, Nov. 1997.

[7] A. Eisele *et al.*, "185 MHz Count Rate, 139 dB Dynamic Range Single-Photon Avalanche Diode with Active Quenching Circuit in 130 nm CMOS Technology," in *Proc. Int. Image Sensor Workshop*, Japan, 2011, pp. 278–281.

[8] E. Sarbazi and H. Haas, "Detection Statistics and Error Performance of SPAD-based Optical Receivers," in *Proc. IEEE 26th Ann. Int. Symp. Personal, Indoor, and Mobile Radio Commun.*, Hong Kong, China, 2015, pp. 830–834.

[9] E. Sarbazi, M. Safari, and H. Haas, "Photon Detection Characteristics and Error Performance of SPAD Array Optical Receivers," in *Proc. IEEE 4th Int. Workshop on Optical Wireless Commun.*, Istanbul, Turkey, 2015, pp. 132–136.

[10] C. Niclass *et al.*, "Design and Characterization of a CMOS 3-D Image Sensor Based on Single Photon Avalanche Diodes," *IEEE J. Solid-State Circuits*, vol. 40, no. 9, pp. 1847–1854, Sep. 2005.

[11] A. Tosi, F. Zappa, and S. Cova, "Single-Photon Detectors for Practical Quantum Cryptography," in *Proc. SPIE, Electr.-Opt. Remote Sensing, Photonic Technol. Appl. VI*, vol. 8542, Edinburgh, UK, 2012, p. 8.

[12] P. I. Hopman *et al.*, "An End-to-End Demonstration of a Receiver Array Based Free-Space Photon Counting Communications Link," in *Proc. SPIE Free-Space Laser Commun. VI*, vol. 6304, San Diego, CA, 2006, p. 13.

[13] R. H. Hadfield, "Single-Photon Detectors for Optical Quantum Information Applications," *Nat. Photon.*, vol. 3, no. 12, pp. 696–705, Nov. 2009.

[14] B. E. A. Saleh and M. C. Teich, *Fundamentals of Photonics*. New York: Wiley, 1991.

[15] R. M. Gagliardi and S. Karp, *Optical Communications*, 2nd ed. New York: Wiley, 1995.

[16] S. H. Lee and R. P. Gardner, "A New G–M Counter Dead Time Model," *Appl. Radiat. Isot.*, vol. 53, no. 4, pp. 731–737, Nov. 2000.

[17] J. H. Lee, I. J. Kim, and H. D. Choi, "On the Dead Time Problem of a GM Counter," *Appl. Radiat. Isot.*, vol. 67, no. 6, pp. 1094–1098, Jun. 2009.

[18] C. E. Shannon, "A Mathematical Theory of Communication," *Bell Syst. Tech. J.*, vol. 27, pp. 379–423, 623–656, Oct. 1948.

[19] R. G. Gallager, *Information Theory and Reliable Communication*. New York: Wiley, 1968.

IEEE TRANSACTIONS ON COMMUNICATIONS, VOL. 66, NO. 9, SEPTEMBER 2018 4043

Statistical Modeling of Single-Photon Avalanche Diode Receivers for Optical Wireless Communications

Elham Sarbazi, *Student Member, IEEE*, Majid Safari, *Member, IEEE*, and Harald Haas, *Fellow, IEEE*

***Abstract*— In this paper, a comprehensive analytical approach is presented for modeling the counting statistics of active quenching and passive quenching single-photon avalanche diode (SPAD) detectors. It is shown that, unlike ideal photon counting receiver for which the detection process is described by a Poisson arrival process, photon counts in practical SPAD receivers do not follow a Poisson distribution and are highly affected by the dead time caused by the quenching circuit. Using the concepts of renewal theory, the exact expressions for the probability distribution and moments (mean and variance) of photocounts in the presence of dead time are derived for both active quenching and passive quenching SPADs. The derived probability distributions are validated through Monte Carlo simulations and it is demonstrated that the moments match with the existing empirical models for the moments of SPAD photocounts. Furthermore, an optical communication system with on–off keying and binary pulse position modulation is considered and the bit error performance of the system for different dead time values and background count levels is evaluated.**

***Index Terms*— Single photon avalanche diode (SPAD), optical wireless communications, photon counting, dead time, active quenching, passive quenching, on-off keying (OOK), binary pulse position modulation (BPPM).**

I. Introduction

In RECENT years, there has been a growing interest in optical wireless communications (OWC) as a promising complementary solution to radio frequency (RF) technologies [1]. OWC systems primarily use positive-intrinsic-negative (PIN) diodes and avalanche photodiodes (APDs) as optical receivers. PIN diodes have simple structure and are relatively inexpensive. The main disadvantage of PIN diodes is their low gain. When operating at extremely low signal levels, their thermal noise can be more significant than the signal. Compared to PIN diodes, APDs are more complicated and expensive. They outperform PIN diodes with respect to sensitivity, as their internal gain reduces the thermal noise effect. However, the random multiplication process introduces additional gain-dependent excess noise, and this limits the maximum achievable gain of an APD. Therefore, high gain low noise transimpedance amplifiers (TIAs) are usually required for detection of relatively weak optical signals [2].

In photon-starving applications and long distance transmissions, the optical signal can be received at levels below the sensitivity of these conventional optical receivers and get lost in the thermal noise. Single photon avalanche diodes (SPADs) appear to be a more proper choice in such applications. SPADs provide very large internal gain, thereby easily overcoming thermal noise and enabling the detection of individual photons without the need for TIAs. Thanks to their high single-photon sensitivity and high gain, SPADs have enabled rapid progress in many applications [3]–[5]. These receivers are able to closely approach quantum-limited sensitivity in the detection of weak optical signals and have drawn particular attention in OWC [6]–[12].

SPADs are semiconductor devices with p-n junctions and operate based on a simple principle: if the reverse bias voltage of the p-n junction is raised slightly above the breakdown threshold voltage, a very high electric field is produced, and a single electron-hole pair, can trigger a strong avalanche, leading to a large internal gain and a measurable current. This current rises rapidly and continues until the avalanche is quenched by lowering the bias voltage down to or below breakdown threshold [13], [14]. To detect a subsequent photon, the bias voltage must be raised again above breakdown level. Reducing the bias voltage below the threshold and restoring the SPAD to the operative level, is accomplished by *quenching circuit*. The quenching process introduces a finite recovery time, known as *dead time*, during which the device does not respond to another incident photon [15].

There are two principal quenching modes: *passive quenching* (PQ) and *active quenching* (AQ). In general, AQ circuits offer shorter dead times and higher count rates compared with PQ circuits, but are more complex, more expensive to fabricate and larger in size [16]. The photon counting process of PQ SPADs is similar to *paralyzable* detectors where any photon arriving during dead time is not counted, but extends the dead time period. In AQ SPADs, similar to *nonparalyzable* detectors, the dead time is constant, and any photon arriving during dead time is neither counted nor it extends the dead time duration [16].

SPADs are still a relatively immature technology whose performance is degraded by the unavoidable dead time.

Manuscript received August 11, 2017; revised January 9, 2018 and March 12, 2018; accepted March 18, 2018. Date of publication April 12, 2018; date of current version September 14, 2018. Professor H. Haas acknowledges support by the UK Engineering and Physical Sciences Research Council (EPSRC) under Grant EP/K008757/1. The associate editor coordinating the review of this paper and approving it for publication was H. Wymeersch. *(Corresponding author: Elham Sarbazi.)*

The authors are with the Li-Fi Research and Development Centre, Institute for Digital Communications, School of Engineering, The University of Edinburgh, Edinburgh EH9 3JL, U.K. (e-mail: e.sarbazi@ed.ac.uk; majid.safari@ed.ac.uk; h.haas@ed.ac.uk).

Color versions of one or more of the figures in this paper are available online at http://ieeexplore.ieee.org.

Digital Object Identifier 10.1109/TCOMM.2018.2822815

The dead time is a limiting factor for the achievable data rate in OWC systems. Because of demands for higher data rates, several studies has been recently dedicated to reducing the effect of dead time by employing arrays of SPADs [17]–[20]. From a communication theory point of view, it is of great importance to investigate the effect of dead time on the performance of an SPAD-based OWC system. For this purpose, the statistical dead time-affected photon counting behavior of SPAD receivers needs to be precisely modeled.

A. Previous Works

In [21], the paralyzable and nonparalyzable count rate models are introduced which are the most well-known models for estimating the count rate of a single-photon detector. These two models have also been adopted for SPAD detectors to predict the approximate count rate [22]. The count rate is a useful metric for assessing how fast the detector can detect incoming photons. However, it does not provide a complete description of the detected and lost photons, required for error performance evaluation of communication systems. In [6], a SPAD-based visible light communications (VLC) system with OOK modulation is proposed to address the problem of continuous downhole monitoring in the oil and gas industry. In this article, a SPAD array is considered, and the counting losses due to SPAD's dead time have not been taken into account. In [7] and [8], a SPAD-based optical orthogonal frequency division multiplexing (OFDM) system is presented and the nonlinear distortion due to the saturation of SPAD receiver, as well as the bit error ratio performance of both DC-biased optical OFDM and asymmetrically clipped optical OFDM are investigated. Li *et al.* [7], [8] have assumed Poisson statistics for the distribution of SPAD photocounts, which is not an accurate approximation in the presence of dead time. In [23], the method of contour integration is used for deriving the photon counting distribution of a single-photon detector with paralyzable dead time. In [24], using the concepts of Poisson point processes, the effect of a nonparalyzable dead time is studied. In [25], a practical photon counting receiver in optical scattering communication with finite sampling rate, paralyzable dead time, and electrical noise is characterized where it is shown that the dead time effect leads to sub-Poisson distribution for the number of recorded pulses. The approximate photocount distribution derived in [25], is only applicable if the photon rate is sufficiently low. In [26], we studied the statistical behavior of an AQ SPAD receiver and investigated the effect of nonparalyzable dead time on the bit error performance of an optical system. We extended our approach in [27] and an array of AQ SPADs was characterized for OWC applications. We also studied the information transfer rate of an AQ SPAD in [28] where the AQ SPAD receiver was modeled as a discrete memoryless channel, and the information transfer rate was studied using an information theoretic approach.

B. Our Contribution

In this study, we establish a mathematical framework and precisely model the photon counting behavior of SPAD receivers. We apply the concepts of renewal theory to develop exact expression for the probability distribution of photon counts in the presence of a general type of dead time, and then provide the exact probability distribution, mean and variance of AQ and PQ SPAD photocounts. Moreover, we study the bit error performance of a SPAD-based optical link. This study shows that the counting process of a SPAD receiver in the presence of dead time cannot be accurately approximated by a Poisson distribution. To the best of our knowledge, there exists limited, if not any analytical work to find the exact photocount distribution of SPAD photocounts, considering the impact of dead time. Although the main focus of this article is on SPAD detectors, but the approach can be applied to a variety of single-photon detectors with similar photon counting behavior.

The rest of this paper is organized as follows. In Section II, the concepts of renewal theory are applied for modeling the exact dead time-modified photocount distribution of a detector with a general type of dead time. The exact photocount distribution of AQ and PQ SPAD receivers are then derived in Section III using the results obtained in Section II, and Monte Carlo methods are employed to verify the validity of the analytical models. The system model of a SPAD-based optical system is described in Section IV, and in Section V, the numerical and analytical results are compared and discussions on the bit error performance of the system are provided. Finally, concluding remarks are given in Section VI.

II. Description of the Theoretical Framework

In this section, first the concepts of "product density functions" and "renewal processes" are introduced. These tools are then applied for modeling the dead time-modified photocount distribution of SPAD receivers based on a general approach that can be applied to both AQ and PQ SPADs.

A. Product Density Functions

Consider a stochastic point process N corresponding to events occurring at times $\{t_i\}$, $i = 0, 1, \ldots$. Let $N(t)$ represent the stochastic variable denoting the number of events in the time interval $(0, t)$. Then $dN(t)$ denotes the number of events in the small interval $(t, t + dt]$. A function $f_1(t)dt$ is defined such that [29]:

$$f_1(t)dt = E[dN(t)], \tag{1}$$

where $E[dN(t)]$ represents the average number of events in interval $(t, t+dt]$. Accordingly, the product of two stochastic variables $dN(t_1)$ and $dN(t_2)$ is defined as [29]:

$$f_2(t_1, t_2)dt_1dt_2 = E[dN(t_1)dN(t_2)], \tag{2}$$

which is also equal to the joint probability that an event occurs in $(t_1, t_1 + dt_1]$ and another event occurs in $(t_2, t_2 + dt_2]$. The function f_2 is called a product density of order 2. Similarly, the product density function of order k, $f_k(t_1, t_2, \ldots, t_k)$, is defined as [29]:

$$f_k(t_1, t_2, \ldots, t_k)dt_1dt_2 \ldots dt_k = E[dN(t_1) \ldots dN(t_k)], \tag{3}$$

where $f_k(t_1, t_2, \ldots, t_k)dt_1dt_2 \ldots dt_k$ represents the probability that an event occurs in the interval between t_1 and $t_1 + dt_1$,

$$\left.\frac{\partial^k G(z,t)}{\partial z^k}\right|_{z=1} = k! \int_0^t dt_k \int_0^{t_k} dt_{k-1} \ldots \int_0^{t_3} dt_2 \int_0^{t_2} f_1(t_1) f_1(t_2 - t_1) \ldots f_1(t_k - t_{k-1}) dt_1, \quad (7)$$

one event between t_2 and $t_2 + dt_2$, ..., and one between t_k and $t_k + dt_k$.

Provided that $t_1, t_2, \ldots, t_k$ are ordered ($t_1 < t_2 < \cdots < t_k$) and the general class of Poisson processes is considered, the following equation holds between the product density of order k and the product densities of order one [29]:

$$f_k(t_1, t_2, \ldots, t_k) = f_1(t_1) f_1(t_2 - t_1) \ldots f_1(t_k - t_{k-1}). \quad (4)$$

We shall now apply the above tools to the problem of modeling the exact counting distribution of a SPAD receiver impaired by dead time. The aim is to determine $p(k,t)$, the probability that k photons have been detected during time interval $(0,t)$. It is clear that what happens between t and $t+dt$ is not only dependent on the fact that k photons have been detected in time interval $(0,t)$, but also upon the detection time of last photon, due to dead time. Hence, the usual method of expressing $p(k,t+dt)$ in terms of $p(k,t)$ is mathematically involved. We first determine $G(z,t)$, the generating function (G.F.) corresponding to $p(k,t)$, which is given by:

$$G(z,t) = \sum_{k=0}^{\infty} p(k,t) z^k. \quad (5)$$

The following property holds for $G(z,t)$ and the product density of order k [29]:

$$\left.\frac{\partial^k G(z,t)}{\partial z^k}\right|_{z=1} = \int_0^t \int_0^t \ldots \int_0^t f_k(t_1, t_2, \ldots, t_k) dt_1 dt_2 \ldots dt_k. \quad (6)$$

Note that f_k is symmetrical in t_1, t_2, ..., t_k, and (6) can be written as (7) at the top of this page. The following equation is then deduced from (7):

$$\left.\frac{\partial G(z,t)}{\partial z}\right|_{z=1} = \int_0^t f_1(t_1) dt_1 \quad (8)$$

Now, let the Laplace transform (L.T.) of the function $f_1(t)$ with respect to the variable t be $F_1(s) = \int_0^\infty f_1(t) e^{-st} dt$. Taking the L.T. of (8) gives:

$$g(z,s) = \frac{1}{s} \times \frac{1}{1 - (z-1) F_1(s)}, \quad (9)$$

where $g(z,s)$ is the L.T. of the function $G(z,t)$. Let also define $P(k,s)$ as the L.T. of the function $p(k,t)$. The following diagram summarizes how the four functions $p(k,t)$, $P(k,s)$, $G(z,t)$, and $g(z,s)$ are connected:

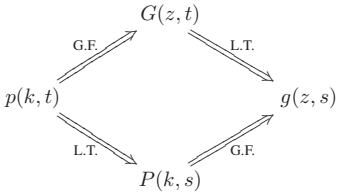

Since $g(z,s)$ is the G.F. of $P(k,s)$, according to (9), $P(k,s)$ can be obtained as [30]:

$$P(k,s) = \frac{1}{s} \times \frac{[F_1(s)]^k}{[1 + F_1(s)]^{k+1}}. \quad (10)$$

From this, it can be concluded that if $f_1(t)$ or $F_1(s)$ is known for the point process associated with the SPAD's photon counting process, $P(k,s)$, and hence, $p(k,t)$ can be obtained.

B. Renewal Processes

By definition, a counting process $\omega = \{N(t) : t \geq 0\}$ with the occurrence time sequence of $\{t_i\}$, is called a renewal process if the inter-occurrence times $w_1 = t_1 - t_0$, $w_2 = t_2 - t_1$, ... are independently and identically distributed random variables. In the case of a Poisson point process, the inter-occurrence times are independently and identically distributed exponential random variables [29]. In this work, assuming a Poisson arrival process for incoming photons, the photon counts form a renewal counting process with:

$$p(k,t) = \Pr\{N(t) = k\}. \quad (11)$$

For renewal processes, the usual method for obtaining $p(k,t)$ is through renewal integral equations in which $p(k,t)$ is expressed in terms of $p(k-1,t)$. This requires the use of product density functions as introduced earlier. First, please note that the equation in (4) between the product densities of order 1 and k implies that given an event at $t = 0$, the probability that an event occurs between t and $t + dt$ is determined by $f_1(t)dt$ and is independent of what happened before $t = 0$.

Consider a SPAD detector with dead time τ (whether paralyzable or nonparalyzable or a combination of both). For simplicity, normalized photon arrival rate is assumed throughout the derivations. Given a photon registered at $t = 0$, if the *next* photon arrives in the time period of $(0, \tau)$ it is not detected, but if it arrives after the dead time of the photon occurring at $t = 0$, it is counted. The probability that the *next* photon arrives between t' and $t' + dt'$, given that the first photon is registered at $t = 0$, can be expressed by the function $(-\partial\phi(t')/\partial t')dt'$ where $\phi(t)$ represents the probability that no photon arrives between 0 and t, given that a photon arrived at $t = 0$ [29]. The integral equation for this renewal process can be written as:

$$p(k,t) = \int_0^t p(k-1, t-t') \left(-\frac{\partial\phi(t')}{\partial t'}\right) dt' + \delta(k)\phi(t), \quad (12)$$

where $\delta(k) = 1$ for $k = 0$ and 0 otherwise. In the above renewal equation, the first term in the right-hand side, accounts for the case where the next photon arrives between t' and $t' + dt'$. This photon is not detected if $0 < t' \leq \tau$. The second term represents the case where no photon arrives

$$p(k,t)=\sum_{r=0}^{K_1}(-1)^r\binom{k+r-1}{r}\frac{(t-k\tau_1-r\tau_2)^{k+r}}{(k+r)!}e^{-(k+r)\tau_2}-\sum_{r=0}^{K_2}(-1)^r\binom{k+r}{r}\frac{(t-(k+1)\tau_1-r\tau_2)^{k+r+1}}{(k+r+1)!}e^{-(k+r+1)\tau_2}, \tag{16}$$

during time interval $(0,t)$. The following equation holds for the G.F. corresponding to $p(k,t)$:

$$G(z,t)=\int_0^t zG(z,t-t')(-\frac{\partial\phi(t')}{\partial t'})dt'+\phi(t). \tag{13}$$

Taking the L.T. of the above equation with respect to the variable t gives:

$$g(z,s)=\frac{\Phi(s)}{1+z(s\Phi(s)-1)}, \tag{14}$$

where $\Phi(s)$, is the L.T. of the function $\phi(t)$. Since $g(z,s)$ is also the G.F. of $P(k,s)$, according to (14), $P(k,s)$ is given by [30]:

$$P(k,s)=\Phi(s)(1-s\Phi(s))^k. \tag{15}$$

Thus, if $\phi(t)$ (and hence, $\Phi(s)$) is known for SPAD's photon counting renewal process, $p(k,t)$ can be obtained by finding the inverse L.T. of the above equation.

C. A Solution for SPAD Receivers with Dead Time

The above results can now be applied to derive the probability distribution function $p(k,t)$ of the number of detected photons, k, in a time interval of $(0,t)$ in the presence of detector dead time. Here, a general approach is proposed which provides the dead time-modified photocount distribution of any photon counting detector. Note that AQ and PQ SPADs are special cases and will be addressed later in Section III.

Suppose that detected and lost photons are followed by two different dead times, τ_1 and τ_2, respectively. Assuming different dead time values for detected and lost photons, helps to clearly reflect distinct effects of paralyzable and nonparalyzable dead times on the total renewal process. For such a detector, we have the following results.

Theorem 1: For a general photon counting detector with dead times τ_1 and τ_2, the probability distribution function, $p(k,t)$, of the number of detected photons, k, in a time interval $(0,t)$ is given by (16) at the top of this page where K_1 and K_2 are integers such that:

$$\frac{t-k\tau_1}{\tau_2}-1<K_1<\frac{t-k\tau_1}{\tau_2}$$
$$\frac{t-(k+1)\tau_1}{\tau_2}-1<K_2<\frac{t-(k+1)\tau_1}{\tau_2}.$$

Proof: Assume that $\tau_1>\tau_2$. The probability $\phi(t)$ that no photon is detected up to time t, given that a photon is registered at $t=0$, is:

$$\phi(t)=[\mathbb{1}(t)-\mathbb{1}(t-(\tau_1-\tau_2))]+\phi^{\mathrm{p}}(t-(\tau_1-\tau_2))\mathbb{1}(t-(\tau_1-\tau_2)), \tag{17}$$

where $\mathbb{1}(t)$ is the unit step function, and is equal to 1 if $t\geq 0$, and 0, otherwise. In the above equation, the total probability of not detecting any photons is obtained as follows: The first term in the right-hand side of (17) expresses the condition that no photon is detected for $t<\tau_1-\tau_2$. If any photon arrives during time interval of $(0,\tau_1-\tau_2)$, it is clearly lost and is followed by a dead time of length τ_2, and this dead time won't extend beyond the dead time caused by the registered photon at $t=0$, i.e. τ_1. Thus, $\phi(t)=1$ for $t<\tau_1-\tau_2$. If any photon arrives after $\tau_1-\tau_2$, the dead time will be extended beyond τ_1. It is then valid to assume that the detector is in paralyzable mode, where $\phi^{\mathrm{p}}(t-(\tau_1-\tau_2))$ represents the probability that no photon is registered in time $t-(\tau_1-\tau_2)$. Applying L.T. to (17) gives:

$$\Phi(s)=\frac{1}{s}(1-e^{-s(\tau_1-\tau_2)})+e^{-s(\tau_1-\tau_2)}\Phi^{\mathrm{p}}(s). \tag{18}$$

In order to obtain $\Phi^{\mathrm{p}}(s)$ and then $\Phi(s)$, the product density of the first order for the paralyzable mode is easily calculated as:

$$f_1{}^{\mathrm{p}}(t)dt=\mathbb{1}(t-\tau_2)e^{-\tau_2}dt. \tag{19}$$

The above expression results from arguing that a photon is detected if it arrives after the dead time of the photon at $t=0$ is finished ($t>\tau_2$) and it is also not preceded by any photon arrival event in time interval $(0,\tau_2)$. Thus:

$$F_1{}^{\mathrm{p}}(s)=\frac{1}{s}e^{-(s+1)\tau_2}. \tag{20}$$

$F_1{}^{\mathrm{p}}(s)$ and $\Phi^{\mathrm{p}}(s)$ are related through (9) and (14):

$$\Phi^{\mathrm{p}}(s)=\frac{1}{s}\times\frac{1}{1+F_1{}^{\mathrm{p}}(s)}. \tag{21}$$

Therefore, (18), (20) and (21) result in:

$$F_1(s)=\frac{1}{se^{s\tau_1+\tau_2}+e^{s(\tau_1-\tau_2)}-1}. \tag{22}$$

The same result is obtained for $\tau_1<\tau_2$ following exactly the same arguments. According to (10), for general values of τ_1 and τ_2, the expression in (23) at the top of next page is obtained for $P(k,s)$. Applying the inverse L.T. then leads to (24). Using the following equality for $t>0$:

$$\frac{1}{2\pi i}\int_{\alpha-i\infty}^{\alpha+i\infty}\frac{e^{st}}{s^k}ds=\frac{t^{k-1}}{(k-1)!},$$

the final expression in (16) for $p(k,t)$ is obtained. This completes the proof for Theorem 1. ■

When $\tau_1\neq 0$ and $\tau_2\neq 0$, $p(k,t)$ is given by a finite series. Particular cases include:

- With $\tau_2=0$, the photocount distribution for an AQ SPAD is obtained.

$$P(k,s) = \frac{1}{s}\left[\left(e^{s\tau_1+\tau_2} + e^{s(\tau_1-\tau_2)}\right)^{-k} - \left(e^{s\tau_1+\tau_2} + e^{s(\tau_1-\tau_2)}\right)^{-(k+1)}\right] \tag{23}$$

$$\begin{aligned} p(k,t) &= \frac{1}{2\pi i}\int_{\alpha-i\infty}^{\alpha+i\infty}\left[\frac{1}{s}\left(e^{s\tau_1+\tau_2} + e^{s(\tau_1-\tau_2)}\right)^{-k} - \frac{1}{s}\left(e^{s\tau_1+\tau_2} + e^{s(\tau_1-\tau_2)}\right)^{-(k+1)}\right]e^{st}ds \\ &= \frac{1}{2\pi i}\int_{\alpha-i\infty}^{\alpha+i\infty}\sum_{r=0}^{\infty}\left[e^{-(k+r)\tau_2}(-1)^r\binom{k+r-1}{r}\frac{e^{s(t-k\tau_1-r\tau_2)}}{s^{k+r+1}}\right]ds \\ &\quad - \frac{1}{2\pi i}\int_{\alpha-i\infty}^{\alpha+i\infty}\sum_{r=0}^{\infty}\left[e^{-(k+r+1)\tau_2}(-1)^r\binom{k+r}{r}\frac{e^{s(t-(k+1)\tau_1-r\tau_2)}}{s^{k+r+2}}\right]ds \end{aligned} \tag{24}$$

- With $\tau_1 = \tau_2$, the photocount distribution for a PQ SPAD is obtained.
- With $\tau_1 = \tau_2 = 0$, the Poisson distribution for an ideal detector is obtained.

Note that the dead time of detected and lost photons are not the same in general, e.g. for an AQ SPAD. In the next section, AQ and PQ SPADs are studied in detail.

III. SPAD's Counting Statistics

In the absence of dead time, photon detection events of a SPAD receiver are modeled as a Poisson process and the probability of counting k photons during a time period of $(0, T_{\rm b})$ is given by [1]:

$$p_0(k) = \frac{(\lambda T_{\rm b})^k e^{-\lambda T_{\rm b}}}{k!}, \tag{25}$$

where the constant λ is the average photon arrival rate (in photons/s), hence, $\lambda T_{\rm b}$ is the average number of photons arriving at the SPAD during the observation time of $T_{\rm b}$ seconds. The photon arrival rate λ is related to the power of the optical signal by [1]:

$$\lambda = \frac{\eta_{\rm QE} P_{\rm r}}{h\nu}, \tag{26}$$

where $\eta_{\rm QE}$ is the quantum efficiency of the SPAD; $P_{\rm r}$ denotes the power of the incident optical signal; h is the Planck's constant; and ν represents the frequency of the optical signal.

In the presence of dead time, however, the photon counts no longer follow a Poisson distribution. In this section, the results of previous section are applied to study the counting statistics of AQ and PQ SPAD receivers. Throughout this work, it is assumed that the sampling rate is very high compared to dead time, so that the counting losses arising from finite sampling rates are negligible. It is also assumed that the SPAD uses the rising edge of a pulse as an event to count. Therefore, the total number of counted photons during the counting interval of $(0, T_{\rm b})$ is obtained by recording the number of rising edges of the pulse train and it can not exceed $k_{\max} = \lfloor T_{\rm b}/\tau \rfloor + 1$, where $\lfloor x \rfloor$ denotes the largest integer that is smaller than x.

A. AQ SPAD

For AQ SPADs, after each photon detection, the detector is inactive for a constant time τ. A photon is detected if and only if no detection event has taken place during a time τ preceding it, and any photon arriving during the dead time is neither counted nor has any influence on the dead time duration.

Theorem 2: The photocount distribution of an AQ SPAD with nonparalyzable dead time of τ, during the time interval of $(0, T_{\rm b})$ is given by:

$$p_K(k) = \sum_{i=0}^{k}\psi(i,\lambda_{k+1}) - \sum_{i=0}^{k-1}\psi(i,\lambda_k), \tag{27}$$

for $k < k_{\max}$. Function $\psi(i,\lambda)$ is defined as $\psi(i,\lambda) = \lambda^i e^{-\lambda}/i!$, and $\lambda_k = \lambda(T_{\rm b} - k\tau)$.

Proof: Assuming $\tau_2 = 0$ in (16), the photocount distribution for an AQ SPAD is obtained:

$$\begin{aligned} p(k,t) &= \sum_{r=0}^{\infty}(-1)^r\binom{k+r-1}{r}\frac{\lambda^{k+r}(t-k\tau)^{k+r}}{(k+r)!} \\ &\quad - \sum_{r=0}^{\infty}(-1)^r\binom{k+r}{r}\frac{\lambda^{k+r+1}(t-(k+1)\tau)^{k+r+1}}{(k+r+1)!} \end{aligned} \tag{28}$$

for $k < k_{\max}$, and $p(k,t) = 0$ for $k \geq k_{\max}$. Note that in (16) normalized photon arrival rate (i.e. $\lambda = 1$) was assumed and in (28) this assumption is released. The expression for $p(k,t)$ can be further simplified to:

$$\begin{aligned} p(k,t) &= \sum_{i=0}^{k}\frac{\lambda^i(t-(k+1)\tau)^i}{i!}e^{-\lambda(t-(k+1)\tau)} \\ &\quad - \sum_{i=0}^{k-1}\frac{\lambda^i(t-k\tau)^i}{i!}e^{-\lambda(t-k\tau)}. \end{aligned} \tag{29}$$

Hence, $p_K(k) = p(k,t)|_{t=T_{\rm b}}$ and the theorem follows. ■

The above expression is in line with results previously derived in [24] and [26]. The probability mass function (PMF) obtained in (27) is plotted in Fig. 1 and compared with Monte Carlo simulation results for different values of dead time ratio, $\delta = \tau/T_{\rm b}$. In this figure, a time interval of $T_{\rm b} = 1$ μs is considered and $\lambda = 3\times10^7$ photons/s. Also, $\delta = 0$, 0.02, 0.05, and 0.07 are assumed. Note that for a receiver without dead time, the photocount distribution is Poisson with mean $\lambda T_{\rm b}$. For the PMF expression in (27), some of the main properties shall be addressed as follows:

1) The Unitary Condition: As required for any valid distribution function, for the PMF in (27), the equality $\sum_k p_K(k) = 1$ holds. Furthermore, it is easily seen that

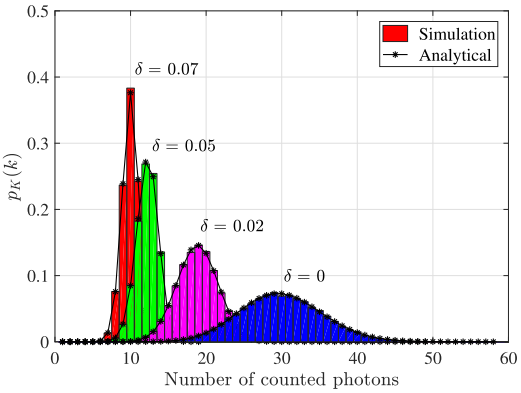

Fig. 1. Probability distribution of AQ SPAD photocounts for $T_\mathrm{b} = 1$ μs, $\lambda = 3 \times 10^7$ photon/s and different values of δ.

$\lim_{\tau \to 0} p_K(k) = p_0(k)$, that is, when τ goes to zero, the original Poisson distribution is recovered.

2) First and Second Moments:

Proposition 3: The mean and variance of the photocount distribution in (27) are:

$$\mu_K = (k_\mathrm{max} - 1) - \sum_{k=0}^{k_\mathrm{max}-2} \sum_{i=0}^{k} \psi(i, \lambda_{k+1}), \tag{30}$$

$$\sigma_K^2 = \sum_{k=0}^{k_\mathrm{max}-2} \sum_{i=0}^{k} (2k_\mathrm{max} - 2k - 3)\psi(i, \lambda_{k+1}) - \left(\sum_{k=0}^{k_\mathrm{max}-2} \sum_{i=0}^{k} \psi(i, \lambda_{k+1}) \right)^2. \tag{31}$$

Proof: Please refer to Appendix B. ∎

Again, as dead time goes to zero, the limiting relations $\lim_{\tau \to 0} \mu_K = \lambda T_\mathrm{b}$ and $\lim_{\tau \to 0} \sigma_K^2 = \lambda T_\mathrm{b}$ in (30) and (31) can be verified, where λT_b is the mean value of the ideal Poisson distribution.

Fig. 2a presents μ_K and σ_K^2 for an AQ SPAD as functions of λ where they are compared to an ideal Poisson counting process. As shown, the difference between μ_K and σ_K^2 becomes more significant as λ increases. Let the ratio of the variance to mean be defined as:

$$\xi = \frac{\sigma_K^2}{\mu_K}. \tag{32}$$

Fig. 2b illustrates this ratio where it approaches to zero as λ goes to infinity, unlike the Poisson distribution where this ratio is equal to one for all values of λ.

3) Asymptotic Mean for Large T_b/τ Ratio: The exact mean value in (30) can also be expressed as follows:

$$\mu_K = (k_\mathrm{max} - 1) - \sum_{k=0}^{k_\mathrm{max}-2} \frac{\Gamma(k+1, \lambda_{k+1})}{\Gamma(k+1)}, \tag{33}$$

where for a positive integer s, $\Gamma(s) = (s-1)!$ and $\Gamma(s,x) = e^{-x}(s-1)! \sum_{i=0}^{s-1} \frac{x^i}{i!}$ are the gamma function and incomplete gamma function, respectively [30]. Defining $\gamma(s,x) = \Gamma(s,x)/\Gamma(s)$, the following approximation holds for $\gamma(k+1, \lambda_{k+1})$ when T_b/τ goes to infinity [30]:

$$\gamma(k+1, \lambda_{k+1}) \approx \begin{cases} 1, & k+1 > \lambda_{k+1} \\ 0, & k+1 \leq \lambda_{k+1} \end{cases}.$$

Therefore, $\gamma(k+1, \lambda_{k+1})$ can be approximated as zero for $k \leq (\lambda T_\mathrm{b} - \lambda\tau - 1)/(1 + \lambda\tau)$, and 1, otherwise. Applying the above approximation to (33) gives:

$$\lim_{T_\mathrm{b}/\tau \to \infty} \mu_K = \frac{\lambda T_\mathrm{b}}{1 + \lambda\tau}. \tag{34}$$

Thus, the asymptotic count rate of an AQ SPAD, i.e. the average number of recorded photons per second, is given by:

$$\lambda' = \frac{\lambda}{1 + \lambda\tau}. \tag{35}$$

This expression is in line with the asymptotic expressions presented in [31] and the practical models provided in [22].

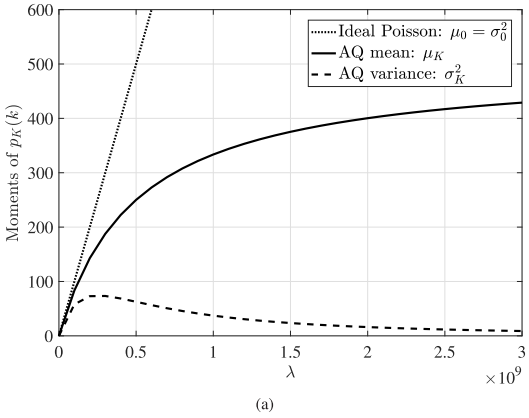

Fig. 2. First and second moments of AQ SPAD photocounts with $T_\mathrm{b} = 1$ μs, $\tau = 2$ ns: (a) comparison of mean and variance with ideal Poisson distribution, (b) the variance to mean ratio.

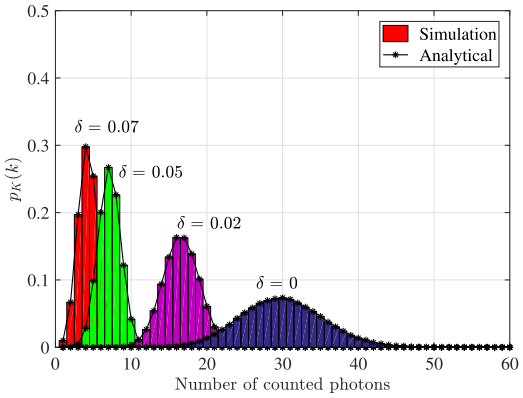

Fig. 3. Probability distribution of PQ SPAD photocounts for $T_\mathrm{b} = 1$ μs, $\lambda = 3 \times 10^7$ photon/s and different values of δ.

B. PQ SPAD

For PQ SPADs, any photon arrival is followed by dead time, and the ones occurring during the dead time of previous photons, extend the dead time duration.

Theorem 4: The photocount distribution of a PQ SPAD with paralyzable dead time of τ, during the time interval of $(0, T_\mathrm{b})$ is given by:

$$p_K(k) = \sum_{i=k}^{k_{\max}-1} (-1)^{i-k} \binom{i}{k} \frac{\lambda^i (T_\mathrm{b} - i\tau)^i}{i!} e^{-i\lambda\tau}, \quad (36)$$

for $k < k_{\max}$ and $p_K(k) = 0$ for $k \geq k_{\max}$.

Proof: Assuming $\tau_1 = \tau_2 = \tau$ in (16), the photocount distribution for a PQ SPAD is obtained which is further simplified to:

$$p(k,t) = \sum_{r=0}^{K} (-1)^r \binom{k+r}{r} \frac{\lambda^{k+r}(t-(k+r)\tau)^{k+r}}{(k+r)!} e^{-(k+r)\lambda\tau}. \quad (37)$$

With a change of variable $i = k + r$:

$$p(k,t) = \sum_{i=k}^{K+k} (-1)^{i-k} \binom{i}{k} \frac{\lambda^i (t - i\tau)^i}{i!} e^{-i\lambda\tau}. \quad (38)$$

where K is an integer such that:

$$\frac{t}{\tau} - (k+1) < K < \frac{t}{\tau} - k$$

With $p_K(k) = p(k,t)|_{t=T_\mathrm{b}}$, and therefore $K + k = k_{\max} - 1$, the expression in (36) is obtained. Hence, the theorem follows. ∎

The PMF obtained in (36) is plotted in Fig. 3 and compared with the Monte Carlo simulation results for different values of $\delta = \tau/T_\mathrm{b}$. In Fig. 3, a time interval of $T_\mathrm{b} = 1$ μs is considered and $\lambda = 3 \times 10^7$ photons/s. Also, $\delta = 0$, 0.02, 0.05, and 0.07 are assumed. Note that for a receiver without dead time, the photocount distribution is Poisson with mean λT_b. For the PMF expression in (36), some of the main properties are addressed as follows:

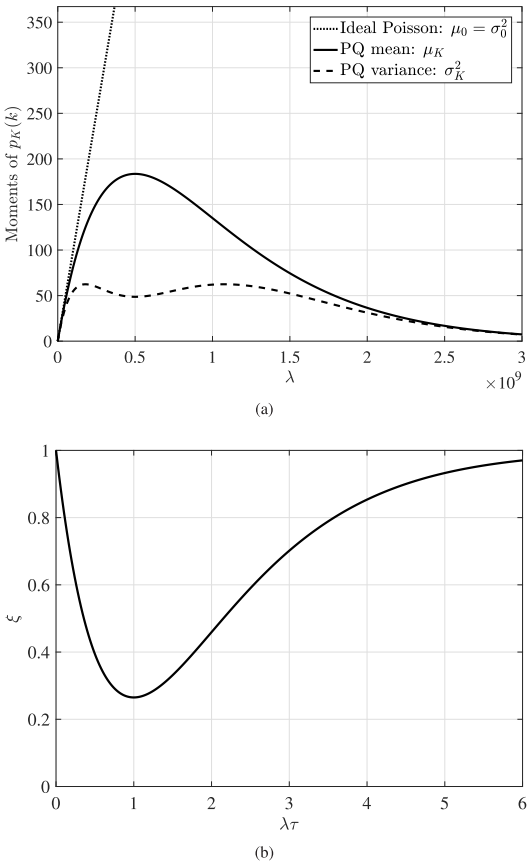

Fig. 4. First and second moments of PQ SPAD photocounts with $T_\mathrm{b} = 1$ μs, $\tau = 2$ ns: (a) comparison of mean and variance with ideal Poisson distribution, (b) the variance to mean ratio.

1) The Unitary Condition: It can easily be verified that the unitary condition $\sum_{k=0}^{\infty} p_K(k) = 1$ holds for the PMF in (36) and $\lim_{\tau\to 0} p_K(k) = p_0(k)$, that is, when τ goes to zero, the PMF in (36) approaches the ideal Poisson distribution.

2) First and Second Moments:

Proposition 5: The mean and variance of the photocount distribution in (36) are derived as:

$$\mu_K = \lambda e^{-\lambda\tau}(T_\mathrm{b} - \tau), \quad (39)$$

$$\sigma_K^2 = \lambda^2 \, e^{-2\lambda\tau}(3\tau^2 - 2\, T_\mathrm{b}\tau) + \lambda e^{-\lambda\tau}(T_\mathrm{b} - \tau). \quad (40)$$

Proof: Please refer to Appendix C. ∎

Similar to AQ SPAD, the limiting relations $\lim_{\tau\to 0} \mu_K = \lambda T_\mathrm{b}$ and $\lim_{\tau\to 0} \sigma_K^2 = \lambda T_\mathrm{b}$ in (39) and (40) can be confirmed, where λT_b is the mean value of the ideal Poisson distribution (see Appendix C). Fig. 4a presents μ_K and σ_K^2 for a PQ SPAD as functions of λ. The mean and variance are also compared to an ideal counting process where it is observed that unlike a Poisson process, μ_K and σ_K^2 can differ greatly. Fig. 4b

illustrates the ratio, ξ, as defined in (32) where the minimum occurs at $\lambda\tau = 1$ and the ratio approaches 1 when $\lambda\tau$ goes to infinity.

3) Asymptotic Mean for Large $T_{\rm b}/\tau$ Ratio: For the case when the ratio $T_{\rm b}/\tau$ is large, yet the dead time cannot be ignored, the following asymptotic expression for mean value is obtained:

$$\lim_{T_{\rm b}/\tau\to\infty} \mu_K = \lambda T_{\rm b} e^{-\lambda\tau}. \tag{41}$$

Therefore, the asymptotic count rate of a PQ SPAD, i.e. the average number of recorded photons per second, is given by:

$$\lambda' = \lambda e^{-\lambda\tau}. \tag{42}$$

This expression is in line with the asymptotic expressions presented in [31] and the practical models provided in [22].

IV. SPAD-Based Optical Communication Systems

SPADs have been used as photon counting receivers in OWC systems [7], [17], [19], [20]. Free space optics (FSO), VLC, wireless IR, deep space communications are all examples of such OWC applications. In this section the effect of dead time on the bit error performance of a SPAD-based optical system with on-off keying (OOK) and binary pulse position modulation (BPPM) is studied. The SPAD's dead time also limits the maximum achievable data rate of the system. The dead time of commercially available SPAD devices varies in the range of a few nanoseconds to tens of nanoseconds. Using binary modulation schemes, a reliable bit error performance with maximum data rate of a few Mbits/s can be achieved. For example, with OOK modulation, the highest data rate to be achieved by an AQ SPAD with dead time τ can not exceed $1/\tau$, and this is due to saturation of SPAD receiver [26]. For a PQ SPAD receiver the maximum achievable data rate is even lower than $1/\tau$. Note that the maximum achievable data rate depends on not only the dead time, but also the operating conditions [28]. Throughout this paper, a data rate of 1 Mbits/s is assumed.

In the following, the bit error performance of a SPAD-based optical system with OOK and BPPM is derived. In these binary modulation schemes, each bit is sent individually by transmitting one of two optical pulses over a duration of $T_{\rm b}$ seconds and the optical intensity modulated signal is transmitted by an optical source. In this system the bit rate is expressed as $R_{\rm b} = 1/T_{\rm b}$ bits/s. At the receiver side, direct detection is applied where the received optical signal is photodetected by the SPAD. The number of photons counted by the SPAD is processed to decide which of two optical pulses was received, and then the transmitted bit during each $T_{\rm b}$ second bit interval is determined. In this photon counting system, the background counts and the SPAD's dead time determine the achievable bit error ratio (BER) of the system.

A. On-Off Keying

OOK is one of the most common modulation techniques for intensity-modulation direct-detection (IM/DD) systems, because of its easy implementation, simple receiver design, bandwidth efficiency and cost effectiveness. In OOK, the information bits are transmitted through the intensity of light, where presence of a pulse denotes bit "1" and absence of a pulse denotes bit "0", during each slot time.

Define the contributions to the signal and background noise counts per bit interval by $K_{\rm s} = \lambda_{\rm s} T_{\rm b}$ and $K_{\rm n} = \lambda_{\rm n} T_{\rm b}$, respectively, where $\lambda_{\rm s}$ and $\lambda_{\rm n}$ are the average photon rates from signal and background noise. When a "0" bit is transmitted, the average number of photons arrived at the SPAD receiver per bit time interval is $K_{\rm n}$, and when a "1" bit is transmitted, the average number of received photons per bit time interval is $K_{\rm s} + K_{\rm n}$. Therefore, $p_{\rm n}(k)$ and $p_{\rm sn}(k)$, the probability that exactly k photons are counted by the SPAD in the counting interval of $T_{\rm b}$ seconds, when "0" or "1" are sent, respectively, are given by:

$$\begin{aligned} p_{\rm n}(k) &= p_K(k; \lambda_{\rm n}, T_{\rm b}, \tau), \\ p_{\rm sn}(k) &= p_K(k; \lambda_{\rm s} + \lambda_{\rm n}, T_{\rm b}, \tau). \end{aligned} \tag{43}$$

OOK demodulation is accomplished by a classical binary detection process: Let hypothesis "H_0" represent the case when a "0" is sent and "H_1" represent the hypothesis that a "1" is transmitted. The aim is to determine the optimum rule for deciding which hypothesis is true based on a single observation. This simple binary hypothesis-testing problem is often formulated using the Bayes criterion, where the decision should be made according to the well-known likelihood-ratio test to minimize the probability of error. In this test, the likelihood ratio is defined as:

$$L(k) = \frac{p_{\rm sn}(k)}{p_{\rm n}(k)} \underset{H_0}{\overset{H_1}{\gtrless}} 1 \tag{44}$$

where it is assumed that H_0 and H_1 are equally probable. With this maximum likelihood detection rule, the probability of error is expressed as:

$$P_e = \frac{1}{2} \sum_{\{k:L(k)>1\}} p_{\rm n}(k) + \frac{1}{2} \sum_{\{k:L(k)\le 1\}} p_{\rm sn}(k). \tag{45}$$

For an ideal photon detector with Poisson statistics (without dead time), the likelihood-ratio test in (44) simplifies to a single threshold detection. For the SPAD receiver, however, the complicated mathematical expressions of $p_{\rm sn}(k)$ and $p_{\rm n}(k)$ (for both AQ and PQ SPADs), makes the algebraic manipulation of $L(k)$ intractable. For given values of $\lambda_{\rm s}$ and $\lambda_{\rm n}$, if $L(k)$ is monotonic with respect to k, the test in (44) is equivalent to a single threshold test, i.e. the maximum likelihood detection is achieved by a threshold comparison. But it is even more challenging to check the monotonicity of $L(k)$ using finite differences (discrete derivatives). For an AQ SPAD with small dead time ratio ($\delta < 0.1$), an approximate photocount distribution can be provided (see Appendix A) and it can be proved that the above likelihood-ratio test leads to a single threshold test (see Appendix D). For other cases, no such proof can be provided. However, we conjecture that the threshold detection is optimum in general. Our extensive numerical investigation of the monotonicity of $L(k)$ and and the BER results in Section V strongly support this conjecture.

Hereinafter, the threshold detection is adopted for error probability calculations, where the number of counted photons

is compared with a threshold m_{T}. An error will occur if $k \leq m_{\mathrm{T}}$ when a "1" bit is sent, or if $k > m_{\mathrm{T}}$, when a "0" bit is sent. The probability of error for equally likely bits is then expressed as:

$$P_e = \frac{1}{2} \sum_{k=m_{\mathrm{T}}+1}^{k_{\max}} p_{\mathrm{n}}(k) + \frac{1}{2} \sum_{k=0}^{m_{\mathrm{T}}} p_{\mathrm{sn}}(k). \tag{46}$$

This equation holds for both AQ and PQ SPADs, however, for each case, the corresponding photocount distribution should be considered. The error probability, P_e, highly depends on m_{T} which can be selected to yield the lowest probability of making an error. This occurs at the value of m_{T} where $dP_e/dm_{\mathrm{T}} = 0$. It is in general challenging to obtain a closed-form expression for (46), nevertheless, for the case of an AQ SPAD, it is shown that (see Appendix E) given same conditions (i.e. same threshold, sampling time, and radiation intensity), the error performance of an AQ SPAD with dead time is the same as that of a similar SPAD without dead time, but with a quantum efficiency reduced by the factor $(1 - (m_{\mathrm{T}} + 1)\tau/T_{\mathrm{b}})$. According to (66):

$$P_e = \frac{1}{2} \left(1 - \sum_{k=0}^{m_{\mathrm{T}}} \psi(k, \lambda_{\mathrm{n}}(T_{\mathrm{b}} - (m_{\mathrm{T}} + 1)\tau)) \right) + \frac{1}{2} \sum_{k=0}^{m_{\mathrm{T}}} \psi(k, (\lambda_{\mathrm{s}} + \lambda_{\mathrm{n}})(T_{\mathrm{b}} - (m_{\mathrm{T}} + 1)\tau)). \tag{47}$$

Solving the equation $dP_e/dm_{\mathrm{T}} = 0$ for finding the optimum threshold value leads to:

$$m_{\mathrm{T}} = \frac{\lambda_{\mathrm{s}} T_{\mathrm{b}} - \lambda_{\mathrm{s}} \tau}{\lambda_{\mathrm{s}} \tau + \ln\left(1 + \frac{\lambda_{\mathrm{s}}}{\lambda_{\mathrm{n}}}\right)}. \tag{48}$$

B. Binary Pulse Position Modulation

The basic disadvantage of OOK signaling is that the average photon rates λ_{s} and λ_{n} must be known, to optimally set the threshold. BPPM signaling avoids this difficulty by using pulse-to-pulse comparison for detection. In BPPM modulation, the optical pulse is sent in one of two adjacent time intervals, each of length $T_{\mathrm{b}}/2$ and then the output counts are compared over each half-bit interval. A "1" bit is sent as a pulse in the first half of the bit interval, and a "0" bit as a pulse in the second half. At the receiver side, the SPAD separately counts the number of photons over the two half-bit intervals and then they are compared for bit decoding. Since the pulse time is half of the bit duration, the receiver bandwidth must be higher than for the OOK system [1].

With the same approach as used for OOK, the bit error probability of the BPPM system is the probability that signal slot photon count does not exceed non-signal slot photon count. Hence:

$$P_e = \sum_{k_1=0}^{\infty} \sum_{k_2=k_1+1}^{\infty} p_{\mathrm{sn}}(k_1) p_{\mathrm{n}}(k_2) + \frac{1}{2} \sum_{k=0}^{\infty} p_{\mathrm{sn}}(k) p_{\mathrm{n}}(k). \tag{49}$$

where the second term in (49) accounts for the possibility of equal counts in each half-bit interval, in which case a random choice will be made.

V. Numerical Results and Discussion

In this section, bit error performance results are presented where analytical results are compared with Monte Carlo simulation results. Throughout the calculations and simulations, independent count statistics are assumed for each transmitted bit and $T_{\mathrm{b}} = 1$ μs is considered. In all figures, BER results are plotted as a function of $\overline{K_{\mathrm{s}}}$ for various $\overline{K_{\mathrm{n}}}$ values and $\delta = \tau/T_{\mathrm{b}}$, where $\overline{K_{\mathrm{s}}}$ and $\overline{K_{\mathrm{n}}}$ are defined as the average signal count and background count per bit interval, respectively. Therefore, for both OOK and BPPM, $\overline{K_{\mathrm{s}}} = 0.5\lambda_{\mathrm{s}} T_{\mathrm{b}}$ and $\overline{K_{\mathrm{n}}} = 0.5\lambda_{\mathrm{n}} T_{\mathrm{b}}$.

A. AQ SPAD

The BER results for an AQ SPAD-based optical system with OOK modulation are provided in Fig. 5. In these figures, the error probability of OOK systems with maximum likelihood (ML) detection and threshold (TH) detection are compared with Monte Carlo simulation results, resulting in perfectly matching curves. The analytical calculations are based on the expressions given in (45) for ML detection, and (47) and (48) for TH detection.

According to Figs. 5a and 5b, ML and TH detection show an excellent match for all cases, confirming that for the specified range of values in these figures, the ML detection and TH detection are equivalent.

In Fig. 5a, moderately small values of $\delta = 0.001$ and $\delta = 0.01$ are assumed, while in Fig. 5b the dead time ratio is $\delta = 0.1$ which is quite large for communication purposes. As observed in Fig. 5b, the large value of dead time ratio degrades the system performance as the SPAD is saturated with lower signal and/or background noise levels. In these cases, $k_{\max}$ and m_{T} are small, and the ripples in the BER curves are direct results of discrete threshold values. For the quantum-limited cases, i.e. $\overline{K_{\mathrm{n}}} = 0$ curves, the threshold m_{T} is zero and no ripples are observed.

According to Fig. 5a, the performance of the AQ SPAD receiver depends strongly on the background count statistics, and even for $\overline{K_{\mathrm{n}}} = 0$ and 1, the error probability is slightly affected by the SPAD dead time. This becomes more significant, when $\overline{K_{\mathrm{n}}}$ increases. Also, it is apparent that for a given $\overline{K_{\mathrm{n}}}$, a higher signal power is needed to maintain the system performance in the presence of longer dead time. In other words, to achieve a particular BER, the larger δ is, the higher $\overline{K_{\mathrm{s}}}$ should be.

Fig. 6 provides the BER results for an AQ SPAD-based optical system with BPPM modulation. It is observed that, in the absence of background noise, the effect of dead time on BER is negligible for small values of $\overline{K_{\mathrm{s}}}$ as in Fig. 6a. However, when background noise is present, the performance becomes very sensitive to the dead time such that higher dead time values lead to higher error rates. It should also be noted that, as seen in Fig. 6b, the error performance severely degrades when large dead time ratio ($\delta = 0.1$) is assumed. In this case, the SPAD gets saturated with lower signal and/or background noise levels. Also, for stronger background counts, the saturation happens at lower signal levels.

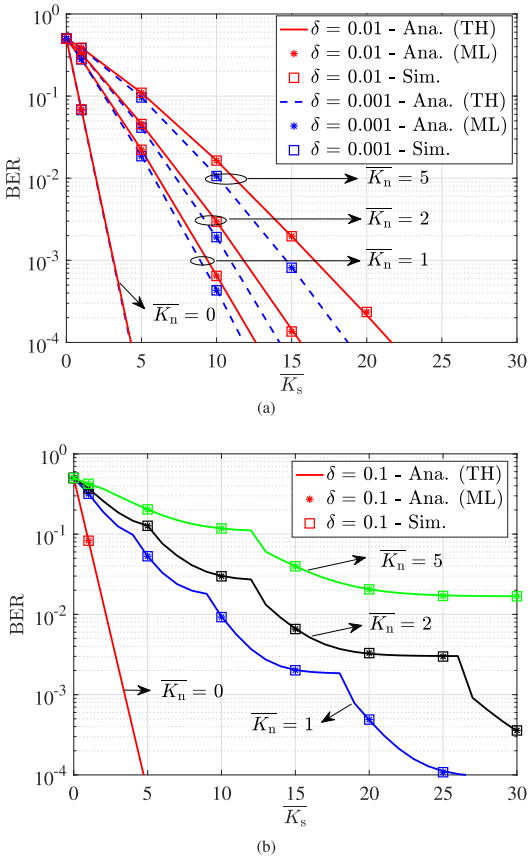

Fig. 5. OOK bit error performance of an AQ SPAD-based system: (a) $\delta = 0.01$, 0.001 and (b) $\delta = 0.1$.

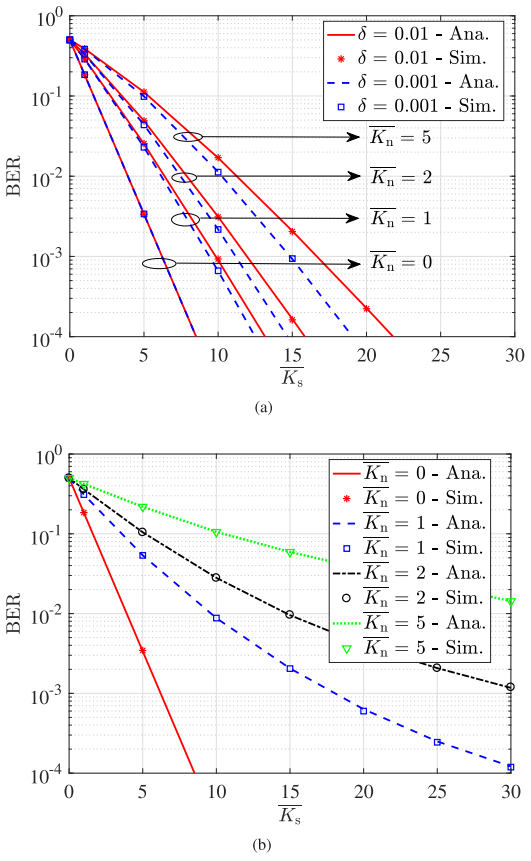

Fig. 6. BPPM bit error performance of an AQ SPAD-based system: (a) $\delta = 0.01$, 0.001 and (b) $\delta = 0.1$.

Note that OOK uses pulses twice as long as BPPM, and has higher signal and background counts. Therefore, a fair comparison between OOK and BPPM systems can be made if the same average signal and background power are assumed. For the systems under consideration, average signal and background noise power are directly proportional to $\overline{K_s}$ and $\overline{K_n}$, respectively. Thus, it is fair to compare the error performance of OOK and BPPM systems as presented in Figs. 5 and 6.

As in Fig. 5a and Fig. 6a, OOK and BPPM show almost similar performance when the background noise is present and the dead time ratio is moderately small. For large dead time ratio ($\delta = 0.1$ as in Fig. 5b and Fig. 6b), in the presence of background counts, OOK system shows slightly better BER values. For ideal quantum-limited photon-counting OOK and BPPM ($\overline{K_n} = 0$) without dead time counting losses, OOK has 3 dB better performance as discussed in [1]. In the presence of dead time, consistent results are achieved, however, the effect of dead time is insignificant in the range of interest as illustrated in Figs. 5 and 6.

B. PQ SPAD

Fig. 7 demonstrates the error performance results of a PQ SPAD-based system with OOK modulation. In this figure, the error probability with ML detection, given in (45), and the error probability with TH detection, given in (46) are numerically evaluated and compared with simulation results. The threshold value is also obtained numerically. It is again observed that ML and TH detection rules result in perfectly matching curves, confirming that these two detection schemes are equivalent in the range of interest.

Similar to BER results for the AQ SPAD, three different values for dead time ratio are considered here. In Fig. 7a, $\delta = 0.001$ and $\delta = 0.01$ are assumed, while in Fig. 7b the dead time ratio is equal to 0.1. Again, large dead time ratio ($\delta = 0.1$) severely degrades the error performance and results in SPAD's saturation. According to (42), for a PQ SPAD, the maximum count rate occurs at the point $\lambda = 1/\tau$. The lowest BER also occurs at this point which is clearly seen in Fig. 7b. After this point, the counting losses due to

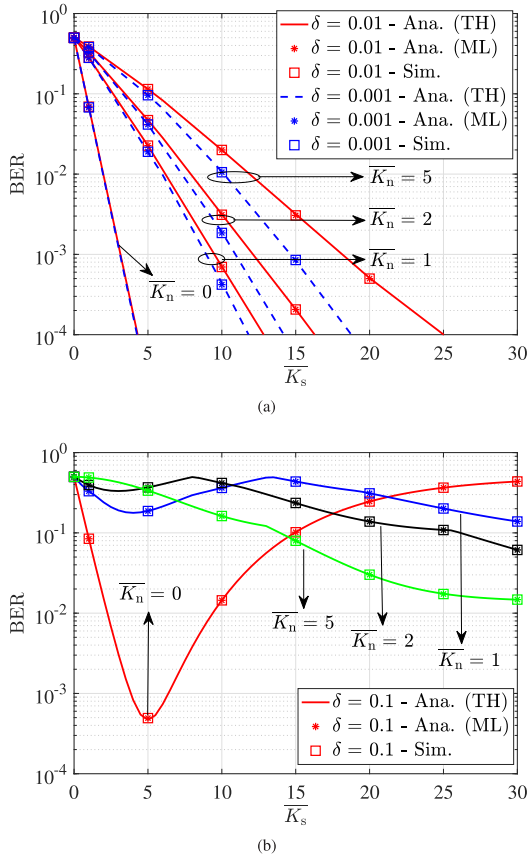

Fig. 7. OOK bit error performance of a PQ SPAD-based system: (a) $\delta = 0.01$, 0.001 and (b) $\delta = 0.1$.

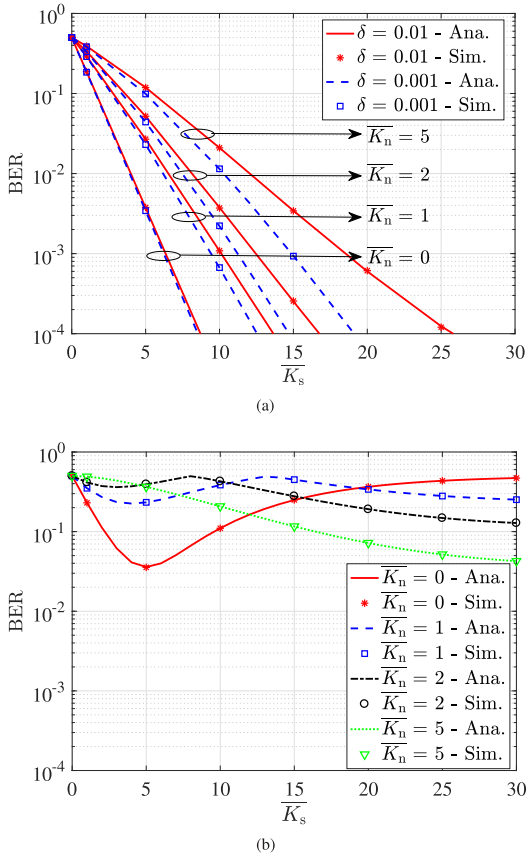

Fig. 8. BPPM bit error performance of a PQ SPAD-based system: (a) $\delta = 0.01$, 0.001 and (b) $\delta = 0.1$.

dead time drastically increase. The BER also increases until the paralysis behaviour (see Fig. 4) results in the average photon count of pulsed slots becoming lower than that of non-pulsed slots. Our extensive numerical calculations show that at this latter point, the monotonicity of the likelihood ratio function $L(k)$, given in (44) changes from monotonically nondecreasing to monotonically nonincreasing. In such cases, keeping the definition of hypotheses H_0 and H_1 as before, the direction of the likelihood ratio test presented in (44) should be reversed and the error probability expressions should be modified accordingly. This has been done for obtaining the results of Fig. 7b.

The probability of error for a PQ SPAD-based optical system with BPPM modulation, given in (49), is in the form of discrete summations, and therefore can be calculated numerically. Fig. 8 shows some plots of the BER results for such a system. Similar to previous cases, in the absence of background noise, the effect of dead time on BER is almost negligible. However, an increase in the dead time value degrades the error performance. Again, it is seen that the error performance is severely affected by large dead time ratio ($\delta = 0.1$) and the lowest BER occurs at the maximum count rate, as predicted.

As seen in Figs. 5–8, the BER of the OWC system strongly depends on the value of dead time and large dead time values increase the BER to levels even beyond 10^{-3}. The dead time of commercially available SPAD devices vary in the range of a few nanoseconds to tens of nanoseconds, causing significant losses for communication links with slot widths of the same order. However, for data rates in the orders of a few tens of Mbits/s and lower, the dead time ratio is small enough ($\leq$0.01) and assuming binary modulation schemes such as OOK and BPPM, BER values of less than 10^{-3} can be achieved, as shown in Figs. 5a, 6a, 7a and 8a for AQ and PQ cases, respectively. These results highlight the need to develop SPAD detectors with much reduced dead time to be able to achieve higher data rates with reliable performance and arbitrary small bit error probability.

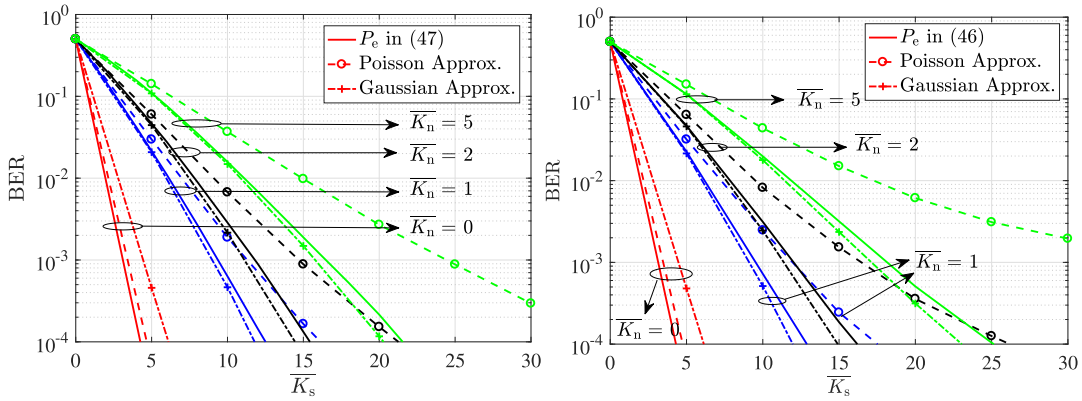

(a) AQ (b) PQ

Fig. 9. BER performance of (a) AQ, and (b) PQ SPAD-based systems with OOK modulation considering exact SPAD photocount distribution, Poisson approximation, and Gaussian approximation.

C. AQ SPAD vs. PQ SPAD

As stated in Section I, when using PQ SPADs any photon arrival occurring during the dead time is not counted but is assumed to extend the dead time period, while for AQ SPAD devices, any photon arriving during the dead time is neither counted nor has any influence on the dead time duration. Thus, assuming the same dead time duration, in a bit interval of T_b seconds, the average number of counted photons by an AQ SPAD is generally higher than that of a PQ SPAD. This can be observed from Figs. 1 and 3. Furthermore, this behavior directly affects the BER performance. When the dead time duration only is one order of magnitude lower than the bit interval ($\delta = 0.1$), the difference of AQ and PQ SPADs is perceptible, as observed in Fig. 5b and Fig. 7b for OOK modulation or in Fig. 6b and Fig. 8b for BPPM. For an AQ SPAD, increasing the signal photon rate (or signal count) results in the saturation of SPAD and the BER will reach a constant value. However, in a PQ SPAD, by increasing the signal photon rate (or signal count), the BER decreases until the SPAD reaches its maximum count rate. At this point, the lowest possible BER is achieved and higher signal counts degrade the error performance.

D. Applicability of Gaussian and Poisson Approximations

The probability distribution of SPAD photocounts is commonly approximated by a Poisson distribution where the effect of dead time is neglected. In order to investigate the accuracy of this approximation, in Fig. 9, the OOK error probabilities of both AQ and PQ SPADs, given in (47) and (46), respectively, are evaluated and compared with the case when the photocount distribution is approximated by a Poisson distribution through moment matching, i.e., the rate parameter of the approximated Poisson distribution is calculated according to (35) and (42) as in [7] and [8], rather than using an ideal Poisson model which does not take into account the effect of dead time. Please note that in Figs. 9a and 9b, $\delta = 0.01$ is assumed, and as can be seen, for both AQ and PQ SPADs, there is a considerable difference between the exact BER values and the Poisson approximation results, especially for higher values of $\overline{K_n}$.

To have a better insight, the AQ and PQ SPAD photocount distributions have also been approximated by Gaussian distribution in Fig. 9, using a similar moment matching approach. The mean and variance of the Gaussian distribution are approximated as in (30) and (31) for AQ SPAD, and as in (39) and (40) for PQ SPAD. Although the Gaussian approximation shows higher accuracy compared with the Poisson approximation, the differences are still noticeable. Note that by increasing the dead time ratio, the accuracy of these approximations will be more degraded. By comparing the results of these approximations for AQ and PQ SPADs, it is observed that the approximations show slightly higher accuracy for AQ SPADs, and the reason is that the counting losses due to paralyzable dead time are generally higher than that of nonparalyzable dead time. According to these observations, the use of Poisson or Gaussian approximations does not provide enough accuracy for assessing the bit error performance of OWC systems, and this highlights the importance of our statistical modeling for a precise bit error analysis for potential optical communication applications.

VI. Conclusions and Future Works

In this paper, a complete analytical framework is presented for modeling the statistical behavior of photon counting receivers. This rigorous analysis expounds the impact of paralyzable and nonparalyzable dead times on the counting statistics of SPAD detectors, and provides exact expressions for the probability distribution, mean and variance of active and passive quenching SPAD photocounts. The proposed expressions for mean of AQ and PQ SPAD photocounts

precisely predict the SPAD effective count rates and are in line with empirical count rate models and experimental data available in literature. The proposed probability distributions are particularly required for maximum likelihood detection analysis and assessing the bit error performance of any SPAD-based OWC system. In this study, the effect of dead time on the bit error performance of an OWC system with OOK and BPPM modulation schemes is investigated and it is found that that the dead time-distorted count statistics result in higher bit error rates, and a higher signal intensity is required to maintain system performance. In the AQ SPAD-based OWC system, assuming OOK modulation and constant average background count of $\overline{K_{\rm n}} = 1$, for a BER value of 10^{-4}, the reduction of dead time by one order of magnitude leads to almost 3 dB improvement in the average signal count. The improvement is about 3.8 dB if BPPM modulation is considered. PQ SPAD-based OWC systems with large dead time ratios ($\delta = 0.1$) can not achieve BER values lower than 10^{-3}. In general, for large dead time values, AQ SPADs outperform PQ SPADs significantly, and for small dead time values, AQ SPADs still provide slightly better bit error performance. It is also found that in quantum-limited OWC systems, the effect of dead time is negligible. Compared with Gaussian and Poisson distributions commonly used in literature, our proposed probability distributions provide significant accuracy in performance analysis of OWC systems. This in turn highlights the importance of our statistical modeling for a precise bit error analysis for potential optical communication applications. Moreover, it is concluded that in applications involving high photon rates, such as high data rate optical wireless communications, the SPAD dead time causes significant data loss. Using commercially available SPAD devices with dead time values in the range of a few nanoseconds to tens of nanoseconds, a reliable bit error performance with maximum data rate of a few Mbits/s could be achieved through binary modulation schemes. Thus, this study highlights the need to develop SPAD devices with much reduced dead time to be able to achieve higher data rates in the range of Gbits/s.

There is much work yet to be done in the analysis of SPAD-based optical systems. It is of great importance to consider modulation schemes with higher spectral efficiencies and less sensitive to the fluctuations in the background and signal strengths. However, in higher order modulation schemes, the existence of dead time does not allow arbitrarily narrow time slots, as the SPAD's dead time can overlap two adjacent time slots. Therefore, for future works, the photocount statistics should be modified accordingly.

Appendix A
Approximate PMF for AQ SPADs With $\lambda \gg I$ or $\tau \ll T_{\rm b}$

The PMF in (27) can be re-written as:

$$p_K(k) = \sum_{i=0}^{k} \psi(i,\lambda_{k+1}) - \sum_{i=0}^{k-1} \psi(i,\lambda_k)$$

$$= \psi(k,\lambda_{k+1}) + \sum_{i=0}^{k-1} \big(\psi(i,\lambda_{k+1}) - \psi(i,\lambda_k)\big)$$

$$= \psi(k,\lambda_{k+1}) + \sum_{i=0}^{k-1} \psi(i,\lambda_{k+1}) \left[1 - \frac{(T_{\rm b}-k\tau)^i}{(T_{\rm b}-(k+1)\tau)^i} e^{-\lambda\tau}\right]. \quad (50)$$

Define A and B as follows:

$$A = \sum_{i=0}^{k-1} \psi(i,\lambda_{k+1}) \underbrace{\left[1 - \frac{(T_{\rm b}-k\tau)^i}{(T_{\rm b}-(k+1)\tau)^i} e^{-\lambda\tau}\right]}_{B}.$$

Two asymptotic cases can be considered:

- $\lambda \gg 1$: The limiting relation $\lim_{t\to\infty} t^\alpha e^{-t} = 0$ results in $\lim_{\lambda\to\infty} A = 0$.
- $\tau \ll T_{\rm b}$: Since $\lim_{\delta\to 0} B = 0$ and $\psi(k,\lambda_{k+1})$ is finite, $\lim_{\delta\to 0} A = 0$ is concluded.

Therefore, for the above two cases, the following approximation can be adopted:

$$p_K(k) \approx \psi(k,\lambda_{k+1}). \quad (51)$$

Appendix B
Mean and Variance of the AQ PMF

By definition, the mean value of the distribution in (27) is:

$$\mu_K = \sum_{k=0}^{k_{\max}-1} k p_K(k)$$

$$= \sum_{k=0}^{k_{\max}-1} k \times \left\{\sum_{i=0}^{k} \psi(i,\lambda_{k+1}) - \sum_{i=0}^{k-1} \psi(i,\lambda_k)\right\}. \quad (52)$$

Replacing k by $k+1$ in the summation index of the second term in the right-hand side of the previous expression gives:

$$\mu_K = \sum_{k=0}^{k_{\max}-1} \sum_{i=0}^{k} k\psi(i,\lambda_{k+1}) - \sum_{k=0}^{k_{\max}-2} \sum_{i=0}^{k} (k+1)\psi(i,\lambda_{k+1})$$

$$= \sum_{i=0}^{k_{\max}-1} (k_{\max}-1)\psi(i,\lambda_{k_{\max}}) - \sum_{k=0}^{k_{\max}-2} \sum_{i=0}^{k} \psi(i,\lambda_{k+1})$$

$$\approx (k_{\max}-1) - \sum_{k=0}^{k_{\max}-2} \sum_{i=0}^{k} \psi(i,\lambda_{k+1}). \quad (53)$$

where the approximation $\sum_{i=0}^{k_{\max}-1} \psi(i,\lambda_{k_{\max}}) \approx 1$ is used, as $\lambda_{k_{\max}}$ is very small. The above expression for μ_K in (53) can be further simplified to:

$$\mu_K = \sum_{k=0}^{k_{\max}-2} \sum_{i=k+1}^{\infty} \psi(i,\lambda_{k+1}). \quad (54)$$

Next, the limit of this expression for $\tau \to 0$ or $k_{\max} \to \infty$ is taken. Although it follows directly from $\lim_{\tau\to 0} p_K(k) = p_0(k)$ that $\lim_{\tau\to 0} \mu_K = \lambda T_{\rm b}$, a direct proof can also be obtained in the following way; the right-hand side of (54) is a

double series whose terms can be ordered in an infinite matrix:

$$e^{-\lambda T_{\rm b}} \times \begin{bmatrix} 0 & \frac{(\lambda T_{\rm b})^1}{1!} & \frac{(\lambda T_{\rm b})^2}{2!} & & \frac{(\lambda T_{\rm b})^m}{m!} & \\ 0 & 0 & \frac{(\lambda T_{\rm b})^2}{2!} & \cdots & \frac{(\lambda T_{\rm b})^m}{m!} & \cdots \\ 0 & 0 & 0 & & \frac{(\lambda T_{\rm b})^m}{m!} & \\ & \vdots & & \ddots & \vdots & \\ 0 & 0 & 0 & \cdots & \frac{(\lambda T_{\rm b})^m}{m!} & \cdots \\ & \vdots & & & \vdots & \ddots \end{bmatrix},$$

The rows and columns of the above matrix are indexed by summation indices of (54), k and i, respectively. Summation of the first m rows of this matrix gives:

$$\begin{aligned} S_m &= e^{-\lambda T_{\rm b}} \times \left[\sum_{i=0}^{m} i \times \frac{(\lambda T_{\rm b})^i}{i!} + m \times \sum_{i=m+1}^{\infty} \frac{(\lambda T_{\rm b})^i}{i!} \right] \\ &= e^{-\lambda T_{\rm b}} \times \Bigg[(\lambda T_{\rm b}) \times \sum_{i=0}^{m-1} \frac{(\lambda T_{\rm b})^i}{i!} \\ &\qquad + m \times \sum_{i=0}^{\infty} \frac{(\lambda T_{\rm b})^i}{i!} - m \times \sum_{i=0}^{m} \frac{(\lambda T_{\rm b})^i}{i!} \Bigg], \end{aligned} \tag{55}$$

As m goes to infinity, the summation of the second and third terms clearly goes to zero. Furthermore, using the Taylor series expression $\lim_{m\to\infty} \sum_{i=0}^{m-1} (\lambda T_{\rm b})^i/i! = e^{\lambda T_{\rm b}}$, one has:

$$\lim_{\tau\to 0} \mu_K = \lim_{m\to\infty} S_m = \lambda T_{\rm b}. \tag{56}$$

With an approach similar to the one used for deriving μ_K, the variance of the distribution in (27) can be obtained as:

$$\begin{aligned} \sigma_K^2 = \sum_{k=0}^{k_{\max}-2} \sum_{i=0}^{k} (2k_{\max} - 2k - 3)\psi(i, \lambda_{k+1}) \\ - \left(\sum_{k=0}^{k_{\max}-2} \sum_{i=0}^{k} \psi(i, \lambda_{k+1}) \right)^2. \end{aligned} \tag{57}$$

and the limiting relation $\lim_{\tau\to 0} \sigma_K^2 = \lambda T_{\rm b}$ is verified, where the product $\lambda T_{\rm b}$ is the variance of the original Poisson distribution.

Appendix C
Mean and Variance of the PQ PMF

According to (5) and (36), the generating function $G(z,t)$ and its derivatives are given by:

$$\begin{aligned} G(z, T_{\rm b}) &= \sum_{k=0}^{k_{\max}-1} p_K(k) z^k \\ &= \sum_{i=0}^{k_{\max}-1} (z-1)^i \frac{\lambda^i e^{-i\lambda\tau}}{i!} (T_{\rm b} - i\tau)^i, \end{aligned} \tag{58}$$

$$\begin{aligned} \frac{\partial G(z, T_{\rm b})}{\partial z} &= \sum_{k=0}^{k_{\max}-1} k p_K(k) z^{k-1} \\ &= \sum_{i=1}^{k_{\max}-1} i(z-1)^{i-1} \frac{\lambda^i e^{-i\lambda\tau}}{i!} (T_{\rm b} - i\tau)^i, \end{aligned} \tag{59}$$

$$\begin{aligned} \frac{\partial^2 G(z, T_{\rm b})}{\partial z^2} &= \sum_{k=0}^{k_{\max}-1} k(k-1) p_K(k) z^{k-2} \\ &= \sum_{i=2}^{k_{\max}-1} i(i-1)(z-1)^{i-2} \frac{\lambda^i e^{-i\lambda\tau}}{i!} (T_{\rm b} - i\tau)^i. \end{aligned} \tag{60}$$

Therefore, the mean and variance of the distribution function in (36) are derived as:

$$\mu_K = \sum_{k=0}^{k_{\max}} k p_K(k) = \left. \frac{\partial G(z, T_{\rm b})}{\partial z} \right|_{z=1} = \lambda e^{-\lambda\tau} (T_{\rm b} - \tau). \tag{61}$$

$$\begin{aligned} \sigma_K^2 &= \sum_{k=0}^{k_{\max}} k^2 \, p_K(k) - \left(\sum_{k=0}^{k_{\max}} k p_K(k) \right)^2 \\ &= \left[\frac{\partial^2 G(z, T_{\rm b})}{\partial z^2} + \frac{\partial G(z, T_{\rm b})}{\partial z} - \left(\frac{\partial G(z, T_{\rm b})}{\partial z} \right)^2 \right] \Bigg|_{z=1} \\ &= \lambda^2 \, e^{-2\lambda\tau} (3\tau^2 - 2T_{\rm b}\tau) + \lambda e^{-\lambda\tau} (T_{\rm b} - \tau). \end{aligned} \tag{62}$$

Finally, the limiting expressions $\lim_{\tau\to 0} \mu_K = \lambda T_{\rm b}$ and $\lim_{\tau\to 0} \sigma_K^2 = \lambda T_{\rm b}$ are verified.

Appendix D
Threshold Detection for AQ SPADs With $\lambda_{\rm n} \gg 1$ or $\tau \ll T_{\rm b}$

With the approximate PMF given in (51), the likelihood ratio test in (44) reduces to:

$$L(k) = \frac{\psi(k, \lambda_{k+1}^{\rm sn})}{\psi(k, \lambda_{k+1}^{\rm n})} \underset{H_0}{\overset{H_1}{\gtrless}} 1 \tag{63}$$

where $\lambda_{k+1}^{\rm n} = \lambda_{\rm n}(T_{\rm b} - (k+1)\tau)$ and $\lambda_{k+1}^{\rm sn} = (\lambda_{\rm s} + \lambda_{\rm n})(T_{\rm b} - (k+1)\tau)$. Substituting $\psi(i, \lambda) = \lambda^i e^{-\lambda}/i!$ gives:

$$L(k) = e^{-\lambda_{\rm s}(T_{\rm b} - (k+1)\tau)} \left(\frac{\lambda_{\rm s} + \lambda_{\rm n}}{\lambda_{\rm n}} \right)^k \underset{H_0}{\overset{H_1}{\gtrless}} 1 \tag{64}$$

Finally, taking the natural logarithm from both sides gives:

$$k \underset{H_0}{\overset{H_1}{\gtrless}} \frac{\lambda_{\rm s} T_{\rm b} - \lambda_{\rm s}\tau}{\lambda_{\rm s}\tau + \ln\left(1 + \frac{\lambda_{\rm s}}{\lambda_{\rm n}}\right)}. \tag{65}$$

Therefore, for an AQ SPAD, the maximum likelihood detection simplifies to a threshold detection if $\lambda_{\rm n} \gg 1$ or $\tau \ll T_{\rm b}$.

Appendix E
Special Property of an AQ SPAD in Threshold Detection

Here, the error probability of threshold detection for an AQ SPAD is derived. Assuming $m_{\rm T} < T/\tau$, the probability of counting at most $m_{\rm T}$ photons, is calculated as:

$$\begin{aligned} \sum_{k=0}^{m_{\rm T}} p_K(k) &\overset{(*)}{=} \sum_{i=0}^{m_{\rm T}} \sum_{k=i}^{m_{\rm T}} \psi(i, \lambda_{k+1}) - \sum_{i=0}^{m_{\rm T}-1} \sum_{k=i+1}^{m_{\rm T}} \psi(i, \lambda_k) \\ &\overset{(**)}{=} \psi(m_{\rm T}, \lambda_{m_{\rm T}+1}) \\ &\quad + \sum_{i=0}^{m_{\rm T}-1} \left[\sum_{k=i}^{m_{\rm T}} \psi(i, \lambda_{k+1}) - \sum_{k'=i}^{m_{\rm T}-1} \psi(i, \lambda_{k'+1}) \right] \end{aligned}$$

$$= \psi(m_{\mathrm{T}}, \lambda_{m_{\mathrm{T}}+1}) + \sum_{i=0}^{m_{\mathrm{T}}-1} \psi(i, \lambda_{m_{\mathrm{T}}+1})$$
$$= \sum_{i=0}^{m_{\mathrm{T}}} \psi(i, \lambda_{m_{\mathrm{T}}+1}) \quad (66)$$

where, in $(*)$, the order of summations is changed and for $(**)$, a change of variable $k' = k - 1$ is used. According to (66), the probability of counting up to m_{T} photons, for an AQ SPAD receiver with dead time τ in a bit interval of T_{b} seconds, is the same as that of a SPAD receiver without dead time counting photons at the same rate, but during a bit interval of $T_{\mathrm{b}} - (m_{\mathrm{T}} + 1)\tau$ seconds, or the same as that of a similar SPAD without dead time, but with a quantum efficiency reduced by the factor $(1 - (m_{\mathrm{T}} + 1)\tau/T_{\mathrm{b}})$. This result greatly simplifies the error probability calculations for an AQ SPAD.

REFERENCES

[1] R. M. Gagliardi and S. Karp, *Optical Communications*, 2nd ed. New York, NY, USA: Wiley, 1995.

[2] S. B. Alexander, *Optical Communication Receiver Design*. Bellingham, WA, USA: SPIE, 1997.

[3] R. H. Hadfield, "Single-photon detectors for optical quantum information applications," *Nature Photon.*, vol. 3, no. 12, pp. 696–705, 2009.

[4] C. Niclass, A. Rochas, P.-A. Besse, and E. Charbon, "Design and characterization of a CMOS 3-D image sensor based on single photon avalanche diodes," *IEEE J. Solid-State Circuits*, vol. 40, no. 9, pp. 1847–1854, Sep. 2005.

[5] A. Tosi, F. Zappa, and S. Cova, "Single-photon detectors for practical quantum cryptography," *Proc. SPIE*, vol. 8542, pp. 85421U-1–85421U-8, Nov. 2012.

[6] Y. Li, S. Videv, M. Abdallah, K. Qaraqe, M. Uysal, and H. Haas, "Single photon avalanche diode (SPAD) VLC system and application to downhole monitoring," in *Proc. IEEE Global Commun. Conf.*, Austin, TX, USA, Dec. 2014, pp. 2108–2113.

[7] Y. Li, M. Safari, R. Henderson, and H. Haas, "Optical OFDM with single-photon avalanche diode," *IEEE Photon. Technol. Lett.*, vol. 27, no. 9, pp. 943–946, May 1, 2015.

[8] Y. Li, M. Safari, R. Henderson, and H. Haas, "Nonlinear distortion in SPAD-based optical OFDM systems," in *Proc. IEEE Global Commun. Conf. Workshops*, San Diego, CA, USA, Dec. 2015, pp. 1–6.

[9] O. Almer *et al.*, "A SPAD-based visible light communications receiver employing higher order modulation," in *Proc. IEEE Global Commun. Conf.*, San Diego, CA, USA, Dec. 2015, pp. 1–6.

[10] J. Kosman, O. Almer, A. V. N. Jalajakumari, S. Videv, H. Haas, and R. K. Henderson, "60 Mb/s, 2 meters visible light communications in 1 klx ambient using an unlensed CMOS SPAD receiver," in *Proc. Photon. Soc. Summer Topics Meeting Ser.*, Newport Beach, CA, USA, Jul. 2016, pp. 171–172.

[11] M.-A. Khalighi, T. Hamza, S. Bourennane, P. Léon, and J. Opderbecke, "Underwater wireless optical communications using silicon photomultipliers," *IEEE Photon. J.*, vol. 9, no. 4, Aug. 2017. Art. no. 7905310.

[12] C. Wang, H.-Y. Yu, and Y.-J. Zhu, "A long distance underwater visible light communication system with single photon avalanche diode," *IEEE Photon. J.*, vol. 8, no. 5, Oct. 2016, Art. no. 7906311.

[13] A. Spinelli and A. L. Lacaita, "Physics and numerical simulation of single photon avalanche diodes," *IEEE Trans. Electron Devices*, vol. 44, no. 11, pp. 1931–1943, Nov. 1997.

[14] M. W. Fishburn, "Fundamentals of CMOS single-photon avalanche diodes," Ph.D. dissertation, Dept. Elect. Eng., Delft Univ. Technol., Delft, The Netherlands, 2012.

[15] A. Migdall, S. V. Polyakov, J. Fan, and J. C. Bienfang, *Single-Photon Generation and Detection: Physics and Applications*, vol. 45. New York, NY, USA: Academic, Nov. 2013.

[16] A. Gallivanoni, I. Rech, and M. Ghioni, "Progress in quenching circuits for single photon avalanche diodes," *IEEE Trans. Nucl. Sci.*, vol. 57, no. 6, pp. 3815–3826, Dec. 2010.

[17] D. Chitnis and S. Collins, "A SPAD-based photon detecting system for optical communications," *J. Lightw. Technol.*, vol. 32, no. 10, pp. 2028–2034, May 15, 2014.

[18] D. Chitnis *et al.*, "A 200 Mb/s VLC demonstration with a SPAD based receiver," in *Proc. IEEE Summer Topics Meeting Ser.*, Jul. 2015, pp. 226–227.

[19] E. Fisher, I. Underwood, and R. Henderson, "A reconfigurable 14-bit 60GPhoton/s single-photon receiver for visible light communications," in *Proc. Eur. Solid-State Circuits Conf.*, Bordeaux, France, Sep. 2012, pp. 85–88.

[20] E. Fisher, I. Underwood, and R. Henderson, "A reconfigurable single-photon-counting integrating receiver for optical communications," *IEEE J. Solid-State Circuits*, vol. 48, no. 7, pp. 1638–1650, Jul. 2013.

[21] J. H. Lee, I. J. Kim, and H. D. Choi, "On the dead time problem of a GM counter," *Appl. Radiat. Isotopes*, vol. 67, no. 6, pp. 1094–1098, Jun. 2009.

[22] A. Eisele *et al.*, "185 MHz count rate, 139 dB dynamic range single-photon avalanche diode with active quenching circuit in 130 nm CMOS technology," in *Proc. Int. Image Sensor Workshop*, Hokkaido, Japan, Jun. 2011, pp. 278–281.

[23] K. Omote, "Dead-time effects in photon counting distributions," *Nucl. Instrum. Methods Phys. Res. A, Accel. Spectrom. Detect. Assoc. Equip.*, vol. 293, no. 3, pp. 582–588, Aug. 1990.

[24] C.-C. Chen, "Effect of detector dead time on the performance of optical direct-detection communication links," *Telecommun. Data Acquisition Prog. Rep.*, vols. 42–93, pp. 146–154, Jan./Mar. 1988.

[25] D. Zou, C. Gong, K. Wang, and Z. Xu, "Characterization of a practical photon counting receiver in optical scattering communication," in *Proc. IEEE Global Commun. Conf.*, Singapore, Dec. 2017, pp. 1–6.

[26] E. Sarbazi and H. Haas, "Detection statistics and error performance of SPAD-based optical receivers," in *Proc. IEEE 26th Annu. Int. Symp. Pers., Indoor, Mobile Radio Commun.*, Hong Kong, Aug./Sep. 2015, pp. 830–834.

[27] E. Sarbazi, M. Safari, and H. Haas, "Photon detection characteristics and error performance of SPAD array optical receivers," in *Proc. IEEE 4th Int. Workshop Opt. Wireless Commun.*, Istanbul, Turkey, Sep. 2015, pp. 132–136.

[28] E. Sarbazi, M. Safari, and H. Haas, "On the information transfer rate of SPAD receivers for optical wireless communications," in *Proc. IEEE Global Commun. Conf.*, Washington, DC, USA, Dec. 2016, pp. 1–6.

[29] D. R. Cox, *Renewal Theory*. New York, NY, USA: Wiley, 1962.

[30] D. Zwillinger, *Table of Integrals, Series, and Products*, 8th ed. New York, NY, USA: Academic, 2014.

[31] D. F. Yu and J. A. Fessler, "Mean and variance of single photon counting with deadtime," *Phys. Med. Biol.*, vol. 45, no. 7, pp. 2043–2056, 2000.

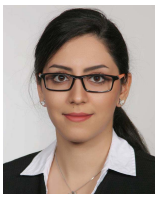

Elham Sarbazi (S'15) received the B.Sc. degree in electrical and computer engineering from the University of Tehran, Tehran, Iran, in 2011, and the M.Sc. degree (Hons.) in electrical engineering with a focus in communication systems from Özyeğin University, Istanbul, Turkey, in 2014. She is currently pursuing the Ph.D. degree in electrical engineering with the Institute for Digital Communications, The University of Edinburgh, Edinburgh, U.K. Her main research interests are in optical wireless and visible light communications.

Majid Safari (S'08–M'11) received the B.Sc. degree in electrical and computer engineering from the University of Tehran, Iran, in 2003, the M.Sc. degree in electrical engineering from the Sharif University of Technology, Iran, in 2005, and the Ph.D. degree in electrical and computer engineering from the University of Waterloo, Waterloo, ON, Canada, in 2011. He is currently an Assistant Professor with the Institute for Digital Communications, The University of Edinburgh. Before joining Edinburgh in 2013, he held a Post-Doctoral Fellowship at McMaster University, Hamilton, ON, Canada. His main research interests include the application of information theory and signal processing in optical communications, including fiber-optic communication, free-space optical communication, visible light communication, and quantum communication. He was the TPC Co-Chair of the 4th International Workshop on Optical Wireless Communication in 2015. He is currently an Associate Editor of the IEEE COMMUNICATION LETTERS.

Harald Haas (S'98–AM'00–M'03–SM'16–F'17) received the Ph.D. degree from The University of Edinburgh in 2001. He is currently the Chair of Mobile Communications at The University of Edinburgh, and he is the Initiator, Co-Founder, and Chief Scientific Officer of pureLiFi Ltd., and the Director of the LiFi Research and Development Center, The University of Edinburgh. He has authored 400 conference and journal papers, including a paper in *Science* and co-authored a book *Principles of LED Light Communications Towards Networked Li-Fi* (Cambridge University Press, 2015). His main research interests are in optical wireless communications, hybrid optical wireless and RF communications, spatial modulation, and interference coordination in wireless networks. He first introduced and coined spatial modulation and LiFi. LiFi was listed among the 50 best inventions in *TIME* Magazine in 2011. He was an invited speaker at TED Global 2011, and his talk on Wireless Data from Every Light Bulb has been watched online over 2.4 million times. He gave a second TED Global lecture in 2015 on the use of solar cells as LiFi data detectors and energy harvesters. This has been viewed online over 1.8 million times. He was elected as a fellow of the Royal Society of Edinburgh in 2017. In 2012 and 2017, he was a recipient of the prestigious Established Career Fellowship from the Engineering and Physical Sciences Research Council (EPSRC) within Information and Communications Technology in the U.K. In 2014, he was selected by EPSRC as one of ten Recognizing Inspirational Scientists and Engineers Leaders in the U.K. He was a co-recipient of the EURASIP Best Paper Award for the *Journal on Wireless Communications and Networking* in 2015 and the Jack Neubauer Memorial Award of the IEEE Vehicular Technology Society. In 2016, he received the Outstanding Achievement Award from the International Solid State Lighting Alliance. He was a co-recipient of recent best paper awards at VTC-Fall, 2013, VTC-Spring 2015, ICC 2016, and ICC 2017. He is an Editor of the IEEE TRANSACTIONS ON COMMUNICATIONS and the IEEE JOURNAL OF LIGHTWAVE TECHNOLOGIES.

The Impact of Long Dead Time on the Photocount Distribution of SPAD Receivers

Elham Sarbazi, Majid Safari and Harald Haas
Li-Fi Research and Development Centre, Institute for Digital Communications, School of Engineering,
The University of Edinburgh, Edinburgh, EH9 3FD, UK.
Email: {e.sarbazi, majid.safari, h.haas}@ed.ac.uk

***Abstract*—A single photon avalanche diode (SPAD) receiver can provide a significantly improved detection sensitivity over conventional photodiodes. However, upon detecting a photon, the SPAD receiver is unable to respond to subsequent incident photons for a certain period of time called dead time. When the SPAD receiver is counting in consecutive intervals and its dead time is relatively long compared to the counting interval, the dead time in one interval may overlap the next intervals, causing counting losses in those intervals. In this paper, the photocount statistics of an active quenching SPAD receiver with a long dead time is investigated. While detecting in consecutive time intervals, the SPAD receiver can be modeled as a Markov chain. It is shown that the SPAD experiences a transient period, before eventually reaching its steady state. The duration of the transient period increases with both the dead time and the signal photon rate. The bit error performance of the system with an on-off keying (OOK) modulated signal is also evaluated. Our results show that the SPAD's dead time significantly degrades the error performance of high data rate links.**

***Index Terms*—Single photon avalanche diode (SPAD), active quenching, dead time, Markov process, blocking probability, inter-symbol interference (ISI).**

I. Introduction

Single photon avalanche diodes (SPADs) are semiconductor devices with extremely high sensitivity. This feature has opened the door to many optical wireless communication (OWC) applications, dealing with very low intensity levels down to a single photon, where conventional positive-intrinsic-negative (PIN) diodes and avalanche photodiodes (APDs) can not provide sufficient optical sensitivity. Examples of potential applications include, but are not limited to, deep space optical communications [1], gas well downhole monitoring systems [2], data transmission over plastic optical fibers [3], and underwater communications [4], [5].

When the SPAD receiver detects a photon, it becomes inactive, or blocked, for a certain period of time called *dead time*, caused by a *quenching circuit*. It is only after this dead time period that the SPAD is able to detect a subsequent photon. Active quenching (AQ) and passive quenching (PQ) are the two main types of quenching circuits. SPADs with AQ circuits have a constant dead time, while in PQ SPADs photons arriving during the dead time extend its duration [6].

Several experiments demonstrate that the performance of SPAD receivers is degraded by their unavoidable dead time [3], [7]–[10]. However, there is limited theoretical studies focusing on the impact of dead time [11]–[14]. In any SPAD-based OWC system, the counting losses arising from the dead time, not only result in higher error probabilities, but also limit the maximum achievable data rate [15]–[18].

In [15] and [18], we presented a thorough characterization of single SPADs, where we derived the exact photocount distribution of both AQ and PQ SPAD receivers in the presence of dead time. It was assumed that the dead time is sufficiently shorter than the counting interval, so that independent counting statistics could be assumed for consecutive counting intervals. Based on this assumption, the bit error performance of a SPAD-based OWC system was investigated. However, if the dead time is long relative to the counting period, the mathematical models of [15] and [18] can not be applied. In such cases, the dead time of the last detected photon in one interval is extended to the next interval(s), and the counting statistics of adjacent time slots are correlated, hence, the memoryless property of the SPAD receiver is lost.

In this paper, we study the effect of a long dead time on the photocount distribution of AQ SPADs. We model the AQ SPAD with a Markov chain and obtain the transient and steady state probabilities for unmodulated and on-off keying (OOK) modulated input signals. The photocount distribution is then derived which can be used for the error performance analysis of a SPAD-based OWC system.

The rest of this paper is organized as follows. In Section II, the photocount statistics of a SPAD detector in a single-slot counting mode are briefly summarized. In Section III, the SPAD's counting behavior in a consecutive-slots counting mode is discussed, where the photocount distribution in the presence of a long dead time is derived based on a Markov model for the SPAD receiver. In Section IV, some numerical results are provided. Finally, concluding remarks are given in Section V.

II. Counting Statistics in A Single Counting Interval

A. Ideal Detector

For an ideal single-photon detector, photon detection events are modeled as a Poisson process for which the probability of detecting k photons over a counting interval of length T is given by [19], [20]:

$$p_0(k) = \frac{(\lambda T)^k e^{-\lambda T}}{k!}, \tag{1}$$

where the constant λ is the average photon arrival rate (in photons/s). The mean and variance of the photon counts over the time period of T seconds are given by:

$$\mu_0 = \sigma_0^2 = \lambda T. \tag{2}$$

B. Short Dead Time

In an AQ SPAD with dead time τ, after each photon detection, the SPAD is blocked, and any incident photon during this period is lost. Assuming that the SPAD is ready to operate at the beginning of a counting interval of length T, the maximum number of photons to be detected is $k_{\max} = \lfloor T/\tau \rfloor + 1$, where $\lfloor x \rfloor$ denotes the largest integer that is smaller than x. Let the dead time ratio be defined as $\delta = \tau/T$. If the dead time duration is short relative to the counting interval, i.e. $\delta < 1$, the probability of detecting k photons is given by [15], [18], [21]:

$$p_K(k) = \begin{cases} \sum\limits_{i=0}^{k} \psi(i,\lambda_k) - \sum\limits_{i=0}^{k-1} \psi(i,\lambda_{k-1}), & k < k_{\max} \\ 1 - \sum\limits_{i=0}^{k-1} \psi(i,\lambda_{k-1}), & k = k_{\max} \\ 0, & k > k_{\max} \end{cases} \tag{3}$$

where the function $\psi(i,\lambda)$ is defined as $\psi(i,\lambda) = \lambda^i e^{-\lambda}/i!$, and $\lambda_k = \lambda(T - k\tau)$. The mean and variance of the photocount distribution in (3) are [18]:

$$\mu_K = k_{\max} - \sum_{k=0}^{k_{\max}-1} \sum_{i=0}^{k} \psi(i,\lambda_k). \tag{4a}$$

$$\sigma_K^2 = \sum_{k=0}^{k_{\max}-1} \sum_{i=0}^{k} (2k_{\max} - 2k - 1)\psi(i,\lambda_k) - \left(\sum_{k=0}^{k_{\max}-1} \sum_{i=0}^{k} \psi(i,\lambda_k) \right)^2. \tag{4b}$$

As dead time approaches zero, the probability mass function (PMF) in (3) approaches the ideal Poisson distribution in (1). Also the limiting relations $\lim_{\tau\to 0} \mu_K = \mu_0$ and $\lim_{\tau\to 0} \sigma_K^2 = \sigma_0^2$ hold.

C. Long Dead Time

In the case of $\delta \geq 1$, the SPAD can detect at most one photon ($k_{\max} = 1$) in the counting interval, and the photocounts follow a Bernoulli distribution:

$$p_K(k) = \begin{cases} e^{-\lambda T}, & k = 0 \\ 1 - e^{-\lambda T}, & k = 1 \end{cases} \tag{5}$$

Accordingly, other than limiting $k_{\max}$, the dead time does not appear in the $p_K(k)$ expression, i.e. if the dead time is longer than the counting interval, no matter how long it is, the photocount distribution is not affected. For the PMF expression in (5), the mean and variance are given by:

$$\mu_K = 1 - e^{-\lambda T}. \tag{6a}$$

$$\sigma_K^2 = e^{-\lambda T}(1 - e^{-\lambda T}). \tag{6b}$$

III. Counting Statistics in Consecutive Counting Intervals

Some applications may require the SPAD receiver to count in consecutive intervals. Of particular interest are SPAD-based OWC systems, where the counting process is performed in consecutive time slots (e.g. bit intervals in OOK modulation). In these systems, the existence of dead time does not allow the use of arbitrarily narrow time slots for transmitting optical pulses; as the SPAD's dead time can overlap two adjacent time slots, causing the detection statistics of neighboring time slots to become correlated. Hence, the photocount statistics over a given time slot also depends on the received optical intensity over the previous time slots. This effect can be considered as inter-symbol interference (ISI) in OWC systems [3]. Depending on the length of the counting time interval compared to the dead time, the following two cases are considered:

A. $\tau < T$

In this case, the aforementioned effect is insignificant, i.e. the counting statistics over different time slots can be assumed as independent. The SPAD detector can then be regarded as a memoryless system. Accordingly, the expressions for the PMF, the mean and the variance of the SPAD's photocounts given in (3) and (4) can be applied for the performance analysis of the OWC systems [15], [17], [18].

B. $\tau \geq T$

In this case, the aforementioned effect becomes apparent, and the memoryless property of the SPAD's photon counting process is lost. Therefore, the PMF, the mean and the variance of the SPAD's photocounts given in (5) and (6) do not describe the real Bernoulli process accurately. In the following, we study this case and are especially concerned with the modifications to the original Bernoulli photocount distribution.

Suppose that $\tau = mT$, where m is an integer value. This assumption is made for simplicity and mathematical tractability, and could be relaxed without changing the key results. During each counting interval of length T, the SPAD is either free or blocked by the dead time of detected photons in current/previous time slot(s). Let the SPAD receiver be modeled by the Markov chain illustrated in Fig. 1.

In the state 0, the SPAD is free. It remains in this state, with probability α, if no photon arrives. If a photon arrives, it is detected and the SPAD proceeds to the state m (with probability $1-\alpha$). Once in the state m, the SPAD proceeds to the state $m-1$ in the next interval (with certainty), provided that $m > 1$. This continues until reaching the state 1. In all of these states apart from the state 1, no incident photon is detectable. In the state 1, the SPAD is still partially blocked. It may return to the state 0 with probability β and the process repeats itself or it may return to the state m with probability $1-\beta$, if another detection event happens.

Denote the number of incident and detected photons during the nth counting interval by X_n and K_n, respectively. Let S_n represent the state of the SPAD detector during the nth

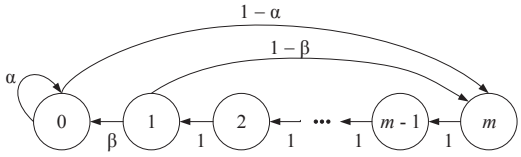

Fig. 1. Markov model of the SPAD receiver.

counting interval. S_n takes values in $\mathcal{S} = \{0, 1, \ldots, m\}$ with $S_n = 0$ indicating that the SPAD is free, $S_n = 1$ indicating that the SPAD is partially blocked, and $S_n = i > 1$ indicating that the SPAD is totally blocked in the nth interval and will remain blocked throughout intervals n, $n+1$, ... , $n+i-2$. Define $q_i^{(n)} = \Pr\{S_n = i\}$, for $i = 0, 1, \ldots, m$. According to the Markov model in Fig. 1, α and β are given by:

$$\alpha = \Pr\{S_n = 0 | S_{n-1} = 0\}. \tag{7}$$

$$\beta = \Pr\{S_n = 0 | S_{n-1} = 1\}. \tag{8}$$

In the following, the state probabilities are determined for two different cases, unmodulated and OOK-modulated X_n.

B.1. Unmodulated Signal

Suppose that X_n is an unmodulated signal, described by a Poisson distribution with rate parameter λ. In this case, X_n and X_m are independent for $m \neq n$. Also, the number of incident photons during any time interval is independent of the SPAD's state, i.e. X_n and S_n are independent. Since $S_{n-1} = 0$ results in S_n being independent of what happened in the previous intervals, the conditional probability α given in (7) can be easily obtained as:

$$\alpha = e^{-\lambda T}. \tag{9}$$

The conditional probability β given in (8), depends on all the non-zero states preceding it. It can be shown that β in the nth interval is given by:

$$\beta^{(n)} = \frac{\sum_{i=1}^{c_{\max}} q_0^{(n-mi)} \psi(i, \lambda T)}{\sum_{i=1}^{c_{\max}} q_0^{(n-mi)} (1 - \sum_{j=0}^{i-1} \psi(j, \lambda T))}, \tag{10}$$

where $c_{\max} = \lfloor \frac{n-1}{m} \rfloor$. The following equations hold for the Markov chain of Fig. 1:

$$\begin{aligned} q_0^{(n)} &= \alpha\, q_0^{(n-1)} + \beta^{(n-1)}\, q_1^{(n-1)}, \\ q_1^{(n)} &= q_2^{(n-1)}, \\ q_2^{(n)} &= q_3^{(n-1)}, \\ &\vdots \\ q_{m-1}^{(n)} &= q_m^{(n-1)}, \\ q_m^{(n)} &= (1-\alpha)\, q_0^{(n-1)} + (1-\beta^{(n-1)})\, q_1^{(n-1)}. \end{aligned} \tag{11}$$

The SPAD undergoes a transient period during which the occupancy probability of each state, $q_i^{(n)}$, changes with n. Since this Markov chain is aperiodic and irreducible, the SPAD will eventually reach a steady state, and the state probabilities will thereafter remain almost constant. Let the steady state probabilities be defined as $q_i = \lim_{n\to\infty} q_i^{(n)}$. The q_i satisfy:

$$\begin{aligned} q_0 &= \alpha\, q_0 + \beta\, q_1, \\ q_1 &= q_2 = \cdots = q_m, \\ q_m &= (1-\alpha)\, q_0 + (1-\beta)\, q_1, \end{aligned} \tag{12}$$

where (see Appendix A),

$$\beta = \lim_{n\to\infty} \beta^{(n)} = \frac{1 - e^{-\lambda T}}{\lambda T}, \tag{13}$$

Solving $\sum_{i=0}^{m} q_i = 1$ gives:

$$\begin{aligned} q_0 &= \frac{1}{1 + m\lambda T} \\ q_i &= \frac{\lambda T}{1 + m\lambda T} \qquad i = 1, \ldots, m. \end{aligned} \tag{14}$$

The limit $\lambda \to \infty$ results in $q_0 \to 0$ and $q_{i>0} \to 1/m$. The SPAD cycles through all of the states continuously and it never goes to the free state (state 0).

Denote $p_K^{(n)}(k)$ the probability of detecting k photons in the nth interval. With $\tau \geq T$, the SPAD can detect at most one photon per counting interval, T. Therefore:

$$p_K^{(n)}(k) = \Pr\{K_n = k\} = \begin{cases} \sum_{i=0}^{m-1} q_i^{(n)}, & k = 0 \\ q_m^{(n)}, & k = 1 \end{cases} \tag{15}$$

In the steady state, the photocounts follow a Bernoulli distribution given by:

$$p_K(k) = \lim_{n\to\infty} p_K^{(n)}(k) = \begin{cases} \dfrac{1 + (m-1)\lambda T}{1 + m\lambda T}, & k = 0 \\ \dfrac{\lambda T}{1 + m\lambda T}, & k = 1 \end{cases} \tag{16}$$

For the above PMF expression, the mean and variance are expressed as:

$$\mu_K = \frac{\lambda T}{1 + m\lambda T}. \tag{17a}$$

$$\sigma_K^2 = \frac{\lambda T + (m-1)\lambda^2 T^2}{(1 + m\lambda T)^2}. \tag{17b}$$

The probability that the SPAD is blocked after each detection event is termed as the *blocking probability* and is a useful metric for assessing its photon counting performance [22]. For the Markov model presented in this paper, the blocking probability is defined as:

$$p_{\mathrm{B}}^{(n)} = 1 - q_0^{(n)}. \tag{18}$$

B.2. On-Off Keying Modulated Signal

In this case, it is assumed that X_n is an OOK modulated signal. Let $B_n \in \{0,1\}$ where $\{B_n\}$ are independent and identically distributed with $\Pr\{B_n = 1\} = 0.5$. The mean photon rate in the nth slot is given by:

$$\lambda(n) = \begin{cases} \lambda_{\rm n}, & B_n = 0 \\ \lambda_{\rm s} + \lambda_{\rm n}, & B_n = 1 \end{cases} \tag{19}$$

where $\lambda_{\rm s}$ and $\lambda_{\rm n}$ represent the signal and background noise photon rates, respectively.

Following a similar approach, the steady state expressions for α and β can be obtained:

$$\begin{aligned} \alpha &= \frac{1}{2}\alpha_{\rm n} + \frac{1}{2}\alpha_{\rm sn} \\ &= \frac{1}{2}e^{-\lambda_{\rm n}T} + \frac{1}{2}e^{-(\lambda_{\rm s}+\lambda_{\rm n})T}. \end{aligned} \tag{20}$$

$$\begin{aligned} \beta &= \frac{1}{2}\beta_{\rm n} + \frac{1}{2}\beta_{\rm sn} \\ &= \frac{1-e^{-\lambda_{\rm n}T}}{2\lambda_{\rm n}T} + \frac{1-e^{-(\lambda_{\rm s}+\lambda_{\rm n})T}}{2(\lambda_{\rm s}+\lambda_{\rm n})T}. \end{aligned} \tag{21}$$

The steady state probabilities are then given by:

$$\begin{aligned} q_0 &= \frac{\beta}{\beta + m(1-\alpha)} \\ q_i &= \frac{1-\alpha}{\beta + m(1-\alpha)}, \qquad i = 1, \ldots, m. \end{aligned} \tag{22}$$

and the steady state Bernoulli distribution is expressed as:

$$p_K(k) = \begin{cases} \dfrac{\beta + (m-1)(1-\alpha)}{\beta + m(1-\alpha)}, & k = 0 \\ \dfrac{1-\alpha}{\beta + m(1-\alpha)}, & k = 1 \end{cases} \tag{23}$$

For this case, the approximate probability of error is:

$$P_e \approx \frac{1}{2} + \frac{q_0}{2}(\alpha_{\rm sn} - \alpha_{\rm n}) + \frac{q_1}{2}(\beta_{\rm sn} - \beta_{\rm n}). \tag{24}$$

IV. Results and Discussions

In this section, some numerical results on the evolution of the state probabilities and the photon counting distributions are provided. Figs. 2–4 correspond to the case of an unmodulated input signal. In these figures, exact numerical results are obtained by initializing the system of Fig. 1 in the state 0, and letting the state probabilities evolve, thus calculating $\beta^{(n)}$ and $q_i^{(n)}$ in each interval, n. For approximate numerical results, $\beta^{(n)}$ is replaced by its steady value given in (13). The Monte Carlo simulation results are obtained by generating a Poisson arrival process, counting the number of detected photons in each interval, and then determining the state probabilities. It is assumed that the SPAD receiver is initially free to detect photons. This assumption is equivalent to $q_0^{(0)} = 1$ in numerical calculations.

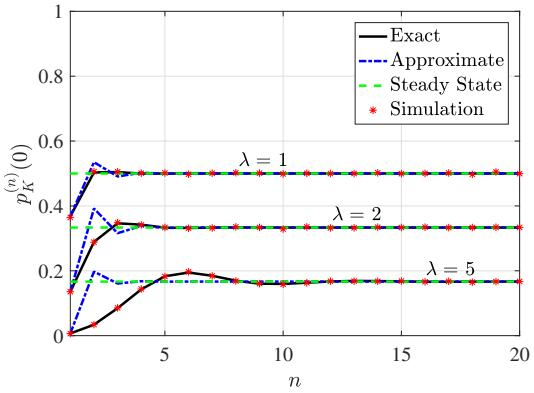

Fig. 2. Evolution of $p_K^{(n)}(0)$ for a SPAD with $\tau = T$. The transient period is shorter for smaller photon rates (unmodulated signal).

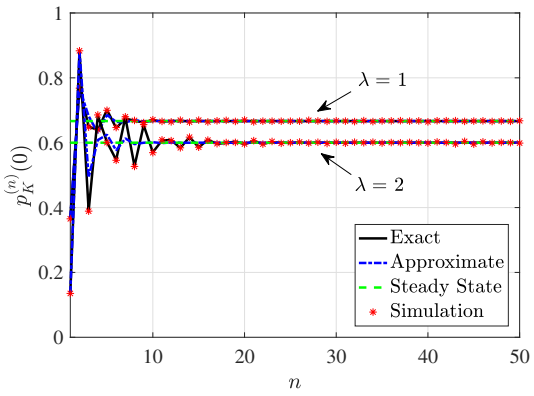

(a) $\lambda = 1, 2$

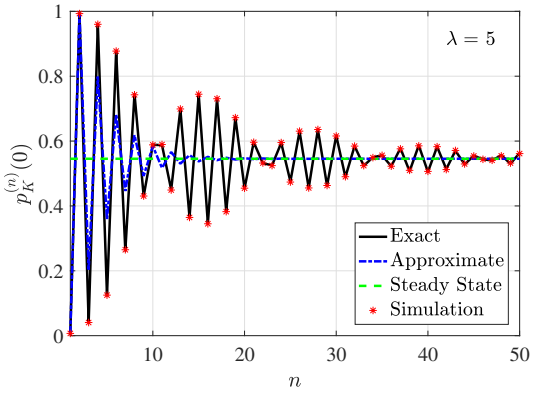

(b) $\lambda = 5$

Fig. 3. Evolution of $p_K^{(n)}(0)$ for a SPAD with $\tau = 2T$ (unmodulated signal).

As the first example, consider a system with $m = 1$. This system consists of two states: 0 and 1, and $p_K^{(n)}(0) = q_0^{(n)}$. Fig. 2 illustrates the evolution of the probability of state 0 for this system. The results for three different values of λ are provided in this figure. Note the transient period before reaching the steady state. As can be seen, for $\lambda = 1$ and $\lambda = 2$, the system reaches the steady state for $n \geq 5$. For larger values of λ, e.g. $\lambda = 5$, this takes longer ($n \geq 10$). Note that for analyzing the performance of such a system (in terms of error probability, capacity, etc.), we can allow the system to pass through the transient period and approximate the system performance by its steady state performance.

Fig. 3 corresponds to a system with $m = 2$. The transient period varies with m and λ significantly as in Figs. 3a and 3b. The duration of the transient period increases nonlinearly with each of these parameters. For $\lambda = 5$, the steady state is not reached even after 50 intervals.

In Fig. 4, the SPAD's steady state blocking probability is plotted for three different values of m. According to this figure, the blocking probability increases rapidly with λ and it approaches 1. In fact, for larger values of λ, the SPAD continuously remains blocked. This effect is termed as the *saturation* of the SPAD receiver.

Fig. 5 illustrates the steady state bit error probability in the presence of an OOK modulated signal as a function of data rate, $R = 1/T$. In this figure, a constant dead time ($\tau = 10$ ns) is considered. $K_\mathrm{s} = \lambda_\mathrm{s} T$ and $K_\mathrm{n} = \lambda_\mathrm{n} T$, are the average signal and background noise counts per bit interval, respectively. Recall from Section III that $m = \tau/T$. As R is increased, m is also increased, hence the SPAD's dead time overlaps more bit intervals, increasing the probability of errors. This figure presents the trade-off between the bit error ratio (BER) and the data rate where the SPAD's dead time does not allow the use of arbitrarily short bit intervals (i.e. high data rates), as this significantly degrades the bit error performance. Note that even for $R = 100$ Mbits/s ($m = 1$), the BER is still high ($\geq 10^{-3}$). This highlights a fundamental limitation of using single SPAD receivers for high data rate communications.

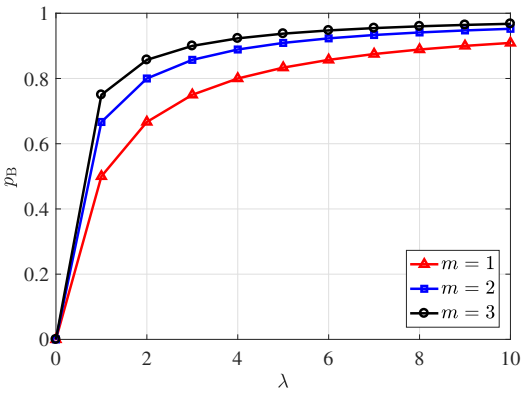

Fig. 4. SPAD's steady state blocking probability (unmodulated signal).

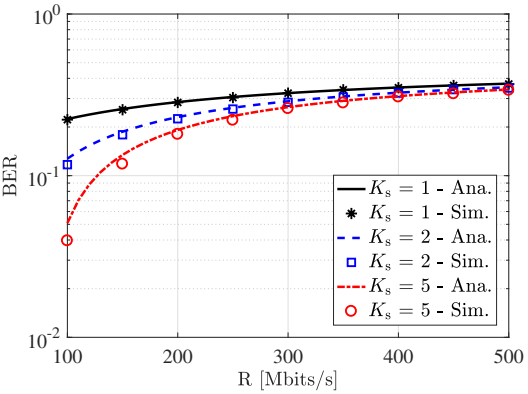

Fig. 5. BER curves of a SPAD-based system with OOK modulation as a function of data rate: $\tau = 10$ ns, and $K_\mathrm{n} = 0.01$ photons/bit.

V. Conclusions

In this paper, we have characterized the counting statistics of an AQ SPAD receiver with a dead time length equal to or longer than the counting interval. We have illustrated that in such a case, the SPAD's counting process is first subject to a transient phase and then, it reaches a steady state. We have shown that in the steady state, the SPAD's photocounts follow a Bernoulli distribution. The steady state Bernoulli probability distribution allows a simple and accurate approximation of blocking losses for scenarios with sparse event arrival rates, and is particularly required when assessing the bit error performance of any high data rate SPAD-based OWC system.

This study provides valuable insights into the fundamental limits of SPAD receivers for optical communication systems. It highlights the trade-off between the photon counting performance and the data rate, as the existence of dead time causes significant counting losses when operating in high data rates.

Appendix A
Calculating β in the Steady State

According to (10), β is given by:

$$\beta^{(n)} = \frac{\sum_{i=1}^{c_\mathrm{max}} q_0^{(n-mi)} \psi(i, \lambda T)}{\sum_{i=1}^{c_\mathrm{max}} q_0^{(n-mi)} \left(1 - \sum_{j=0}^{i-1} \psi(j, \lambda T)\right)}$$

where $c_\mathrm{max} = \lfloor \frac{n-1}{m} \rfloor$. In the following, the steady state value of β is obtained. For this, the limit of the above expression

for $n \to \infty$ is taken. $\beta^{(n)}$ can be rewritten as:

$$\beta^{(n)} = \frac{\sum_{i=1}^{c_{\max}} q_0^{(n-mi)} \psi(i, \lambda T)}{\sum_{i=1}^{c_{\max}} q_0^{(n-mi)} \sum_{j=i}^{\infty} \psi(j, \lambda T)} \tag{25}$$

Assume a threshold n_{TH}, for which $\psi(i, \lambda T) \approx 0$ if $i > n_{\mathrm{TH}}$. For $c_{\max} \to \infty$, $n_{\mathrm{TH}} < c_{\max}$ holds. Hence,

$$\beta^{(n)} = \frac{\sum_{i=1}^{n_{\mathrm{TH}}} q_0^{(n-mi)} \psi(i, \lambda T)}{\sum_{i=1}^{n_{\mathrm{TH}}} q_0^{(n-mi)} \sum_{j=i}^{\infty} \psi(j, \lambda T) + \sum_{i=n_{\mathrm{TH}}+1}^{c_{\max}} q_0^{(n-mi)} \sum_{j=i}^{\infty} \psi(j, \lambda T)} \tag{26}$$

The right term in the denominator is approximately zero as $q_0^{(n-mi)}$ is finite and $\psi(j, \lambda T) \approx 0$ for $j > n_{\mathrm{TH}}$. Also, as n approaches ∞, $q_0^{(n-mi)}$ in (26) can be replaced by the steady state value q_0. Therefore,

$$\begin{aligned} \beta^{(n)} &= \frac{\sum_{i=1}^{n_{\mathrm{TH}}} q_0 \psi(i, \lambda T)}{\sum_{j=1}^{n_{\mathrm{TH}}} \sum_{i=1}^{j} q_0 \psi(j, \lambda T)} \\ &= \frac{\sum_{i=1}^{n_{\mathrm{TH}}} \psi(i, \lambda T)}{\sum_{j=1}^{n_{\mathrm{TH}}} j \psi(j, \lambda T)} \end{aligned} \tag{27}$$

Define:

$$A = \sum_{i=1}^{n_{\mathrm{TH}}} \frac{(\lambda T)^i}{i!}$$

$$B = \sum_{i=1}^{n_{\mathrm{TH}}} \frac{(\lambda T)^i}{(i-1)!}$$

As it was previously assumed that n_{TH} is sufficiently large, such that $\psi(i, \lambda T) \approx 0$ for $i > n_{\mathrm{TH}}$, A and B can be approximated as follows:

$$A \approx e^{\lambda T} - 1$$

$$B \approx \lambda T e^{\lambda T}$$

Therefore,

$$\beta = \lim_{n \to \infty} \beta^{(n)} = \frac{1 - e^{-\lambda T}}{\lambda T} \tag{28}$$

Acknowledgment

Professor Haas gratefully acknowledges the support of this research by the Engineering and Physical Sciences Research Council (EPSRC) under an Established Career Fellowship grant, EP/R007101/1. He also acknowledges the financial support of his research by the Wolfson Foundation and the Royal Society.

References

[1] P. I. Hopman *et al.*, "An End-to-End Demonstration of a Receiver Array Based Free-Space Photon Counting Communications Link," in *Proc. SPIE Free-Space Laser Communications VI*, vol. 6304, San Diego, CA, 2006, p. 13.

[2] Y. Li *et al.*, "Single Photon Avalanche Diode (SPAD) VLC System and Application to Downhole Monitoring," in *Proc. IEEE Global Commun. Conf.*, Austin, TX, 2014, pp. 2108–2113.

[3] D. Chitnis and S. Collins, "A SPAD-Based Photon Detecting System for Optical Communications," *J. Lightw. Technol.*, vol. 32, no. 10, pp. 2028–2034, May 2014.

[4] C. Wang, H.-Y. Yu, and Y.-J. Zhu, "A Long Distance Underwater Visible Light Communication System with Single Photon Avalanche Diode," *IEEE Photon. J.*, vol. 8, no. 5, pp. 1–11, 2016.

[5] M. A. Khalighi, T. Hamza *et al.*, "Underwater Wireless Optical Communications Using Silicon Photo-Multipliers," *IEEE Photon. J.*, vol. 9, no. 4, pp. 1–10, Aug. 2017.

[6] A. Eisele *et al.*, "185 MHz Count Rate, 139 dB Dynamic Range Single-Photon Avalanche Diode with Active Quenching Circuit in 130 nm CMOS Technology," in *Proc. Int. Image Sensor Workshop*, Japan, 2011, pp. 278–281.

[7] D. Chitnis, L. Zhang *et al.*, "A 200 Mb/s VLC Demonstration with a SPAD Based Receiver," in *IEEE Summer Topicals Meeting Series*, Jul. 2015, pp. 226–227.

[8] E. Fisher, I. Underwood, and R. Henderson, "A Reconfigurable Single-Photon-Counting Integrating Receiver for Optical Communications," *IEEE J. Solid-State Circuits*, vol. 48, no. 7, pp. 1638–1650, Jul. 2013.

[9] J. Kosman, O. Almer, A. V. Jalajakumari, S. Videv, H. Haas, and R. K. Henderson, "60 Mb/s, 2 Meters Visible Light Communications in 1 klx Ambient Using an Unlensed CMOS SPAD Receiver," in *Photonics Society Summer Topical Meeting Series*, Newport Beach, CA, 2016, pp. 171–172.

[10] O. Almer, D. Tsonev *et al.*, "A SPAD-Based Visible Light Communications Receiver Employing Higher Order Modulation," in *Proc. IEEE Global Commun. Conf.*, San Diego, CA, 2015.

[11] Y. Li, M. Safari, R. Henderson, and H. Haas, "Optical OFDM with Single-Photon Avalanche Diode," *IEEE Photon. Technol. Lett.*, vol. 27, no. 9, pp. 943–946, May 2015.

[12] ——, "Nonlinear Distortion in SPAD-Based Optical OFDM Systems," in *Proc. IEEE Global Commun. Conf. Workshops*, San Diego, CA, 2015.

[13] D. Zou, C. Gong, K. Wang, and Z. Xu, "Characterization of a Practical Photon Counting Receiver in Optical Scattering Communication," in *Proc. IEEE Global Commun. Conf.*, Singapore, 2017.

[14] T. Mao, Z. Wang, and Q. Wang, "Receiver Design for SPAD-Based VLC Systems under Poisson–Gaussian Mixed Noise Model," *Optics Express*, vol. 25, no. 2, pp. 799–809, 2017.

[15] E. Sarbazi and H. Haas, "Detection Statistics and Error Performance of SPAD-based Optical Receivers," in *Proc. IEEE 26th Ann. Int. Symp. Personal, Indoor, and Mobile Radio Communications*, Hong Kong, China, 2015, pp. 830–834.

[16] E. Sarbazi, M. Safari, and H. Haas, "Photon Detection Characteristics and Error Performance of SPAD Array Optical Receivers," in *Proc. IEEE 4th Int. Workshop on Optical Wireless Communications*, Istanbul, Turkey, 2015, pp. 132–136.

[17] ——, "On the Information Transfer Rate of SPAD Receivers for Optical Wireless Communications," in *Proc. IEEE Global Commun. Conf.*, Washington, DC, Dec. 2016, pp. 1–6.

[18] ——, "Statistical Modeling of Single-Photon Avalanche Diode Receivers for Optical Wireless Communications," *IEEE Trans. Commun.*, pp. 1–1, 2018.

[19] B. E. A. Saleh and M. C. Teich, *Fundamentals of Photonics*. New York: Wiley, 1991.

[20] R. M. Gagliardi and S. Karp, *Optical Communications*, 2nd ed. New York: Wiley, 1995.

[21] C.-C. Chen, "Effect of Detector Dead Time on the Performance of Optical Direct-Detection Communication Links," *TDA Progress Rep.*, vol. 42–93, pp. 146–154, 1988.

[22] B. Moision, M. Srinivasan, and J. Hamkins, "The Blocking Probability of Geiger-Mode Avalanche Photo-diodes," in *Proc. SPIE, Satellite Data Compression, Communications, and Archiving*, San Diego, CA, 2005.

References

[1] R. M. Gagliardi and S. Karp, *Optical Communications*. New York: Wiley, 2 ed., 1995.

[2] H. Elgala, R. Mesleh, and H. Haas, "Indoor Optical Wireless Communication: Potential and State-of-the-Art," *IEEE Commun. Mag.*, vol. 49, pp. 56–62, Sept. 2011.

[3] Z. Ghassemlooy, W. Popoola, and S. Rajbhandari, *Optical Wireless Communications: System and Channel Modelling with MATLAB®*. CRC Press, 1 ed., 2012.

[4] S. Dimitrov and H. Haas, *Principles of LED Light Communications: Towards Networked Li-Fi*. Cambridge University Press, 2015.

[5] S. B. Alexander, *Optical Communication Receiver Design*. Bellingham: SPIE Press, 1997.

[6] V. W. Chan, "Free-Space Optical Communications," *IEEE/OSA J. Lightw. Technol.*, vol. 24, pp. 4750–4762, Dec. 2006.

[7] Y. Li, M. Safari, *et al.*, "Single Photon Avalanche Diode (SPAD) VLC System and Application to Downhole Monitoring," in *Proc. IEEE Global Commun. Conf.*, (Austin, TX), pp. 2108–2113, 2014.

[8] D. Chitnis and S. Collins, "A SPAD-Based Photon Detecting System for Optical Communications," *IEEE/OSA J. Lightw. Technol.*, vol. 32, pp. 2028–2034, May 2014.

[9] E. Fisher, I. Underwood, and R. Henderson, "A Reconfigurable 14-bit 60GPhoton/s Single-Photon Receiver for Visible Light Communications," in *Proc. European Solid-State Circuits Conf.*, (Bordeaux, France), pp. 85–88, 2012.

[10] E. Fisher, I. Underwood, and R. Henderson, "A Reconfigurable Single-Photon-Counting Integrating Receiver for Optical Communications," *IEEE J. Solid-State Circuits*, vol. 48, pp. 1638–1650, July 2013.

[11] J. P. Donnelly, E. K. Duerr, *et al.*, "Design Considerations for 1.06-μm InGaAsP–InP Geiger-Mode Avalanche Photodiodes," *IEEE J. Quantum Electron.*, vol. 42, pp. 797–809, Aug. 2006.

[12] S. Verghese, J. P. Donnelly, *et al.*, "Arrays of InP-based Avalanche Photodiodes for Photon Counting," *IEEE J. Sel. Topics Quantum Electron.*, vol. 13, pp. 870–886, July 2007.

[13] A. Migdall, S. V. Polyakov, J. Fan, and J. C. Bienfang, *Single-Photon Generation and Detection: Physics and Applications*, vol. 45. Academic Press, Nov. 2013.

[14] S. Cova, M. Ghioni, A. Lacaita, C. Samori, and F. Zappa, "Avalanche Photodiodes and Quenching Circuits for Single-Photon Detection," *Applied Optics*, vol. 35, pp. 1956–1976, Apr. 1996.

[15] R. G. Brown, K. D. Ridley, and J. G. Rarity, "Characterization of Silicon Avalanche Photodiodes for Photon Correlation Measurements. 1: Passive Quenching," *Applied Optics*, vol. 25, pp. 4122–4126, Nov. 1986.

[16] R. G. Brown, R. Jones, J. G. Rarity, and K. D. Ridley, "Characterization of Silicon Avalanche Photodiodes for Photon Correlation Measurements. 2: Active Quenching," *Applied Optics*, vol. 26, pp. 2383–2389, June 1987.

[17] S. Donati and T. Tambosso, "Single-Photon Detectors: From Traditional PMT to Solid-State SPAD-Based Technology," *IEEE J. Sel. Topics Quantum Electron.*, vol. 20, no. 6, pp. 204–211, 2014.

[18] S. Cova, A. Lacaita, M. Ghioni, G. Ripamonti, and T. Louis, "20-ps Timing Resolution with Single-Photon Avalanche Diodes," *Review of Scientific Instruments*, vol. 60, pp. 1104–1110, June 1989.

[19] A. Rochas, "Single photon avalanche diodes in CMOS technology," tech. rep., Citeseer, 2003.

[20] A. Gallivanoni, I. Rech, and M. Ghioni, "Progress in Quenching Circuits for Single Photon Avalanche Diodes," *IEEE Trans. Nucl. Sci.*, vol. 57, pp. 3815–3826, Dec. 2010.

[21] M. W. Fishburn, *Fundamentals of CMOS Single-Photon Avalanche Diodes*. PhD thesis, Dept. Elect. Eng., TU Delft, Delft, Netherlands, 2012.

[22] A. Spinelli and A. Lacaita, "Physics and Numerical Simulation of Single Photon Avalanche Diodes," *IEEE Trans. Electron Devices*, vol. 44, pp. 1931–1943, Nov. 1997.

[23] R. McIntyre, "A New Look at Impact Ionization-Part I: A Theory of Gain, Noise, Breakdown Probability, and Frequency Response," *IEEE Trans. Electron Devices*, vol. 46, pp. 1623–1631, Aug. 1999.

[24] P. Yuan, K. Anselm, *et al.*, "A New Look at Impact Ionization-Part II: Gain and Noise in Short Avalanche Photodiodes," *IEEE Trans. Electron Devices*, vol. 46, pp. 1632–1639, Aug. 1999.

[25] Y. Kang, H. X. Lu, *et al.*, "Dark Count Probability and Quantum Efficiency of Avalanche Photodiodes for Single-Photon Detection," *Applied Physics Letters*, vol. 83, pp. 2955–2957, Oct. 2003.

[26] R. H. Hadfield, "Single-Photon Detectors for Optical Quantum Information Applications," *Nature Photonics*, vol. 3, pp. 696–705, Nov. 2009.

[27] D. Bronzi, F. Villa, S. Tisa, A. Tosi, and F. Zappa, "SPAD Figures of Merit for Photon-Counting, Photon-Timing, and Imaging Applications: A Review," *IEEE Sensors J.*, vol. 16, pp. 3–12, Jan. 2016.

[28] H. Dautet, P. Deschamps, B. Dion, A. D. MacGregor, D. MacSween, R. J. McIntyre, C. Trottier, and P. P. Webb, "Photon Counting Techniques with Silicon Avalanche Photodiodes," *Applied Optics*, vol. 32, pp. 3894–3900, July 1993.

[29] A. Eisele *et al.*, "185 MHz Count Rate, 139 dB Dynamic Range Single-Photon Avalanche Diode with Active Quenching Circuit in 130 nm CMOS Technology," in *Proc. Int. Image Sensor Workshop*, (Japan), pp. 278–281, 2011.

[30] S. H. Lee and R. P. Gardner, "A New G–M Counter Dead Time Model," *Appl. Radiat. Isot.*, vol. 53, pp. 731–737, Nov. 2000.

[31] J. H. Lee, I. J. Kim, and H. D. Choi, "On the Dead Time Problem of a GM Counter," *Appl. Radiat. Isot.*, vol. 67, pp. 1094–1098, June 2009.

[32] B. Moision, M. Srinivasan, and J. Hamkins, "The Blocking Probability of Geiger-Mode Avalanche Photo-diodes," in *Proc. SPIE, Satellite Data Compression, Communications, and Archiving*, (San Diego, CA), 2005.

[33] B. Moision and S. Piazzolla, "Blocking Losses on an Optical Communications Link," in *Proc. Int. Conf. Space Optical Systems and Applications*, (Santa Monica, CA), pp. 368–377, 2011.

[34] V. Savuskan, I. Brouk, M. Javitt, and Y. Nemirovsky, "An Estimation of Single Photon Avalanche Diode (SPAD) Photon Detection Efficiency (PDE) Nonuniformity," *IEEE Sensors J.*, vol. 13, pp. 1637–1640, May 2013.

[35] E. Sarbazi and H. Haas, "Detection Statistics and Error Performance of SPAD-based Optical Receivers," in *Proc. IEEE 26th Ann. Int. Symp. Personal, Indoor, and Mobile Radio Communications*, (Hong Kong, China), pp. 830–834, Sept. 2015.

[36] E. Sarbazi, M. Safari, and H. Haas, "Photon Detection Characteristics and Error Performance of SPAD Array Optical Receivers," in *Proc. IEEE 4th Int. Workshop on Optical Wireless Communications*, (Istanbul, Turkey), pp. 132–136, Sept. 2015.

[37] E. Sarbazi, M. Safari, and H. Haas, "Statistical Modeling of Single-Photon Avalanche Diode Receivers for Optical Wireless Communications," *IEEE Trans. Commun.*, vol. 66, pp. 4043–4058, Apr. 2018.

[38] E. Sarbazi, M. Safari, and H. Haas, "On the Information Transfer Rate of SPAD Receivers for Optical Wireless Communications," in *Proc. IEEE Global Communications Conf.*, (Washington, DC, USA), pp. 1–6, Dec. 2016.

[39] E. Sarbazi, M. Safari, and H. Haas, "The Impact of Long Dead Time on the Photocount Distribution of SPAD Receivers," in *Proc. IEEE Global Communications Conf.*, (Abu Dhabi, UAE), pp. 1–6, Dec. 2018.

[40] C. C. Chen and C. S. Gardner, "Comparison of Direct and Heterodyne Detection Optical Intersatellite Communication Links," *NASA Tech. Rep. EOSL NO. 87-002*, Mar. 1987.

[41] F. Xu, M.-A. Khalighi, and S. Bourennane, "Impact of Different Noise Sources on the Performance of PIN- and APD-Based FSO Receivers," in *Proc. of the IEEE 11th Int. Conf. on Telecommunications (ConTEL)*, (Graz, Austria), pp. 211–218, June 2011.

[42] B. E. A. Saleh and M. C. Teich, *Fundamentals of Photonics*. New York: Wiley, 1991.

[43] N. S. Kopeika and J. Bordogna, "Background Noise in Optical Communication Systems," *Proc. of the IEEE*, vol. 58, no. 10, pp. 1571–1577, 1970.

[44] R. J. McIntyre, "The Distribution of Gains in Uniformly Multiplying Avalanche Photodiodes: Theory," *IEEE Trans. Electron Devices*, vol. 19, pp. 703–713, June 1972.

[45] J. Conradi, "The Distribution of Gains in Uniformly Multiplying Avalanche Photodiodes: Experimental," *IEEE Trans. Electron Devices*, vol. 19, pp. 713–718, June 1972.

[46] R. McIntyre, "Multiplication Noise in Uniform Avalanche Diodes," *IEEE Trans. Electron Devices*, vol. 13, pp. 164–168, Jan. 1966.

[47] P. Webb, "Properties of Avalanche Photodiodes," *RCA Review*, vol. 35, pp. 234–278, Sept. 1974.

[48] C. Niclass, M. Soga, H. Matsubara, M. Ogawa, and M. Kagami, "A 0.18-μm CMOS SoC for a 100-m-Range 10-Frame/s 200 $\times$ 96-Pixel Time-of-Flight Depth Sensor," *IEEE J. Solid-State Circuits*, vol. 49, pp. 315–330, Jan. 2014.

[49] C. Niclass *et al.*, "Design and Characterization of a CMOS 3-D Image Sensor Based on Single Photon Avalanche Diodes," *IEEE J. Solid-State Circuits*, vol. 40, pp. 1847–1854, Sept. 2005.

[50] L. H. C. Braga, L. Gasparini, L. Grant, R. K. Henderson, N. Massari, M. Perenzoni, D. Stoppa, and R. J. Walker, "A Fully Digital 8$\times$ 16 SiPM Array for PET Applications With Per-Pixel TDCs and Real-Time Energy Output," *IEEE J. Solid-State Circuits*, vol. 49, pp. 301–314, Jan. 2014.

[51] D.-U. Li, J. Arlt, J. Richardson, R. Walker, A. Buts, D. Stoppa, E. Charbon, and R. Henderson, "Real-Time Fluorescence Lifetime Imaging System with a 32$\times$ 32 0.13 μm CMOS Low Dark-Count Single-Photon Avalanche Diode Array," *Opt. Express*, vol. 18, pp. 10257–10269, May 2010.

[52] A. Tosi, F. Zappa, and S. Cova, "Single-Photon Detectors for Practical Quantum Cryptography," in *Proc. SPIE, Electr.-Opt. Remote Sensing, Photonic Technol. Appl. VI*, vol. 8542, (Edinburgh, UK), p. 8, 2012.

[53] P. Hopman, P. Boettcher, L. M. Candell, J. Glettler, R. Shoup, and G. Zogbi, "An End-to-End Demonstration of a Receiver Array Based Free-Space Photon Counting Communications Link," in *Proc. SPIE Free-Space Laser Communications VI*, vol. 6304, (San Diego, CA), p. 13, 2006.

[54] C. Wang, H.-Y. Yu, and Y.-J. Zhu, "A Long Distance Underwater Visible Light Communication System with Single Photon Avalanche Diode," *IEEE Photon. J.*, vol. 8, pp. 1–11, Oct. 2016.

[55] M. A. Khalighi, T. Hamza, *et al.*, "Underwater Wireless Optical Communications Using Silicon Photo-Multipliers," *IEEE Photonics J.*, vol. 9, pp. 1–10, Aug. 2017.

[56] O. Almer, D. Tsonev, *et al.*, "A SPAD-Based Visible Light Communications Receiver Employing Higher Order Modulation," in *Proc. IEEE Global Communications Conf.*, (San Diego, CA), pp. 1–6, Dec. 2015.

[57] J. Kosman, O. Almer, A. V. Jalajakumari, S. Videv, H. Haas, and R. K. Henderson, "60 Mb/s, 2 Meters Visible Light Communications in 1 klx Ambient Using an Unlensed CMOS SPAD Receiver," in *Photonics Society Summer Topical Meeting Series*, (Newport Beach, CA), pp. 171–172, 2016.

[58] F.-X. Wang, W. Chen, Y.-P. Li, *et al.*, "Non-markovian property of afterpulsing effect in single-photon avalanche detector," *IEEE/OSA J. Lightw. Technol.*, vol. 34, pp. 3610–3615, Aug. 2016.

[59] D. Renker, "Geiger-Mode Avalanche Photodiodes, History, Properties and Problems," *Nuclear Instruments and Methods in Physics Research Section A: Accelerators, Spectrometers, Detectors and Associated Equipment*, vol. 567, pp. 48–56, Nov. 2006.

[60] Y. Huang, Y. Xu, and P. Xiatig, "A High-Fill-Factor SPAD Array Cell with a Shared Deep N-Well," in *Semiconductor Tech. Int. Conf.*, (China), pp. 1–3, Mar. 2016.

[61] D. P. Palubiak and M. J. Deen, "CMOS SPADs: Design Issues and Research Challenges for Detectors, Circuits, and Arrays," *IEEE J. Sel. Top. Quantum Electron*, vol. 20, no. 6, pp. 409–426, 2014.

[62] Z. Cheng, X. Zheng, D. Palubiak, M. J. Deen, and H. Peng, "A Comprehensive and Accurate Analytical SPAD Model for Circuit Simulation," *IEEE Trans. Electron Devices*, vol. 63, no. 5, pp. 1940–1948, 2016.

[63] G. Giustolisi, R. Mita, and G. Palumbo, "Behavioral Modeling of Statistical Phenomena of Single-Photon Avalanche Diodes," *Wiley Int. J. Circuit Theory Appl.*, vol. 40, no. 7, pp. 661–679, 2012.

[64] G. Zhang, C. Yu, C. Zhu, and L. Liu, "Feasibility Study of Multi-Pixel Photon Counter Serving as the Detector in Digital Optical Communications," *Optik–Int. J. Light Electron. Opt.*, vol. 124, no. 22, pp. 5781–5786, 2013.

[65] D. Chitnis, L. Zhang, *et al.*, "A 200 Mb/s VLC Demonstration with a SPAD Based Receiver," in *IEEE Summer Topicals Meeting Series*, pp. 226–227, July 2015.

[66] L. Zhang, H. Chun, G. Faulkner, D. O'Brien, and S. Collins, "A Comparison Between the Sensitivities of VLC Receivers Containing an Off-the-Shelf SPAD Array and an APD," in *Proc. IEEE Photonics Conf.*, (Orlando, FL, USA), pp. 27–28, Oct. 2017.

[67] L. Zhang, D. Chitnis, *et al.*, "A Comparison of APD-and SPAD-Based Receivers for Visible Light Communications," *IEEE/OSA J. Lightw. Technol.*, vol. 36, no. 12, pp. 2435–2442, 2018.

[68] B. Steindl, M. Hofbauer, *et al.*, "Single-Photon Avalanche Photodiode Based Fiber Optic Receiver for up to 200 Mb/s," *IEEE Journal of Selected Topics in Quantum Electronics*, vol. 24, no. 2, pp. 1–8, 2018.

[69] D. Milovancev, J. Weidenauer, *et al.*, "Visible Light Communication at 50 Mbit/s Using a Red LED and an SPAD Receiver," in *Int. Symp. on Communication Systems, Networks & Digital Signal Processing*, pp. 1–4, 2018.

[70] J. Zhang, L.-H. Si-Ma, B.-Q. Wang, J.-K. Zhang, and Y.-Y. Zhang, "Low-Complexity Receivers and Energy-Efficient Constellations for SPAD VLC Systems," *IEEE Photon. Technol. Lett.*, vol. 28, no. 17, pp. 1799–1802, 2016.

[71] L.-H. Si-Ma, J. Zhang, B.-Q. Wang, and Y.-Y. Zhang, "Energy-Efficient Multidimensional Hellinger Modulation for SPAD-Based Optical Wireless Communications," *Opt. Express*, vol. 25, pp. 22178–22190, Sept. 2017.

[72] L.-H. Si-Ma, J. Zhang, B.-Q. Wang, and Y.-Y. Zhang, "Hellinger-Distance-Optimal Space Constellations," *IEEE Commun. Lett.*, vol. 21, pp. 765–768, Apr. 2017.

[73] Y.-D. Zang, J. Zhang, and L.-H. Si-Ma, "Anscombe Root DCO-OFDM for SPAD-Based Visible Light Communication," *IEEE Photon. J.*, vol. 10, pp. 1–9, Apr. 2018.

[74] L. Zhang, H. Chun, G. Faulkner, D. O'Brien, and S. Collins, "Efficient Pulse Amplitude Modulation for SPAD-Based Receivers," in *Global LiFi Congress*, (Paris, France), pp. 1–5, Feb. 2018.

[75] T. Shafique, O. Amin, M. Abdallah, *et al.*, "Performance Analysis of Single-Photon Avalanche Diode Underwater VLC System Using ARQ," *IEEE Photon. J.*, vol. 9, no. 5, pp. 1–11, 2017.

[76] M. Elamassie and M. Uysal, "Performance Characterization of Vertical Underwater VLC Links in the Presence of Turbulence," in *Int. Symp. Communication Systems, Networks & Digital Signal Processing*, pp. 1–6, 2018.

[77] C. Wang, H.-Y. Yu, Y.-J. Zhu, T. Wang, and Y.-W. Ji, "Multi-LED Parallel Transmission for Long Distance Underwater VLC System with One SPAD Receiver," *Elsevier Opt. Commun.*, vol. 410, pp. 889–895, 2018.

[78] C. Wang, H.-Y. Yu, Y.-J. Zhu, and T. Wang, "Blind Detection for SPAD-Based Underwater VLC System Under P–G Mixed Noise Model," *IEEE Commun. Lett.*, vol. 21, no. 12, pp. 2602–2605, 2017.

[79] C. Wang, H.-Y. Yu, Y.-J. Zhu, T. Wang, and Y.-W. Ji, "Multiple-Symbol Detection for Practical SPAD-Based VLC System with Experimental Proof," in *Proc. IEEE Global Commun. Conf. Workshops*, (Singapore), pp. 1–6, 2017.

[80] C. Wang, H. Yu, Y.-J. Zhu, T. Wang, and Y. Ji, "One Symbol Training Receiver for the SPAD-Based UVLC System," *Applied optics*, vol. 57, no. 20, pp. 5852–5858, 2018.

[81] T. Mao, Z. Wang, and Q. Wang, "Receiver Design for SPAD-Based VLC Systems under Poisson–Gaussian Mixed Noise Model," *Opt. Express*, vol. 25, no. 2, pp. 799–809, 2017.

[82] J. Xiang, Y. Jia, *et al.*, "Channel Likelihood Correction for Photon-Counting Array Receivers in the Presence of Dead Time and Jitters," *Opt. Express*, vol. 26, no. 3, pp. 2848–2856, 2018.

[83] Y. Li, M. Safari, R. Henderson, and H. Haas, "Optical OFDM with Single-Photon Avalanche Diode," *IEEE Photon. Technol. Lett.*, vol. 27, pp. 943–946, May 2015.

[84] Y. Li, M. Safari, R. Henderson, and H. Haas, "Nonlinear Distortion in SPAD-Based Optical OFDM Systems," in *Proc. IEEE Global Commun. Conf. Workshops*, (San Diego, CA), 2015.

[85] T. Hamza, M.-A. Khalighi, S. Bourennane, P. Leon, and J. Opderbecke, "On the Suitability of Employing Silicon Photomultipliers for Underwater Wireless Optical Communication links," in *Int. Symp. on Communication Systems, Networks & Digital Signal Processing*, pp. 1–5, July 2016.

[86] A. Griffiths, J. Herrnsdorf, C. Lowe, *et al.*, "Temporal Encoding to Reject Background Signals in a Low Complexity, Photon Counting Communication Link," *Materials*, vol. 11, p. 1671, Sept. 2018.

[87] A. Griffiths, J. Herrnsdorf, C. Lowe, *et al.*, "Poissonian Communications: Free Space Optical Data Transfer at the Few-Photon Level," *arXiv preprint arXiv:1801.07994*, 2018.

[88] D. Zou, C. Gong, K. Wang, and Z. Xu, "Characterization of a Practical Photon Counting Receiver in Optical Scattering Communication," in *Proc. IEEE Global Commun. Conf.*, (Singapore), 2017.

[89] D. Zou, C. Gong, K. Wang, and Z. Xu, "Characterization on Practical Photon Counting Receiver in Optical Scattering Communication," *IEEE Transactions on Communications*, 2018.

[90] H. Mahmoudi, M. Hofbauer, B. Steindl, K. Schneider-Hornstein, and H. Zimmermann, "Modeling and Analysis of BER Performance in a SPAD-Based Integrated Fiber Optical Receiver," *IEEE Photon. J.*, vol. 10, no. 6, pp. 1–11, 2018.

[91] Y. Ji, G. Wu, and Y. Zuo, "Performance Analysis of SPAD-Based Underwater Wireless Optical Communication Systems," *Elsevier Proc. Comp. Science*, vol. 131, pp. 1134–1141, 2018.

[92] D. L. Snyder and M. I. Miller, *Random Point Processes in Time and Space*. New York: Springer-Verlag, 1991.

[93] D. R. Cox, *Renewal Theory*. New York: John Wiley & Sons Inc., 1962.

[94] R. G. Gallager, *Stochastic Processes: Theory for Applications*. Cambridge University Press, 2 ed., 2013.

[95] D. Zwillinger, *Table of Integrals, Series, and Products*. New York: Academic Press, 8 ed., 2014.

[96] C. C. Chen, "Effect of Detector Dead Time on the Performance of Optical Direct Detection Communication Links," *TDA Progress Rep.*, vol. 42–93, pp. 146–154, Mar. 1988.

[97] D. F. Yu and J. A. Fessler, "Mean and Variance of Single Photon Counting with Deadtime," *Phys. Med. Biol.*, vol. 45, no. 7, pp. 2043–2056, 2000.

[98] S. M. Kay, *Fundamentals of Statistical Signal Processing: Detection Theory*, vol. 2. Prentice Hall, 1998.

[99] R. G. Gallager, *Information Theory and Reliable Communication*. New York: Wiley, 1968.

[100] W. Hirt, *Capacity and Information Rates of Discrete-Time Channels with Memory*. PhD thesis, ETH Zurich, Zurich, Switzerland, 1988.

[101] H. D. Pfister, *On the Capacity of Finite State Channels and the Analysis of Convolutional Accumulate-m Codes*. PhD thesis, University of California, San Diego, CA, USA, 2003.

[102] D. M. Arnold, *Computing Information Rates of Finite-State Models with Application to Magnetic Recording*. PhD thesis, ETH Zurich, Zurich, Switzerland, 2003.

[103] D. M. Arnold, H. A. Loeliger, P. O. Vontobel, A. Kavcic, and W. Zeng, "Simulation-Based Computation of Information Rates for Channels with Memory," *IEEE Trans. Inf. Theory*, vol. 52, no. 8, pp. 3498–3508, 2006.

[104] T. M. Cover and J. A. Thomas, *Elements of Information Theory*. John Wiley & Sons, 2012.

[105] R. Blahut, "Computation of Channel Capacity and Rate-Distortion Functions," *IEEE Trans. Inf. Theory*, vol. 18, no. 4, pp. 460–473, 1972.

[106] S. Arimoto, "An Algorithm for Computing the Capacity of Arbitrary Discrete Memoryless Channels," *IEEE Trans. Inf. Theory*, vol. 18, no. 1, pp. 14–20, 1972.

[107] S. Shamai, L. H. Ozarow, and A. D. Wyner, "Information Rates for a Discrete-Time Gaussian Channel with Intersymbol Interference and Stationary Inputs," *IEEE Trans. Inf. Theory*, vol. 37, no. 6, pp. 1527–1539, 1991.

[108] S. Ghavami, R. S. Adve, and F. Lahouti, "Information Rates of ASK-Based Molecular Communication in Fluid Media," *IEEE Trans. Mol. Biol. Multi-Scale Commun.*, vol. 1, no. 3, pp. 277–291, 2015.

[109] J. G. Smith, "The Information Capacity of Amplitude- and Variance-Constrained Scalar Gaussian Channels," *Inf. Ctrl.*, vol. 18, no. 3, pp. 203–219, 1971.

[110] T. H. Chan, S. Hranilovic, and F. R. Kschischang, "Capacity-Achieving Probability Measure for Conditionally Gaussian Channels with Bounded Inputs," *IEEE Trans. Inf. Theory*, vol. 51, pp. 2073–2088, June 2005.

[111] S. M. Moser, "Capacity Results of an Optical Intensity Channel with Input-Dependent Gaussian Noise," *IEEE Trans. Inf. Theory*, vol. 58, pp. 207–223, Jan. 2012.